ICRR ANNUAL REPORT 2021

INSTITUTE

FOR

COSMIC RAY RESEARCH

THE UNIVERSITY OF TOKYO

ANNUAL REPORT
(APRIL 2021 – MARCH 2022)

ICRR
Institute for Cosmic Ray Research
University of Tokyo

5-1-5, Kashiwanoha, Kashiwa, Chiba 277-8582, Japan

Telephone: (81) 4-7136-3102
Facsimile: (81) 4-7136-3115
WWW URL: http://www.icrr.u-tokyo.ac.jp/

TABLE OF CONTENTS

PREFACE

This report summarizes the scientific activities of the Institute for Cosmic Ray Research (ICRR) of The University of Tokyo in the Japanese FY (JFY) 2021.

ICRR is an inter-university research institute for studies of cosmic rays. The headquarters of ICRR is located in Kashiwa, Chiba prefecture, Japan. In order to promote various cosmic-ray-related studies efficiently, ICRR has three research divisions; Neutrino and Astroparticle division, High Energy Cosmic Ray division, and Astrophysics and Gravity division. ICRR have four observatories in Japan; Kamioka Observatory and KAGRA Observatory (Kamioka underground, Gifu prefecture), Norikura Observatory (2770 meters above sea level, Mt. Norikura, Gifu prefecture), and Akeno Observatory (Yamanashi prefecture), together with 1 research center; Research Center for Cosmic Neutrinos (Kashiwa, Chiba prefecture). In addition, there are three major experimental facilities outside of Japan. They are located in Utah in USA, Yangbajing in Tibet, China and the La Palma island in Spain.

Many researchers from various Japanese institutions as well as those from overseas are involved in the research programs of ICRR. It should be noted that most of the scientific outputs from ICRR are the results of the collaborative efforts by many researchers from various institutions. In order to produce outstanding results, it is very important to carry out an experiment by an international collaboration composed of top-level researchers all over the world. Hence, all of the experimental collaborations that ICRR is involved are international ones. With these activities, ICRR has been selected as one of the institutions of the "International Joint Usage/Research Center" program by Ministry of Education, Culture, Sports, Science and Technology -Japan (MEXT) in November 2018.

In JFY 2021, our inter-university research activities have been largely affected by COVID-19. In many countries, overseas travels have been strictly restricted. Even the domestic travels within Japan have been limited. Even during the pandemic, ICRR has carried out various researches as described in this report.

We hope that this report is useful for the understanding of the current research activities of ICRR. Finally, we appreciate the strong support of our colleagues in this research field, The University of Tokyo and MEXT. They are indispensable for the continuing, and exciting scientific outcome of ICRR.

M. Nakahata

Masayuki Nakahata,
Director,
Institute for Cosmic Ray Research,
The University of Tokyo

The ICRR building at Kashiwa, Chiba, Japan.

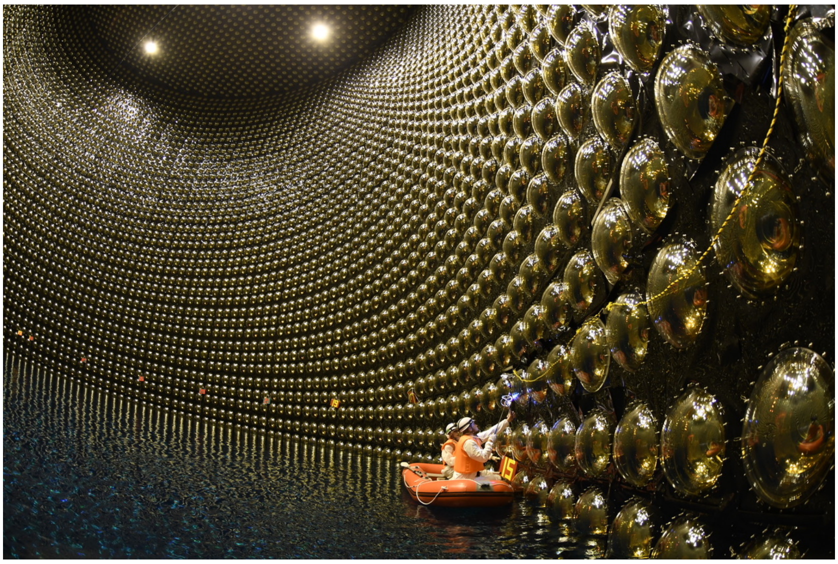

The Super-Kamiokande detector (the photo was taken during refurbishment work in 2018).

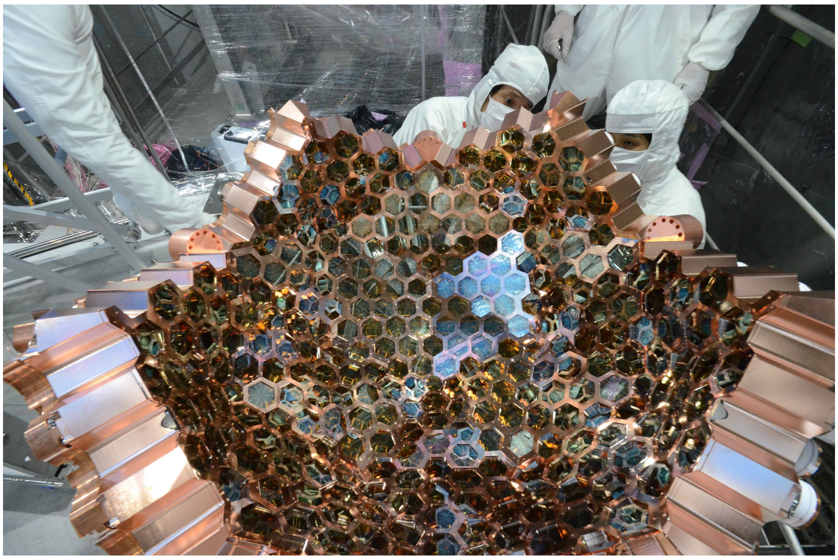

The XMASS detector (the photo was taken during the refurbishment work in 2013).

The first Large Size Telescope of CTA installed at Observatory Roque de los Muchachos inaugurated on October 10 2018.

Tibet-III air shower array (37000 m^2) at Yangbajing, Tibet (4300 m in altitude).

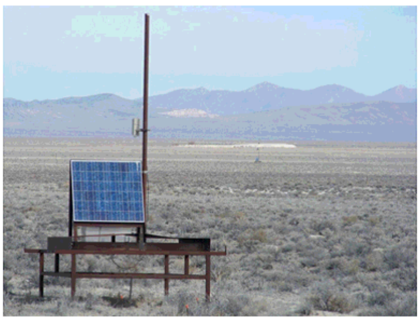

Air fluorescence telescopes (left) and a scintillator surface detector (right) of the Telescope Array experiment in Utah, USA to explore the origin of extremely high energy cosmic rays.

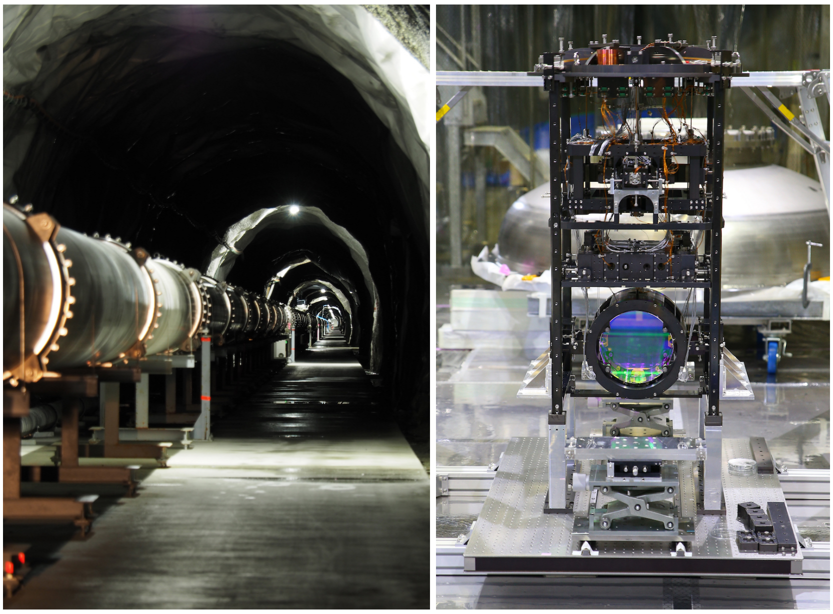

KAGRA's (left) 3km-long arm tunnel and (right) a sapphire mirror installed in a cryogenic suspension system.

Online public lecture co-organized with the Institute for the Physics and Mathematics of the Universe (Kavli IPMU).

Organization

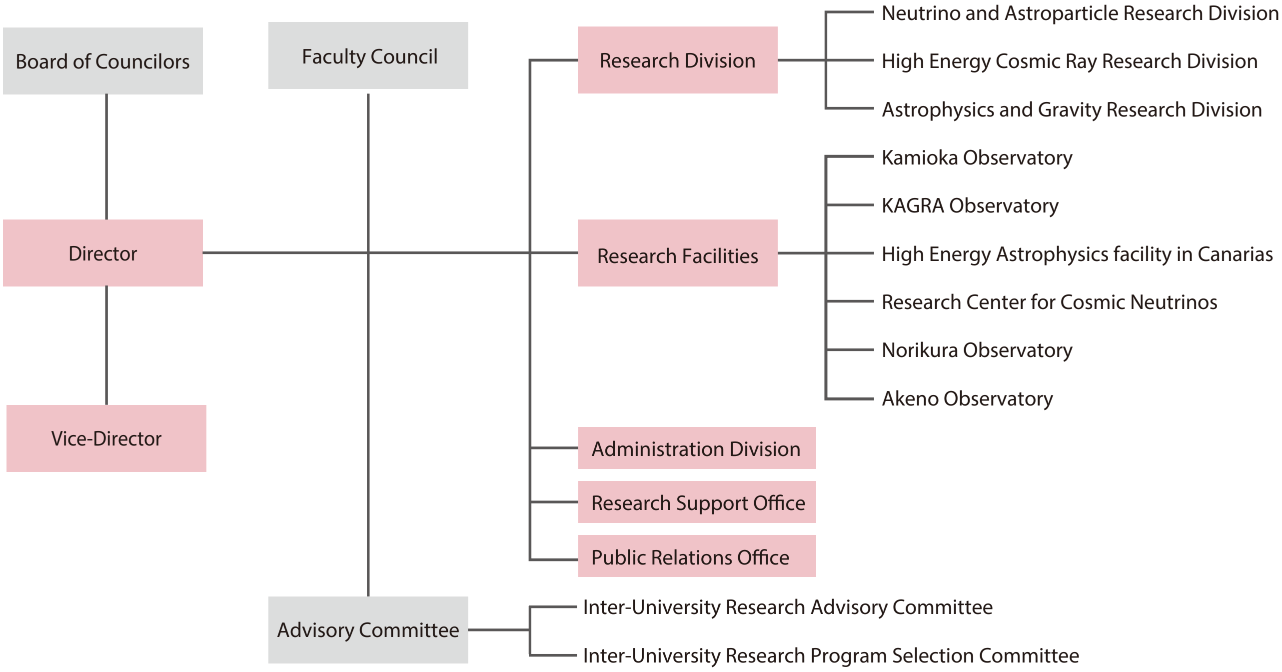

Number of Staff Members (As of May 1, 2021)

	Scientific Staff	Technical Staff	Research Fellows	Administrators and Secretaries	Total
Neutrino and Astroparticle Div.	23	6	0	19	48
High Energy Cosmic Ray Div.	20	12	9	3	44
Astrophysics and Gravity Div.	17	8	13	9	47
Administration	0	0	0	21	21
Total	60	26	22	52	160

FY 2014-2021 Budget

	2014	2015	2016	2017	2018	2019	2020	2021
Personnel expenses	706 000	684 000	683 000	779 000	823 000	872 000	898 000	898 000
Non-personnel expenses	1 282 000	1 595 000	1 288 000	1 514 000	1 729 000	1 611 000	1 173 000	2 078 000
Total	1 988 000	2 279 000	1 971 000	2 293 000	2 552 000	2 483 000	2 071 000	2,976,000

(in 1 000 yen)

RESEARCH DIVISIONS

Neutrino and Astroparticle Division

Overview

Super-Kamiokande

T2K Experiment

XMASS Experiment

XENON Experiment

Hyper-Kamiokande

High Energy Cosmic Ray Division

Overview

Cherenkov Cosmic Gamma-Ray Group

TA: Telescope Array Experiment

Tibet ASγ Experiment

ALPACA Project

High Energy Astrophysics Group

Other Activities

Astrophysics and Gravity Division

Overview

Gravitational Wave Group

KAGRA Project

Observational Cosmology Group

Theory Group

Particle Phenomenology

Particle Cosmology

NEUTRINO AND ASTROPARTICLE DIVISION

Overview

This division aims to study particle physics with prime interests in physics of neutrinos and proton decay, and astroparticle physics with the use of underground experimental facilities.

The Super-Kamiokande (SK) detector is a 50 kton water Cherenkov detector using 11,129 50 cm-diameter photomultipliers (PMTs) for its inner detector and 1,885 20 cm-diameter PMTs for its outer detector. The data taking of SK started in April 1996 and 20th anniversary was celebrated in 2016. The neutrino oscillations in atmospheric neutrinos were discovered in 1998 and thereby it was demonstrated that neutrinos have a finite mass. In 2001, the accurate measurements of the ^{8}B solar neutrino flux by SK and SNO discovered that neutrino oscillations are the solution of the solar neutrino problem beyond doubt. These findings became the research achievement for which the Nobel Prize in Physics was awarded in 2015. After the epoch-making discoveries, precise measurements of atmospheric neutrinos and solar neutrinos have been performed and they unraveled various phenomena of neutrino oscillations. The evidence of tau neutrino appearance in atmospheric neutrinos was confirmed in 2013 and atmospheric neutrino anomaly has been finally concluded. The indication of day-night asymmetry of the solar neutrino flux, which is expected from the matter effect of neutrino oscillations, was reported in 2014. At present, the most interesting subjects in those observations are the determination of neutrino mass hierarchy using atmospheric neutrinos and the consistency check of solar(ν_e) and reactor($\bar{\nu}_e$) oscillations.

A high intensity neutrino beam experiment using the J-PARC accelerator (T2K) was started in 2009. The T2K experiment uses the SK detector as the far detector. Search for leptonic *CP* violation and the high precision measurement of oscillation parameters are main physics subjects in T2K. An indication of electron neutrino appearance was found in June 2011, and later the electron appearance has been established with greatly improved significance. Since 2014, anti-neutrino beam data also have been taken in order to search for *CP* violation. T2K later reported the exclusion of the conservation of *CP* symmetry in neutrino oscillations at more than 95% CL.

The search for nucleon decay is another important subject at SK because it gives a direct evidence for the Grand Unified Theories (GUTs). SK gives the current best limit which strongly constrains various GUT models.

If a supernova happens in our galaxy, thousands of neutrino interactions are expected at SK and they will reveal detailed mechanism of the supernova explosion. SK is the only detector in the world which can identify the direction of the supernova neutrinos. So, SK has been operated almost all the time with small dead time and if a supernova is observed at SK, we will send burst information to astronomers as soon as it is detected. In addition, SK aims to observe supernova relic neutrinos, which is an accumulated supernova burst neutrinos from the beginning of the universe. For this purpose, it is planned to add 0.1% of gadolinium into the Super-K tank (called SK-Gd project) in order to tag neutrons for $\bar{\nu}_e$ detection. A feasibility study for the SK-Gd project is being performed using a 200 ton tank which mimics the Super-K detector. Refurbishment of the Super-K tank and upgrade of the water circulation system had been conducted in 2018 and 0.01% gadolinium has been dissolved in the detector water in the summer 2020.

Another activity of the Neutrino and Astroparticle division is a multi-purpose experiment using liquid xenon aiming at the detection of cold dark matter, neutrino absolute mass using neutrinoless double beta decay, and low energy solar neutrinos. A 800 kg liquid xenon detector was constructed in an experimental hall near the SK site. Data taking continued for more than five years and finished in February 2019. Searches for dark matter interactions and rare phenomena in liquid xenon are being conducted.

The Hyper-Kamiokande (Hyper-K or HK) experiment is proposed as a joint project of the University of Tokyo and KEK by combining a next generation underground water Cherenkov detector and upgraded J-PARC neutrino beam. The Hyper-K detector is an order of magnitude larger in detector fiducial mass than Super-K and has discovery potential of leptonic *CP* violation and proton decays. The project has officially started by receiving its first Japanese funding in the beginning of 2020. Its construction schedule includes 5 years of the cavern excavation, 2 years of instrumentation, and data taking commencement in 2027. In parallel, the J-PARC beam delivered to the detector will be upgraded from 0.5 to 1.3 MW over the same time period.

SUPER-KAMIOKANDE

[Spokesperson : Masayuki Nakahata
(Kamioka Observatory, ICRR, The University of Tokyo)]

Atmospheric neutrinos

Atmospheric neutrinos are produced from the decays of secondary particles produced in the collision of primary cosmic rays with nuclei in the atmosphere. Atmospheric neutrinos have several remarkable features:

- The flavor ratio, $(\nu_\mu + \bar{\nu}_\mu)/(\nu_e + \bar{\nu}_e)$ is 2 (>2 for above few GeV)
- Zenith angle distribution is up/down symmetry above a few GeV.

These features are realized without neutrino oscillations, and provide a useful constraint in the study of these neutrinos.

Super-Kamiokande has been observing atmospheric neutrinos since 1996 and has accordingly made several important measurements with them, including the discovery of neutrino oscillations [1].

After the first phase of Gd loading in the summer of 2020, SK has been operating its sixth run period, SK6, and has been accumulating atmospheric neutrino data ever since. Figure 1 shows the atmospheric neutrino data taken with Gd-loaded water (SK6) in comparison to data taken with pure water (SK5). There is no large charge in the detector's ability to observe atmospheric neutrinos and the SK6 data are judged to be of similarly high quality as those in previous pure-water periods.

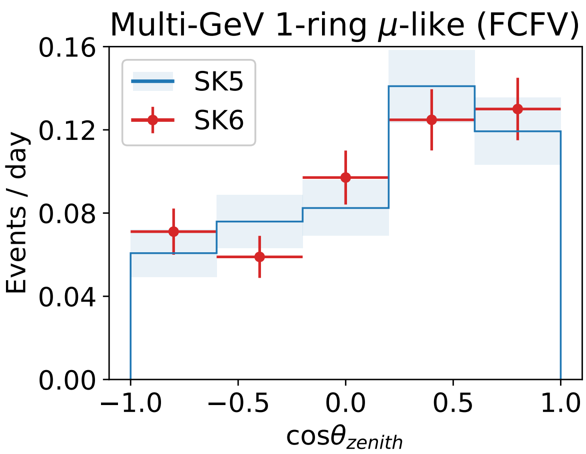

Fig. 1. Comparison of the atmospheric neutrino event rate in SK5 and SK6 for the multi-GeV μ-like sample.

Three flavor oscillations and the neutrino mass hierarchy

The SK atmospheric neutrino data are described at leading order by two-flavor $\nu_\mu \to \nu_\tau$ oscillations with maximal mixing (θ_{23}=π/4). However, sub-leading contributions via $\nu_\mu \to \nu_e$ oscillations induced by the mixing angle θ_{13} as well as the "solar" mixing parameters ($\Delta m^2_{12}, \theta_{12}$) provide the ability to probe currently unknown aspects of the standard neutrino oscillation paradigm, such as the existence of leptonic *CP* violation and the neutrino mass ordering (hierarchy). Understanding these open questions may bring important insight into larger questions, such as the origin and evolution of today's matter-dominated universe.

Several sub-leading oscillation effects are expected to appear in atmospheric neutrinos:

- Resonant enhancement of $\nu_\mu \to \nu_e$ oscillations due to the effects of matter is expected to occur at energies between 2 and 10 GeV and will manifest as an excess of upward-going electron-like events (e-like) in the atmospheric sample.

- This enhancement exists for either ν_e or $\bar{\nu}_e$ depending on the mass hierarchy. Therefore the mass hierarchy can be probed by understanding the relative amount of neutrino and antineutrino interactions in the detector.

- The combination of the solar oscillation parameters and the octant of $\sin^2\theta_{23}$ may enhance or suppress the event rate and, to some extent, alter the spectral shape of Sub-GeV electron-like data due to the $\nu_\mu \leftrightarrow \nu_e$ oscillations they induce.

- The standard oscillation paradigm includes a *CP*-violating factor, δ_{cp}, which is expected to induce several sub-dominant oscillation effects in many of the SK atmospheric neutrino samples, even if CP is conserved.

Super-Kamiokande has studied the effects of these oscillations on atmospheric neutrino data separated into fully-contained (FC) events, partially-contained (PC) events, and upward-going muon (UPMU) topologies. Fully-contained events are characterized by a primary interaction vertex that is located inside the fiducial volume of the detector and whose visible particles stop within the inner detector. On the other hand, though the primary vertex position of PC events is within the fiducial volume, they are characterized by having at least one charged particle escaping the inner detector and depositing light in the outer detector. In most cases the escaping particle is a muon. Upward-going muons originate from high energy muon-neutrino interactions in the rock surrounding the detector. Since all other particles are lost to interactions in the rock, only the muon is penetrating enough to reach the detector and be identified. The FC sample is separated into electron-like and muon-like (μ-like) subsamples by applying a particle identification algorithm to the most energetic Cherenkov ring of each event. Since PC and upward-going events are predominantly produced by muon neutrinos, no particle identification is applied. Though SK cannot distinguish on an event-by-event basis neutrino and antineutrino interactions, statistical separation of multi-GeV electron-like subsamples is performed to improve sensitivity to the mass hierarchy. A likelihood method designed to enhance the kinematic differences between neutrino and antineutrino interactions is applied to separate events into ν_e-like and $\bar{\nu}_e$-like subsamples.

Since the start of SK4 SK has had the ability to identify neutrons, albeit with a limited efficiency of 25%. In 2020 atmospheric neutrino events from this data set were separated into neutrino-like and antineutrino-like samples taking advantage of the fact that the former are expected to produce fewer neutrons on average than the latter. Further, a novel event selection based on a boosted decision tree was introduced to improve the classification of multi-ring events in all data periods. Using these new event selections all SK data until the end of the SK4 period (2018) were analyzed to update the analysis presented in [2, 3]. With an expected increase in hierarchy sensitivity of $\sim$ 15% this new analysis found a preference for the normal mass ordering of of between 71.4% and 90.3% over the range of oscillation parameters allowed at 90% C.L.. This result is somewhat weaker than that of the publication, whose preference was 81.9% to 96.7%. Similarly, the updated analysis prefers the first octant of $\sin^2\theta_{23}$ at roughly 1σ

and has a weak preference for a non-zero CP-violating phase. These results are summarized in Table 1 and in Figure 2.

A search for flavor changing neutral current and lepton universality-violating interactions using atmospheric neutrino data has also been performed by incorporating their effects on the predicted oscillations. In particular, these exotic interactions can be represented as additional potentials arising from exotic interactions with environmental quarks:

$$H_{matter} = V_{MSW} + \sqrt{2}G_F N_f(\vec{r}) \begin{pmatrix} \varepsilon_{ee} & \varepsilon^*_{e\mu} & \varepsilon^*_{e\tau} \\ \varepsilon_{\mu e} & \varepsilon_{\mu\mu} & \varepsilon^*_{\mu\tau} \\ \varepsilon_{\tau e} & \varepsilon_{\tau\mu} & \varepsilon_{\tau\tau} \end{pmatrix}. \quad (1)$$

Here the ε_{ij} represent additional non-standard interactions (NSI), N_f is the position-dependent fermion density, and V_{MSW} is the standard matter potential used to probe the mass hierarchy above. To avoid the computational complexity of fitting all of these parameters simultaneously, the analysis is broken into two parts. The first probes new interactions in the $\mu - \tau$ sector, allowing for NSI effects to appear atop of the normal atmospheric disappearance. In the second part the $e - \tau$ parameters, which modify the appearance of electron-type neutrinos, are studied. Note that this analysis is an update and upgrade of that in Ref. [4], that studied these phenomena using SK data up until 2005. The present analysis updates all aspects of the analysis, using the full data set up to 2016 and the event selection found in Ref. [3].

Neither of the NSI analyses found evidence of oscillations beyond the standard paradigm. At the 90% C.L. the parameters in the $\mu - \tau$ sector are constrained as

$$-4.5 \times 10^{-2} < \varepsilon_{\mu\tau} < 1.9 \times 10^{-2} \quad (2)$$

$$-5.1 \times 10^{-2} < \varepsilon_{\mu\mu} - \varepsilon_{\tau\tau} < 1.4 \times 10^{-1}. \quad (3)$$

Constraints on these parameters are shown in the left panel of Figure 3. The situation in the $e\tau$ sector is complicated by the inability of the SK data set to simultaneously determine the three relevant parameters. Instead the three are related as

$$\varepsilon_{\tau\tau} = \frac{\varepsilon_{e\tau}}{1 + \varepsilon_{ee}}. \quad (4)$$

Here, constraints are extracted in the $\varepsilon_{\tau\tau}$ and $\varepsilon_{e\tau}$ plane for a series of fixed values of ε_{ee}. An example constraint is shown in the right panel of the figure. In both sectors the fit is slightly improved by allowing non-zero values of the NSI parameters.

Searches for Neutrinos Associated with Gravitational Waves

Since the direct observation of gravitational waves in the LIGO and subsequently LIGO and VIRGO detectors, there has been considerable effort to observe coincident signals with other forms of radiation. In addition to electromagnetic signals already observed in, for instance, neutron star-neutron star merger events, astrophysical objects creating gravitational waves may also emit MeV (or higher) neutrinos. At present, no such coincident observation of neutrinos and gravitational waves has been achieved.

Based on a preliminary version of the GWTC-2 [5] catalog of gravitational waves detected from the LIGO-Virgo Collaboration (LVC), Super-Kamiokande performed follow-up observations of the triggers listed therein. The search was performed in time intervals of 1000 s around each trigger and found 8 events, 6 FC and 2 UPMU events, in coincidence. For this search the expected background was 7.13 events, indicating no statistically significant excess. Given the large distances (∼Mpc) to the black hole or neutron star mergers that produce these triggers, the neutrino signal, if any, is expected to be weak. On the other hand, as the origin of the gravitational wave signal can be somewhat localized by LVC comparisons of the arriving neutrino direction with each trigger's skymap were used to calculate a p-value for coincident event. Even with this additional directional information, all neutrino events were found to be consistent with the background expectation. Table 2 summarizes the SK coincident observation and Figure 4 shows the skymap for the event with the smallest p-value, a FC event arriving just before trigger S190602aq.

Bibliography

[1] Y. Fukuda *et al.* [Super-Kamiokande Collaboration], Phys. Rev. Lett. **81**, 1562 (1998).

[2] R. Wendell *et al.* [Super-Kamiokande Collaboration], Phys. Rev. D **81**, 092004 (2010).

[3] K. Abe *et al.* [Super-Kamiokande Collaboration], Phys. Rev. D **97**, no. 7, 072001 (2018).

[4] G. Mitsuka *et al.* [Super-Kamiokande Collaboration], Phys. Rev. D **85**, 113008 (2011).

[5] R. Abbott *et al.* Phys. Rev. X **11**, 021053 (2021)

Solar Neutrinos

Introduction

Solar neutrinos constitute by far the largest component of neutrino flux on the Earth among those produced from natural sources. Most of solar neutrinos are produced by proton-proton fusion, $p + p \to d + e^+ + \nu_e$, and its subsequent fusion reactions (pp-chain)[1]. They are categorized into the *pp*, *pep*, ^{7}Be, ^{8}B and *hep* neutrinos. Among these, Super-Kamiokande is sensitive to ^{8}B and *hep* neutrinos, which have relatively higher energy that extends up to ∼20 MeV.

Past observations of solar neutrino flux by Super-Kamiokande (SK) [1] and the Sudbury Neutrino Observatory (SNO) [2] led to the discovery of solar neutrino flavor conversion. Our current interest for solar neutrino measurements with the SK detector [3] is to make a precision test of the neutrino flavor conversion through the Mikheyev-Smirnov-Wolfenstein (MSW) effect [4, 5]. The MSW effect leads to a resonant conversion of the solar neutrinos within the Sun and results in an about 30% level of the survival probability above ∼5 MeV. The survival probability of lower energy neutrinos are described by the vacuum oscillation probability of ∼ 50%, and the transition region between the two lies at a few MeV region. This transition from the matter dominant oscillation to the vacuum dominant oscillation is often called as the

*1 with a subdominant (∼1%) contribution from the CNO cycle

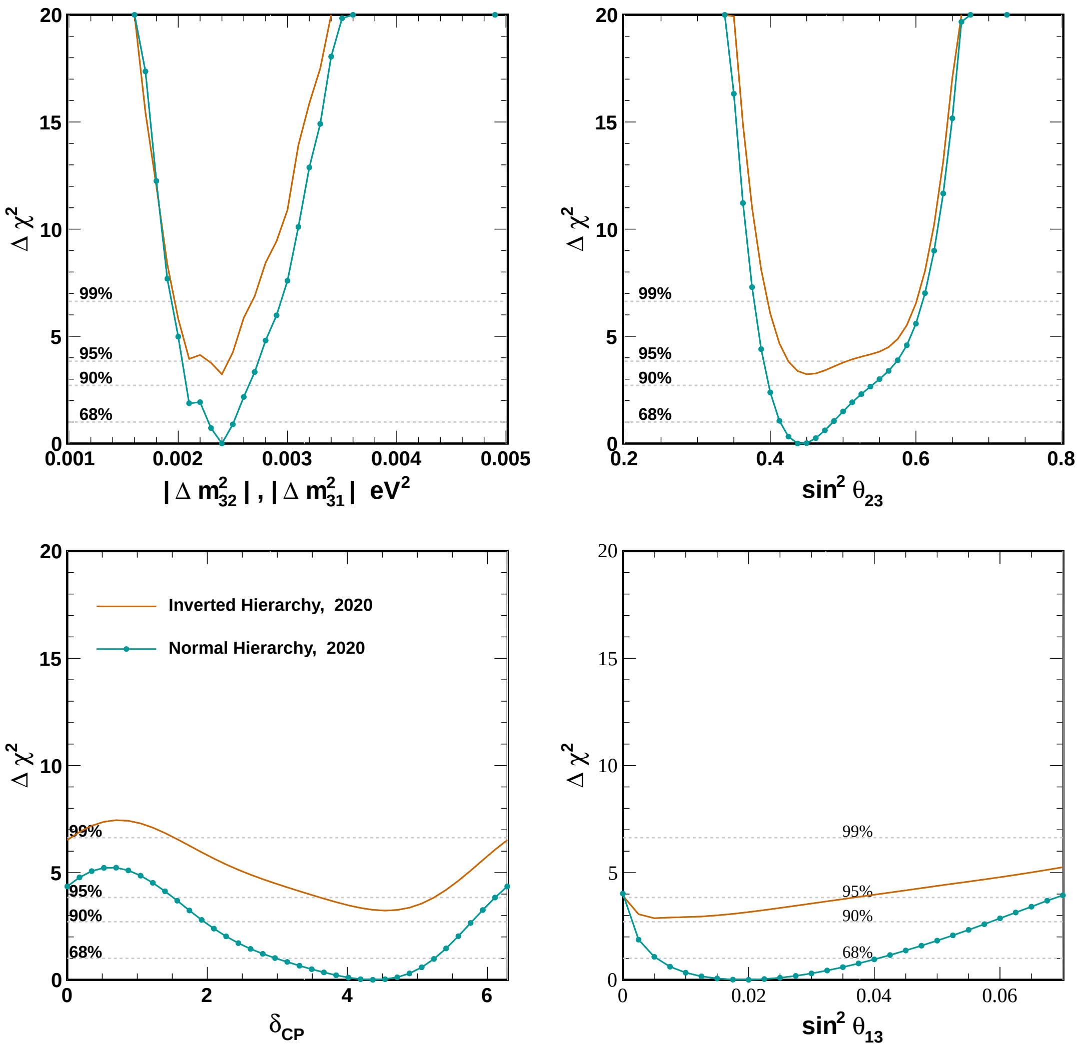

Fig. 2. The $\Delta\chi^2$ as a function of $\Delta m^2_{23,31}$, $\sin^2\theta_{23}$, and δ_{cp}. Fits to the normal (blue) and inverted (orange) hierarchy hypotheses are shown in the top two and bottom left plots. These are the results of a fit with $\sin^2\theta_{13}$ constrained to the preferred value from reactor measurements. Relaxing this constraint, results in a measurement of this parameter and in shown in the bottom right figure. With the extra degree of freedom the hierarchy significance (roughly the distance between the two lines) is reduced relative to the other plots.

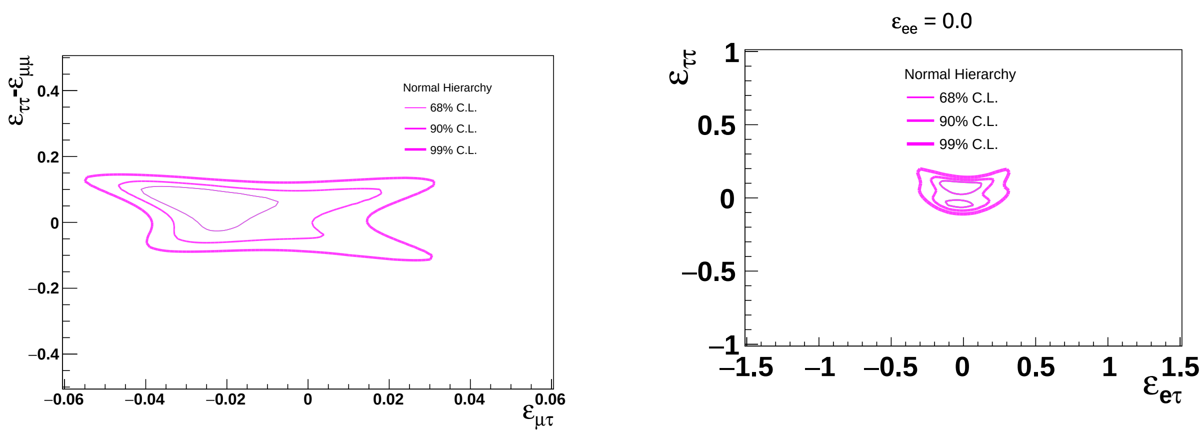

Fig. 3. Constraints on NSI parameters in the $\mu-\tau$ sector (left) and in the $e-\tau$ sector (right). These calculations assume standard PMNS oscillations at the best fit of the the 2018 SK analysis [3].

Fit	Hierarchy	$\sin^2\theta_{23}$	$\lvert\Delta m^2_{32,31}\rvert$ [$\times10^{-3}$ eV^2]	δ_{CP}
SK only	NH	$0.44^{+0.05}_{-0.02}$	$2.40^{+0.11}_{-0.12}$	$4.36^{+0.88}_{-1.39}$
	IH	$0.45^{+0.09}_{-0.03}$	$2.40^{+0.09}_{-0.32}$	$4.54^{+0.88}_{-1.32}$

Table 1. Best fit oscillation parameters obtained by the three flavor oscillation analysis. Fits are conducted for both the normal (NH) and inverted (IH) hierarchy assumptions The fit was performed assuming $\sin^2\theta_{13}$=0.0218, which is taken from PDG.

Name	Alert UTC	Obs.events (Δt)	p_Λ (%)	p_{χ^2} (%)
S190426c	2019-04-26 15:21:55	UPMU (+279 s)	100.0	51.0
S190513bm	2019-05-13 20:54:28	FC (−183 s)	5.7	15.5
S190602aq	2019-06-02 17:59:27	FC (−287 s)	2.8	1.6
S190728q	2019-07-28 06:45:10	FC (+103 s)	11.7	26.4
S190814bv	2019-08-14 21:10:39	FC (+249 s)	48.1	57.9
S190924h	2019-09-24 02:18:46	FC (+412 s)	48.1	76.5
S191213g	2019-12-13 04:34:08	FC (+289 s)	15.4	11.7
S200316bj	2020-03-16 21:57:56	UPMU (−366 s)	52.3	99.7

Table 2. Summary of atmospheric neutrino events found within 1000s of a gravitational wave trigger in the GWTC-2 catalog. Here Δt shows the time of the neutrino event to the trigger and the p-values describing the compatibility with the background hypothesis incorporating directional information p_Λ and additionally time information p_{χ^2}.

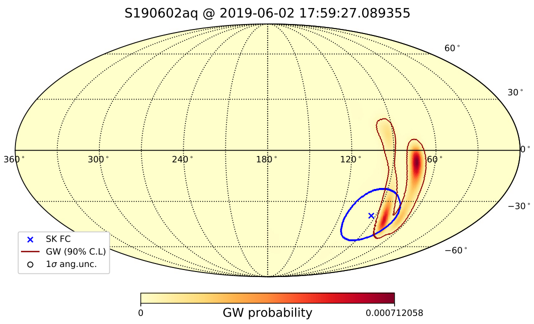

Fig. 4. Skymap showing the gravitational wave probability distribution from trigger S190602aq overlaid with the FC event found within 1000 s of its trigger time. The cross denotes the arrival direction of the neutrino and the circle indicates the expected directional resolution.

"up-turn" of the solar neutrino spectrum. Current experimental data is not enough to directly demonstrate this "up-turn" because of the experimental sensitivity as well as the statics.

SK aims to directly test the "Spectrum up-turn" by precisely measuring energy spectrum of ^{8}B solar neutrino in this transition region. This measurement is important not only to test the MSW effect but also to test several alternative theoretical models, such as sterile neutrinos [6, 7], mass-varying neutrinos [8], non-standard interactions [9, 10] and so on.

The matter effect can also be tested with the matter in the interior of the Earth. Electron flavor neutrinos are regenerated due to the matter effect of the Earth, making the neutrino flux in night is larger than that in day by about a few % level depending on the neutrino oscillation parameters.

In this article, we report results of solar neutrino measurements using the data taken through the end the fourth SK data taking phase (SK-IV) in May 2018, with an analysis method improved from our previous publication [11]. The total livetime used for this analysis is 5,805 days, with 2970 days from the SK-IV phase.

In addition to the standard neutrino oscillation analysis, we report the results of searching for solar electron antineutrinos due to spin-flavor precession in the Sun [12]. Finally, we briefly report the status of solar neutrino observation in the SK detector after loading the Gadolinium [13].

Analysis

For precisely measuring the energy spectrum of recoil electrons, the energy scale should be reduced and the removal of background events is essential. For that purpose, the detector simulation was improved with more accurate modeling of the PMT timing response and the non-uniformity of the water quality. For example, the energy reconstruction method was improved with a correction for the PMT gain drift and with a new correction of the energy scale non-uniformity. The correction for the gain drift was first introduced in 2017 and then refined in this analysis with an improved correction for the dark noise contribution. Furthermore, the correction for the PMT angular response was improved with more realistic simulation of the PMT response and arrangement. By introducing those improvements, the standard variation of the energy scale variation was reduced down to $\pm$0.5%, which is three times smaller than that previously estimated.

In addition to the energy scale improvements, the rejection method for the spallation backgrounds is also improved by tagging neutrons in the hadronic shower induced by cosmic muons. By applying this cut to the data sample, the signal efficiency improved about 12% while keeping the removal efficiency of muon spallation events about 90% [14].

^{8}B solar neutrino flux measurement

The SK detector observes solar neutrinos via elastic scatterings with electrons in pure water. The direction of a recoiled electron is highly correlated with the direction of the incident neutrino. Figure 5 shows the distribution of $\cos\theta_{\rm Sun}$ for solar neutrino candidates observed during the SK-IV phase. With the 2970 days of data in SK-IV, more than 60,000 events are observed over the background. Adding the solar neutrino events observed in other phases, the total number of the solar neutrino events is more than 100,000. Based on this data, the ^{8}B solar neutrino flux is determined to be $(2.35\pm0.04)\times10^6$ /cm^2/sec assuming a pure electron neutrino flavor content. The ratio between the SK result and the SNO NC current flux (5.25×10^6 /cm^2/sec) [15] is found to be 0.447 ± 0.008.

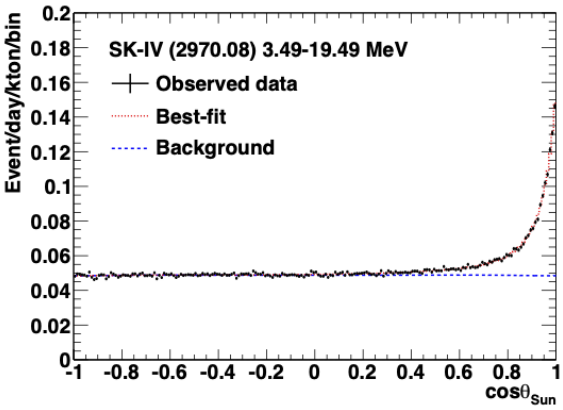

Fig. 5. The solar angle distribution in SK-IV. The horizontal axis shows the cosine of the solar angle $\cos\theta_{\rm Sun}$ and the vertical axis shows the number of the observed events. The black points shows the observed data, and the red (blue) histogram shows the best-fit (background) shape.

The solar activity cycle is the 11 years periodic change of sunspots releasing the magnetic flux at the surface of the Sun. The number of the sunspots strongly correlated with the solar activity cycle. The solar neutrino data set which is used for this analysis spans more than 21 years and covers about two solar activity cycles. Figure 6 shows the SK yearly flux measured throughout the different phases of SK together with the corresponding sunspot number (Source: WDC–SILSO, Royal Observatory of Belgium, Brussels [16]). The χ^2 between observed data and no time dependence hypothesis is calculated with the total experimental uncertainties as $\chi^2 = 23.25/22$ d.o.f., which corresponds to a probability of 38.8%. The SK solar rate measurements are fully consistent with a constant solar neutrino flux emitted by the Sun.

Energy spectrum analysis

Analysis of solar neutrino energy spectrum was done using all the data from SK-I to SK-IV [1, 17, 18, 11]. The data quality for SK-IV was significantly improved thanks to the new front-end electronics for SK-IV [19], the upgraded water circulation system and the upgraded calibration methods [20]. Owing to these upgrades, SK has achieved the lowest background (induced by radioisotopes in pure water, especially ^{214}Bi) among all the SK phases [21]. The energy threshold in SK-IV have been lowered to 3.49 MeV in recoil electron kinetic energy (SK-I: 4.49 MeV, SK-III: 3.99 MeV) and

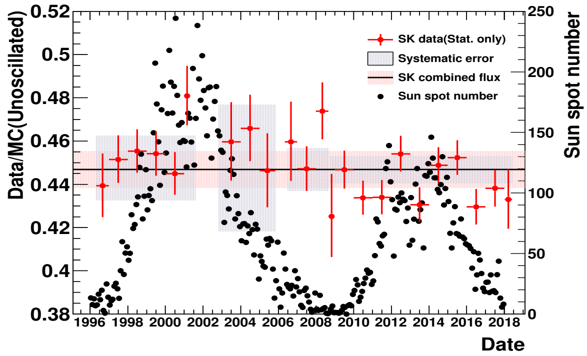

Fig. 6. The ratio of ^{8}B solar neutrino flux in SK over the SNO's NC current flux from 1996 to 2018. The red points show the yearly flux measured by SK (statistical uncertainty only), the gray bands show the systematic uncertainties for each SK phase, the black-horizontal line shows the combined measured flux with the uncertainty drawn as the red horizontal band. The back points show the sunspot number provided from [16].

this enabled SK to measure the solar neutrino energy spectrum with higher sensitivity. In addition, in May 2015, the trigger threshold was changed from 34 observed PMT signals within 200 nsec to 31 hits [22, 23]. Because of this lower threshold, the detection efficiency between 3.49 MeV and 3.99 MeV was improved from $\sim$86% to $\sim$100%. This improvement led to further reduction of the statistical uncertainty below 4.99 MeV in SK-IV.

Figure 7 shows the energy spectra obtained from SK-I, -II, -III and -IV, overlaid with the best-fits with generic polynomial and exponential functions, and the predictions assuming the current oscillation parameters described in the next section. Figure 8 shows the combined energy spectrum from SK-I to SK-IV with the predictions. Note that all SK the phases are combined without regard to energy resolution or systematic uncertainties in Figure 8, but those uncertainties are taken into account in the χ^2 calculation between the data and the prediction. Comparing χ^2 between the data (black) and the predictions (green or blue), the energy spectrum of SK is consistent within $\sim1\sigma$ with the MSW up-turn with both the SK+SNO best fit parameters (green in Fig. 10) and the KamLAND best-fit parameters (blue in Fig. 10). The data also slightly disfavors the flat oscillation probability by $\sim1\sigma$ significance.

Day-night asymmetry

The day-night asymmetry of the solar neutrino flux for the full SK-IV data set was extracted with the same method described in Ref. [24]. Here, the day-night asymmetry is defined as,

$$A_{D/N} = \frac{\Phi_{\rm day}-\Phi_{\rm night}}{0.5(\Phi_{\rm day}+\Phi_{\rm night})},$$

where $\Phi_{\rm day(night)}$ is the observed solar neutrino flux during day(night). Figure 9 shows the result of a day-night asymmetry amplitude fit as a function of Δm^2_{21} for the solar neutrino sample at $3.5 < E_{\rm kin} < 19.5$ MeV. The fitted day-night asymmetry, $A^{\rm Fit}_{D/N}$, assuming the SK+SNO best fit oscillation

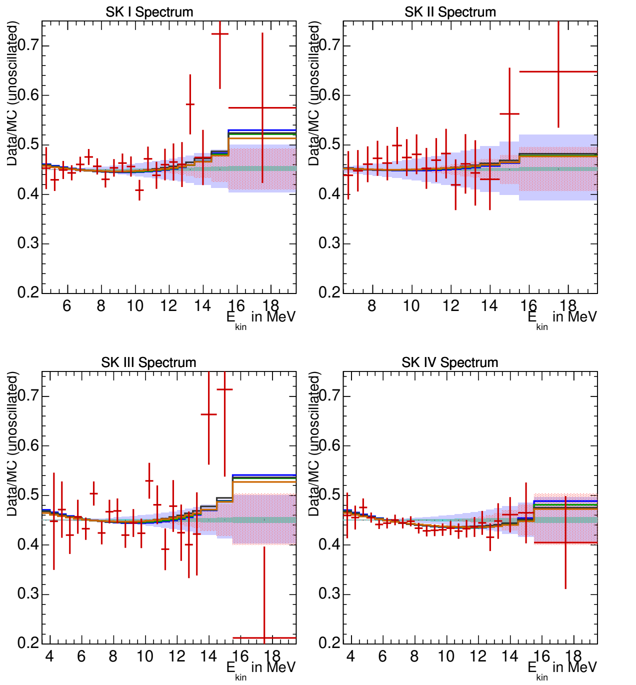

Fig. 7. SK-I, II, III and IV recoil electron spectra divided by the unoscillated expectation. The green (blue) line represents the best–fit to SK data using the oscillation parameters from the fit to SK and SNO (KamLAND) data. The orange (black) line is the best-fit to SK data of a general exponential or quadratic (cubic) P_{ee} survival probability. Error bars on the data points give the statistical plus systematic energy-uncorrelated uncertainties while the shaded purple, red, and green histograms give the energy-correlated systematic uncertainties arising from energy scale, energy resolution, and neutrino energy spectrum shift.

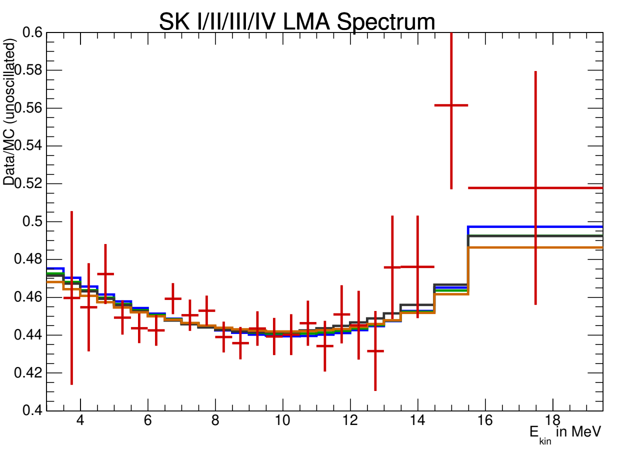

Fig. 8. The energy spectrum combining SK-I through SK-IV as a function of the recoil electron energy. The red points show the ratio of the data to the expected flux using a non-oscillated ^{8}B solar neutrino spectrum. The green (blue) curve shows the expected energy spectrum assuming the MSW effect inputting oscillation parameters of SK and SNO (KamLAND). The orange (black) line is the best-fit to SK data of a general exponential or quadratic (cubic) P_{ee} survival probability.

parameters (green in Fig. 10) was obtained as,

$$A^{\mathrm{Fit}}_{D/N} = (-2.1 \pm 1.1(\mathrm{stat.}))\% \quad (3.5 < E < 19.5\ \mathrm{MeV}).$$

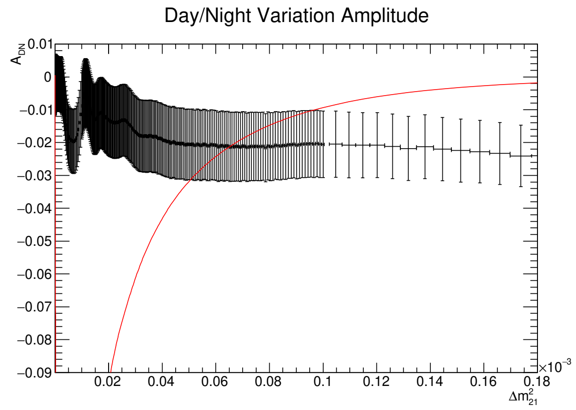

Fig. 9. Result of the day-night asymmetry amplitude fit as a function of the input Δm^2_{21} value. The black points show the data fit results with the statistical uncertainties, while the red curve show the expectation.

Oscillation parameter extraction

The oscillation parameters were extracted using the results from the solar neutrino measurements at SK and SNO [15], as well as the reactor antineutrino measurement by KamLAND [25, 26]. Figure 10 shows the allowed parameter region from the SK+SNO data as well as the KamLAND data. SK significantly contributes to the measurement of the solar angle θ_{12}. From the SK+SNO data, the mixing angle is determined to be $\sin^2\theta_{12} = 0.306 \pm 0.014$ and the mass difference is determined to be $\Delta m^2_{21} = 6.11^{+1.21}_{-0.68} \times 10^{-5}$ eV^2 as shown in Fig. 10. The SK+SNO fit results favors a lower Δm^2_{21} value compared to the KamLAND best fit value of $\Delta m^2_{21} = 7.54^{+0.19}_{-0.18} \times 10^{-5}$ eV^2. Currently, the SK+SNO data disfavors the KamLAND best fit value at $\sim 1.4\sigma$, while it was $\sim 2\sigma$ in the previous analysis. Adding the KamLAND result, the oscillation parameters are determined to be $\sin^2\theta_{12} = 0.306^{+0.013}_{-0.012}$ and $\Delta m^2_{21} = 7.51^{+0.19}_{-0.18} \times 10^{-5}$ eV^2.

Solar neutrino observation after Gd-loading

As reported in the later section, the Gadolinium was loaded into the Super-Kamiokande's pure water in 2020 summer [13] to enhance detector's sensitivity to supernova relic neutrinos by tagging neutrons originated from the inverse beta decay of electron anti-neutrino interactions.

In order to validate the detector performance, calibration data were taken after loading Gadolinium and compared with the results in pure water phase. For example, Figure 11 shows the reconstructed electron kinetic energy with the DT calibration device [27] before and after the Gd loading. The differences of the peak position and resolution between SK-V (pure water) and SK-VI (Gd concentration 0.011%) are less than $\pm 1\%$. Hence, the detector's energy scale is enough to continue to observe the solar neutrinos in the MeV region.

Figure 12 shows the typical distributions of $\cos\theta_{\mathrm{Sun}}$ before and after the Gd-loading. The peak of solar neutrinos around $\cos\theta_{\mathrm{Sun}} = 1$ is clearly observed even through we added the Gd into pure water. Figure 12 also demonstrates that no additional background exist in the energy range above 6.49 MeV after the Gd-loading. The background events below that level is under investigation since the detection efficiency for such events

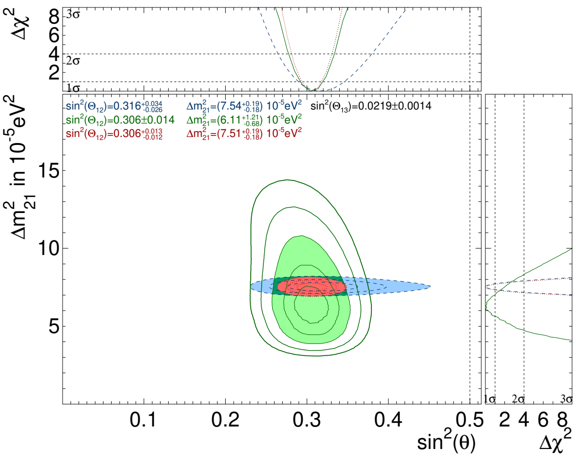

Fig. 10. The allowed contours for Δm^2_{21} vs. $\sin^2\theta_{12}$ from solar neutrino data at SK and SNO (green solid line). The allowed contour from KamLAND is also shown in blue. The combined allowed region is shown in red.

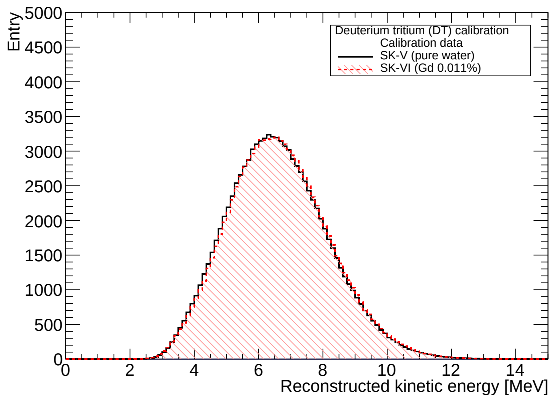

Fig. 11. The comparison of energy distribution between SK-V (pure water) and SK-VI (Gd concentration 0.011%). The calibration data was taken at the center position of the SK detector.

is different from that evaluated in pure water phase mentioned in the previous section.

Solar electron anti-neutrinos due to spin-flavor precession in the Sun

Due to a very low production rate of electron anti-neutrinos ($\bar{\nu}_e$) via nuclear fusion in the Sun, a flux of solar $\bar{\nu}_e$ is basically unexpected. An appearance of $\bar{\nu}_e$ in solar neutrino flux opens a new window for the new physics beyond the standard model. In particular, a spin-flavor precession process is expected to convert an electron neutrino into an electron anti-neutrino ($\nu_e \to \bar{\nu}_e$) when neutrino has a finite magnetic moment [28, 29].

In order to search for solar-$\bar{\nu}_e$ in the energy range of ^{8}B solar neutrinos, we required the delayed time coincidence technique to tag the neutron originated from the inverse beta decay

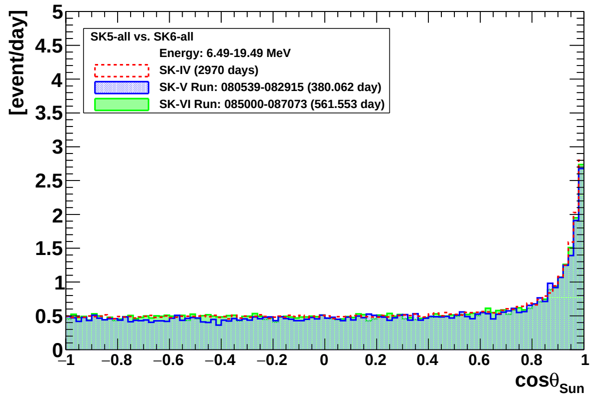

Fig. 12. The comparison of the cosine theta distribution between 6.49 and 19.49 MeV before and after the Gd-loading. The phases of SK-IV (red) and -V (blue) were operated by filling pure water while SK-VI (light green) was operated by adding Gd into the detector's pure water.

of solar-$\bar{\nu}_e$. For this purpose, the data reduction, which previously used for the supernova relic neutrino searches, was optimized by lowering the energy threshold down to 7.49 MeV of the produced positron kinetic energy. Figure 13 shows the selected events and the predicted spectrum of kinetic energy for solar-$\bar{\nu}_e$ events in an assumption of the conversion probability $P_{\nu_e\to\bar{\nu}_e} = 10^{-4}$. In this analysis, the number of solar-$\bar{\nu}_e$ events is derived after the fitting with the signal and background spectra. The observed numbers of events for the four energy bins are compared to the best-fit signal and background predictions. The amplitude of the signal is a free parameter. The signal and backgrounds have a known spectral shape which is included in the fit. Therefore, the upper limit of the conversion probability is evaluated in this study.

Figure 14 shows the $\Delta\chi^2$ as a function of the conversion probability $P_{\nu_e\to\bar{\nu}_e}$. As a result, the upper limit is determined to be $P_{\nu_e\to\bar{\nu}_e} < 4.7\times10^{-4}$ at 90% C.L., which corresponding to 36 events of solar-$\bar{\nu}_e$ signal. This limit is a factor of 17 more stringent than the SK-I sensitivity [30]. The neutrino magnetic moment derived from the $P_{\nu_e\to\bar{\nu}_e}$ probability in the spin-flavour precession model is calculated as $\mu \leq 1.7\times10^{-9}\mu_B$ $(10\ \mathrm{kG}/B_T)$ at 90% C.L., i.e. $\mu \leq 3\times10^{-8}\mu_B$ and $\mu \leq 2\times10^{-12}\mu_B$ at 90% C.L. in the assumption of $B_T \sim$ 600 G [31] and $\sim$ 7 MG [32], respectively.

Summary and outlook

In summary, Super-Kamiokande has precisely measured the ^{8}B solar neutrino flux, its time variation and recoil electron spectrum. Using 5,805 days of data, more than 100,000 solar neutrino interactions were extracted over the background. No significant correlation between the observed solar neutrino flux and the sunspot number was found with more than 21 years of continuous observation of the solar neutrino flux. The measured energy spectrum of ^{8}B solar neutrino is consistent within $\sim$1σ with the MSW up-turn with both the solar best-fit parameters and the KamLAND best-fit parameters. The previously existed $\sim$2σ tension between the solar and KamLAND best fit Δm^2_{21} values was reduced to $\sim$1.4σ in this analysis. Combining the solar neutrino oscillation anal-

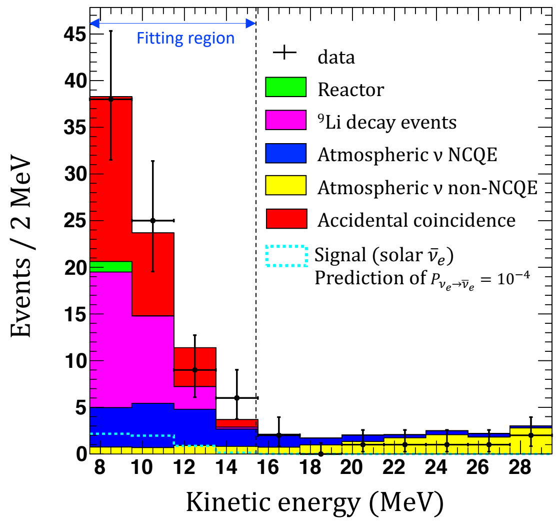

Fig. 13. Fit result in the kinetic energy range of 7.5–15.5 MeV. The black dots are data. The green, magenta, blue, yellow, and red histograms show best-fit predictions for reactor antineutrino events, ^{9}Li decay events, atmospheric neutrino's NCQE interactions and non-NCQE interactions, and accidental coincidences, respectively. The cyan dashed line is solar antineutrino signal events in an assumption of 10^{-4} of a neutrino-to-antineutrino conversion probability.

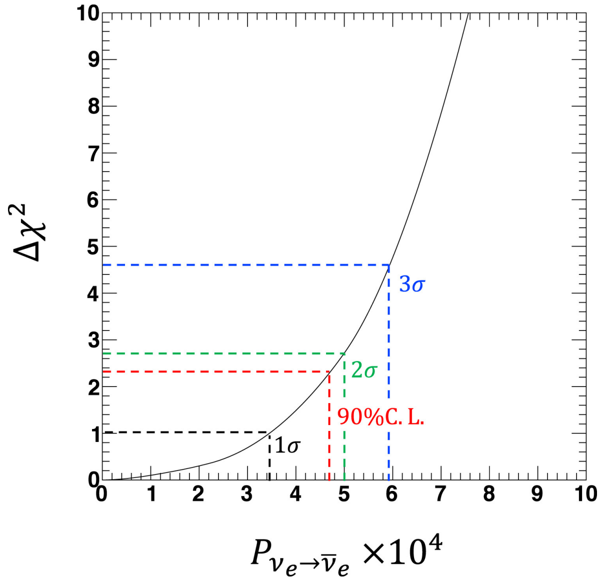

Fig. 14. Relation between $\Delta\chi^2$ and conversion probability of neutrinos to antineutrinos. The upper limits on $P_{\nu_e \to \bar{\nu}_e}$ for $\Delta\chi^2 = 1.0$, 2.3, 2.7, and 4.6 correspond to 3.5×10^{-4}, 4.7×10^{-4}, 5.0×10^{-4}, and 6.0×10^{-4}, respectively.

yses by SK, SNO and KamLAND, the oscillation parameters are determined as $\Delta m^2_{21} = 7.51^{+0.19}_{-0.18} \times 10^{-5}$ eV^2 and $\sin^2 \theta_{12} = 0.306^{+0.013}_{-0.012}$.

The Super-Kamiokande detector was recently upgraded by dissolving Gadolinium (Gd), and started a new phase of observation as SK-Gd. In order not to cause significant harm to the solar neutrino observation, ultra-pure $Gd_2(SO_4)_3$ powder with extremely low radio-impurity was newly developed and dissolved into the SK detector. Furthermore, the calibration data after the Gd-loading has been taken Enhanced neutron detection capability with Gd can be used to further reduce the cosmic-ray spallation backgrounds. We aim to further improve our solar neutrino measurements with additional data and analysis improvements in the SK-Gd era.

Bibliography

[1] J. Hosaka *et al.*, Phys. Rev. D **73**, 112001 (2006).

[2] Q.R. Ahmad *et al.*, Phys. Rev. Lett. **87**, 071301 (2001).

[3] Y. Fukuda *et al.*, Nucl. Instrum. Meth. A **501**, 418 (2003).

[4] S.P. Mikheyev and A. Y. Smirnov, Sov. Jour. Nucl. Phys. **42**, 913 (1985).

[5] L. Wolfenstein, Phys. Rev. D **17**, 2369 (1978).

[6] P.C. de Holanda and Y. Smirnov, Phys. Rev. D **69**, 113002 (2004).

[7] P.C. de Holanda and Y. Smirnov, Phys. Rev. D **83**, 113011 (2011).

[8] V. Barger *et al.*, Phys. Rev. Lett. **95**, 211802 (2005).

[9] A. Friedland *et al.*, Phys. Rev. B **594**, 347 (2004).

[10] O.G. Miranda *et al.*, J. High Energy Phys. **10** 008 (2006)

[11] K. Abe *et al.*, Phys. Rev. D **94**, 052010 (2016).

[12] K. Abe *et al.*, Astropart. phys. **139**, 102702 (2022).

[13] K. Abe *et al.*, Nucl. Instrum. Meth. A **1027**, 166248 (2022).

[14] S. Locke *et al.*, arXiv:2112.00092 [hep-ex].

[15] B. Aharmin *et al.*, Phys. Rev. C **88**, 025501 (2013).

[16] WDC-SILSO, Royal Observatory of Belgium, Brussels. http://www.sidc.be/silso/datafiles

[17] J.P. Cravens *et al.*, Phys. Rev. D **78**, 032002 (2008).

[18] K. Abe *et al.*, Phys. Rev. D **83**, 052010 (2011).

[19] H. Nishino *et al.*, Nucl. Instrum. Meth. A **610**, 710 (2009).

[20] K. Abe *et al.*, Nucl. Instrum. Meth. A **737**, 253 (2014).

[21] Y. Nakano, J. Phys. Conf. Ser. **888**, 012191 (2017).

[22] S. Yamada *et al.*, IEEE Trans. Nucl. Sci. **57**, 428 (2010).

[23] Y. Nakano, PhD thesis, The Univ. of Tokyo (2016).

[24] A. Renshaw *et al.*, Phys. Rev. Lett. **112**, 091805 (2014).

[25] S. Abe *et al.*, Phys. Rev. Lett **100**, 221803 (2008).

[26] A. Gando *et al.*, Phys. Rev. D **88**, 033001 (2013).

[27] E. Blaufuss *et al.*, Nucl. Instrum. Meth. A **458**. 636 (2001).

[28] A. Cisneros, Astrophys. Space. Sci **10**, 87 (1971).

[29] L. B. Okun *et al.*, Sov. J. Nucl. Phys. **44**, 440 (1986).

[30] A. Gando *et al.*, Astrophys. J., 745, 193 (2012).

[31] L.L. Kitchatinov, Astro. Repo. **52**, 3 (2008).

[32] A. Friedland and A. Gruzinov, Astrophys. J., **601**, 570 (2004).

Searches for neutrinos associated with powerful solar flares

Solar flares are the largest explosive events that occur around the surface of the Sun. This phenomenon is caused by the reconnection of magnetic field lines above sun spots and produces electromagnetic radiation from radio to γ-rays. Solar flares sometime occur associated with coronal mass ejections (CMEs), which are eruptions of the atmospheric plasma into interplanetary space. The frequency of these explosive events is strongly correlated with the activity of the Sun.

Neutrinos are only produced by accelerated protons above 300 MeV [1, 2], which can generate pions ($\pi^{\pm}$ and π^{0}) by interacting with dense plasma in the lower solar atmosphere during solar flares. The generated $\pi^{\pm}$ produce neutrinos in their decay chain. Neutrinos associated with solar flares (solar-flare neutrinos) provide information on particle acceleration mechanisms during the impulsive phase of solar flares.

We searched using the SK detector for neutrinos from solar flares that occurred during solar cycles 23 and 24, including the largest solar flare (X28.0) on November 4th, 2003. In order to minimize the background rate we searched for neutrino interactions within narrow time windows coincident with γ-rays and soft X-rays recorded by satellites [3]. In addition, we performed the first attempt to search for solar-flare neutrinos from solar flares on the invisible side of the Sun by using the emission time of coronal mass ejections (CMEs).

By selecting twenty powerful solar flares above X5.0 on the visible side and eight CMEs whose emission speed exceeds 2000 $\mathrm{km\,s^{-1}}$ on the invisible side from 1996 to 2018, we found two (six) neutrino events coincident with solar flares occurring on the visible (invisible) side of the Sun, with a typical background rate of 0.10 (0.62) event flare^{-1} in the energy range from 100 MeV to 10 GeV. Figure 15 shows an example of observed neutrino event from the largest solar flare occurring on November 4th, 2002 (X28.0) at the visible side of the Sun together with the light curve of soft X-ray (as well as its time derivative) recorded by GOES satellite. The event on November 4th 2003 was observed during the impulsive phase of the solar flare, where particle acceleration is expected to be active. Furthermore, Ref. [4] reported that relativistic neutrons associated with this solar flare were observed by the neutron monitors on the ground at 19:45 (UTC), which is about 3 minutes after the detection of the neutrino candidate in SK. This simultaneous observation also indicates that hadrons (ions) were accelerated to more than 1 GeV during this solar flare.

Although two (six) events observed from solar flares in the visible (invisible) side of the Sun, no significant solar-flare neutrino signal above the estimated background rate was observed. As a result we set the following upper limit on neutrino fluence at the Earth $\Phi < 1.1 \times 10^{6}\ \mathrm{cm^{-2}}$ at the 90% confidence level for the largest solar flare on November 4th, 2003. The resulting fluence limits allow us to constrain some of the theoretical models for solar-flare neutrino emission.

The Homestake experiment reported an excess of neutrino interactions when energetic solar flares occurred [5]. This observation suggested a possible correlation between solar flares and the neutrino capture rate on ^{37}Cl.

Based on the observed event below 100 MeV in the SK detector, we calculated the upper limit of neutrino fluence associated from solar flares. Figure 16 shows the upper limits of neutrino fluence obtained by the SK detector below about 100 MeV together with the experimental limits by other underground neutrino experiments [5, 6, 7, 8, 9].

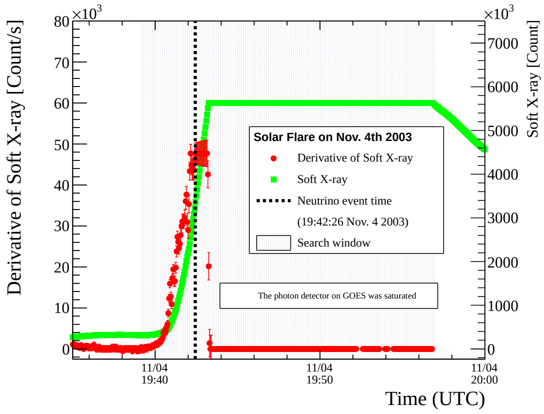

Fig. 15. The time of observed neutrino event for the solar flare on November 4th, 2003. The black vertical line shows the time of neutrino event in the SK detector. The red (green) plot shows the derivative of the light curves (original light curve) recorded by the GOES satellite. The shaded region shows the search windows determined by using the derivative of soft X-ray according to the method developed by [3]. In the case of the solar flare on November 4th, 2003, the instrument on the GOES satellite saturated due to the high intensity of soft X-rays. That resulted in the satellite not recording data for more than 15 minutes from 19:45 to 20:00.

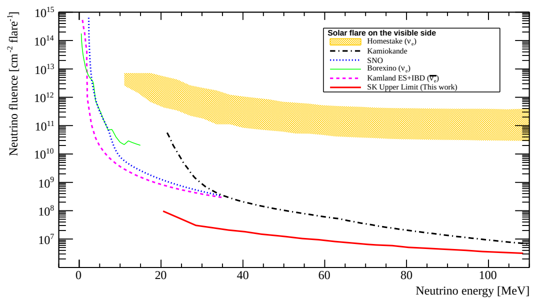

Fig. 16. The upper limit of neutrino fluence from the data taken by SK-I, II, III, and IV (red thick-solid) together with the other experimental results. The orange contour shows the allowed parameter region from the Homestake experiment [5]. Black long-dashed–dotted, blue dotted, green thin-solid, and pink dashed lines show the upper limits from Kamiokande [6], SNO [7], Brexino [8], and KamLAND [9] experiments, respectively.

Comparing to other experimental limits of neutrino fluence, the SK limit is improved by at least an order of magnitude in the energy region from 20 to 110 MeV. The SK limit excludes the allowed parameter region which was favored by the Homestake experiment and gives a strong constraint for neutrino fluence from powerful solar flares.

As prospect, the solar activity is expected to reach at its maximum around 2026 in solar cycle 25 and to have a powerful flare. The SK-Gd experiment has a high sensitivity to the electron anti-neutrino because of the existence of Gadolinium in the water tank and this improvement is also helpful to distinct anti-electron-neutrinos from electron neutrinos from solar flares in the next solar cycle.

Bibliography

[1] R. Ramaty, B. Kozlovsky, and R.E. Lingenfelter, Spa. Sci. Rev., **18**, 341–388 (1975).

[2] H. Hudson and J. Ryan, Ann. Rev. Astron. Astrophys., **33**, 239–282 (1995).

[3] K. Okamoto *et al.*, Sol. Phys., **295**, 133 (2020).

[4] K. Watanabe *et al.*, Astrophys. J., **636**, 1135 (2006).

[5] R. Davis, Prog. Part. Nucl. Phys., **23**, 13 (1994).

[6] K. Hirata *et al.*, Phys. Rev. Lett., **61**, 2653 (1998).

[7] B. Aharmim *et al.*, Astropart. Phys., **55**, 1 (2014).

[8] M. Agostini *et al.*, Astropart. Phys., **125**, 102509 (2021).

[9] S. Abe *et al.*, Astrophys. J., **924**, 103 (2022).

Search for nucleon decay

Proton decays and bound neutron decays (nucleon decays in general) are the most dramatic predictions of Grand Unified Theories (GUTs) in which three fundamental forces of elementary particles are unified into a single force. Super-Kamiokande (SK) is the world's largest detector to search for nucleon decays. Various nucleon decay modes have been looked for, but we have found no significant signal excess so far.

A proton decay into one charged lepton and one neutral pion ($p \to e^+\pi^0$, $p \to \mu^+\pi^0$) which baryon number is changed by 1, is one of the popular decay modes which most of GUT models predict and have relatively large detection efficiency. However, the predicted proton life time by minimal SU(5) has been rejected by SK results [1]. On the other hand, the dominant decay mode in ome SUSY GUTs have a different generation of quarks appears in the final state due to the contribution of the color triplet Higgs boson as $p \to \bar{\nu}K^+$ and $p \to \mu^+K^0$. In past, the results of $p \to \mu^+K^0$ with SK-I - SK-III data was published [2]. We updated the results with SK-IV data resulting 0.37 Mton· year in total exposure. Analysis was also updated for the new data: (1) an improved event reconstruction was applied [3] ; (2) the selection criteria were optimized separately for each K^0_L decay mode (the same selection criteria were applied to all K^0_S decay modes in the previous analysis); (3) the number of tagged neutrons was used to suppress the background.

There are 5 selections to extract each K^0 decay mode, two for K^0_S decay ($K^0_S \to 2\pi^0$, $K^0_S \to \pi^+\pi^-$), with following series of criteria A and B, respectively, and three for K^0_L decay ($K^0_L \to \pi^\pm l^\mp \nu$ where l is electron or muon, $K^0_L \to 3\pi^0$, and $K^0_L \to \pi^+\pi^-\pi^0$) with criteria C.

The following cuts are applied to select $K^0_S \to 2\pi^0$, mode.

A-1 Events should pass FCFV and E_{vis} selection.

A-2 The number of rings should be three, four or five.

A-3 There must be one non-showering ring corresponds to the primary muon.

A-4 There must be one Michel electron.

A-5 The reconstructed momentum of non-showering ring should be $150 < P_\mu < 400\ MeV/c$.

A-6 The reconstructed invariant mass of showering rings should be $400 < M_K < 600\ MeV/c^2$.

A-7 The reconstructed total momentum should be $P_{tot} < 300\ MeV/c$.

A-8 The reconstructed total invariant mass should be $800 < M_{tot} < 1050\ MeV/c^2$.

A-9 There should be no tagged neutrons.

To select $K^0_S \to \pi^+\pi^-$ mode, the following criteria is used.

B-1 Events should pass FCFV and E_{vis} selection.

B-2 The number of rings should be three.

B-3 All rings should be non-showering.

B-4 The number of Michel electrons should be one or two.

B-5 The reconstructed invariant mass of the second and third energetic non-showering rings should be $450 < M_K < 550\ MeV/c^2$.

B-6 The reconstructed total momentum should be $P_{tot} < 300\ MeV/c$.

B-7 The reconstructed total invariant mass should be $800 < M_{tot} < 1050\ MeV/c^2$.

K^0_L has longer lifetime than K^0_S and another selection is utilized.

C-1 Events should pass FCFV and E_{vis} selection.

C-2 Total observed photoelectrons (p.e.) should be $500 < Q_{tot} < 8000$ p.e.

C-3 The number of rings should be 2-3 for $K^0_L \to \pi^\pm l^\mp \nu$, 4-6 for $K^0_L \to 3\pi^0$, and 3-4 for $K^0_L \to \pi^+\pi^-\pi^0$.

C-4 The number of showering rings should be 0-1 for $K^0_L \to \pi^\pm l^\mp \nu$, , the number of non-showering rings should be 1 for $K^0_L \to 3\pi^0$, and the number of showering rings should be 2 for $K^0_L \to \pi^+\pi^-\pi^0$.

C-5 The number of Michel electrons should be 2-3 for $K_L^0 \to \pi^{\pm} l^{\mp} \nu$, 1 for $K_L^0 \to 3\pi^0$, and 2-3 for $K_L^0 \to \pi^+\pi^-\pi^0$.

C-6 The reconstructed muon momentum should be $260 < P_\mu < 410\ MeV/c$.

C-7 The reconstructed vertex separation should be $1.5\ m < v_{sep}$.

C-8 There should be no tagged neutrons.

Fiducial volume (FV) is defined 2 m away from the inner tank wall and total visible energy (E_{vis}) is requred to be more than 30 MeV to reject low energy BG. Figure 17 shows muon momentum after selection A-4, Kaon invariant mass after selection A-5 and number of neutrons after selection A-8. A peak around $150\,\mathrm{MeV}/c^2$ in Kaon invariant mass distribution is due to neutral pion either from the atmospheric neutrino interaction or decay of Kaon from proton decay.

K_L^0 has relatively longer lifetime and the secondary particles have another vertex separated from the primary one. The improved event reconstruction tool can find multiple vertices in a event. However, it is difficult to reconstruct all secondary particles from K_L^0 and we can not apply invariant mass cut used in other selections. Instead, a distance between the primary and secondary vertices is used to distinguish the signal events from the background. Figure 18 shows vertex separation distributions after applying all cuts except the cut on itself. The peak positions are different between the signal and atmospheric neutrino MC.

The results of these selections are summarized in Table 3. It contains the signal efficiency, the number of background events and the number of candidate events for each selection. Systematic uncertainties are also shown in the signal efficiencies and the background rates.

As a result, no candidates are remained for the final samples for all K^0 decays and the proton lifetime limit for $p \to \mu^+ K^0$ is obtained as 3.6×10^{33} years with 0.37 Mton $\cdot$ year exposure which is two times longer than the previous paper.

Bibliography

[1] K. Abe *et al.* [Super-Kamiokande Collaboration], Phys. Rev. D **102**, 112022 (2020).

[2] C. Regis *et al.* [Super-Kamiokande Collaboration], Phys. Rev. D, **85**, 112001 (2012).

[3] M. Jiang *et al.* [Super-Kamiokande Collaboration], Prog. Theor. Exp. Phys. **2019**, 053F01 (2019).

EGADS: From R&D for the gadolinium project to standalone Supernova monitor

As mentioned above, although at SK a few SRN events a year are expected, SRNs have not been detected yet because of the large backgrounds that constrain our search. The observation of SRNs in general or neutrinos from distant supernovae in particular, would give us some information about the universe, for example the core collapse rate from SRNs, and about the neutrino itself too, for example its lifetime. The main signal from SRN is expected to be the inverse beta decay reaction ($\bar{\nu}_e + p \to e^+ + n$), in which a positron and a neutron are produced, the delayed coincidence between the positron interaction and the neutron capture should allow to reduce the background affecting this analysis.

Before Gd loading in 2020, the SK detector had a poor neutron detection efficiency. It was then proposed to add 0.2% of gadolinium (Gd) sulfate by mass into SK in order to achieve a high neutron detection efficiency. Since Gd has a neutron capture cross section of 49.000 barns (about 5 orders of magnitude larger than that of protons) and emits a gamma cascade of 8 MeV, neutrons could be easily detected at SK (in space, vertices within tens of cm and in time, with the neutron capture delayed about 30 μsec).

EGADS (Evaluating Gadolinium's Action on Detector Systems) project was funded in 2009. The main motivation of EGADS was to show that by adding Gd, SK will be able to detect anti-neutrinos using the delayed coincidence technique, while keeping all its capabilities in the other analyses like solar and atmospheric neutrinos. Since then, a new hall near the SK detector has been excavated and a 200-ton tank with its ancillary equipment has been installed, see Fig.19, to mimic the conditions at SK. The selective water filtration system filters out water impurities while keeping the Gd in the water.

EGADS has been renamed as Employing Gadolinium to Autonomously Detect Supernovas after the installation of the new QBee electronics in 2017, following the Super-Kamiokande collaboration approbation of the SK Gd loading.

Water system operations

From January 2010 to July 2011 we circulated pure water through the 200-ton tank and proved that our water system is stable and achieves a high water quality. In 2013, from February 6th to April 20th, the 200-ton tank has been step wise loaded with Gd sulfate until the final 0.2% concentration was reached. Two values are monitored at three different depths: the Cerenkov light left after travelling 15 m (LL15) in water and the Gd concentration. Both values confirmed that we can achieve and maintain a good water quality and that Gd sulfate homogeneously and quickly dissolves in the 200-ton tank.

In summer 2013, we installed 240 photo-multipliers and the data taking started from September without Gd and with a DAQ based on old SK ATM modules. In April 2015, the target concentration of 0.2% $Gd_2(SO_4)_3$ was achieved. Figure 20 shows the time variation of LL15. The blue band in the figure shows typical values for SK-III and SK-IV. As shown in the figure, the transparency of 0.2% $Gd_2(SO_4)_3$ water is within the SK range. In addition to the good water transparency, no Gd loss has been detected since the EGADS detector reached the final concentration until it was emptied again after about 2 years and 5 months, in October 2017.

Detailed studies have evaluated the impact on current analyses at SK. These studies show that current analyses will be basically unharmed after adding Gd in SK and all other tests and studies conducted have shown no showstoppers. As a consequence, the SK collaboration decided in spring 2015 to approve the SuperK-Gd project. The results of these analysis were published in [1].

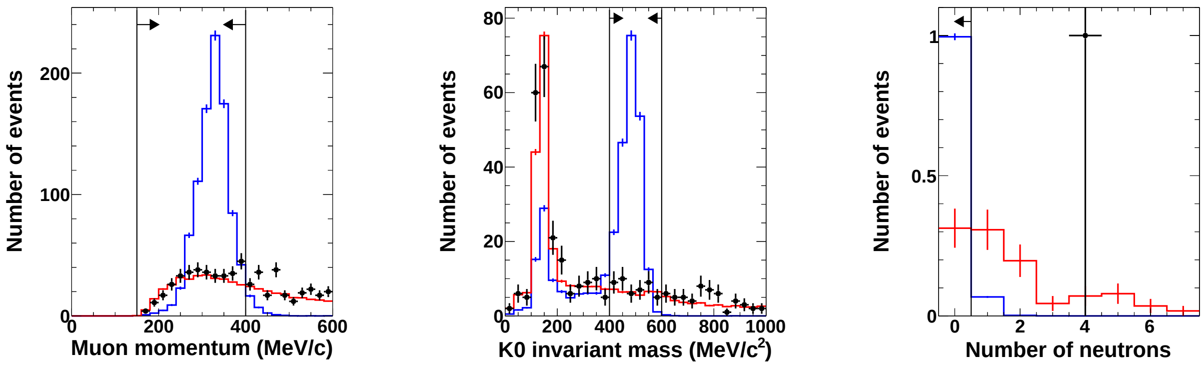

Fig. 17. Reconstructed muon momentum after selection A-4 (left), Kaon invar iant mass after selection A-5 (center) and number of tagged neutrons after sele ction A-8 (right). The data (black dots) are compared with the atmospheric neutrino MC (red) normalized by the livetime, and the signal MC (blue) normalized to the atmospheric neutrino MC.

Table 3. Summary of the $p \to \mu^+ K^0$ search. Uncertainties are quadratic sum of statistical and systematic errors.

Search mode	Efficiency (%)	Background (events)	Candidates (events)	Lower limit (10^{33} years)
$K_S^0 \to 2\pi^0$	9.7 ± 1.0	0.31 ± 0.14	0	2.7
$K_S^0 \to \pi^+\pi^-$	4.98 ± 0.54	0.8 ± 0.2	0	1.4
$K_L^0 \to \pi^\pm l^\mp \nu$	0.91 ± 0.17	1.0 ± 0.3	0	0.2
$K_L^0 \to 3\pi^0$	0.36 ± 0.06	0.12 ± 0.06	0	0.1
$K_L^0 \to \pi^+\pi^-\pi^0$	0.18 ± 0.04	0.16 ± 0.07	0	0.05
SK-IV combined (199 kton·years)				4.6
SK-I+SK-II+SK-III+SK-IV combined (372 kton·years)				3.6

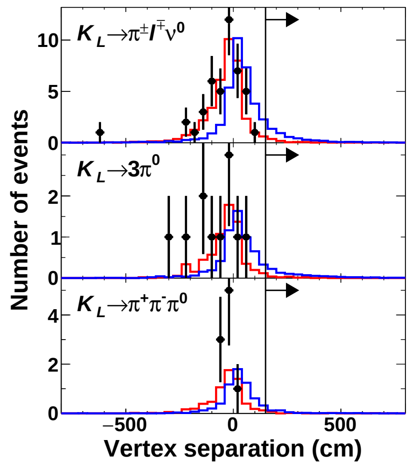

Fig. 18. Reconstructed vertex separation distribution in $K_L^0 \to \pi^\pm l^\mp \nu$ (top), $K_L^0 \to 3\pi^0$ (center) and $K_L^0 \to \pi^+\pi^-\pi^0$ (bottom) selections. All cuts except vertex separation are applied. The data (black dots) are compared with the atmospheric neutrino MC (red) normalized by the livetime, and the signal MC (blue) normalized to the atmospheric neutrino MC.

Fig. 19. In the new cavern, the 200-ton tank (a) with currently 240 photo-multipliers installed, the Gd pre-mixing and pre-treatment 15-ton tank (b), the selective filtration system (d), Gd removal resins (c) for test and a device to measure the water transparency (e) have been installed.

In order to test the Gd-loading in SK, the detector was refilled with pure-water in November 2017, and loaded with 0.02% $Gd_2(SO_4)_3$ in the end of March 2018. This loading was performed using only the pre-treatment and the fast re-circulation systems, with one pass, similar to what is expected for SK 0.02% loading.

Since then, different configurations of the water system have been tested in order to determine what is needed to ensure high water transparency in SK without band-pass system. Figure 21 shows the time variation of LL15 since this loading until May 2020. From March 2018 to June 2018 a slow but continuous decrease of the water transparency has been observed ith the fast re-circulation system only. From June 2018 to August 2018 the use of the band-pass system allowed to recover high water transparency. There-after the fast-re-circulation system only has been used.

In May 2019, the water system was stopped for about one

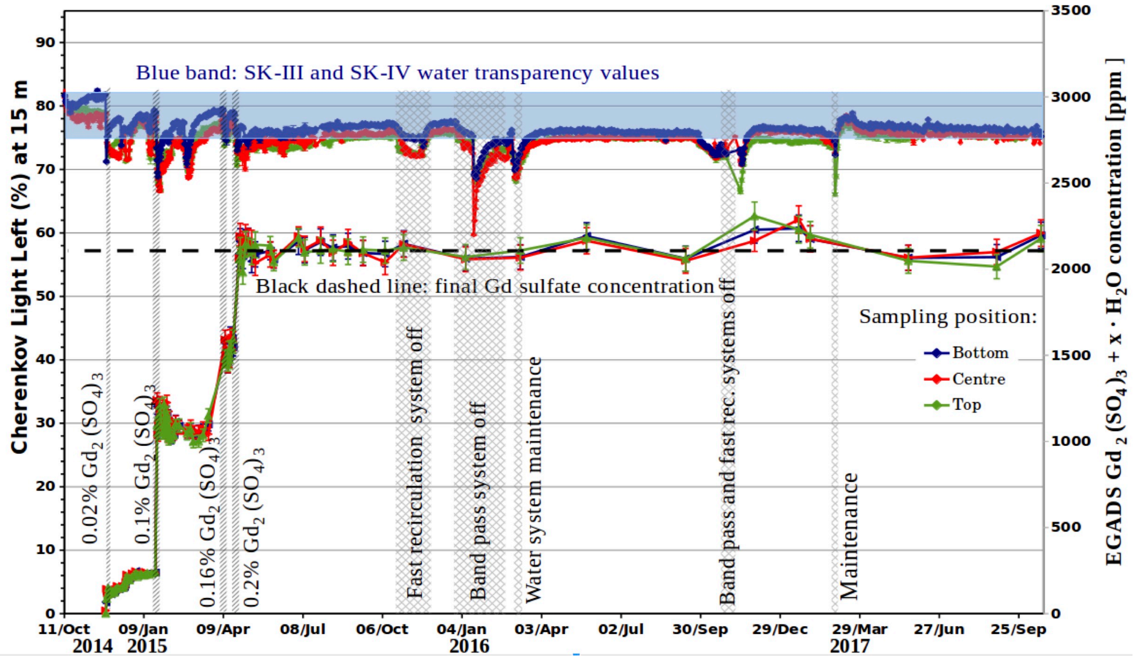

Fig. 20. Cerenkov light left at 15 m for Gd loaded water in EGADS until September 2017. The horizontal blue band are the typical values for SK-III and SK-IV. The vertical lines shows the injection dates where we also indicate the concentration (% in mass) in the 200-ton tank. The black dashed line shows the final expected concentration.

week due to electrical damage following a power-cut. This led to a reduction of the water transparency. After restarting, the water transparency was recovered. On September 2019 the water flow was modified so that only half of the flow pass through the special cation exchange resin. The water transparency remained stable and high. Finally, in November 2020, in order to simulate the future additional Gd loading in Super-Kamiokande, EGADS was loaded from 0.01% to 0.03% Gd concentration.

Ion exchange resin tests

Impurities in water Cerenkov detector's water can be removed using anion and cation resins as a standard method.

In case of Gd-loaded water, standard cation exchange resins are expected to also remove Gd. Hence, a special cation exchange resin has been developed and installed in EGADS, in addition to the usual anion exchange resin. The installation was done in January-February 2019 (in January, the new cation exchange resin was used alone, leading a water transparency drop). As showed in Figure 21, we observed an improvement of the water transparency compared than with only anion exchange resin. This increase was enhanced following the replacement of the TOC and UV lamps in March 2019, which stresses the importance of the ionization lamps for the water transparency.

In 2020, we learned the AmberJet 4400 anion exchange resin will be discontinued soon by its manufacturer. In order to replace it we started to test several other resin substitute candidates. In May 2021, we started to test AmberJet 4002 which allowed to quite a high water transparency. The initial drops following the installation of this new resin were due to a too short resin flushing period.

From November 2021, we learned the AmberJet 1020 (Gd) special cation resin was also going to be discontinued by its manufacturer. A substitute candidate, Amberlite IR120B (Gd), was installed in the water system in December 2021. Preliminary results shows acceptable results, though not as good as the AmberJet 1020 (Gd).

DAQ operations

In June 2017, EGADS electronics have been upgraded from the ATM electronics to SK's QBee electronics, the DAQ system was also upgraded to use these new electronics. Thanks to this upgrade, the stability of the DAQ has been greatly improved, specially at high rate. Several SN tests were performed, and demonstrated that EGADS is able to detect and process a 10 second long burst of more than 100k Hz without trouble. This is much more than what is expected from a very close galactic SN burst: in case of Betelgeuse, about 25k events are expected according to Nakazato's model.

We developed an online fitter, HEIMDALL, based on SK WIT. It is able to reconstruct all the events online during a SN burst and then provides an alarm within few seconds. HEIMDALL is looking for IBD candidates, therefore taking advantage of the delayed coincidence to reduce the background. Thanks to this, EGADS is able to look for SN in the far end of our galaxy. This enable us to instantly and autonomously detect a galactic SN and report to local experts and neutrino and astronomy community.

Bibliography

[1] Marti, Ll. et al., NIM-A 959, 163549 (2020)

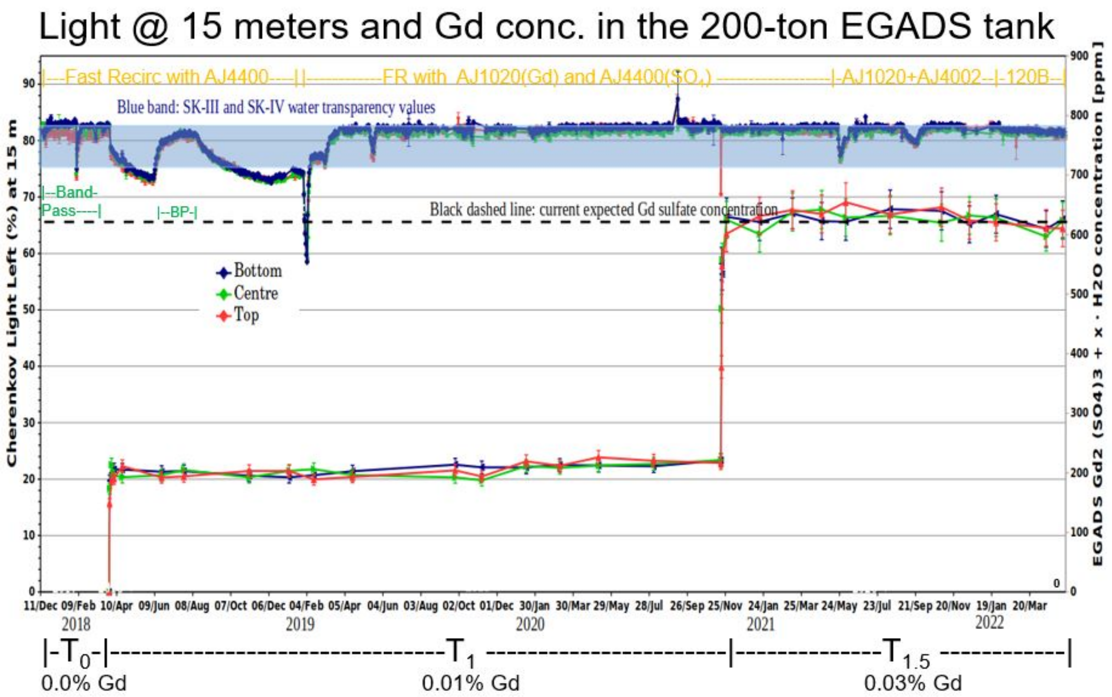

Fig. 21. Cerenkov light left at 15 m for Gd loaded water in EGADS since December 2018. The horizontal blue band are the typical values for SK-III and SK-IV. The vertical lines shows the injection dates where we also indicate the concentration (% in mass) in the 200-ton tank. The black dashed line shows the final expected concentration.

SK-Gd

In SK-Gd project, the sensitivity of anti-electron neutrino observation has been improved significantly by detecting neutrons with gadolinium (Gd) (specifically, gadolinium sulfate octahydrate ($Gd_2(SO_4)_3 \cdot 8H_2O$)). Already in 2020, 0.01% Gd (about 13 tons in total weight of $Gd_2(SO_4)_3 \cdot 8H_2O$) has been introduced, achieving about 50% neutrino capture efficiency [1]. As a next step, we plan to increase Gd to 0.03% during June - July 2022 to achieve 75% neutron capture efficiency. The plan aims to dissolve twice as much $Gd_2(SO_4)_3 \cdot 8H_2O$ (the total weight of $Gd_2(SO_4)_3 \cdot 8H_2O$ for this time is about 26 tons) in a month as it did in 2020. In order to achieve it, the dissolving system was improved in this fiscal year while continuing the physics observation. In parallel, the sensitivities of Super-K at the next Gd concentration have been estimated. In this report, the sensitivities regarding the observations of the supernova neutrinos will be explained, which are main physics targets of SK-Gd.

Supernova Relic Neutrinos

Neutrinos flying like background radiation originating from numerous supernova explosions that have occurred since the beginning of the universe are called “supernova relic neutrinos (SRN)”. Observation of SRN will be a key to describe an average picture of a supernova explosion, but it has not been discovered yet. The energy spectrum of anti-electron neutrinos on the earth is shown in Fig.22. The SRN is the expected to be the main component of the anti-electron neutrino that reaches the earth in the energy range of 10-30 MeV while reactor neutrinos dominate in 10 MeV or less, and atmospheric neutrinos dominate in 30 MeV or more. After the next loading in 2022, the neutron capture efficiency by Gd will be enhanced to 75% which increases the detection efficiency for signals by about 50% compared to the current Gd concentration. Furthermore, it is expected that the accuracy of the atmospheric neutrino component, which is a main background of SRN, will be improved by using the results of the T2K experiment and the new results from nuclear experiments. Fig.23 shows the sensitivity for SRN. In SK-Gd, it is possible to search for SRN with much higher sensitivity than before in a short period of time. By 2022, the sensitivity is expected to exceed the results of the pure water period with about 16 years observation, and in the next 5 years until 2027, the sensitivity will be expanded to the region predicted by most models. Then, we are aiming for the world’s first observation of SRN.

Supernova Burst Neutrinos

One of the most important observable in the supernova neutrino burst observation by Super-K is the direction of a supernova. Since neutrino bursts can escape from supernovae faster than light, they are expected to reach Earth minutes to hours earlier than light. Therefore, an announcement of the direction of the supernova makes it possible to direct astronomical telescopes to the supernova before the light from the supernova actually arrives. Super-K is the only detector that can make such an announcement by itself. SK-Gd also improves the directional accuracy of a supernova. The direction of the observed particles and the direction of the neutrinos differ depending on the neutrino reaction. In the inverse beta decay reaction (IBD), the angular distribution is almost uni-

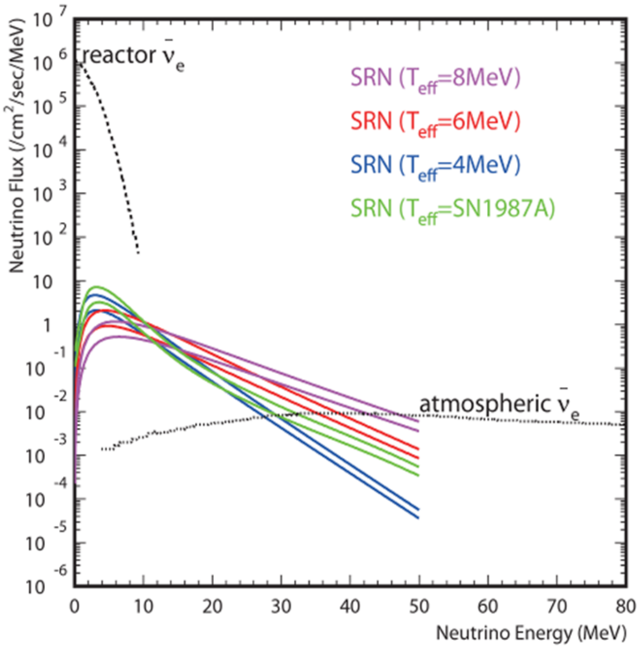

Fig. 22. Expected energy spectrum of SRN.

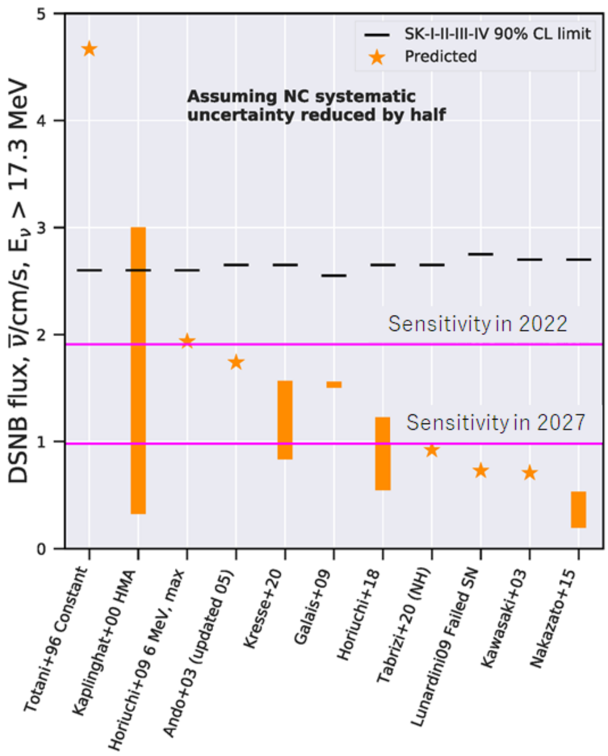

Fig. 23. Expected sensitivity of SRN detection compared to SRN model predictions.

form, and information about the direction of the supernova is lost. On the other hand, in a electron scattering, the scattered electron is scattered in the direction of the neutrino, so this information can be used to determine the direction of the supernova. Since electron scattering events account for only about 5% of the total, the excess caused by them is not clearly visible without separating IBDs and electron scatterings. In SK-Gd, since it is possible to distinguish electron scattering events from IBD events, the directional accuracy can get better. Fig.24 shows directional resolution of a supernova as a function of the distance to the supernova. Here, the efficiency identified as the IBD is assumed to be 68% (neutron capture efficiency by Gd is 75%, selection efficiency by data analysis is 90%). As shown in the figure, the directional resolution (68% C.L.) for a 10 kpc supernova is 4 to 5 degree with pure water, but it is about 3 degree with SK-Gd.

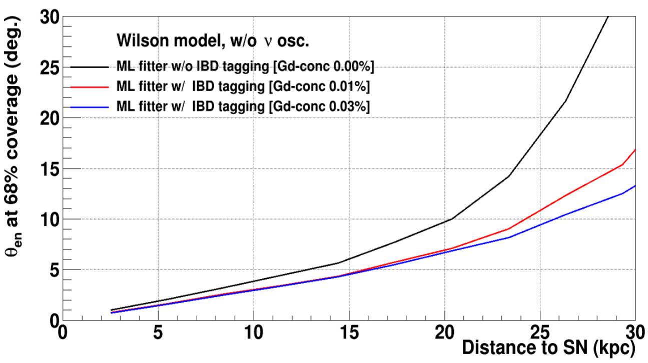

Fig. 24. Directional resolution for pointing a supernova as functions for the distance to the supernova.The blue line shows the expected improvement after the next Gd loading in 2022.

Pre-Supernova Neutrinos

In SK-Gd, Super-K can also detect neutrino signals that come before the collapse of iron core. Massive stars have a process of burning silicon (Si) just before gravitational collapse and a supernova burst. At that time, low-energy anti-electron neutrinos called pre-supernova neutrinos are emitted, and they can be detected via IBD with Gd neutron capture signals. Fig.25 shows the number of reactions that occur in the SK tank for a supernova at a distance of 200 pc (corresponding to the distance to Betelgeuse). Depending on the mass of the star and the model, supernova bursts can be predicted 8 hours before the explosion with a significance of 3σ. Fig.26 shows the detection efficiency of pre-SN neutrinos as a function of the distance to the supernova. As shown in the figure, it is possible to observe pre-SN neutrinos with a 100% probability up to around 500 pc, and there are about 20 candidates for supernovae including Betelgeuse.

Bibliography

[1] K. Abe et al., Nucl. Instrum. Meth. A, 1027, 166248 (2022), arXiv:2109.00360

T2K EXPERIMENT

[Spokesperson : Atsuko Ichikawa] Tohoku University

The Tokai to Kamioka (T2K) experiment [1] is a long

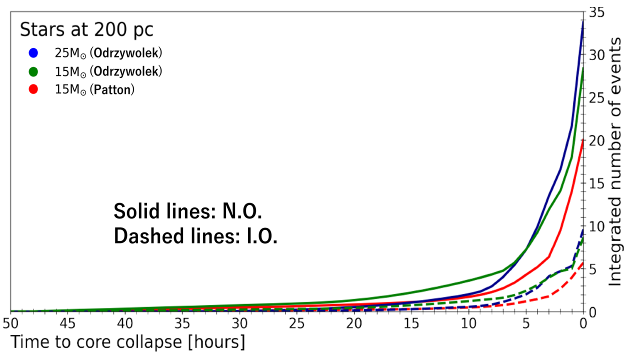

Fig. 25. Expected number of integrated events before the core collapse. The solid lines are the cases with the normal mass ordering, while the dashed lines are the cases with the inverted mass ordering.

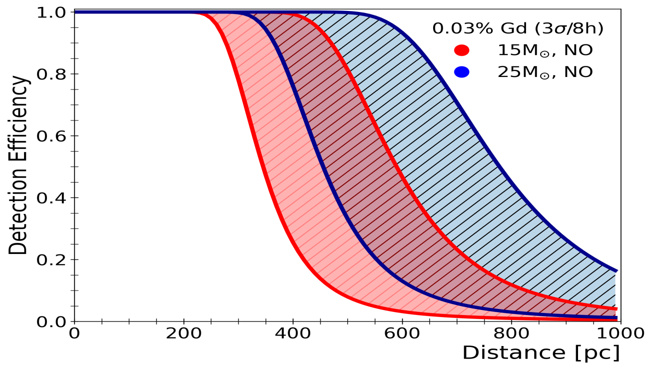

Fig. 26. Expected detection efficiency of pre-SN neutrinos. The efficiency is a probability to observe pre-SN signals more than 3σ significance. Blue shows the case with a progenitor mass of 15 solar mass, while red shows the case with a progenitor mass of 20 solar mass. In both cases, the neutrino mass ordering is assumed to be the normal mass ordering.

baseline neutrino oscillation experiment: a man-made beam of neutrinos is used to do precise studies of the oscillations of neutrinos. Accelerated protons are used to produce the neutrinos in the J-PARC center in the Ibaraki prefecture, which then travel 295 km to reach the Super-Kamiokande (Super-K) detector in the Gifu prefecture where they can be detected after oscillations. A complex of near detectors located 280 meters away from the proton target is used to monitor the neutrino beam, and constrain systematic uncertainties on the neutrino fluxes and interactions. T2K was the first long baseline experiment to use the off-axis beam technique [2]: the beam is not aimed directly at Super-K, but in a direction making a 2.5° angle with the far detector direction. This gives increased sensitivity to neutrino oscillations while reducing the backgrounds by producing a narrow band neutrino beam centered on the energy corresponding to the first maximum of the $\nu_\mu \to \nu_e$ oscillation probability.

T2K realized the first observation of the appearance of a flavor of neutrinos through oscillation by detecting electron neutrinos in a beam of neutrinos produced in the muon flavor [3]. After achieving this milestone, the experiment has been using its ability to produce a beam of either neutrinos or anti-neutrinos to compare the oscillations of neutrinos and their antiparticles. This allows to study the main remaining open questions in neutrino oscillations (CP symmetry and ordering of the neutrino mass states) by looking at the differences between the oscillations $\nu_\mu \to \nu_e$ and $\bar{\nu}_\mu \to \bar{\nu}_e$. At the same time, T2K's physics goals include the precise measurement of the neutrino oscillation parameters θ_{23} and Δm^2_{32} through a precise study of the pattern of disappearance of the muon neutrinos in conjunction with the data used to study the oscillation to the electron flavor. The experiment additionally performs searches for physics beyond the standard model, such as oscillations due to sterile neutrinos and CPT violation. Finally, the near detectors are used to perform a wide range of neutrino and anti-neutrino cross-section measurements.

In J-PARC, protons are accelerated to 30 GeV by a series of three accelerators, and hit a 1.9 interaction-length graphite target. The collisions produce hadrons, in particular charged pions and kaons, which are focused by three electromagnetic horns. The hadrons then go through a 96m long decay tunnel where they decay in flight into neutrinos. A beam dump at the end of the decay tunnel stops the remaining hadrons, while high energy muons (5 GeV/c or higher) can pass through this beam dump and are measured to provide a first, indirect monitoring of the neutrino beam. The horns can be used either with a positive current (ν-mode), in which case the beam is mainly made of ν_μ, or with a negative current ($\bar{\nu}$-mode) which gives a mainly $\bar{\nu}_\mu$ beam.

The near detectors are separated into two groups. On the axis of the beam, the INGRID detector, made of fourteen identical modules is used to monitor the beam direction and rate stabilities. Each module is made of an succession of iron plates to provide large target mass (7.1 tons per module) alternating with scintillator planes for detection. Using the number of events reconstructed in each module, the beam direction can be measured daily with better than 0.4 mrad accuracy. Located in the direction of Super-K, the off-axis detector ND280 is made of several detectors located inside a 0.2T magnet. The higher precision of those off-axis detectors allow to do more detailed measurements of the unoscillated neutrino beam. In neutrino oscillation analyses, the ND280 is used to provide information on the ν_μ and $\bar{\nu}_\mu$ unoscillated spectra directed at SK, constrain the dominant backgrounds, and constrain the combination of flux and interaction cross sections.

The far detector, Super-K, is a 50 kton water Cherenkov detector, shielded from atmospheric muons by 1000 m of rock, or 2700 meters-water-equivalent (m.w.e.) mean overburden. To select events corresponding to the T2K beam, Super-K is synchronized via GPS to the J-PARC beamline. Hit information within $\pm 500 \mu s$ from the beam arrival timing are used for T2K data analysis. Events where only one ring was reconstructed (corresponding to one charged particle above Cherenkov threshold) are used in oscillation analysis. Those events are separated into muon-like and electron-like events based on the light pattern of this ring, and additional selection cuts are applied to produce samples enriched in certain interaction modes.

To study neutrino oscillations, the data observed at the far detector are compared to the predictions of the three-flavor oscillation model for different values of the oscillation parameters. To this end, a model of the experiment is constructed: the fluxes of the different flavors of neutrinos reaching the detectors are predicted by a series of simulations, and the interactions of ν and $\bar{\nu}$ in the detectors are simulated using the NEUT Monte Carlo event generator [7]. First, the flux and properties of the proton beam reaching the target are measured by the proton beam line monitors. Interactions of the protons in the graphite target and production of secondary hadrons are then simulated using the FLUKA package [4]. Measurements from hadron production experiments, in particular NA61/SHINE [5], are used to tune this part of the simulation and the out-of-target interactions. The propagation and decay in flight of the hadrons in the decay tunnel are then simulated using the GEANT3 and GCALOR [6] packages. The predictions from this model are compared to the data observed in the near detectors to tune the predictions for the far detector by constraining the model parameters. The result of this near detector fit provides the initial values and uncertainties of the flux and interaction model parameters used in the far detector analysis to measure parameters describing neutrino oscillations.

T2K started collecting physics data in January 2010, and has now completed its 11th run. This 11th run corresponds to the first data taking with gadolinium dissolved in Super-K water following the upgrade of the detector for the SK-Gd project. The data from this last run have not yet been used for physics analyses, but their quality was checked and confirmed the proper functioning of the experiment with this new setting. Additionally, evidence for the signal corresponding to the capture of neutrons on gadolinium was seen in those data: an excess of low energy events is seen after the trigger. The number of events in this excess follows an exponential decrease in time, with a time constant compatible with the expected capture time on gadolinium (Fig 27).

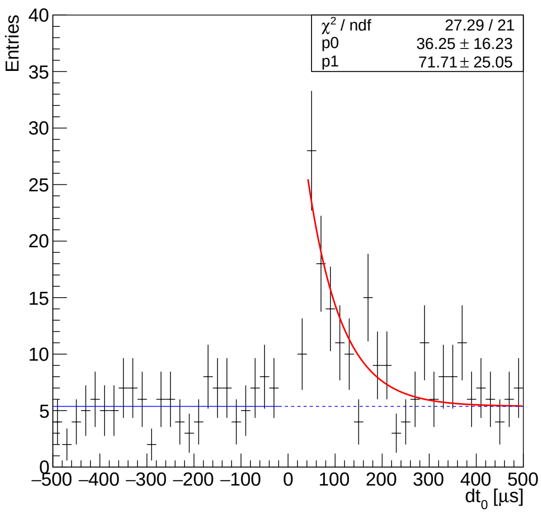

Fig. 27. Number of low energy events seen in run 11 as a function of time since beam trigger (dt_0). An exponential fit is performed: $n(t) = p0 \times e^{-p1/t} + cte$, and the time constant obtained is compatible with expected capture time at the current Gd concentration (115μs).

Table 4. T2K data taking periods and integrated numbers of protons on target (POT) used in the far detector analysis. The numbers for run 11 are still under preparation and have not been included.

Run Period	Dates	$\times 10^{20}$ POT ν	$\bar{\nu}$
Run 1	Jan.2010 - Jun.2010	0.32	–
Run 2	Nov.2010 - Mar.2011	1.11	–
Run 3	Mar.2012 - Jun.2012	1.60	–
Run 4	Oct.2012 - May.2013	3.60	–
Run 5	May.2014 - Jun.2014	0.24	0.51
Run 6	Oct.2014 - Jun.2015	0.19	3.55
Run 7	Feb.2016 - May.2016	0.48	3.50
Run 8	Oct.2016 - Apr.2017	7.17	–
Run 9	Oct.2017 - May.2018	0.20	8.79
Run 10	Oct.2019 - Feb.2020	4.73	–
Total	**Jan.2010 - Feb.2020**	**19.66**	**16.35**

The details of the data that have been used to date in the far detector analysis can be found in table4. The run 11 data correspond to an additional 1.78×10^{20} POT (before quality cut at the far detector) collected in March and April 2021. Over the whole period, the event rates and the beam direction were found to be consistent with the expectations and stable by the measurements of the muon monitor and the on-axis near detector. In particular, the beam direction remained stable well within the $\pm$1mrad target. During run 10 and 11, stable operation at more than 500 kW was achieved.

A long shutdown of the experiment is currently on-going, for upgrades of both the accelerator used to produce the neutrino beam, and of the off-axis near detector. The experiment plans to restart data taking at the beginning of 2023, with increased beam power, and a new set of detectors to replace the π^0 detector part of the current ND280. Those new detectors will give improved ability to study neutrino interactions, with a larger efficiency for high angle events, lower threshold to detect protons, and the ability to reconstruct neutron energy. A selection of results published during FY2021 is presented below.

Improved constraints on neutrino mixing from the T2K experiment with 3.13×10^{21} protons on target

T2K presented in [9] the details of the analysis used to study neutrino oscillations with the run 1 to 9 data, which led to the exclusion of the conservation of CP symmetry with 2σ statistical significance, as reported earlier in [8]. This new paper provides a fuller description of the method and a broader range of results and tests of the validity of the analysis.

This analysis uses a SK dataset collected up to the end of May 2018. This corresponds to an exposure of 14.94 $\times 10^{20}$ protons on target (POT) in neutrino mode and 16.35 × $\times 10^{21}$ in antineutrino mode, the same dataset as used to report indications of CP violation in [8]. Compared to the previous update [10] this is a nominal increase of 1% in neutrino mode, but 116% in antineutrino mode, which is particularly of interest for indications of $\bar{\nu}_e$ appearance, and an update to this search is reported in the paper. In parallel with the statistical increase, our event selection has been refined: event reconstruction is now based on an algorithm that matches the pattern of light observed in SK directly [11]. This makes use of more information about the event, providing better discrimination between event categories and improving the resolution of the lepton momentum and vertex location. As a result, the fiducial volume can also be expanded, roughly equivalent to a 20% increase in statistics for the ν_e samples.

A large fraction of the analysis development focuses on the interaction model, which incorporates constraints from a number of new external datasets and theoretical improvements. The dominant charged-current quasielastic (CCQE) models have been updated in various respects, including the handling of weak charge screening in nuclei; the handling of nucleon removal energy and its effect on lepton kinematics; and additional freedom allowed in the kinematic dependence of interactions involving correlated nucleon pairs (2p2h). Modeling of (and uncertainties assigned to) subdominant processes have also been improved, including coherent scattering and neutral-current interactions.

The neutrino oscillation probability depends upon the energy of the neutrino and its path length from creation to interaction. In long-baseline accelerator-based neutrino experiments the neutrino path length is fixed. All neutrino experiments use models to link the observed final states back to the initial neutrino energy. There is no set of models that describe the world's neutrino data but there are a number of models that are in comparable agreement to the world's data. However, these models map true neutrino energy to reconstructed neutrino energy in different ways. The choice of interaction model therefore affects the neutrino energy distribution that experiments infer from their observed neutrino events, which in turn can affect their measurement of the neutrino oscillation parameters. In this analysis a comprehensive set of neutrino interaction models have been tested using simulated data studies (procedure described in [12]) to quantify their effect on the T2K oscillation result. In all cases the observed bias on $\sin^2\theta_{23}$ and δ_{CP} was insignificant compared to existing systematic uncertainty on the parameter and so no additional uncertainty was introduced. Non-negligible bias was observed for Δm^2_{32} . The quadrature sum of the observed biases, $4.1\times10^{-5}\mathrm{eV}^2\mathrm{c}^{-4}$, was added as an additional uncertainty on Δm^2_{32}.

Measurements of the parameters $\sin^2\theta_{23}$, Δm^2_{32} and δ_{CP} were performed using different statistical approaches, both frequentist and Bayesian (with analysis of sensitivity to prior). The global best fit was found to be for the normal ordering, and the data show a preference for the upper octant. Bayesian posterior probabilities were computed to quantify those preferences, and found to be 0.889 for the normal ordering and 0.795 for the upper octant. The obtained 90% confidence regions for ($\sin^2\theta_{23}$, δ_{CP}) are displayed on Fig 28. The 2σ CL intervals for δ_{CP} constructed using the Feldman-Cousins unified approach do not include the CP-conserving values of 0 and π, meaning that the conservation of CP symmetry in neutrino oscillations is excluded at the 2σ level. Additional checks on the validity of this results were performed, and this exclusion was found to be robust with respect to the effects checked.

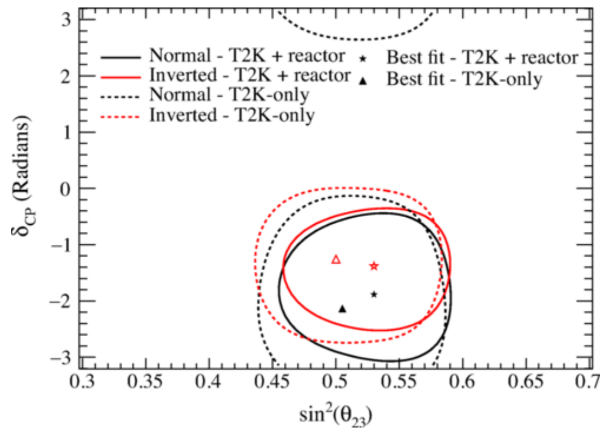

Fig. 28. The observed constant $\Delta\chi^2$ 90% confidence regions of $\sin^2\theta_{23}$ and δ_{CP} with normal and inverted mass orderings and with and without the constraint on $\sin^2(2\theta_{13})$ from reactor experiments. Normal and inverted mass ordering contours are independent. $\Delta\chi^2$values are calculated independently for the functions with and without the reactor constraint.

A search for $\bar{\nu}_e$ appearance was performed by evaluating the significance of the $\bar{\nu}_\mu \to \bar{\nu}_e$ oscillation under the assumption of two different hypotheses, corresponding to no $\bar{\nu}_e$ appearance, and to $\bar{\nu}_e$ appearance consistent with our current knowledge of the PMNS mixing parameters. The analysis is performed by multiplying the $\bar{\nu}_\mu \to \bar{\nu}_e$ PMNS oscillation probability by a factor, β, i.e. $P\left(\bar{\nu}_\mu \to \bar{\nu}_e\right) = \beta \times P_{PMNS}\left(\bar{\nu}_\mu \to \bar{\nu}\right)$. The parameter β is set to either 0 or 1 to select a null hypothesis for two independent tests: when $\beta = 0$, the null hypothesis under consideration is that there is no $\bar{\nu}_e$ appearance, while for $\beta = 1$ the null hypothesis is that $\bar{\nu}_e$ appearance occurs according to the current best knowledge of the PMNS parameters. For each hypothesis, p-values are produced from two analyses: rate-only and rate+shape.

The expected and observed test statistic distributions produced are shown in Fig. 29. The hypothesis of no $\bar{\nu}_e$ appearance ($\beta = 0$) is excluded at the 1.9σ and 2.4σ levels, respectively using the rate-only and rate+shape analyses. Our data are consistent with the PMNS $\bar{\nu}_e$ appearance hypothesis ($\beta = 1$), with p-values of 0.32 and 0.30 for the rate-only and rate+shape analyses, respectively (corresponding to a 1σ exclusion).

First T2K measurement of transverse kinematic imbalance in the muon-neutrino charged-current single-π^++ production channel containing at least one proton

To achieve the designed sensitivity of future long baseline experiments, nuclear effects have to be modelled accurately and consistently amongst all interaction channels. Experimental studies probing nuclear effects in carbon, through the measurement of transverse kinematic imbal ance (TKI) in CC interactions, have been performed in T2K [13] and MINERνA [14]. TKI explores the lepton-hadron correlations on the plane that is transverse to the initial neutrino direction and helps precisely identify intranuclear dynamics, or the absence thereof, in neutrino-nucleus interactions. These measurements focused either on final-state topologies without any

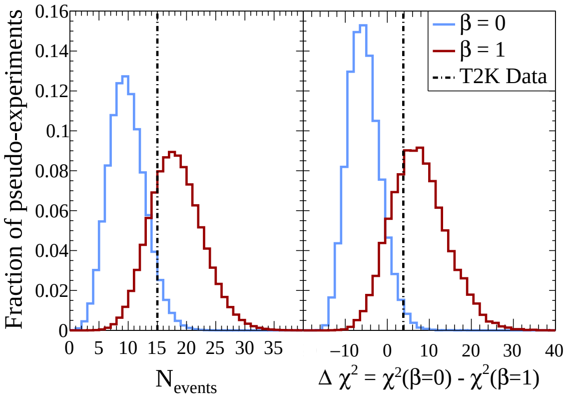

Fig. 29. Distributions of the observed rate-only (left) and rate+shape (right) test statistics compared to the value for the data. Here N_{events} denotes the number of observed events in the antineutrino mode single-ring e-like sample.

pions, or final-state topologies with at least one neutral pion, while none with one charged pion has been performed. These studies suggest that modeling nuclear effects with Fermi gas initial state models is insufficient, but more data are needed to draw solid conclusions. Positively charged pion production from electron neutrinos is one of the signal channels measured at the T2K far detector and employed in the oscillation analyses. Studying the same interaction channel in CC muon neutrino interactions can provide a better understanding of the common underlying nuclear effects and pion production mechanics. Furthermore, it will provide valuable information towards the future inclusion of such sample among the one used in T2K oscillation analysis. In [15], T2K described its first measurement of the ν_μ cross section on hydrocarbon as a function of TKI variables in CC production of exactly one π^+ and no other mesons, and at least one proton.

The standard set of three TKI variables, δp_{TT}, p_N and $\delta\alpha_T$ are used. These observables are designed to characterize the nuclear effects that are most relevant to oscillation experiments: the initial nuclear state, such as the Fermi motion of initial state nucleon and the nucleon removal energy, and the final state interactions (FSI) of outgoing hadrons. The first observable δp_{TT} is the double-transverse momentum imbalance, The second observablep_N is the initial nucleon momentum and the third observable $\delta\alpha_T$ is the transverse boosting angle which quantifies whether the hadronic system is accelerated or decelerated by nuclear effects.

An extensive comparison of the extracted results to state-of-the-art neutrino interaction models shows a slight preference for GiBUU (Fig. 30), which uses a more realistic nuclear ground state to handle all interaction channels consistently. Our results are statistically limited and a large part of the model separation power comes from normalization differences. In general the simple Fermi gas models (RFG and LFG) show a large disagreement in p_N with χ^2_{tot}/ndof ¿ 2, which indicates a mismodeling of the nucleon Fermi motion. The similar data-MC comparison to the MINERνA CCπ^0 results [16] seems to confirm that the mismodeling is general in pion production channels. While tight phase space restrictions limit our sensitivity to FSI modeling, the relatively flat $\delta\alpha_T$ in T2K results is in strong contrast to MINERνA results, indicating a possible energy dependence of hadronic FSI.

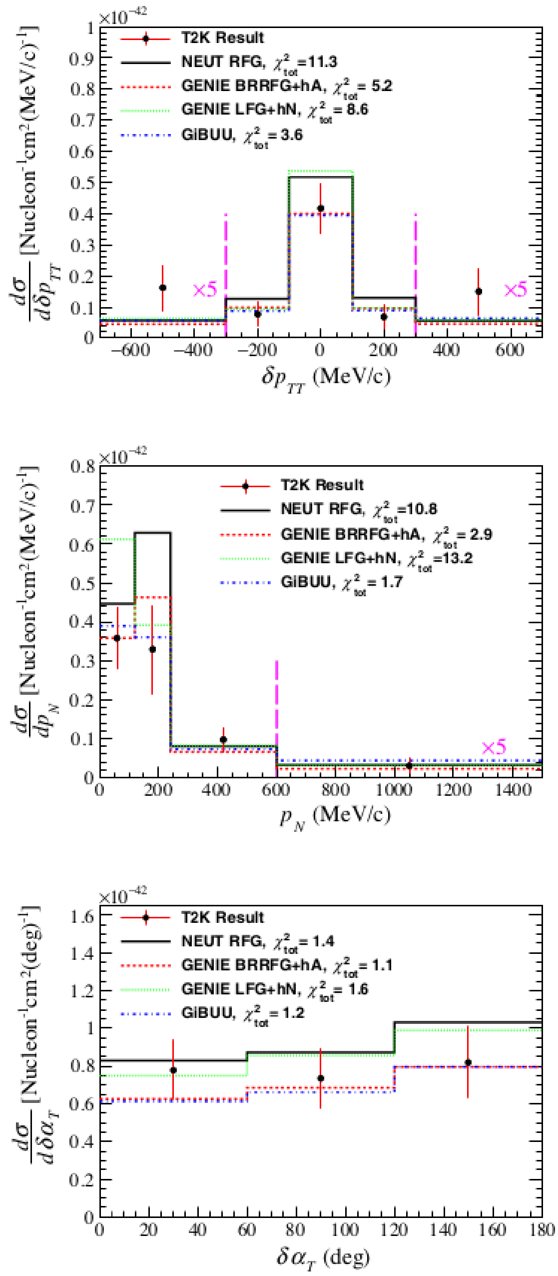

Fig. 30. Measured differential cross sections per nucleon as a function of δp_{TT} (top), p_N (middle), and $\delta\alpha_T$ (bottom), together with predictions from NEUT, GENIE and GiBUU. In the tails of δp_{TT} and p_N (beyond the magenta lines), the cross sections are scaled by a factor of 5 for better visualization. The legend also shows the χ^2_{tot} used to quantified the agreement between the measurement and the predictions.

Future analyses will aim to unfold cross sections in multiple TKI variables simultaneously and obtain their correlations which can then be used to separate effects due to the initial nuclear state and FSI. The upcoming ND280 upgrade is going to expand the measurable phase space, especially in the low energy and high angle regions. Thus the ND280 upgrade is expected to increase our statistics and model sensitivity significantly.

Bibliography

[1] K. Abe *et al.* (T2K Collaboration), Nucl. Instrum. Meth. A **659**, 106 (2011).

[2] D. Beavis, A. Carroll, I. Chiang, *et al.*, Long Baseline Neutrino Oscillation Experiment at the AGS (Proposal E889), 1995. Physics Design Report, BNL 52459.

[3] K. Abe *et al.* (T2K Collaboration), Phys. Rev. Lett. **112**, 061802 (2014).

[4] T. Bhlen *et al.*, Nucl. Data Sheets **120**, 211 (2014).

[5] N. Abgrall et al. (NA61/SHINE Collaboration), Eur. Phys. J. C **76**, 84 (2016).

[6] C. Zeitnitz and T. A. Gabriel, Proceedings of International Conference on Calorimetry in High Energy Physics (World Scientific, Corpus Christi, Texas, 1992), ISBN 9789810213039, pp. 394-404.

[7] Y. Hayato, Acta Phys. Pol. B **40**, 2477 (2009).

[8] K. Abe *et al.* (T2K Collaboration), Nature, 2020, 580(7803), pp. 339–344

[9] K. Abe *et al.* (T2K Collaboration), Phys. Rev. D **103**, 112008 (2021)

[10] K. Abe *et al.* (T2K Collaboration), Phys. Rev. Lett. **121**, 171802 (2018)

[11] M. Jiang et al. (Super-Kamiokande Collaboration), Prog. Theor. Exp. Phys. **2019**, 053F01 (2019)

[12] K. Abe *et al.* (T2K Collaboration), Phys. Rev. D **96**, 092006 (2017); **98**, 019902(E) (2018)

[13] K. Abe *et al.* (T2K Collaboration), Phys. Rev. D **98**, 032003 (2018)

[14] X. Lu et al. (MINERvA Collaboration), Phys. Rev. Lett. **121**, 022504 (2018).

[15] K. Abe *et al.* (T2K Collaboration), Phys. Rev. D 103, 112009 (2021)

[16] D. Coplowe et al. (MINERvA Collaboration), Phys. Rev. D **102**, 072007 (2020)

XMASS EXPERIMENT

[Spokesperson : Shigetaka Moriyama]
Kamioka Observatory, ICRR, the University of Tokyo

Introduction

The XMASS project was designed to detect dark matter, neutrinoless double beta decay, and ^{7}Be/*pp* solar neutrinos using highly-purified liquid xenon (LXe) scintillator in an ultra-low radioactivity environment [1]. The advantages of using LXe are a large amount of scintillation light yield, scalability of the size of the detector mass, easy purification to reduce internal radioactive backgrounds (BGs), and shielding ability against radiation from outside the detector due to a high atomic number ($Z = 54$) [2]. A breakthrough technology was developed to purify liquid xenon from the radioactive contaminant of ^{85}Kr found in commercial gas xenon [3]. This makes liquid xenon detectors suitable for rare event searches. The detector containing $\sim$830 kg of LXe, was constructed in September 2010. Commissioning data was taken from December 2010 to May 2012. Based on commissioning data results were published on DM searches [4, 5, 6], solar axions [7], and two-neutrino double electron capture on ^{124}Xe [8]. We also studied the possibility of detecting galactic supernova neutrinos via coherent elastic neutrino-nucleus scattering [9].

Analyzing the commissioning data we found that a majority of events at low energy originated from radioactive contamination in the aluminum seal of the photomultiplier tube (PMT) window. In order to minimize the impact of this BG, the detector was refurbished. The contaminated seals were covered with copper rings and plates to stop scintillation lights and radiation caused by this contamination to reach the inner detector volume. The PMT windows were cleaned with nitric acid, and copper parts were electropolished in order to remove possible surface contamination. After a year of detector refurbishment, data-taking resumed in November 2013 with background significantly reduced and continued for more than five years. We completed data taking in February 2019. Results were published from searches for annual modulation from dark matter [10, 11], solar Kaluza-Klein axions [12], two-neutrino double electron capture on ^{124}Xe [13], dark matter through elastic-scattering [14], hidden photons [15], inelastic-scattering off ^{129}Xe [16], sub-GeV dark matter [17], exotic neutrino-electron interactions [18], and for events coincident with the arrival of gravitational waves [19].

In the following sections, we briefly introduce the XMASS-I detector and report the latest physics results from XMASS data collected after the refurbishment.

The XMASS-I detector

XMASS-I was a single-phase LXe scintillator detector located underground (2700 m water equivalent) at the Kamioka Observatory [20]. Fig. 31 shows a schematic drawing of the XMASS-I detector. It contained $\sim$830 kg of LXe in its active region. The active volume is viewed by 630 hexagonal

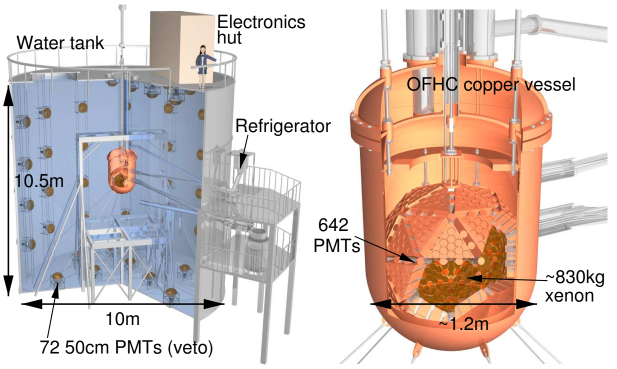

Fig. 31. Schematic drawing of the XMASS-I detector.

and 12 cylindrical Hamamatsu R10789 PMTs arranged on an 80 cm diameter pentakis-dodecahedron support structure. These PMTs were developed to achieve low background requirements [21]. The largest contributions to the reduction of radioactivity came from the PMTs' stem and its dynode support. The glass stem was exchanged for a the Kovar alloy one, and the ceramic support was changed to a quartz one. The R10789 is the first model of Hamamatsu Photonics K. K. that adopted these materials for low background purposes and provided a groundbreaking step for further reductions of radioactivity in PMTs. A total photocathode coverage of more than 62% of the inner surface was achieved in XMASS. The almost spherical array of PMTs was supported in a double-walled vessel made of oxygen-free high conductivity copper [22]. The waveforms of each PMT were recorded with CAEN V1751 waveform digitizers with a 1 GHz sampling rate and 10 bit resolution. The detector was calibrated regularly with a ^{57}Co source inserted along its central vertical axis and an external ^{60}Co source. From the data taken with the ^{57}Co source at the center of the detector volume, the photoelectron (PE) yield was determined to be $\sim$14 PE/keV. Two different energy scales were used: $\mathrm{keV_{ee}}$ represents an electron equivalent energy, and $\mathrm{keV_{nr}}$ denotes the nuclear recoil energy. The scintillation decay time constant was investigated in liquid xenon with the XMASS detector. The results were summarized in [23] and [24].

In order to shield the LXe detector from external gammas, neutrons, and muon-induced BGs, the copper vessel was placed at the center of a ϕ10 m$\times$ 10.5 m cylindrical tank filled with pure water. This water tank was equipped with 72 Hamamatsu R3600 20-inch PMTs to provide both an active muon veto and a passive shield against external BGs. XMASS-I was the first direct detection dark matter experiment equipped with such an active water Cherenkov shield. The LXe and water Cherenkov detectors were called the Inner Detector (ID) and the Outer Detector (OD), respectively.

It is also worth noting that there were some important technical studies related to pulse-shape discrimination between nuclear recoils and electron recoils [25], radon removal using charcoal filters [26], scintillation performance of liquid xenon at room temperature [27], a ^{220}Rn calibration source [28], and 3-inch low background photomultiplier tubes [29], though we did not use them for XMASS-I.

Search for event burst in XMASS-I associated with gravitational-wave events [19]

In 2015, the gravitational-wave (GW) signal from a binary black-hole merger was first detected by the Advanced LIGO experiment. During LIGO/Virgo's observing periods O1 (September 2015–January 2016) and O2 (November 2016–August 2017), 10 binary black-hole mergers and a binary neutron-star merger were observed. Moreover, electromagnetic counterparts were detected for the first time, associated with the GW event from the binary neutron-star merger named GW170817. Follow-up searches for neutrino events associated with these GW events were also conducted by large neutrino detectors all over the world. The neutrino follow-up searches are of interest because there are some theoretical predictions of emission of neutrinos with energies of a few tens of MeV, and even higher-energy neutrinos are expected from binary neutron-star mergers. The XMASS-I detector accumulated data with a stable condition continuing from November 2013 until February 2019, resulting in an entire data set with a total live time of 4.4 years.

We use the full 832 kg of xenon as an active target in this particular analysis. Events with four or more hits in the inner-detector without an associated outer-detector trigger were selected. We then applied four furhter selection cuts that mostly remove obvious backgrounds. The detection efficiency after those cuts is properly accounted for. The data are divided into four NPE ranges: $<$450 (referred to as Low-E), 450–4500 (Middle-E), 4500–45000 (High-E), and $>$45000 (Very High-E, or V. H. E. hereinafter), corresponding to energy ranges of approximately $<$30, 30–300, 300–3500, and $>$3500 $\mathrm{keV_{ee}}$, respectively.

The event burst search was conducted in a time window between -400 and $+10,000$ s around each GW event. This search window is motivated by two arguments. The time window within $\pm$400 s from each GW event is considered in the search for neutrinos. In addition, the extended time window up to 10,000 s is considered in the model-independent search because for massive axion-like particles, for instance, the travel time would depend on their mass.

To search for event bursts without assuming any particular burst model, the number of events in a sliding time window is scanned for each energy range. The coincidence time window is slid at a step of 0.01 s and various width of the window (t_{width}) are tested: 0.02, 0.04, 0.1, 0.2, 0.4, 1, 2, 4, and 10 s. As the result of the model-independent search, no coincidence time window with a global significance of more than 3σ was found in the time range between -400 and $+10,000$ s from the GW170817 event. The same analysis is performed for other 10 GW events classified as binary black hole mergers. Among them, a burst candidate with a small probability was found in the High-E energy range for the GW151012 event. After considering the look-elsewhere effect of the 4 energy ranges, the global significance of this burst candidate identified in association with GW151012 is 3.0σ. Since we perform the analysis separately on the 11 GW events, there is an additional look-elsewhere effect. The significance of finding such a burst candidate in any of the 11 GW events is 2.1σ. By investigating energy and vertex distributions, no significant deviation from the background distributions is found.

For the GW170817 event, we also derive constraints on neutrino fluence for the sum of all neutrino flavors via CEvNS under the assumption of two types of neutrino energy distributions: a Fermi-Dirac spectrum with average neutrino energy of 20 MeV and mono-energetic neutrinos in the range between 14 and 100 MeV. The simulated neutrino events are found to concentrate at low energy, and hence the Low-E sample (below 450 PE) is used to derive constraints on neutrino fluence. The detection efficiency crosses 50% at 4.5 PE which corresponds to 3.8 $\mathrm{keV_{nr}}$. No significant event burst is observed in the Low-E sample, the 90% confidence level (CL) upper limit on neutrino fluence is calculated. Figure 32 shows the 90% CL upper limits on neutrino fluence for the Fermi-Dirac spectrum as a function of the coincidence time width t_{width}. Figure 33 shows our 90% CL upper limits on fluence for mono-energetic neutrinos as a function of neutrino energy between 14 and 100 MeV. Limits obtained by Super-Kamiokande are also shown. The XMASS limit is comparable to the $\nu_{\mu,\tau}$ and $\bar{\nu}_{\mu,\tau}$ limits of Super-Kamiokande.

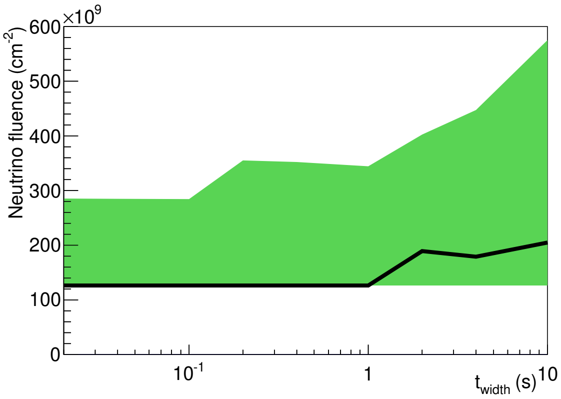

Fig. 32. 90% CL upper limits on neutrino fluence for GW170817 assuming the Fermi-Dirac spectrum with $\langle E_\nu \rangle$=20 MeV as a function of the coincidence time width t_{width}. The black solid line shows the upper limit from the on-time window centered at $t = t_{\mathrm{GW}}$ with a width t_{width}, and the green band represents the range of limits from the sliding window with width t_{width} within the ± 400 s search window. Note that t_{width} is scanned discretely at 0.02, 0.04, 0.1, 0.2, 0.4, 1, 2, 4, and 10 s.

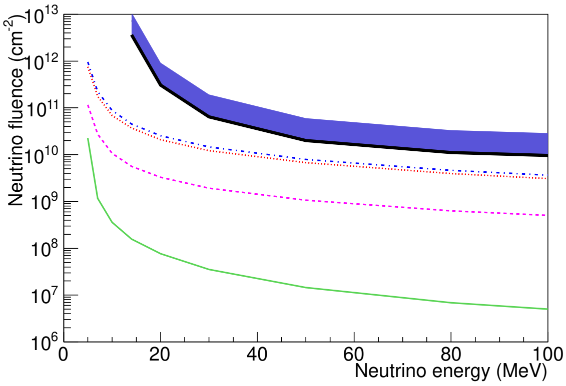

Fig. 33. 90% CL upper limits on mono-energetic neutrino fluence for GW170817 as a function of neutrino energy. The black solid line shows the upper limit from the on-time window, and the blue band represents the range of limits from the sliding window within the ± 400 s search window. Limits obtained by Super-Kamiokande for $\bar{\nu}_e$ (green solid), ν_e (magenta dashed), $\nu_{\mu,\tau}$ (red dotted), and $\bar{\nu}_{\mu,\tau}$ (blue dash-dotted) are also shown.

Bibliography

[1] Y. Suzuki *et al.*, hep-ph/0008296.

[2] K. Abe *et al.* (XMASS Collaboration), Astropart. Phys. **35** (2012) 609.

[3] K. Abe *et al.* (XMASS Collaboration), Astropart. Phys. **31** (2009) 290.

[4] K. Abe *et al.* (XMASS Collaboration), Phys. Lett. B **719** (2013) 78.

[5] H. Uchida *et al.* (XMASS Collaboration), Prog. Theor. Exp. Phys. (2014) 063C01.

[6] K. Abe *et al.* (XMASS Collaboration), Phys. Rev. Lett. **113** (2014) 121301.

[7] K. Abe *et al.* (XMASS Collaboration), Phys. Lett. B **724** (2013) 46.

[8] K. Abe *et al.* (XMASS Collaboration), Phys. Lett. B **759** (2016) 64.

[9] K. Abe *et al.* (XMASS Collaboration), Astropart. Phys. **89** (2017) 51.

[10] K. Abe *et al.* (XMASS Collaboration), Phys. Lett. B **759** (2016) 272.

[11] K. Abe *et al.* (XMASS Collaboration), Phys. Rev. D **97** (2018) 102006.

[12] N. Oka *et al.* (XMASS Collaboration), Prog. Theor. Exp. Phys. **2017** (2017) 103C01.

[13] K. Abe *et al.* (XMASS Collaboration), Prog. Theor. Exp. Phys. **2018** (2018) 053D03.

[14] K. Abe *et al.* (XMASS Collaboration), Phys. Lett. B **789** (2019) 45.

[15] K. Abe *et al.* (XMASS Collaboration), Phys. Lett. B **787** (2018) 153.

[16] T. Suzuki *et al.* (XMASS Collaboration), Astropart. Phys. **110** (2019) 1.

[17] M. Kobayashi *et al.* (XMASS Collaboration), Phys. Lett. B **795** (2019) 308.

[18] K. Abe *et al.* (XMASS Collaboration), Phys. Lett. B **809** (2020) 135741.

[19] K. Abe *et al.* (XMASS Collaboration), Astropart. Phys. **129** (2021) 102568.

[20] K. Abe *et al.* (XMASS Collaboration), Nucl. Instrum. Meth. A **716** (2013) 78.

[21] K. Abe *et al.* (XMASS Collaboration), Nucl. Instrum. Meth. A **922** (2019) 171.

[22] K. Abe *et al.* (XMASS Collaboration), Nucl. Instrum. Meth. A **884** (2018) 157.

[23] H. Takiya *et al.* (XMASS Collaboration), Nucl. Instrum. Meth. A **834** (2016) 192.

[24] K. Abe *et al.* (XMASS Collaboration), JINST **13** (2018) P12032.

[25] K. Abe *et al.* (XMASS Collaboration), Nucl. Instrum. Meth. A **659** (2011) 161.

[26] K. Abe *et al.* (XMASS Collaboration), Nucl. Instrum. Meth. A **661** (2012) 50.

[27] K. Abe *et al.* (XMASS Collaboration), Nucl. Instrum. Meth. A **594** (2008) 148.

[28] M. Kobayashi, M. Yamashita, A. Takeda, K. Kishimoto, S. Moriyama, Journal of Physics: Conference Series 718 (2016) 042069 (TAUP2015).

[29] K. Abe *et al.* (XMASS Collaboration), JINST **15** (2020) P09027.

XENON EXPERIMENT

XENON ICRR group
[Principal investigator : Shigetaka Moriyama]
Kamioka Observatory, ICRR, the University of Tokyo

Introduction

The XENONnT experiment [1] is the most sensitive direct dark matter search experiment conducted at LNGS in Italy. The XENON collaboration includes about 180 collaborators from 27 institutions in 12 countries. From Japan, the University of Tokyo (ICRR and Kavli IPMU), Nagoya University, and Kobe University participate since 2017. The XENON group uses liquid xenon and employs a time projection chamber (TPC), characterized by its ability to discriminate between nuclear and electron recoil. The Japanese group is making a significant contribution toward the discovery of DM particles contributing a purification technology for liquid xenon developed in XMASS and the neutron detection technology developed for Super-Kamiokande. The XENON collaboration completed XENONnT detector construction in 2020 and started data taking in 2021. Japan also participated in the data analysis of the predecessor XENON1T experiment, from which the XENON collaboration reported a significant 3.3σ excess of electron recoil events over the background in 2020 [2]. Since this could be interpreted as a signal of axions produced in the Sun, the ICRR members, who have also searched for solar axions in XMASS [3], contributed to interpreting the data. In the XENONnT experiment, where data taking is ongoing, the background is expected to be further reduced, and its large sensible volume is expected to soon provide new insight into that excess seen in XENON1T. The contributions of the ICRR group are described below.

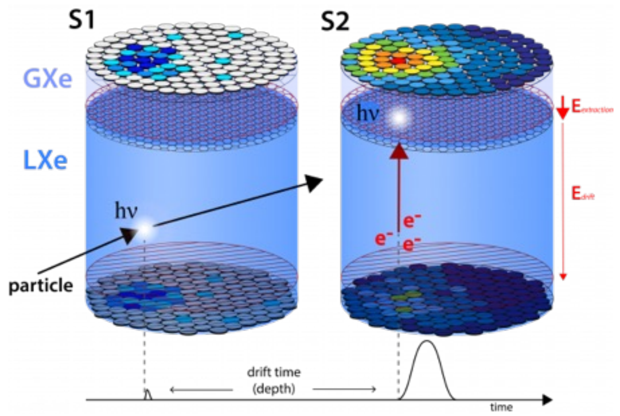

Fig. 34. Principle of operation of liquid xenon time projection chamber (TPC). The interaction of dark matter produces scintillation light S1, and electrons drifted by an electric field give a delayed signal S2; the observed pattern of S2 can identify the planar location of the interaction, and the time difference between S1 and S2 provides depth information. The ratio of S1 to S2 also holds information about the type of particle that caused the interaction. Figure from the XENON collaboration.

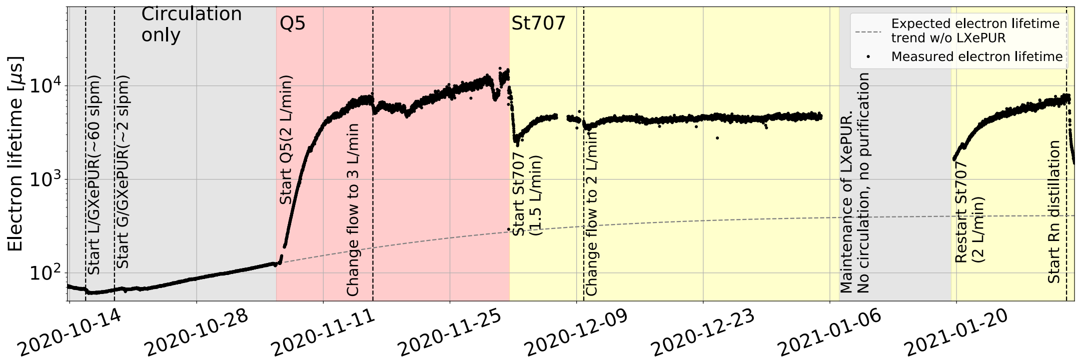

Fig. 35. Lifetimes of electrons in liquid xenon compared with different purification methods. It is measured with a purity monitor developed by ICRR. Gray, red, and yellow areas indicate purification by gas and getter, liquid and Q5, and liquid and St707, respectively. For the first time in the world, we were able to establish a method for directly purifying liquids. St707 is expected to be used for long-term operation since it emits almost no radon compared to Q5. Since the XENONnT detector is 1.5 m high, it is expected to have a lifetime of more than 3 ms, which was sufficient to obtain a good performance. Figure from Ref. [5].

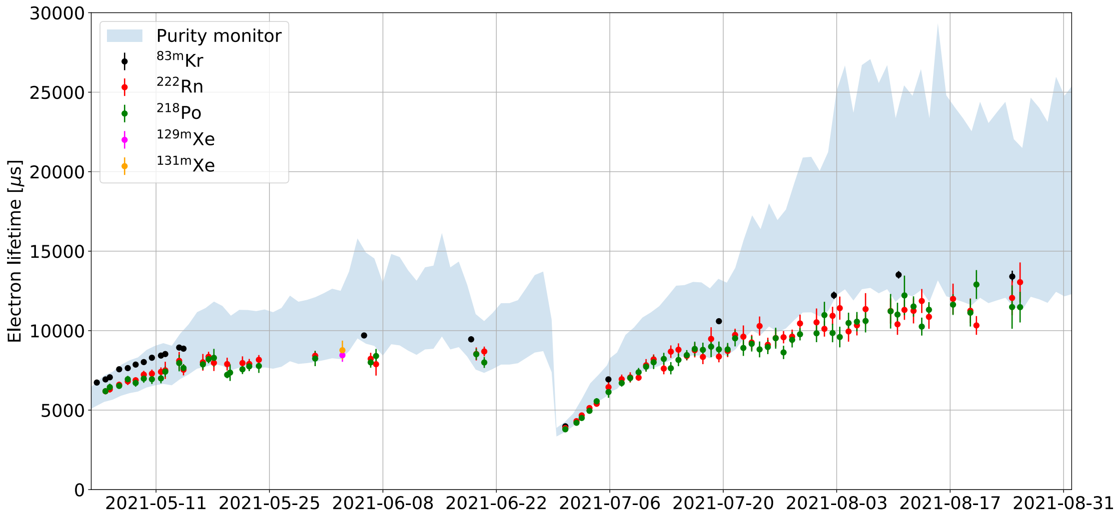

Fig. 36. Electron lifetime measured by the XENONnT detector (dots) and by the purity monitor (blue band showing uncertainty of the measurement) during science run data taking. Figure from Ref. [5].

Liquid xenon purification and monitoring

Purifying liquid xenon is an essential technique for observing interactions of dark matter particles with the liquid xenon target. As shown in Figure 34, the signal from a liquid xenon TPC consists of a scintillation light S1 signal when recoil occurs, and an S2 signal obtained when an applied electric field extracts the generated ionization electrons. If S2/S1 is large, it is classified as an electron recoil (ER) event, whereas if S2/S1 is small, it is classified as a nuclear recoil (NR) event, such as from a WIMP dark matter event candidate. For such discrimination to perform well, ionized electrons must be extracted efficiently. In particular, impurities in liquid xenon that trap electrons before they can be extracted will reduce the S2 signal and adversely affect the discrimination.

Our research was to develop a technique to reduce these electron-capturing impurities. A typical example of impurities that capture electrons is oxygen. It is important to note, however, that the addition of new contaminants such as radon need to be negligible compared with our target values, 1 μBq/kg in the case of radon, when these impurities are removed. In previous experiments, such as the XENON1T experiment [2], purification was performed by evaporating liquid xenon into the gas phase, passing it through a device called a getter that can remove oxygen and other impurities, and then liquefy it again. In the XENONnT experiment, on the other hand, the amount of liquid xenon was about five times larger than in XENON1T, and it was thought that the required performance could not be obtained because the purification speed would not be sufficient with the gas purification. Therefore, purification in the liquid phase was planned and conducted. The R&D was conducted in collaboration with Columbia University. The filter material Q5, which had been used in liquid argon, was a candidate, but it was known to emit radon gas, which is harmful to the search for dark matter. The Japanese group proposed to use the getter material St707, which is normally used for gas purification in high temperature, also for the purification in the liquid phase since this material emits a negligible amount of radon gas. With the help of the Colombia group, the material was tested and confirmed to be useful for liquid xenon purification [4]. Since Q5 has a high performance in removing impurities, it was proposed to use for reducing impurities in the early stages of the experiment. Then St707 was used to continually remove impurities slowly emitted from the detector components. This is because the half-life of radon is 3.8 days, so even if Q5 emits radon, it will decay within a certain period and have no negative impact. In this way, the St707 was adopted for liquid xenon purification during XENONnT data taking.

Figure 35 shows the performance during the commissioning phase. At different times, purification was performed using gas alone (gray), purification using Q5 (red), and purification using St707 (yellow). The vertical axis is the electron lifetime, and since the goal was to achieve more than 3 ms, we can see that both Q5 and St707 were sufficient to achieve that goal after optimizing amount and shape of the filter. During the actual science run, Fig. 36 shows electron lifetime during science data taking. As can be seen, we confirmed purity from electronegative contaminants well beyond the goal of 3 ms. It will be applied to larger detectors in the future. These results were summarized in a doctoral dissertation from the University of Tokyo [5].

Neutron background tagging utilizing SK-Gd technology

Purifying liquid xenon, discussed in the previous section, is an essential technique for maximizing the dark matter signal. On the other hand, background reduction is critical in rare event searches, and there are two primary background sources important in XENONnT: one is radon in liquid xenon, and the other is neutrons emitted from instrument components. The Japanese group is contributing to the realization and operation of a neutron veto detector that tags these neutrons and reduces the background by event basis, using the gadolinium-doped water Cherenkov detector technology developed at Kamioka for Super-Kamiokande [6]. Figure 37 shows a full view of the XENONnT detector, which is entirely housed in a water tank with a white reflective material optically isolating the neutron veto immediately surrounding the liquid xenon TPC at its center. The neutron veto is equipped with 120 PMTs. By adding 0.2% of Gd to the water in the whole tank, neutrons emitted from the detector components are expected to be captured by Gd with a high probability if they reach the neutron veto after recoiling from xenon nuclei in the TPC. After capturing the neutron on Gd, we expect PMTs in the neutron veto detector to observe Cherenkov light caused by gamma rays emitted from the Gd nucleus that captured the neutron. This enables us to tag neutrons that cause background for the WIMP search and thus maximize the experiment's sensitivity. XENONnT aims to tag approximately 87% of such neutron events that are otherwise indistinguishable from dark matter events. During the construction period, the neutron veto detector was completed. With the help of the Super-Kamiokande collaboration, about 1.7 tons of the purest grade of gadolinium sulfate was obtained in Japan and delivered to LNGS [7]. In 2021, the installation of a gadolinium-loaded water purification plant was completed. The Super-Kamiokande collaboration also helped us to design the water plant for our application. At present, the plant operates with pure water. The gadolinium loading into the water in the tank will be done after the commissioning of the water plant.

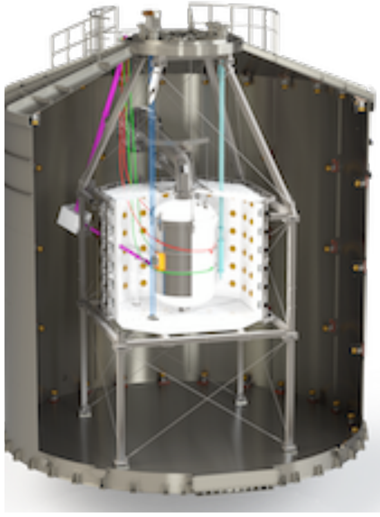

Fig. 37. Overview of the XENONnT detector. The white part is the neutron veto detector. The liquid xenon TPC is at the center, surrounded by the white reflective material, and 120 photomultiplier tubes are used to detect the Cherenkov lights produced by gamma rays when neutrons are captured by gadolinium or other nuclei and used to identify the neutrons. The water tank is 10 m in diameter and 10 m high, and 0.2% of gadolinium will be added to the entire system. Figure from the XENON collaboration.

Data analysis for XENON1T

The XENON1T experiment, the predecessor of the XENONnT experiment, found no WIMP signal and gave the world's best limit on WIMPs. The WIMP search used events classified as NR events, as described in the introduction section. However, so-called ER events, which were discarded as radioactive background events in that search, are still at the world's lowest level in this energy range. In XMASS, the lowest background was at around 60 keV at a level of about 0.4×10^{-3} events/kg/keV/day [8], but in the larger XENON1T, it was only 0.2×10^{-3} events/kg/keV/day around three keV. This can be utilized to search for new physics signals that could not be searched for before. Here, we searched for phenomena produced by axions that may be produced in the sun, a magnetic moment of neutrinos from the sun, and absorption of bosonic types of dark matter by xenon atoms. Analysis of the data showed a statistical excess of 3.3 σ over the expected background at 2-7 keV, as shown in Figure 38. At this stage, it was pointed out that liquid xenon may contain a radioactive impurity, tritium, which was included in the data analysis. The results showed a significance of 3.4σ for the solar axion hypothesis, 3.2σ for the tritium hypothesis, and 3.2σ for solar neutrinos with a magnetic moment [2]. The difference in these significance levels depends on how well the expected energy spectrum matches the observed data. In the

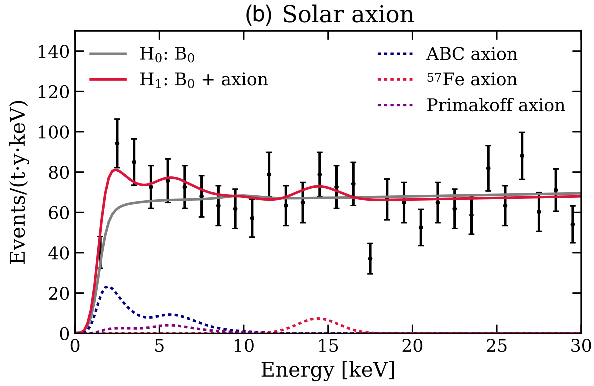

Fig. 38. Energy spectra of electron recoil events obtained with XENON1T. The black dots are data, the gray line is the background event, and the red line is the background event plus the spectrum expected from the axion produced in the Sun. Figure from Ref. [2].

search for solar axions, in addition to the coupling of axions to electrons and photons, the coupling to nucleons [9] was additionally considered based on our ICRR suggestion. By fitting all three constants independently, information of the details of the axion models can be obtained. There are many papers, more than a hundred, that were published in response to our paper. The observed excess is expected to be confirmed or rejected by the XENONnT experiment very soon.

Bibliography

[1] E. Aprile *et al.* (XENON collaboration), JCAP 11 (2020) 031.

[2] E. Aprile *et al.* (XENON collaboration), Phys. Rev. D **102**, 072004 (2020).

[3] K. Abe *et al.* (XMASS collaboration), Phys. Lett. B 724 (2013) 46.

[4] G. Plante *et al.*, arXiv: 2205.07336.

[5] N. Kato, doctoral dissertation, The University of Tokyo, 2021.

[6] L. Marti, *et al.* (Super-Kamikande collaboration), Nucl. Instrum. Meth. A, 959, 163549 (2020); K. Abe *et al.* (Super-Kamiokande collaboration), Nucl. Instr. Meth. A, 1027 (2022) 166248.

[7] E. Aplile *et al.* (XENON collaboration), arXiv: 2112.05629.

[8] K. Abe *et al.* (XMASS Collaboration), Phys. Lett. B **787** (2018) 153.

[9] S. Moriyama, Phys. Rev. Lett. 95 (1995) 3222.

HYPER-KAMIOKANDE

[Co-Spokespersons: Masato Shiozawa[1], Francesca Di Lodovico[2]]
1: Kamioka Observatory, ICRR, The University of Tokyo
2: Department of Physics King's College London

Introduction

The Hyper-Kamiokande (Hyper-K or HK) project [1] is the world-leading international scientific research project hosted by the university of Tokyo and High Energy Accelerator Research Organization (KEK) consisting of a next generation underground water Cherenkov detector and upgraded Japan Proton Accelerator Research Complex (J-PARC) neutrino beam. The supplementary budget for FY2019 including the first-year construction budget for Hyper-K project was approved by the Japanese Diet on January 2020 and the Hyper-K project has officially started.

Figure 39 shows a schematic drawing of the Hyper-K cylindrical detector. The detector is filled with 0.260 million metric tons of ultra pure water, which serves an order of magnitude larger fiducial mass of 0.188 million metric tons than Super-K, equipped with newly developed high-sensitivity photosensors, and a high-intensity neutrino beam produced by an upgraded J-PARC accelerator facility. It provides an enormous potential to discover leptonic charge-parity (CP) violation by observing neutrino and anti-neutrino beams from J-PARC, investigate the Grand Unified Theory by exploring proton decay, and determine the neutrino mass ordering by observing atmospheric neutrinos combining beam data. Hyper-K will also have far better capabilities to observe solar neutrinos and neutrinos from other astronomical sources than those of predecessor experiments.

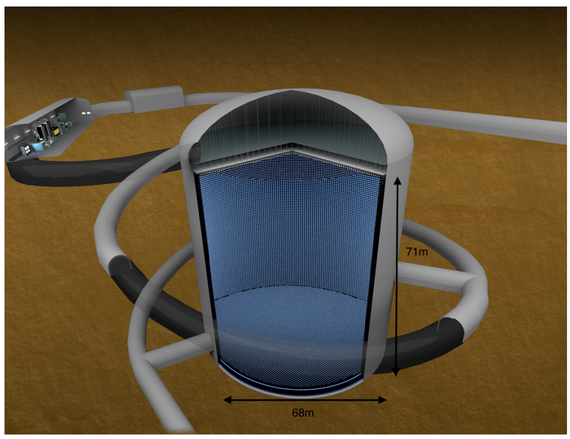

Fig. 39. Schematic view of the Hyper-K water tank.

The Hyper-K international collaboration consists of about 500 researchers from 99 institutes in 20 countries. The detector technology has been developed based upon the successful Super-K experiment and feasibility studies have been completed by international group. The Hyper-K operation plans to start in 2027.

Hyper-K will have capability to measure the magnitude of the CP violation with high precision, which could explain the baryon asymmetry in the Universe. Figure 40 shows an expected significance of the CP violation discovery by ten years operation. With expected systematic error improvement, Hyper-K covers the 60% of the parameter space with 5σ or more as red dotted line shows in the figure. More than 8σ significance will be expected if $\delta_{CP} = -\pi/2$ as suggested by T2K [2] and NOνA [3] results.

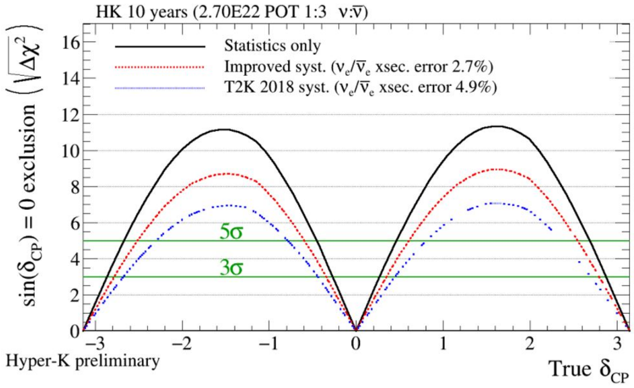

Fig. 40. Significance of the leptonic CP violation discovery with a 10-year observation in Hyper-K (HK) as a function of the unknown CP phase assuming the normal neutrino mass hierarchy. Red dotted line shows the result with expected systematic error improvement, blue dotted line shows the result with achieved systematic error by T2K 2018 and black line shows the result with only statistical error.

A proton decay $p \to e^+\pi^0$ is an important signal favored by many Grand Unified Theory models with a prediction close to the current limit of the proton decay life time. High sensitive Hyper-K PMTs result in strong background (atmospheric neutrinos) reduction and $p \to e^+\pi^0$ search in Hyper-K is expected to be "background-free" particularly in the free-proton enhanced signal region. Figure 41 shows the 3σ discovery potential for the $p \to e^+\pi^0$ mode as a function of year. Hyper-K is an only realistic proposal which can go beyond the proton lifetime of 1×10^{35} years.

As well as the supernova burst neutrino that was successfully observed in Kamiokande at once, undiscovered supernova relic neutrinos, accumulated by past all supernovae since the beginning of the universe, are interesting events to explore the history of heavy elements and the onset of stellar formation.

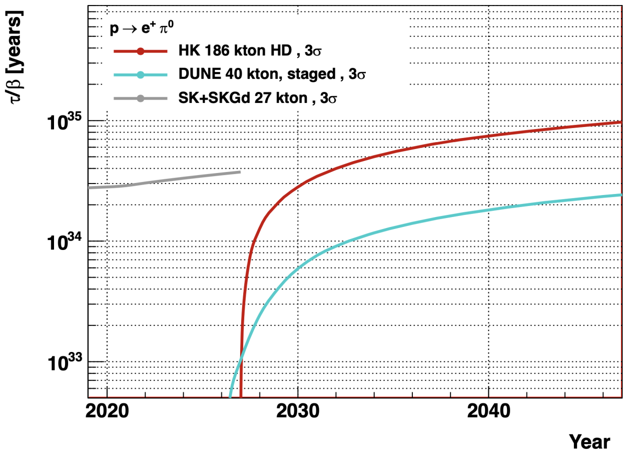

Fig. 41. The $p \to e^+\pi^0$ discovery reach in proton lifetime with 3σ significance as a function of year. It shows Hyper-K (HK) planing to start in 2027, superimposed with the ongoing Super-K (SK) and planned DUNE experiments. The DUNE project assumes 10 kton operation from 2026, toward full 40 kton by increasing 10 kton every year [4].

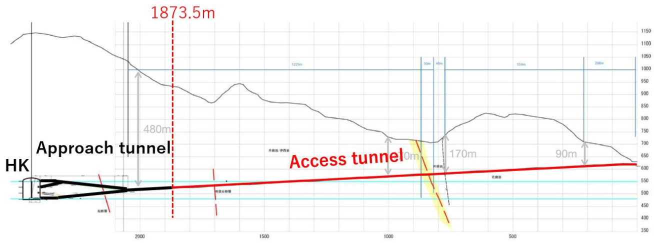

Fig. 42. Overview of the Hyper-Kamiokande excavation. The first part of tunnel is called as the access tunnel (red line). The black line after the access tunnel is the approach tunnel required for the cavern excavation.

Construction status

Figure 42 is schematic drawing of Hyper-K tunnels and the cavern. The excavation of the tunnel toward the Hyper-K cavern site was started from 6th May, 2021 after the completion of the entrance yard construction. Without any serious trouble, the first part of the tunnel, 1873.5m access tunnel excavation was finished at February as scheduled. Though the excavation started lower speed, excavation speed was improved gradually owing to hard and stable bedrock status and tiny amount of spring water. We achieved another significant milestone towards the realization of the Hyper-Kamiokande project. Photos in Fig. 43 shows the start of access tunnel excavation and the groundbreaking ceremony held on 28th May at the tunnel entrance. The excavated tunnel is shown in the top pannel of Fig. 44. The bottom panel of the figure was taken at 25th Feb. at the end of the access tunnel.

The second part of the tunnel, the approach tunnel excavation started from March. After the approach tunnel, the excavation of Hyper-K cavern is scheduled to start from October 2022. Fig. 45 shows first branch of the approach tunnels.

20-inch PMT, Delivery and inspection

Newly developed photomultiplier tubes R12860 by Hamamatsu Photonics K.K is shown in Fig. 46. The total detection efficiency of R12860 for single photon is twice higher than that of the Super-K PMT owing to 1.4 times higher quantum efficiency (about 32%) and improved photoelectron collection efficiency. The timing and charge resolutions at single photoelectron also becomes much better as 1.1 ns and 35% which can be compared with 2.1 ns and 53% of the Super-K PMT, respectively. Pressure tolerance of PMT was also improved up to the 125 m water depth, so that new PMT can be used under about 70 m depth of the detector water.

Since the start of mass production at October 2020, delivery of $\tilde{3}00$ R12860 for every month is ongoing. Total delivered number reached about 3300 by the end of FY2021 without any delay from the schedule. At the facility where delivered PMTs

Fig. 43. Photos at the start of the access tunnel excavation. The excavation started from 6th May, 2021(top). Hyper-K ground breaking ceremony held on 28th May at the tunnel entrance(bottom). As nine areas including Tokyo and Osaka were under the COVID-19 state of emergency, about half of the 50 participants attended online.

have been stored, inspections of the PMTs are also ongoing. The inspections are consist of three items, visual inspection for bulb and waterproof quality, signal check for signal property and noise rate, and long term stability check. Optimized setup of those inspections are shown in Fig. 47, top pannel is the signal check setup, middle is the eye inspection and bottom is the long term stability check setup. After all the first 700 PMTs were inspected, 10% sample has been inspected every month.

Fig. 44. The excavated access tunnel(top). Edge of the access tunnel at 25th Feb. 2022(bottom). The approach tunnel excavation started beyond this point).

Fig. 45. The first branch of the approach tunnels. One goes upward to the cavern dome and the other goes down to the bottom of the cavern.

Bibliography

[1] “Hyper-Kamiokande Design Report,” arXiv: 1805.04163.

[2] K. Abe *et al.* [T2K Collaboration], Nature 580, 339-344 (2020).

[3] P. Adamson *et al.* [NOνA Collaboration], Phys. Rev. Lett. 118, 231801.

[4] R. Acciarri *et al.* [The DUNE Collaboration], arXiv:1601.05471 [physics.ins-det].

[5] H. Sekiya [Super-K Collaboration], PoS(ICHEP2016) 982 (2016).

[6] ICRR News (2016), `http://www.icrr.u-tokyo.ac.jp/2016/06/30101400.html`.

[7] F. An *et al.* [JUNO Collaboration], J. Phys. G **43**, no. 3, 030401 (2016).

[8] Yu-Feng LI, Presentation at ”Workshop on Supernova at Hyper-Kamiokande” (2017).

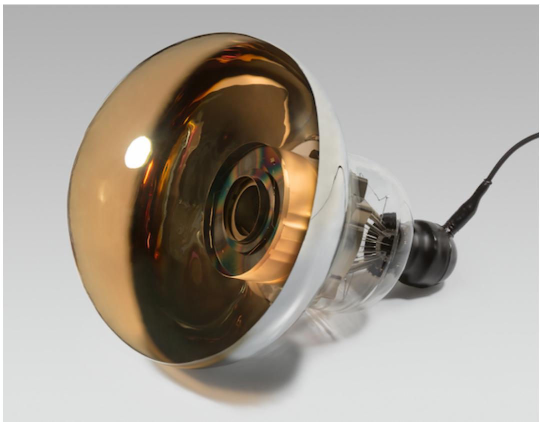

Fig. 46. New 50 cm photomultiplier tube with a box-and-line dynode (R12860, Hamamatsu Photonics K.K.).

Fig. 47. Inspections of PMTs.

HIGH ENERGY COSMIC RAY DIVISION

Overview

There are three major experimental research activities in the High Energy Cosmic Ray Division, the study of high energy gamma rays and the development of the next generation gamma-ray telescopes by the Cherenkov Cosmic Gamma Ray group, the study of extremely high energy cosmic rays by the Telescope Array (TA) group, and the study of very high energy cosmic rays and gamma rays by the Tibet ASγ group.

Other activities, such as experiments utilizing the Akeno observatory, the Norikura observatory, the Mt. Chacaltaya observatory (jointly operated with Bolivia) are closely related to inter-university joint research programs. Also an all-sky high resolution air-shower detector (Ashra) is in partial operation on the Hawaii island. The High Energy Astrophysics group created in the fiscal year 2009 aims to explore various high energy astrophysical phenomena, through theoretical and observational approaches.

The CANGAROO telescopes had been in operation in South Australia since 1992, with a 3.8 m small telescope and then with four 10 m telescopes. The major scientific objective was the study of Very High Energy (VHE) gamma-ray sources in our galaxy in the southern hemisphere. The mission of these telescopes was completed and the CANGAROO observation site was closed in 2011.

For further development of VHE gamma-ray astronomy, the Cherenkov Cosmic Gamma Ray group is working on the design study and development and construction of the next generation international ground-based gamma-ray observatory CTA which will offer an order of magnitude better sensitivity than currently running Cherenkov telescopes, three times better angular resolution, and wider energy coverage from 20 GeV to 100 TeV or higher. The construction of the first Large-Sized Telescope (LST) was completed on the CTA-North site in La Palma in 2018. High Energy Astrophysics Facility in Canarias was established as a base for the project in April, 2019.

At the Akeno observatory, a series of air shower arrays of increasing geometrical sizes were constructed and operated to observe extremely high energy cosmic rays (EHECRs). The Akeno Giant Air Shower Array (AGASA) was operated from 1991 to January 2004 and covered the ground area of 100 km^2 as the world largest air shower array. In 13 years of operation, AGASA observed a handful of cosmic rays exceeding the theoretical energy end of the extra-galactic cosmic rays (GZK cutoff) at around 10^{20} eV.

The Telescope Array (TA), a large plastic scintillator array with air fluorescence telescopes, has been constructed in Utah, USA, which succeeds AGASA and measures the EHECRs with an order of magnitude larger aperture than that of AGASA for the further study of EHECRs. The full-scale TA is accumulating data as the largest array viewing the northern sky and observed the energy spectrum with high statistics, which is in good agreement with the GZK suppression and found evidence for anisotropy of arrival directions of EHECRs. The TAx4, which is aimed at quadrupling TA, was partially constructed by March of 2019.

An air shower experiment aiming to search for celestial gamma-ray point sources started in 1990 with Chinese physicists at Yangbajing (Tibet, 4,300 m a.s.l.). This international collaboration is called the Tibet ASγ Collaboration. An extension of the air shower array was completed in 1995 and an emulsion chamber has been combined with this air shower array since 1996 to study the primary cosmic rays around the knee energy region. After successive extensions carried out in 1999, 2002 and 2003, the total area of the air shower array amounts to 37,000 m^2. The sun's shadow in cosmic rays affected by the solar magnetic field was observed for the first time in 1992, utilizing its good angular resolution at multi-TeV energy region. The group added underground water Cherenkov muon detector to detect cosmic gamma rays above 100 TeV. The group is planning to construct a new air shower array, called ALPACA, to cover the sky in the Southern hemisphere, and started the construction of its partial array in Bolivia in 2019.

The High Energy Astrophysics group is conducting theoretical researches on fundamental processes responsible for non-thermal particle acceleration in various astrophysical environments, including first-order diffusive shock acceleration, second-order stochastic acceleration in shock downstream regions, modification of shock structure by pick-up interstellar neutrals, as well as injection processes of suprathermal particles. In addition to these theoretical works, R/D studies for radio observations of pulsars and cosmic ray air showers are also being made.

Cherenkov Cosmic Gamma-Ray Group

CTA Project (Cherenkov Telescope Array)

CTA-Japan Consortium

[Spokespersons : M. Teshima and H. Kubo]

Collaboration list:

Institute for Cosmic Ray Research, The University of Tokyo, Chiba, Japan; Department of Physics, Aoyama Gakuin University, Tokyo, Japan; Department of Physics, Hiroshima University, Hiroshima, Japan; Hiroshima Astrophysical Science Center, Hiroshima University, Hiroshima, Japan; Faculty of Science, Ibaraki University, Ibaraki, Japan; Institute of Particle and Nuclear Studies, High Energy Accelerator Research Organization (KEK), Ibaraki, Japan; Department of Physics, Konan University, Hyogo, Japan; Faculty of Medical Engineering and Technology, Kitasato University, Kanagawa, Japan; Graduate School of Science and Technol-

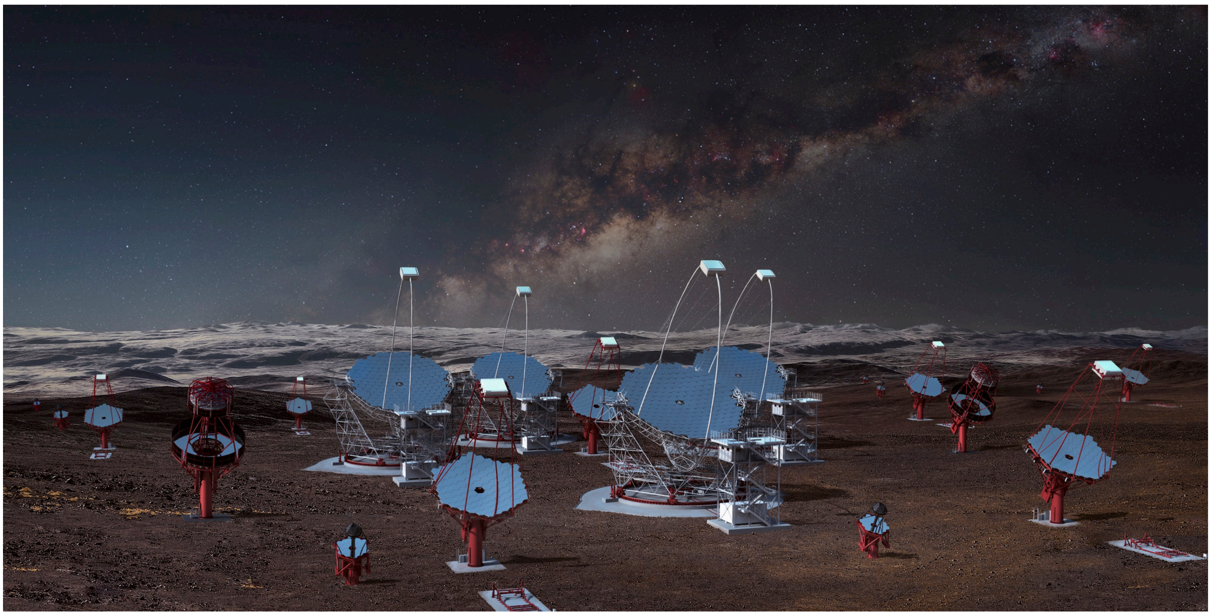

Fig. 1. Artist view of the CTA observatory. CTA consists of three types of telescopes, Large Size Telescopes (23 m diameter), Mid Size Telescopes (12 m) and Small Size Telescopes (4 m), and covers the broad energy band from 20 GeV to 300 TeV. [Credit: Gabriel Pérez Diaz (IAC)/Marc-André Besel (CTAO)/ESO/ N. Risinger (skysurvey.org)]

ogy, Kumamoto University, Kumamoto, Japan; Department of Physics, Kyoto University, Kyoto, Japan; Department of Applied Physics, University of Miyazaki, Miyazaki, Japan; Department of Physics, Nagoya University, Aichi, Japan; Solar-Terrestrial Environment Laboratory, Nagoya University, Aichi, Japan; Kobayashi-Maskawa Institute, Nagoya University, Aichi, Japan; Department of Earth and Space Science, Osaka University, Japan; Astrophysical Big Bang laboratory, RIKEN, Wako, Japan; Department of Physics, Rikkyo University, Tokyo, Japan; Department of Physics, Saitama University, Saitama, Japan; Department of Physics, Tokai University, Kanagawa, Japan; Faculty of Integrated Arts and Sciences, The University of Tokushima, Tokushima, Japan; Department of Astronomy, The University of Tokyo, Tokyo, Japan; Department of Physics, The University of Tokyo, Tokyo, Japan; Faculty of Science and Engineering, Waseda University, Tokyo, Japan; Department of Physics, Yamagata University, Yamagata, Japan; Faculty of Management Information, Yamanashi Gakuin University, Yamanashi, Japan.

CTA Project

During the past years, Very High Energy (VHE) gamma-ray astronomy has made spectacular progress and has established itself as a vital branch of astrophysics. To advance this field even further, we are constructing the Cherenkov Telescope Array (CTA) [6], the next generation VHE gamma ray observatory, in the framework of a worldwide, international collaboration. CTA is the ultimate VHE gamma-ray observatory, whose sensitivity and broad energy coverage will attain an order of magnitude improvement above those of current Imaging Atmospheric Cherenkov Telescopes (IACTs). By observing the highest energy photons known, CTA will clarify many aspects of the extreme Universe, including the origin of the highest energy cosmic rays in our Galaxy and beyond, the physics of energetic particle generation in neutron stars and black holes, as well as the star formation history of the Universe. CTA will also address critical issues in fundamental physics, such as the identity of dark matter particles and the nature of space and time.

VHE gamma rays from 100 GeV to 10 TeV can be observed with ground-based current IACTs. The history of VHE gamma ray astronomy began with the discovery of VHE gamma rays from the Crab Nebula by the Whipple Observatory in 1989. To date, the current generation IACTs featuring new technologies, such as H.E.S.S., MAGIC, and VERITAS, have discovered more than 200 Galactic and extragalactic sources of various types.

CTA is designed to achieve superior sensitivity and performance, utilizing established technologies and experiences gained from the current IACTs. The project is presently in its pre-construction (prototyping) phase, with international efforts from Japan, US, and EU countries. It will consist of several 10s of IACTs of three different sizes (Large Size Telescopes, Mid Size Telescopes, and Small Size Telescopes). With a factor of 10 increase in sensitivity (1 mCrab $\sim 10^{-14}$erg s^{-1} cm^{-2}), together with a much broader energy coverage from 20 GeV up to 300 TeV, CTA will bring forth further dramatic advances for VHE gamma-ray astronomy. The discovery of more than 1000 Galactic and extragalactic sources is anticipated with CTA.

CTA will allow us to explore numerous diverse topics in physics and astrophysics. The century-old question of the origin of cosmic rays is expected to be finally settled through detailed observations of supernova remnants and other Galactic objects along with the diffuse Galactic gamma-ray emission, which will also shed light on the physics of the interstellar medium. Observing pulsars and associated pulsar wind nebulae will clarify physical processes in the vicinity of neutron stars and extreme magnetic fields. The physics of accretion onto supermassive black holes, the long-standing puzzle of the origin of ultra-relativistic jets emanating from them, as well as their cosmological evolution, will be addressed by extensive studies of active galactic nuclei (AGN). Through dedicated observing strategies, CTA will also elucidate many aspects of the mysterious nature of gamma ray bursts (GRBs), the most energetic explosions in the Universe. Detailed studies of both AGNs and GRBs can also reveal the origin of the highest energy cosmic rays in the Universe, probe the cosmic history of star formation including the very first stars, and provide high precision tests of theories of quantum gravity. Finally, CTA will search for signatures from elementary particles constituting dark matter with the highest sensitivity yet. Realisation of the rich scientific potential of CTA is very much feasible, thanks to the positive experiences gained from the current IACTs.

The CTA-Japan consortium [1] is contributing particularly to the construction of the Large Size Telescopes (LSTs, Fig.2) and is involved in their development. The LST covers the low energy domain from 20 GeV to 3 TeV and is especially important for studies of high redshift AGNs and GRBs. The diameter and area of the mirror are 23 m and 400 m^2, respectively, in order to achieve the lowest possible energy threshold of 20 GeV. All optical elements and detectors require high specifications, such as high reflectivity, high collection efficiency, high quantum efficiency, ultra-fast digitization of signals, and so on. For this purpose, CTA-Japan has developed high quantum efficiency photomultipliers and ultrafast readout electronics (Fig. 3), and high precision segmented mirrors (Fig. 4). On the strength of their experiences gained from the construction of the MAGIC telescope, Max-Planck-Institute for Physics in Munich is responsible for the design of the 23-m diameter telescope structure, based on a carbon fiber tube space frame. The LSTs require very fast rotation (180 degrees in 20 seconds) to promptly observe GRBs. The first LST (LST-1) has been built in the CTA North, La Palma, Spain, in 2018, and now in the engineering run. Three more LSTs will be built until 2023, then four more LSTs in the CTA South are expected to be built in the ESO site in Paranal, Chile.

The results of the commissioning of the LST-1 camera has been presented in the international conference [10]. The noise level, the charge calibration precision, the trigger rates, the DAQ performance and operation stability were well studied characterized there. Fig.6 shows one of those results, showing the stability of noise level as a function of time and the night sky background intensity.

The Critical Design Review of LST-1 was held by CTAO engineers and external experts from high energy physics. The LST-1 has been regularly operated since January 2020, and has already shown an excellent performance as expected, even in a single telescope mode, through the observation of Crab Nebula, Crab Pulsar, and nearby Active Galactic Nuclei (AGN). These results certify LST-1 achieved the design performance expected by Monte Carlo simulations. The phase diagram of the Crab Pulsar observation is shown in Fig. 7, which certifies the low threshold energy of LST-1 and also the accuracy of the recorded event timings. In July 2021, the LST collaboration issued the first telegram of reporting the detection of the AGN BL Lac with LST-1 [11]. The location of the

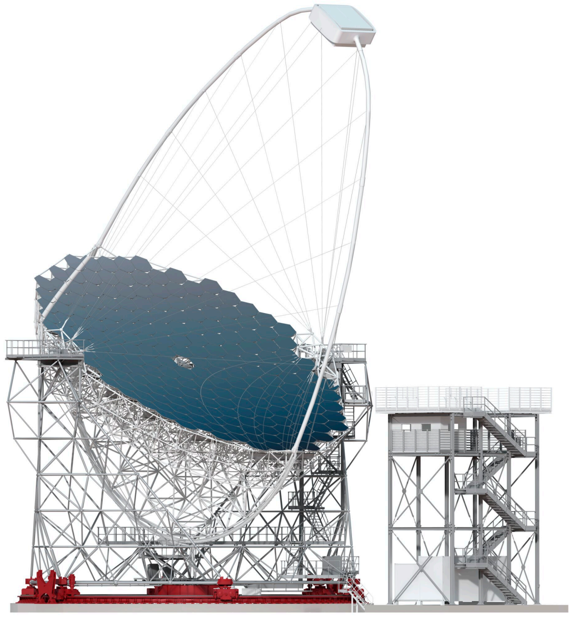

Fig. 2. Large Size Telescope (23 m diameter) designed by Max–Planck-Institute for Physics. CTA Japan is contributing to the design and construction of the imaging camera at the focal plane, ultrafast readout electronics, and high precision segmented mirrors.

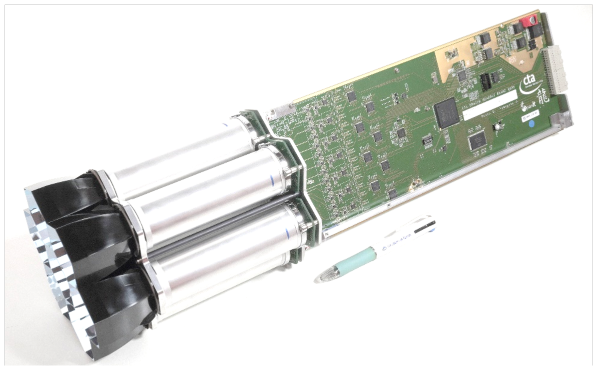

Fig. 3. Camera cluster for the Large Size Telescope (LST) developed by CTA-Japan. This cluster consists of seven high quantum efficiency photomultipliers (R11920-100), CW High Voltages, pre-amplifier, Slow Control Board, DRS4 Ultra fast waveform recording system and Trigger. The LST camera can be assembled with 265 of these clusters, cooling plates and camera housing.

LST array in the CTA North has an overlap with MAGIC telescopes, which will allow us to perform the cross-calibration between LST and MAGIC telescopes and to operate the three telescopes together in the early phase of the construction.

On 19th September, 2021, a volcanic eruption initiated in Cumbre Vieja (El Paso) more than 20 km away in a straight line from the Roque de los Muchachos Observatory (ORM) where LST-1 is located. The LST collaboration decided to stop the LST-1 operation. The eruption continued until 25th December, 2021. After the inspection of LST-1 and the recovery works, an observation with LST-1 restarted on 21th January, 2022.

In addition to the LST activities, CTA-Japan members are also contributing to the overall CTA project in the Analysis

Fig. 4. The high precision segmented mirrors for the Large Size Telescope (LST) developed by CTA-Japan in cooperation with Sanko Co.LTD. The mirror is made of a 60-mm thick aluminum honeycomb sandwiched by 3-mm thin glass on both sides. A surface protection coat consisting of the materials SiO_2 and HFO_2 is applied to enhance the reflectivity and to elongate the lifetime.

Fig. 5. The Large Size Telescope prototype (LST-1) constructed at Observatory de Roque de los Muchachos is now in the engineering run. The diameter of dish and mirror surface area are 23 m and 400 m^2.

and Simulations Working Group (ASWG). The performance of the planned CTA layout is estimated by simulations and the resulting IRFs (Instrument Response Functions) are public at [12]. Since the most important factor in determining the gamma-ray sensitivity of an IACT array is the rate of misidentified cosmic-ray proton backgrounds, the accuracy of the description of hadronic showers affects the estimation of the gamma-ray sensitivity. By testing recent four hadronic interaction models (QGSJET-II-03, QGSJET-II-04, EPOS-LHC, and SIBYLL2.3c) in the CTA simulation, variations in background rates of up to a factor 2 with respect to QGSJET-II-03 are observed between the models, which leads to $\sim$30% differences in the estimated gamma-ray sensitivity in the 1 - 30 TeV region (50-hour case, for a point source). The results also show that IACTs have a significant capability in the verification of hadronic interaction models [13].

The Cherenkov Cosmic Gamma Ray group is also operating the MAGIC Telescopes [14] on La Palma, Canary Islands (See the next subsection). This facility is used not only for

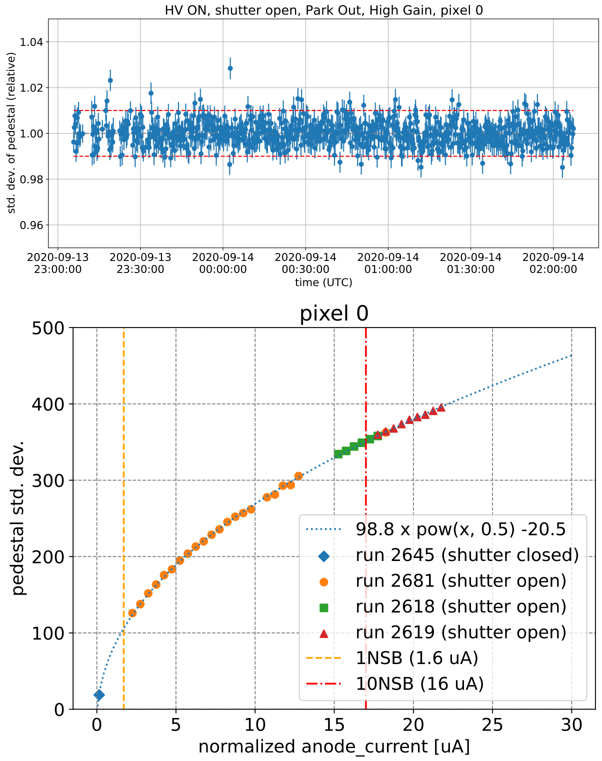

Fig. 6. (Top) Time evolution of the noise for a single pixel for three hours. Each point represents ~ 50000 events (~ 12 seconds) and error bars show standard deviation of the noise for this single pixel. (Bottom) Noise level during multiple observation runs as a function of the anode current. Orange and red dotted lines show dark night sky background (NSB) and 10 times higher than dark NSB level, respectively.

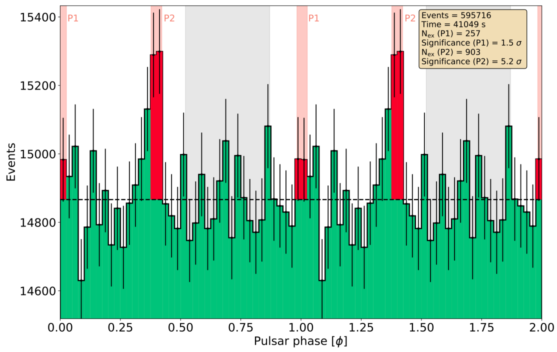

Fig. 7. Phase diagram of Crab Pulsar as measured by LST-1. The pulsar is known to emit pulses of gamma rays during phases P1 and P2. The energy threshold in this observation is estimated about 40-50 GeV.

scientific observations but also for technological development toward the future observatory CTA.

Bibliography

[1] CTA Consortium website: `http://www.cta-observatory.jp/` and `http://www.cta-observatory.org/`.

[2] Science with the Cherenkov Telescope Array,

arXiv:1709.07997

[3] The Cherenkov Telescope Array potential for the study of young supernova remnants, Astropart. Phys. 62 (2015) 152-164.

[4] Introducing the CTA concept, The CTA Consortium, Astropart. Phys. 43 (2013) 3-18.

[5] Gamma-ray burst science in the era of the Cherenkov Telescope Array, S. Inoue et al., Astropart. Phys. 43 (2013) 252-275.

[6] Design Concepts for The Cherenkov Telescope Array, The CTA Consortium, Exper. Astron. 32 (2011) 193-316.

[7] Status of Very High Energy Gamma Ray Astronomy and Future Prospects, M. Teshima, The Astronomical Herald, 104 (2011) 333-342.

[8] Design Study of a CTA Large Size Telescope, Proc. of ICRC2012 at Beijing China, M. Teshima, arXiv:1111.2183.

[9] Introducing the CTA Concept, B. Acharya et al., Astroparticle Physics, 34 (2013) 3.

[10] Commissioning of the camera of the first Large Size Telescope of the Cherenkov Telescope Array, Proc. of ICRC2021 at Berlin Germany (Online), T. Saito et al., arXiv:2108.01920.

[11] Detection of very-high-energy gamma-ray emission from BL Lac with the LST-1, ATEL #14783.

[12] CTA Observatory website (CTAO performance) `https://www.cta-observatory.org/science/ctao-performance/`

[13] Effect of the uncertainty in the hadronic interaction models on the estimation of the sensitivity of the Cherenkov Telescope Array, M. Ohishi et al., J. Phys. G: Nucl. Part. Phys. 48 075201 (2021)

[14] MAGIC Collaboration website: `http://magic.mppmu.mpg.de/`.

MAGIC

The MAGIC Collaboration has built in 2004 a first large atmospheric imaging Cherenkov telescope, MAGIC-I, with a mirror surface of 236 m^2 and equipped with photomultiplier tubes of optimal efficiency. In 2009, a second telescope of essentially the same characteristics was added; MAGIC-II was installed at a distance of 85 m from MAGIC-I. With the accent of these instruments on large mirror surface and best light collection, cosmic gamma-rays at an energy threshold lower than any existing or planned terrestrial gamma-ray telescope have become accessible. So far achieved has been a threshold of 25 GeV. The Japanese group has joined the MAGIC collaboration since 2010, and contributed to the operation, observations and data analyses. The MAGIC telescopes are upgraded with new cameras, electronics and partially new mirrors in 2012,

Fig. 8. MAGIC Stereo System with two Cherenkov telescopes of 17 m diameters, so far achieved the threshold energy of 25 GeV with the sum trigger. It locates near the mountain top of the Roque de los Muchachos on the Canary Island of La Palma. Two telescopes are located with the distance of 85 m.

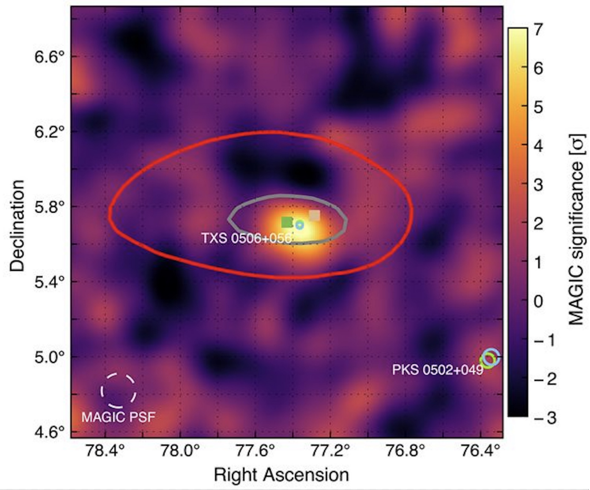

Fig. 9. Sky position of IceCube-170922A in the equatorial coordinate with contour of 50% and 90% confidence level overlaying the gamma-ray colour contour map observed by MAGIC (7 sigma in the peak) [5].

and are now operated with an unprecedented sensitivity by an international collaboration of about 165 scientists from 24 institutes and consortia from 12 countries.

The recent highlights from MAGIC are, 1) The first detection of the Gamma Ray Burst GRB 190114C with the ground-based gamma-ray telescope MAGIC [1], [2], [3], 2) Observation of sub-TeV gamma rays from the IceCube 170922A [4], [5] (Fig. 9), 3) the successful observation of pulsed gamma ray signal from the Crab pulsar up to TeV regime [6], 4) the discoveries of the most distant blazers 3S 0218+35 with the redshift of 0.944 and PKS 1441+25 with the redshift of 0.939 [7], 5) the observation of the very fast flare of 1-min time scale from the blazar inside Perseus cluster, IC310 [8], 6) the conclusions of a 15 years joint observation campaign of the gamma-ray binary HESS J0632+057 together with the Cherenkov telescope experiments H.E.S.S. and VERITAS [14]. These results brought new questions on the pulsar emission mechanism, the EBL energy density, and gamma ray emission mechanism from the supermassive blackholes or vicinity of them.

Gamma Ray Bursts

In January 2019, the MAGIC telescopes, for the first time, observed the TeV Gamma-Ray Burst GRB 190114C with the redshift of 0.42 [1],[2], [3]. The observation shows the 100 times higher flux of gamma rays than the Crab Nebula at T_0 + 80 sec, and the resultant statistical significance of gamma-rays was more than 50 sigma. The highest-energy photon reaches above 1 TeV, and the observed spectrum after the EBL de-absorption did not show any roll-off feature in the energy spectrum [2]. This observation will require the new gamma-ray emission mechanism in the GRB to explain the TeV emission, possibly the inverse Compton emission. The light curve shows the power-law decay $t^{-1.6}$, which is surprisingly parallel to the X-ray lightcurve measured by XRT [2]. It is worth mentioning that the energetics of the TeV emission is comparable with that of the X-ray emission. The two bump structure in the spectral energy distribution can be fit consistently with the Synchroton Self-Compton model as shown in Fig. 10 [3]. In 2020 MAGIC published a followup paper, a constraint on Lorentz invariance violation using the data of the GRB [9].

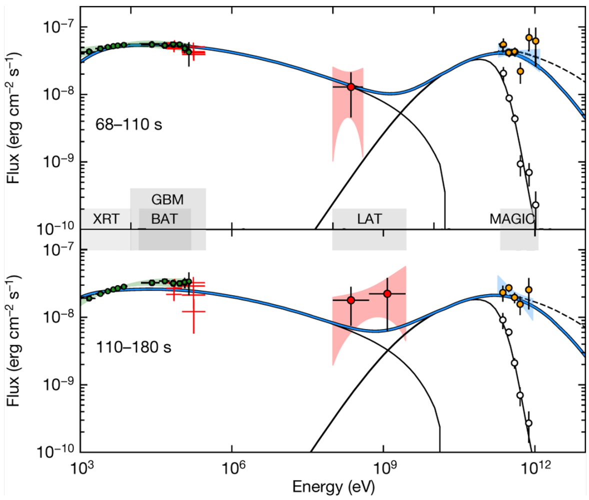

Fig. 10. Modelling of the broadband spectra in the time intervals 68-110 s and 110-180 s for GRB 190114C [3].

In 2021 an important paper was published about a hint of detection from GRB 160821B. The GRB is a short GRB at $z = 0.162$, which is the closest GRB observed by MAGIC (before 190829A), and it has a kilonova emission reported in 2019. After informed of the report, we have revised the modeling of the TeV flux suggested by MAGIC data, revealing that the Synchrotron Self-Compton model does not work well for this GRB [10]. In ICRC 2021 we have shown other two important results about long GRBs; a hint of detection from a low-luminosity GRB 201015A [11], and a clear detection from the farthest VHE GRB 201216C at $z = 1.1$ [12]. Both contributions have been led by Japanese colleagues in MAGIC Collaboration. These results show an importance of continuing GRB observations to increase the number of detections both for long and short GRB types.

Broadband Multi-wavelength Properties of M87 during the 2017 Event Horizon Telescope Campaign

In 2017, the Event Horizon Telescope (EHT) Collaboration succeeded in capturing the first direct image of the center of the M87 galaxy. The asymmetric ring morphology and size are consistent with theoretical expectations for a weakly accreting supermassive black hole of mass $\sim 6.5 \times 10^9 M_\odot$. The EHTC also partnered with several international facilities in space and on the ground, to arrange an extensive, quasi-simultaneous multi-wavelength campaign [13]. MAGIC participated in the campaign, together with other major TeV instruments such as H.E.S.S. and VERITAS. During the campaign M87 was captured in a historically low state, and the core flux dominates over HST-1 at high energies, making it possible to combine core flux constraints with the more spatially precise very long baseline interferometry data.

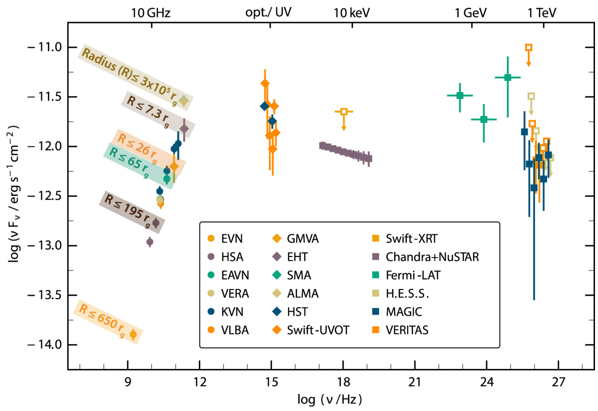

Fig. 11. Simultaneous multi-wavelength spectrum of M87 during the EHT campaign in 2017 [13].

We present the most complete simultaneous multi-wavelength spectrum of the active nucleus to date in Figure 11. Applying two heuristic, isotropic leptonic single-zone models to provide insight into the basic source properties, we conclude that a structured jet is necessary to explain M87's spectrum. We can exclude that the simultaneous γ-ray emission is produced via inverse Compton emission in the same region producing the EHT mm-band emission, and further conclude that the γ rays can only be produced in the inner jets (inward of HST-1) if there are strongly particle-dominated regions. Direct synchrotron emission from accelerated protons and secondaries cannot yet be excluded.

The gamma-ray binary HESS J0632+057

The three Cherenkov telescope experiments H.E.S.S., MAGIC and VERITAS carried out the deepest study of the gamma-ray binary HESS J0632+057, comprising a total of 450 h of data spanning almost 15 years [14]. This multi-year campaign is embedded in a multi-wavelength context, which includes X-ray (*Swift*-XRT, Chandra, *XMM*-Newton, NuStar and Suzaku) and optical Hα observations obtained using the HIDES (High-Dispersion Echelle Spectrograph), deployed on a 188 cm telescope at Okayama Astrophysical Observatory. For the first time, the orbital period at TeV energies was determined, yielding a value of 316.7 ± 4.4 days. This solution is in agreement with the 317.3 ± 0.7-day period derived from the latest *Swift*-XRT X-ray data set. The ratio of gamma-ray to X-ray flux underlines the equality or even dominance of the gamma-ray energy range for the emission of HESS J0632+057. In the phase-folded light curve (Fig. 12), two well-differentiated peaks are visible, a dip phase and a broader plateau phase. The VHE SEDs for all of these phases (except the dip phase, where only upper limits could be derived) are generally characterized as power-laws, showing no variability in the spectral slope within statistical errors. Only the spectrum measured with VERITAS during the phases 0.2–0.4 favors a power-law with exponential cutoff at 1.75 TeV. The strong correlation between X-rays and gamma rays suggest a common origin of the radiation, indicating the existence of a single population of particles. An indication for an X-ray source partially not related to the gamma-ray emission was however found. The lack of correlation between Hα and X-ray or gamma-rays might point towards a negligible role of the disk of the Be star in the modulation of the non-thermal emission, but is possibly an effect of the fast variability of Hα compared with the sparse overlap of the datasets at different energies. Two outbursts during orbits 9 (2011, January) and 17 (2018, January) revealed enhanced gamma-ray and X-ray emission comparable to the highest flux ever observed from this binary. Furthermore, a flux decay of roughly 20 days or less was detected for two orbits. Contemporaneous Hα data taken on 2018, January 25 indicate that the size of the circumstellar disk had increased during those days, suggesting that the decretion disk was larger and its structure had changed. The determination of the orbital geometry of the system is of utmost importance and requires a coordinated multi-year optical campaign. Finally, the wealth of data presented for HESS J0632+057 awaits theoretical modelling taking consistently all aspects of the spectral and temporal measurements into account.

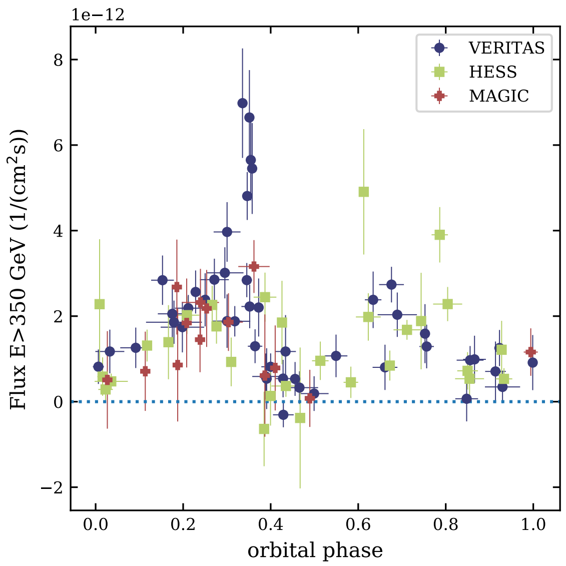

Fig. 12. Gamma-ray (>350 GeV) lightcurve as a function of the orbital phase, assuming an orbital period of 317.3 days (MJD$_0$=54857.0)). Vertical error bars indicate statistical uncertainties [14].

Bibliography

[1] The first detection of a GRB at sub-TeV energies; MAGIC detects the GRB190114C., ATEL # 12390.

[2] Teraelectronvolt emission from the γ-ray burst GRB 190114C, Nature 575, 455 (2019).

[3] Observation of inverse Compton emission from a long γ-ray burst; MAGIC collaboration et al. Nature 575, 459 (2019).

[4] First-time detection of VHE gamma rays by MAGIC from a direction consistent with the recent EHE neutrino event IceCube-170922A, ATel #10817.

[5] Multimessenger observations of a flaring blazar coincident with high-energy neutrino IceCube-170922A, Science 12 July 2018, Science.eaat1378.

[6] Phase-resolved energy spectra of the Crab pulsar in the range of 50-400 GeV measured with the MAGIC telescopes, the MAGIC Collaboration, Aleksić et al. A&A 540 (2012) A69.

[7] Discovery of Very High Energy Gamma-Ray Emission from the distant FSRQ PKS 1441+25 with the MAGIC telescopes, ATEL # 7416.

[8] Black hole lightning due to particle acceleration at sub-horizon scales, the MAGIC collaboration, Science 346 (2014) 1080-1084.

[9] Bounds on Lorentz Invariance Violation from MAGIC Observation of GRB 190114C, the MAGIC collaboration, PRL 125 (2020) 021301.

[10] MAGIC Observations of the Nearby Short Gamma-Ray Burst GRB 160821B, the MAGIC collaboration, ApJ 908 (2021) 90.

[11] Observation of a relatively low luminosity long duration GRB 201015A by the MAGIC telescopes, Y. Suda et al., PoS ICRC2021 (2021) 797.

[12] Very-high-energy gamma-ray emission from GRB 201216C detected by MAGIC, S. Fukami et al., PoS ICRC2021 (2021) 788.

[13] Broadband Multi-wavelength Properties of M87 during the 2017 Event Horizon Telescope Campaign, J.C. Algaba et al. (the Event Horizon Telescope Collaboration, the Fermi Large Area Telescope Collaboration, H.E.S.S. Collaboration, MAGIC Collaboration, VERITAS Collaboration, EAVN Collaboration), The Astrophysical Journal Letters, L11 (2021) 911.

[14] Observation of the Gamma-Ray Binary HESS J0632+057 with the H.E.S.S., MAGIC, and VERITAS Telescopes, the MAGIC + H.E.S.S. + VERITAS collaborations, ApJ 923 (2021) 241A.

Fig. 13. Akeno atmospheric Cherenkov telescope of 3 m diameter, located in the Akeno Observatory.

Other Activities

As a test bench for domestic R & D activities of future ground-based gamma-ray observatory projects, an old atmospheric Cherenkov telescope of 3 m diameter was repaired and then placed at the Akeno Observatory in November 2010. This telescope shown in Figure 13 (Akeno telescope, hereafter) is currently the only atmospheric Cherenkov telescope located in Japan [1]. We have developed an R & D imaging camera system with the Akeno telescope since 2009, the purpose of which is to make a battery-powered data acquisition system for a future mobile imaging atmospheric Cherenkov telescope array [2]. The system consists of 32 PMTs, of which detected Cherenkov light signals are read out by only four GHz-sampling analog memory ASICs.

Utilizing some central PMTs of the above system, we have also observed the optical Crab pulsar in Akeno. The purpose of this study is to investigate the efficient acceleration site of the Crab Nebula in a microscopic way with simultaneous observations of radio and optical pulses passing through the nebula plasma. We performed the first observations of the optical Crab pulsar in January 2020 after developing a dedicated pulse counting system, which were followed by further observations in 2021 and 2022 with some improvements in the system. From about 10 hr data taken in 2021, we found a marginal signal which coincides with the Crab main pulse phase, at a 3σ level. The 2022 data taken with further improvements are still under analysis.

Bibliography

[1] M. Ohishi et al., Proc. of 33rd Internat. Cosmic Ray Conf. (Rio de Janeiro), 587 (2013).

[2] T. Yoshikoshi et al., Proc. of 34th Internat. Cosmic Ray Conf. (The Hague), 887 (2015).

TA: Telescope Array Experiment

Spokespersons: S. Ogio[1,2], C.C.H. Jui[3]

1 : Graduate School of Science, Osaka City University
2 : ICRR, The Univ. of Tokyo, Kashiwa, Chiba 277-8582
3 : Dept. of Physics and Astronomy, University of Utah

Collaborating Institutions:

Chubu Univ., Kasugai, Japan; ERI, Univ. of Tokyo, Tokyo, Japan; Hiroshima City Univ., Hiroshima, Japan; Hanyang Univ., Seoul, Korea; ICRR, Univ. of Tokyo, Kashiwa, Japan; INR, Moscow, Russia; CEICO, Inst. of Phys, Czech Acad. of Sci., Prague, Czech Republic; Kanagawa Univ., Yokohama, Japan; KEK/IPNS, Tsukuba, Japan; Kochi Univ., Kochi, Japan; Kyoto Univ., Kyoto, Japan; Loyola Univ., Chicago, USA; Moscow M.V. Lomonosov State University, Moscow, Russia; NICT, Tokyo, Japan; Osaka Electro-Comm. Univ., Neyagawa, Japan; Osaka City Univ., Osaka, Japan; RIKEN, Wako, Japan; Ritsumeikan Univ., Kusatsu, Japan; Saitama Univ., Saitama, Japan; Shibaura IT, Tokyo, Japan; Shinshu Univ., Nagano, Japan; SKKU, Suwon, Korea; Tokyo City Univ., Tokyo, Japan; Tokyo Inst. of Tech., Tokyo, Japan; Tokyo Univ. of Science, Noda, Japan; ULB, Brussels, Belgium; UNIST, Ulsan, Korea; Univ. of Nova Gorica, Nova Gorica, Slovenia; Univ. of Utah, Salt Lake City, USA; Univ. of Yamanashi, Kofu, Japan; Yonsei Univ., Seoul, Korea

1. Introduction

The Telescope Array (TA) is the largest Ultra-High Energy Cosmic Ray (UHECR) observatory in the northern hemisphere. The main aim of TA is to explore the origin and nature of UHECRs by measuring the energy spectrum, arrival direction distribution and mass composition. The TA collaboration consists of approximately 140 researchers from USA, Russia, Korea, Belgium, Czech, Slovenia and Japan.

The TA detector consists of a surface array of 507 plastic scintillator detectors (SD) and three stations of fluorescence detectors (FD). It is located in the desert, approximately 200 km south of Salt Lake City in Utah in USA. The SDs were deployed on a square grid with 1.2-km spacing, and the SD array covers an area of approximately 700 km^2. Each SD has two layers of 1.2-cm-thick scintillator with an area of 3 m^2. The full operation of SDs started in March 2008. The duty cycle is approximately 95% on average. One northern FD station at the Middle Drum (MD) site uses 14 refurbished HiRes telescopes. Two southern FD stations at the Black Rock Mesa (BRM) and Long Ridge (LR) sites were built newly each with 12 telescopes. The MD FD views 3° - 31° and the BRM and LR FDs view 3° - 33° above horizon. All three FD stations started the observation in November 2007, and have duty cycles of approximately 10%.

TA found evidence for intermediate-scale anisotropy of arrival directions of cosmic rays with greater than 5.7×10^{19} eV of energy. With enhanced statistics, it is expected to observe the structure of the hotspot along with other possible excesses and point sources along with the correlations with extreme phenomena in the nearby universe. TA proposed TAx4 project to quadruple the effective area of the TA SD aperture including the existing TA SD array by installing additional 500 newly designed SDs on a square grid with wider, 2.08-km spacing between each. The layout of TAx4 is shown in Fig. 14.

The design of SD for the TAx4 experiment is identical to the design of SD for the TA Low energy Extension(TALE) experiment, which will be described in detail later. The basic design is common to TA , but the number and arrangement of wavelength shifter fibers (WLSF), the performance of the photomultiplier tubes (PMTs), and the wireless LAN module and used protocols are different. In the TAx4 and TALE, we use a PMT with significantly improved quantum efficiency and surface uniformity. This has allowed us to reduce the total length of WLFSs by 67% while maintaining the performance of the SD as a whole. A new wireless LAN module is used for the TAx4 and TALE SDs because the one used in TA was out of production.

Detector installation for TAx4 began in 2019, and 257 SDs were deployed in February and March 2019. By this installation, the total coverage area with SDs including the original TA SD array has been increased by a factor of 2.5. The new SD array started the data acquisition in April 2019. Since the new SD array is divided into two lobes, two FD stations are required to overlook each lobe in order to increase the number of hybrid events for the measurement of $X_{\max}$ and to confirm the energy scale. These FD stations consist of refurbished HiRes telescopes: four telescopes at the MD site and eight telescopes at the BR site. The TAx4 FD station at the northern site was constructed and started the stable observation in June 2018. The TAx4 FDs at the southern site were constructed and started the observation in 2019. The recent status of TAx4 was reported in [1]. Fig. 15 show the footprint, the event display on the FD and the time fit using hybrid reconstruction for a typical TAx4 hybrid event.

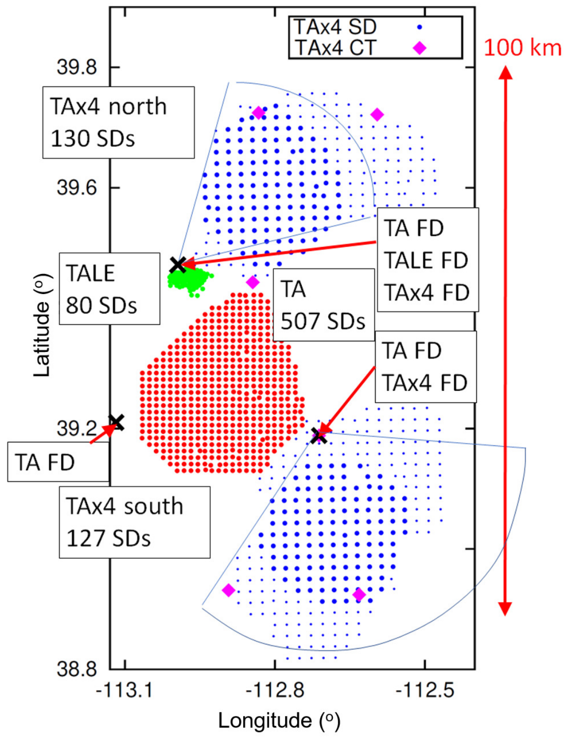

Fig. 14. The layout of the proposed TAx4. The array of 507 SDs (red filled circles on the left) is the original TA SD array. There are three TA FD stations (MD to the north, LR to the west, and BRM to the east of the TA SD array) with black cross symbols. The array of surface detectors (green) to the north of the TA SD array is the TALE SD array. The additional TAx4 500 surface detectors (blue) are located in separate lobes on the northeast and southeast sides of the TA SD array. The 257 large blue filled circles denote deployed SDs, whereas remaining blue dots denote SDs to be deployed. Additional two FD stations with refurbished HiRes telescopes for the TAx4 are located at the MD and BRM FD sites and view to the northeast and southeast as denoted each by the blue frame of the fan. Purple diamond symbols denote TAx4 communications towers.

The TA Low energy Extension (TALE) enables detailed studies of the energy spectrum and composition from $\sim 10^{16.5}$ eV upwards. The main target of TALE is to clarify the expected transition from galactic to extra-galactic cosmic rays and the comparison of the data with Monte Carlo (MC) simulation that takes into account the results of the latest LHC experiments. The TALE detector is located north of the TA site (MD site). This FD station consists of 10 refurbished HiRes telescopes. The TALE FD views 31° - 59° in elevation angle. The TALE detectors are located at the northern corner of the TA detectors. The TALE FD operation was commenced in the spring of 2013. The TALE SD array consists of 80 SDs (40 SDs with 400-meter spacing and 40 SDs with 600-meter spacing). The TALE SD array was completed in February 2018 and is in stable operation. The mode energy of TALE hybrid events is $10^{16.8}$ eV. There is a plan to install additional 54 SDs with 200-meter spacing near the TALE FD station to observe even lower-energy cosmic rays, for which the mode energy is $10^{15.5}$ eV.

The Non-Imaging CHErenkov (NICHE) array is planned to have graded spacings, ranging from 100 meters to 400 meters. The NICHE Prototype Array consists of 14 counters each with a 3-inch PMT that collects non-imaging air-Cherenkov light, which started stable observation in May 2018 [2]. The array is situated 600-1000 m from the TALE FD. NICHE and TALE work together as a hybrid detector for cosmic rays with energies in the range between 10^{15} eV and $10^{18.5}$ eV.

TA, TAx4 and TALE SD arrays continued regular operations during recent two years even if various activities ceased due to the spread of COVID-19. On the other hand, FD observations that require on-site operations had been suspended. However, in June 2020, TA FDs and TAx4 FDs at the MC site resumed operations. In addition, the operation of TAx4 FDs at the BRM site and TALE FDs resumed in July 2020 and January 2021, respectively. The TA FDs at the BRM and the LR site are not operational as of the end of JFY2021.

2. Publications in refereed journals

The results from the TA collaboration published in refereed journal papers in JFY 2021 are reported below.

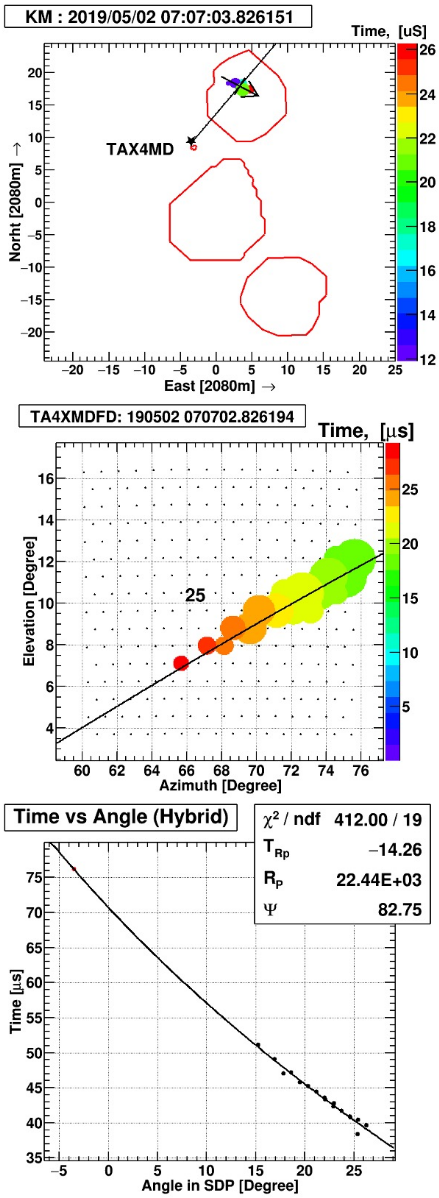

Fig. 15. A typical TAx4 hybrid event. (*top*) The footprint of an observed air-shower event.The horizontal and vertical axes denote the SD position IDs in the east-west and north-south directions, respectively. Circle centers correspond to the SD positions. Circle areas are proportional to the logarithmic sizes of signals. Colors denote arrival times at the detectors. (*middle*) FD event display of the event. (*bottom*) Time verse angle plot using hybrid reconstruction. The red data point is taken from the timing of the closest SD to the shower core.

Observation of variations in cosmic ray single count rates during thunderstorms

We have published the first surface detector observations of the effect of thunderstorms on the development of cosmic ray single count rate intensity over a 700 square kilometer area [3]. In this study, we studied the variation of cosmic ray intensity (single count rate) with thunderstorm clouds using surface detectors and found average levels of 0.5 to 1% and a maximum of 2%. These observations also showed both excesses and deficits. In addition, we found variations that correlated not only with thunderstorms, but also with lightning strikes. These variations lasted for several tens of minutes, and the footprints on the ground were 6 to 24 km in diameter and moved in the same direction as the thunderstorms.

Technical report on the TAx4 surface detectors

The design and the expected performance based on simulations of the TAx4 SDs are reported [4]. The status of SD construction, the results of calibration, quality checks and the data acquisition system are also explained in the paper.

3. Other physics results

Update of UHECR spectrum measured by the TA SDs

We presented an updated TA combined energy spectrum produced using an 11 year TA SD spectrum above $10^{18.2}$ eV and the 22 months TALE FD monocular spectrum below $10^{18.2}$ eV as shown in Fig. 16 [5].

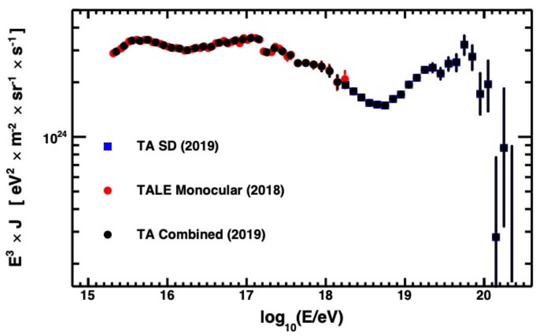

Fig. 16. The TA combined energy spectrum (black points) composed of 11 years of the TA SD data (blue squares) and 22 months of TALE monocular data (red circles). The combined TA spectrum exhibits the knee feature at about $10^{15.5}$ eV, the low energy ankle feature at $10^{16.22\pm0.02}$ eV, the second knee at $10^{17.04\pm0.04}$ eV, the ankle at $10^{18.69\pm0.01}$ eV, and the suppression at $10^{19.81\pm0.03}$ eV.

In 2020, a new feature called "shoulder" or "instep" was first observed by the Pierre Auger Observatory (PAO) [6]. Most of PAO's observational field of view is concentrated in the southern hemisphere. It is interesting to see if this new feature also exists in the Northern Hemisphere. Following PAO's report, we combined HiRes I monocular, TA BRM-LR monocular, and TA SD measurements to search for the new feature in the Northern Hemisphere.

The result are shown in Fig. 17. The three spectra were fit into a thrice broken power law. We found the "shoulder" feature at $10^{19.25\pm0.03}$ eV, and the statistical significance of the feature is estimated to be 5.3 standard deviations.

UHECR spectrum measured by the TAx4 SDs

The TAx4 SD array began operation in 2019 as an air shower array of 257 SDs and has been collecting data steadily since then. In JFY2021 we reported an observed cosmic ray energy distribution based on TAx4 SD data obtained from November 2019 to October 2020, as well as a preliminary cosmic ray energy spectrum based on the energy distribution. (

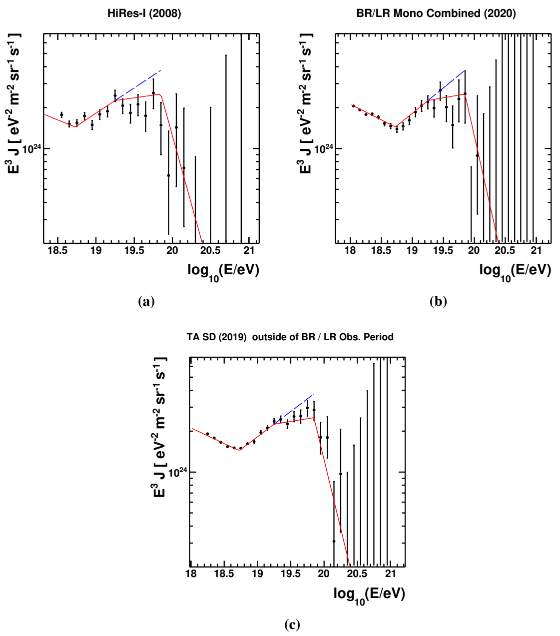

Fig. 17. Joint fit (red line) to (a) HiRes I monocular, (b) TA BRM–LR monocular, and (c) TA SD spectra.

see Fig. 18) The data analysis method used for this was almost identical to that of the TA experiment, and the same energy correction factor for the energy scale of 1/1.27, which was determined in the TA SD array, was used [7].

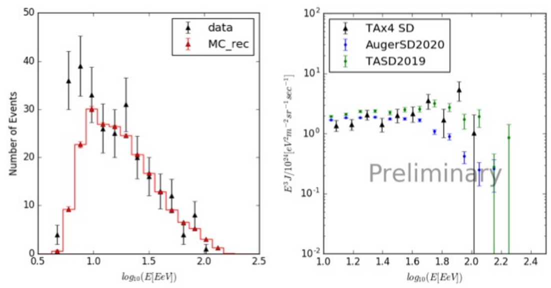

Fig. 18. (*left*) Energy distribution measured by the TAx4 SD array. (*right*) A preliminary energy spectrum measured by the TAx4 SD array together with the TA SD and the PAO SD spectra.

Averaged $X_{\max}$ measured by TA hybrid

The TA experiment is designed to allow simultaneous observations of UHECR air showers with FDs and SDs, so-called hybrid observations. Hybrid analysis using both FD and SD data is generally known to provide better reconstruction accuracy of shower geometry than FD or SD analysis alone. Since hybrid analysis is valid even when information from only one SD is added, the TA SD array implements a so-called hybrid trigger function, in which the FD trigger is sent to the SD array and the SD array data is collected by this external trigger. The energy threshold for hybrid events is much lower than for simultaneous SD array and FD observation events, i.e., events in which both trigger conditions are satisfied. In ICRC2021, we reported a preliminary result of the cosmic ray energy spectrum and the depth of maximum shower development based on hybrid trigger event data obtained from October 2010 to September 2014 [8]. Fig. 19 is a preliminary mean Xmax as a function of primary energy based on four years of observation data from TA hybrid comparing with the pure proton and iron MC predictions.

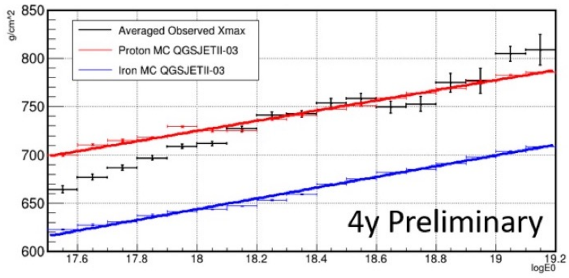

Fig. 19. The preliminary mean Xmax (black) as a function of primary energy based on four years of observation data from TA hybrid comparing with the pure proton (red) and iron (blue) MC predictions.

Cosmic ray composition study with TA SD data

Mass composition is one of the characteristics of cosmic rays that is not only related to the propagation of UHECRs, but also to the cosmic ray acceleration mechanism at the sources and source population. It can be measured from extensive air showers observed on the Earth. The most widely used method is FD observation to derive the depth of the shower maximum, Xmax, as a composition-sensitive observable. However, FD observations are limited in their statistics by small duty cycles. Therefore, we are conducting study on the determination of mass composition using only SD array observations. Specifically, we extracted some observables sensitive to mass composition from the SD data and used a machine learning method, called Boosted Decision Tree, to determine the mass composition. We used 12 years of data from the TA SD array to determine the energy change in the average of the natural logarithm of the mass number, $< \ln A >$. The results are shown in Fig. 20 [9].

Update on the large-scale cosmic-ray anisotropy

Following the significant detection of a large-scale anisotropy in the arrival direction distribution of UHECRs above 8 EeV in the southern sky by PAO [10], the TA experiment also investigated and reported large-scale anisotropy in the northern sky using 11 years of TA SD observation data [11]. In FY2021, we reported the updated results with more data [12].

The right ascension distribution and the sky map of the residual intensity are shown in Fig. 21. The energy threshold is 8.8 EeV, which was determined a priori to account for the 10% systematic difference in energy scale from the PAO. The PAO result has an amplitude of 4.7% and a phase of 100 degrees, and the updated results of the TA experiment agree with this within errors. However, it should be noted that the results

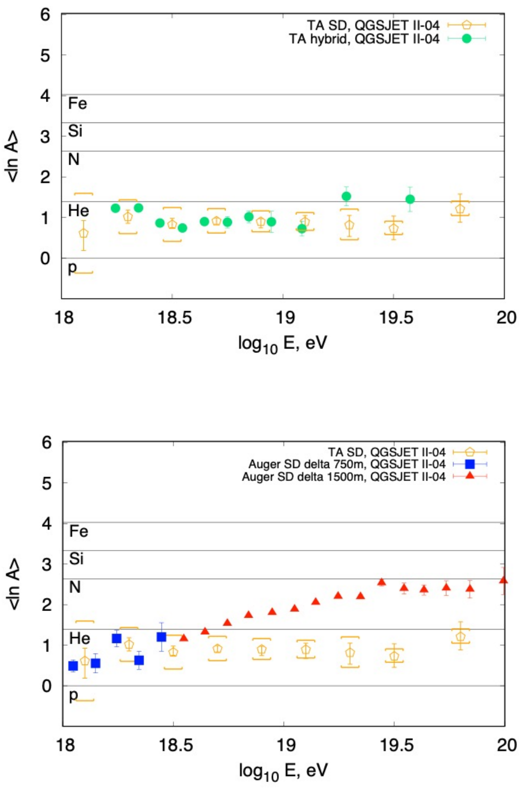

Fig. 20. $< \ln A >$ values for 12-year dataset derived with QGSJET II-04 (orange) compared with the TA MD hybrid (*upper*, green) results and with the Pierre Auger Observatory SD delta results (*lower*, blue and red).

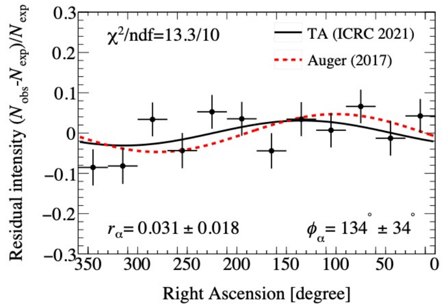

(a) Equatorial dipole

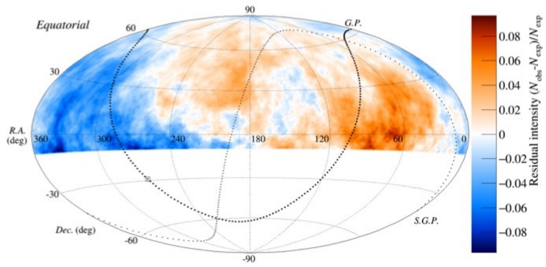

(b) Residual-intensity sky-map

Fig. 21. (a) Residual intensities of UHECRs above 8.8 EeV observed in 12 years of TA data. The black curve represents the fitted dipole to the TA and the red dashed line represents the dipole reported by PAO. (b) Sky map of residual intensities in the equatorial coordinate. The arrival direction is oversampled by a cylindrical function of radius 45 degrees. The galactic plane (G.P.) and the supergalactic plane (S.G.P.) are indicated by thick and thin dotted lines, respectively. The galactic center (G.C.) is shown as an open square.

of the TA experiment are also consistent with an isotropic distribution due to the small statistical significance; the upper limit of the amplitude at 99% CL is 7.6%.

Update on the Hotspot and a new excess

Based on 11 years of observations with the TA SD array, we find a new excess in the arrival direction distribution of UHECRs above $10^{19.4}$ eV, with a local significance of 4 σ for the results of the 20 degree radius oversampling analysis. The maximum excess appears at the position (RA, dec) = (17.4°, 36.0°,) and it appears in the region of the Perseus-Pisces supercluster. The chance probability of finding such an excess in the direction of the Perseus-Pisces supercluster is estimated to be 3.5 σ. The result is shown in Fig. 22(a) [13].

In 2014, we reported indications of a cosmic ray arrival direction above 57 EeV concentrated in the direction of Ursa Major, or rather a hot spot [14]. We have now updated our analysis of this hot spot based on the latest 11 years of observations. The number of events above 57 EeV observed was 179. Of these, 40 events came from within a 25-degree radius centered at (RA, dec) = (144°, 40.5°), which is 5.1 σ significant compared to the expected value of 14.6 from an isotropic distribution as shown in Fig. 22(b) [13]. The post trial significance is 3.2 σ, and also we conclude that the increase rate of the events inside the hotspot circle is consistent with a constant within ± 1 σ fluctuation.

4. Other activities

Other research results and activities reported at ICRC2021, JPS meetings and/or other conferences are listed and introduced below.

- Search for UHECR sources considering the deflection by the galactic magnetic field [15]
- Monocular energy spectrum using the TAx4 FDs [16]
- Energy spectrum and composition in the second knee region measured with the TALE hybrid detector [17]
- Energy spectrum and the shower maxima measured with the NICHE detectors [18]
- Anisotropy search in UHECR spectrum [19]
- Measurement of the p-air cross section with TA BRM, LR, SD array in hybrid mode [20]
- Performance evaluations of the TALE SD array [21]
- Measurement of optical properties of atmospheric fluorescence telescope using UAV-mounted light source
- Joint analysis of the energy spectrum measured at PAO and TA [22]

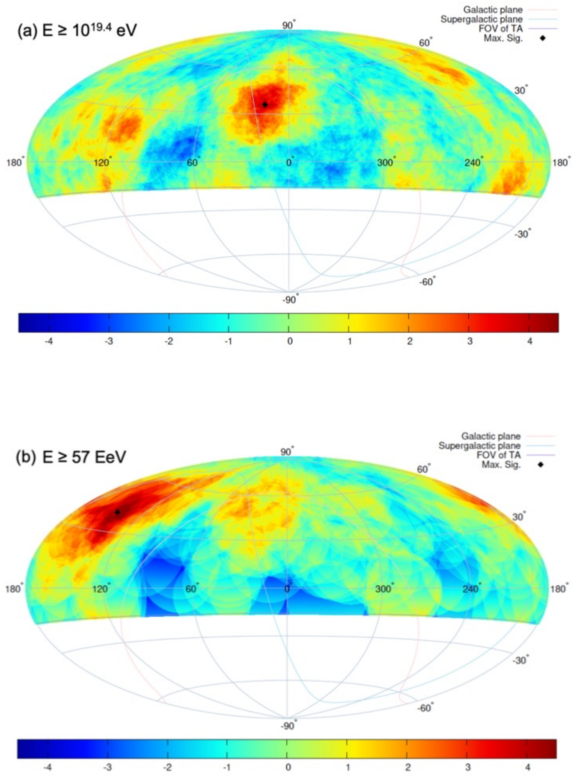

Fig. 22. Sky maps in equatorial coordinates. The color scheme indicates the Li-Ma significance and shows the excess (red) or deficit (blue) of events compared to isotropy. The positions of maximum excesses are marked with the black diamonds. An intermediate angular scale of $20°$-radius circles was used for oversampling analysis for different energy thresholds. The energy threshold for each map is (a) $10^{19.4}$ eV and (b) 57 EeV. Note that the right ascension of $0°$ is at the center of the sky map.

- Joint correlation study of directional correlation between the arrival direction of UHECRS and nearby galaxies [23]
- Joint analysis of the large scale anisotropy measured at PAO and TA [24]

5. Future Plans

TALE infill SD array

We are planning to lower the energy threshold of the TALE hybrid observations by installing additional SDs at higher densities between the TALE SD array and the TALE FD station. 54 SDs will be placed within 2 km of the TALE FD station with 100 m or 200 m intervals. The SDs will be deployed to cover 0.32 km^2. A map of the planed installation site is shown in Fig. 23. From this arrangement the expected mode energy of the infill SD array is $10^{15.3}$ eV, and $10^{15.8}$ eV for the infill hybrid observation.

Although we have already obtained permission to use all installation points and have completed preparation of hardware, the transportation of equipment from Japan and installation work in the field has been suspended due to the spread of COVID-19. The installation is scheduled to be completed in FY2022.

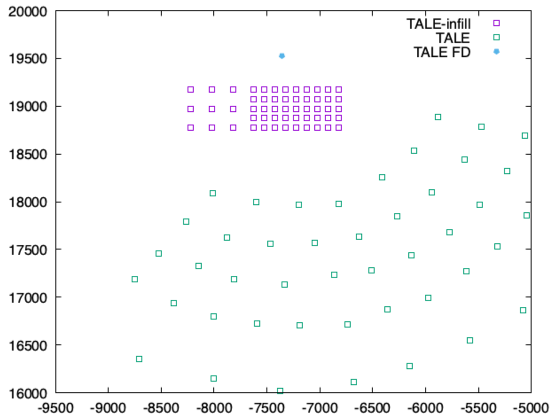

Fig. 23. The layout of TALE infill SDs. Purple squares denote the planned locations of 54 SDs for the infill array. The array controlled with a host PC at the TALE FD station indicated with the filled circle.

Research and development of next-generation detectors

On site research and development activities with the prototypes of the next-generation UHECR detectors at the TA BRM site such as EUSO-TA [25] for the JEM-EUSO mission [26] in space, and FAST [27] and CRAFFT [28] as low-cost wide-area ground detectors were suspended in 2021 due to COVID-19. However, activities in data analysis and instrument developments have been maintained, and each group has reported its results.

Discussions are also underway for the next-generation observatories, to measure the properties of the highest-energy cosmic rays with unprecedented accuracy in the future such as TA2 and GCOS (The Global Cosmic Ray Observatory). In May 2021, he first international workshop of GCOS was held [29].

Bibliography

[1] R. Abbasi *et al.*, “Current status and prospects of surface detector of the TAx4 experiment”, PoS(ICRC2021), 203, 2021.

[2] Y. Omura *et al.*, “TA experiment 381: jNICHE - Energy spectrum and composition analysis of cosmic rays measured with the NICHE detectors at the TA site”, 2022 Annual JPS Meeting.

[3] R.U. Abbsi *et al.*, “Observation of Variations in Cosmic Ray Single Count Rates During Thunderstorms 2 and Implications for Large-Scale Electric Field Changes”, Phys. Rev. D 105, 062002, 2022.

[4] R.U. Abbsi *et al.*, “Surface detectors of the TAx4 experiment”, NIM A 1019, 165726, 2021.

[5] D. Ivanov *et al.*, “Recent measurement of the Telescope Array energy spectrum and observation of the shoulder feature in the Northern Hemisphere”, PoS(ICRC2021), 341, 2021.

[6] A. Aab *et al.*, "Features of the Energy Spectrum of Cosmic Rays above 2.5×10^{18} eV Using the Pierre Auger Observatory", Phys. Rev. Lett., 125, 121106, 2020.

[7] H. Jeong *et al.*, "Reconstruction of Air Shower Events Measured by the Surface Detectors of the TAx4 Experiment", PoS(ICRC2021), 331, 2021.

[8] H. Shin *et al.*, "The measurements of the cosmic ray energy spectrum and the depth of maximum shower development of Telescope Array Hybrid trigger events", PoS(ICRC2021), 305, 2021.

[9] Y. Zhezher *et al.*, "Cosmic-ray mass composition with the TA SD 12-year data", PoS(ICRC2021), 300, 2021.

[10] A. Aab *et al.*, "Observation of a Large-scale Anisotropy in the Arrival Directions of Cosmic Rays above 8×10^{18} eV", Science, 357, 1266, 2017.

[11] R.U. Abbasi *et al.*, "Search for Large-scale Anisotropy on Arrival Directions of Ultra-high-energy Cosmic Rays Observed with the Telescope Array Experiment", Astrophys. J. Lett, 898, L28, 2020.

[12] T. Fujii *et al.*, "Update on the large-scale cosmic-ray anisotropy search at the highest energies by the Telescope Array Experiment", PoS(ICRC2021), 291, 2021.

[13] J. Kim *et al.*, "Hotspot Update, and a new Excess of Events on the Sky Seen by the Telescope Array Experiment ", PoS(ICRC2021), 328, 2021; R.U. Abbasi *et al.*, "Indications of a Cosmic Ray Source in the Perseus-Pisces Supercluster", arXiv:2110.14827, 2021

[14] R.U. Abbasi *et al.*, "Indications of intermediate-scale anisotropy of cosmic rays with energy greater than 57 EeV in the northern sky measured with the surface detector of the Telescope Array experiment", Astrophys. J. Lett, 790, L21, 2014.

[15] R. Higuchi *et al.*, "Effects of Galactic magnetic field on the UHECR anisotropy studies", PoS(ICRC2021), 358, 2021; R. Higuchi, "Search for UHECR sources considering the deflection by the galactic magnetic field", Ph. D. thesis (U. Tokyo), 2022

[16] M. Potts *et al.*, "Monocular Energy Spectrum using the TAx4 Fluorescence Detector", PoS(ICRC2021), 343, 2021.

[17] K. Fujita *et al.*, "Cosmic Ray Composition in the Second Knee Region as Measured by the TALE Hybrid Detector", PoS(ICRC2021), 353, 2021.

[18] Y. Omura *et al.*, "Energy spectrum and the shower maxima of cosmic rays above the knee region measured with the NICHE detectors at the TA site", PoS(ICRC2021), 329, 2021.

[19] T. Nonaka *et al.*, "Anisotropy search in the Ultra High Energy Cosmic Ray Spectrum in the Northern Hemisphere using latest data obtained with Telescope Array surface detector", PoS(ICRC2021), 344, 2021.

[20] R. Abbasi *et al.*, "Measurement of the Proton-Air Cross Section with Telescope Arrays Black Rock, Long Ridge, and Surface Array in Hybrid Mode", PoS(ICRC2021), 395, 2021.

[21] K. Sato *et al.*, "Cosmic ray energy spectrum in the 2nd knee region measured by the TALE-SD array", PoS(ICRC2021), 362, 2021.

[22] Y. Tsunesada *et al.*, "Joint analysis of the energy spectrum of ultra-high-energy cosmic rays measured at the Pierre Auger Observatory and the Telescope Array", PoS(ICRC2021), 337, 2021.

[23] A. di Matteo *et al.*, "UHECR arrival directions in the latest data from the original Auger and TA surface detectors and nearby galaxies", PoS(ICRC2021), 308, 2021.

[24] P. Tinyakov *et al.*, "The UHECR dipole and quadrupole in the latest data from the original Auger and TA surface detectors", PoS(ICRC2021), 375, 2021.

[25] Z. Plebaniak *et al.*, "Study of the calibration method using the stars measured by the EUSO-TA telescope", PoS(ICRC2021), 240, 2021.

[26] M. Bertaina "An overview of the JEM-EUSO program and results", PoS(ICRC2021), 406, 2021.

[27] T. Fujii, "Latest results of ultra-high-energy cosmic ray measurements with prototypes of the Fluorescence detector Array of Single-pixel Telescopes (FAST)", PoS(ICRC2021), 402, 2021.

[28] Y. Tameda *et al.*, "Progress and future prospect of the CRAFFT project for the next generation UHECR observationy", PoS(ICRC2021), 408, 2021.

[29] GCOS workshop, May 17-21, 2021; https://agenda.astro.ru.nl/event/18/

Tibet ASγ Experiment

[Spokesperson: M. Takita]

ICRR, The Univ. of Tokyo, Kashiwa, Chiba 277-8582

1. Experiment

The Tibet air shower experiment has been successfully operated at Yangbajing (90°31′ E, 30°06′ N; 4300 m above sea level) in Tibet, China since 1990. It has continuously made a wide field-of-view (approximately 2 steradian) observation of cosmic rays and gamma rays in the northern sky.

The Tibet I array was constructed in 1990 and it was gradually upgraded to the Tibet II by 1994 which consisted of 185 fast-timing (FT) scintillation counters placed on a 15 m square

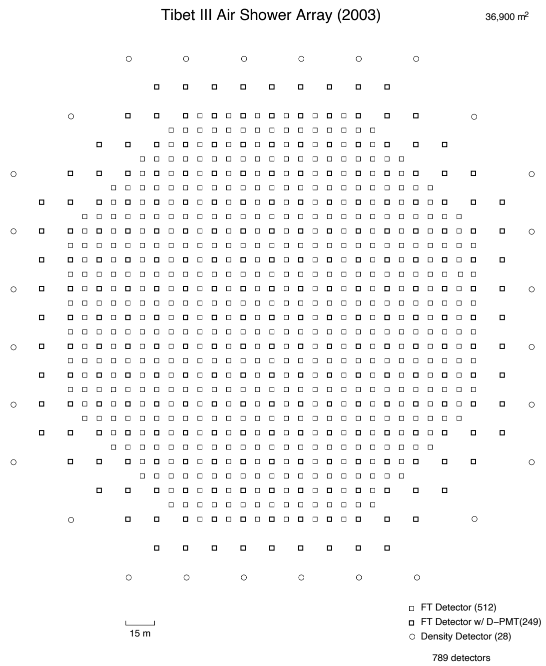

Fig. 1. Schematic view of Tibet III.

grid covering 36,900 m^2, and 36 density (D) counters around the FT-counter array. Each counter has a plastic scintillator plate of 0.5 m^2 in area and 3 cm in thickness. All the FT counters are equipped with a fast-timing 2-inch-in-diameter photomultiplier tube (FT-PMT), and 52 out of 185 FT counters are also equipped with a wide dynamic range 1.5-inch-in-diameter PMT (D-PMT) by which we measure up to 500 particles which saturates FT-PMT output, and all the D-counters have a D-PMT. A 0.5 cm thick lead plate is put on the top of each counter in order to increase the counter sensitivity by converting gamma rays into electron-positron pairs in an electromagnetic shower. The mode energy of the triggered events in Tibet II is 10 TeV.

In 1996, we added 77 FT counters with a 7.5 m lattice interval to a 5,200 m^2 area inside the northern part of the Tibet II array. We called this high-density array Tibet HD. The mode energy of the triggered events in Tibet HD is a few TeV.

In the late fall of 1999, the array was further upgraded by adding 235 FT-counters so as to enlarge the high-density area from 5,200 m^2 to 22,050 m^2, and we call this array and further upgraded one Tibet III. In 2002, all of the 36,900 m^2 area was covered by the high-density array by adding 200 FT-counters more. Finally we set up 56 FT-counters around the 36,900 m^2 high density array and equipped 8 D-counters with FT-PMT in 2003. At present, the Tibet air shower array consists of 761 FT-counters (249 of which have a D-PMT) and 28 D-counters as in Fig. 1.

The performance of the Tibet air shower array has been well examined by observing the Moon's shadow (approximately 0.5 degrees in diameter) in cosmic rays. The deficit map of cosmic rays around the Moon demonstrates the angular resolution to be around 0.9° at a few TeV for the Tibet III array. The pointing error is estimated to be better than ∼0.01°, as shown in Fig. 2, by displacement of the shadow center from the apparent center in the north-south direction, as the east-west component of the geomagnetic field is very small at the experimental site. On the other hand, the shadow center displacement in the east-west direction due to the geomagnetic field enables us to spectroscopically estimate the energy scale uncertainty at ±12 % level, as shown in Fig. 3. Thus, the Tibet air shower experiment introduces a new method for energy scale calibration other than the conventional estimation by the difference between the measured cosmic-ray flux by an air shower experiment and the higher-energy extrapolation of cosmic-ray flux measured by direct measurements by balloon-borne or satellite experiments.

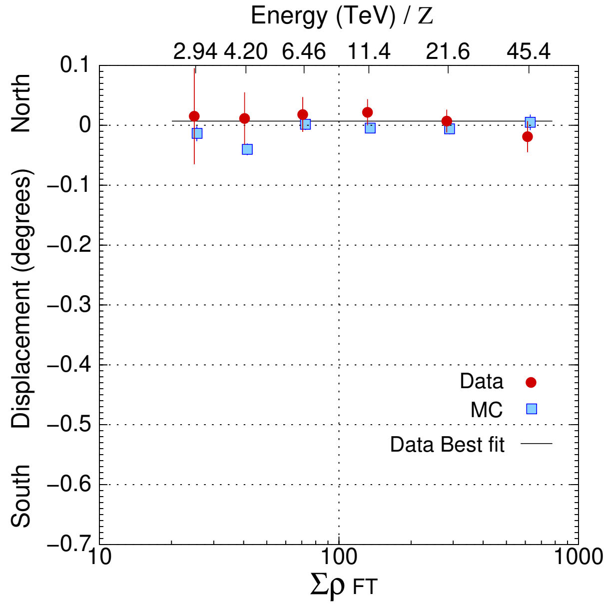

Fig. 2. From [1]. The Moon's shadow center displacement from the apparent position in the north-south direction as a function of energy, observed by Tibet III.

In 2007, a prototype 100-m^2 underground water Cherenkov muon detector was successfully constructed in Tibet to demonstrate the technical feasibility, cost estimate, validity of our Monte Carlo simulation. Data analyses demonstrate that our MC simulation reproduces real data quite reasonably.

After the success of the prototype underground muon detector, we added a large underground muon detector (MD) array and the experimental configuration was changed starting from February 2014. The current array consists of 597 plastic scintillation detectors with an area of 0.5 m^2 as shown by small dots in Fig. 4, covering an area of 65,700 m^2. The Tibet MD array (3,400 m^2 in total area) consists of 64 water-Cherenkov-type detectors located at 2.4 m underground of the AS array as shown by open squares in Fig. 4. Each detector is a waterproof concrete cell filled up with water of 1.5 m in depth, 7.35 m × 7.35 m in area, equipped with a 20-inch-diameter downward-facing photomultiplier tube (PMT)

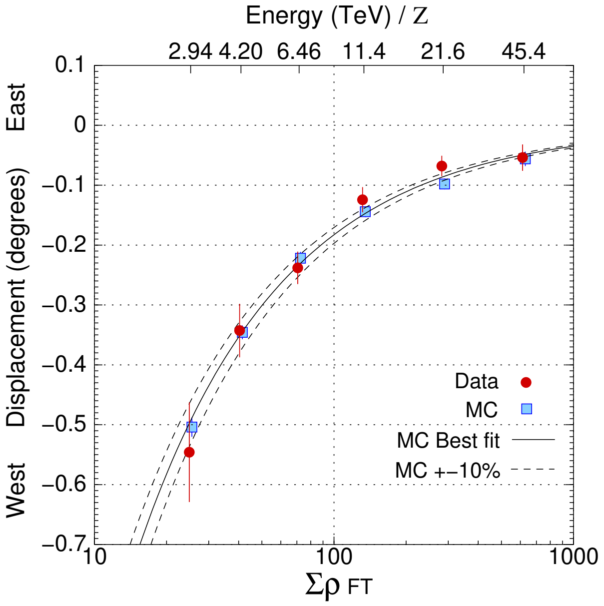

Fig. 3. From [1]. The Moon's shadow center displacement from the apparent position in the east-west direction as a function of energy, observed by Tibet III.

on the ceiling. The inner walls and floor have a white Tyvek sheet lining to efficiently gather catoptric water Cherenkov light. The electromagnetic component is shielded by the soil overburden which corresponds to $\sim$19 radiation lengths. The energy threshold for muons is approximately 1 GeV. A photon induced air shower has much less muons compared with a cosmic-ray induced one. The Tibet MD array enables us to significantly discriminate a cosmic-ray background event from a photon signal by means of counting the number of muons in an air shower.

2. Physics Results

Our current research theme is classified into 4 categories:

(1) TeV celestial gamma-ray point/diffuse sources,

(2) Chemical composition and energy spectrum of primary cosmic rays in the knee energy region,

(3) Cosmic-ray anisotropy in the multi-TeV region with high precision,

(4) Global 3-dimensional structure of the solar and interplanetary magnetic fields by observing the Sun's shadow in cosmic rays.

We will introduce a part of the results obtained in this fiscal year[2],[3].

We successfully detected gamma-rays in the 100 TeV region from Cygnus OB1 and OB2 regions.

A photon induced air shower contains much less muons compared with a cosmic-ray induced air shower. Therefore, the MD array enables us to distinguish a photon signal event from a cosmic-ray induce background event. Using the AS and MD arrays, we analyzed the air shower data and muon data during 719 live days from February 2014 to May 2017.

Figure 4 (a) and (b) show the event display and the lateral distribution, respectively, of a typical photon-like event observed with $E = 251$ TeV from the Crab nebula[4]. The total uncertainty of the energy ΔE is defined as the quadratic sum of the absolute energy-scale error (12%) [1] and the energy resolution estimated by using MC events with the same θ and core distance from the array center (R). The ΔE of the 251 TeV photon-like event is estimated to be $^{+45}_{-43}$ TeV.

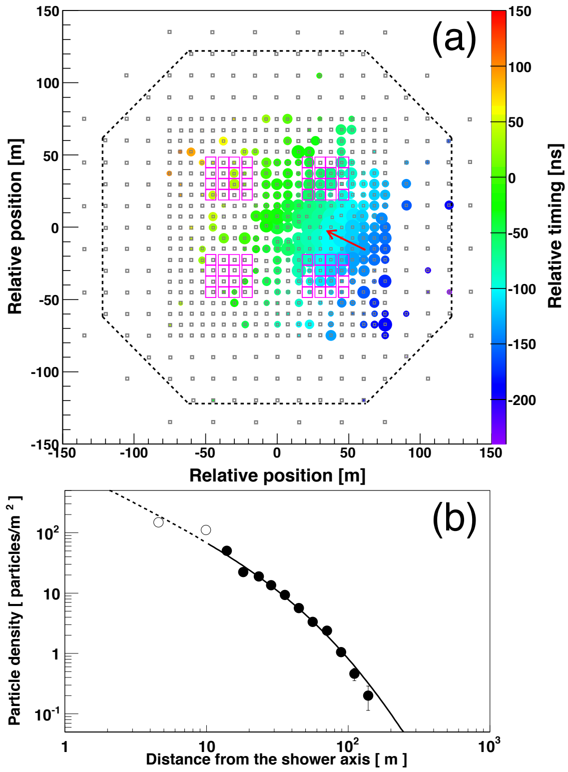

Fig. 4. From Ref.[4], references therein. (a) An event display of the observed photon-like AS of energy 251 TeV. The size and color of each circle represent the logarithmic particle density and the relative timing in each detector, respectively. The arrow head and direction indicate the AS core location and incident direction, respectively. Dots and open squares denote scintillation detectors and underground MDs, respectively. The enclosed area by the dashed line indicates the fiducial area of the AS array. (b) Lateral distribution of the photon-like shower event in panel (a). The solid circles and curve show the experimental data and fitting result by the Nishimura-Kamata-Greisen (NKG) function to the data recorded by detectors more than 10 m apart from the AS axis. The dashed curve and open circles are an extrapolation of the NKG function fitting and the unused data within 10 m from the AS axis.

We reconstruct the arrival direction of an air shower by means of the relative timing information recorded at each scintillation detector. The color scale and circle size in Fig. 4 (a) stand for the relative timing (t) and the number of particle density (ρ) in an air shower. In the first place, we estimate the air shower core location weighted by ρ. The arrow head position and direction in the figure indicate the estimated core position and azimuthal direction. The t's in the air shower front are fitted by a conical shape, and its cone angle is optimized by the MC simulation depending on the air shower size. The angular resolutions (50% containment) are estimated to be approximately 0.5° and 0.2° for 10 TeV and 100 TeV photon, respectively.

The secondary particles in an air shower deposit energy, which is proportional to ρ, in a scintillator. The ρ at each detecto r is defined as the PMT output charge divided by the single particle peak which is monitored every 20 minutes to correct temperature dependence of each detector gain. The energy of each air shower is reconstructed using the lateral distribution of ρ, above 10 TeV. Figure 4 (b) shows an example of the lateral distribution of ρ. As an energy estimator, we use $S50$[5], which is defined as ρ at a distance of 50 m from the air shower axis in the best-fit Nishimura-Kamata-Greisen (NKG) function. The energy resolutions with $S50$, which depend on air shower core location and zenith angle, are roughly estimated to be 40% at 10 TeV and 20% at 100 TeV. On the other hand, the energy below 10 TeV was estimated directly from $\Sigma\rho$ corresponding to the sum of of the particle density measured by each scintillatoin detector, as the number of hit detectors is too low to fit $S50$. The absolute energy scale uncertainty is estimated to be 12 by the westward displacement of the Moon shadow position.

The electromagnetic cascade in the air shower is strongly suppressed by the bremsstrahlung process in the overburden, while muons and a part of hadronic components penetrate into the underground MD array. The number of detected particles at an MD (N_μ) is defined as the output charge divided by the single muon peak which is monitored every 20 minutes. The sum of detected particles in all MDs (ΣN_μ) is used as a parameter to separate between photon and cosmic-ray induced air showers.

An event trigger is issued at any 4-fold coincidence with detectors recording more than 0.6 particles within the area enclosed by the dashed lines in Fig. 4. At air shower energies smaller than 10 TeV, we employ the same selection criteria and estimate the event energy as in the previous work[1], except for the MD selection criterion. At air shower energies greater than 10 TeV, we employ the following event selections: (1) zenith angle of arrival direction (θ) should be $\theta < 40°$; (2) number of available detectors for the air shower reconstruction should be ≥ 16; (3) among 6 detectors recorded with the largest ρ's, 5 should be contained in the fiducial area enclosed by the dashed lines in Fig. 4; (4) $\log(S50)$ should be > -1.2; (5) age parameter (s) in the best-fit NKG function should be $0.3 < s < 1.3$. (6) ΣN_μ should be $\Sigma N_\mu < 0.15(\Sigma\rho)^{2.8}$ or $\Sigma N_\mu < 3.6\times10^{-4}(\Sigma\rho)^{1.4}$, where $\Sigma\rho$ is the sum of particle density measured by the AS array. The MD cut is optimized for photon detection by our MC simulation.

To estimate the background contribution from cosmic rays, we adopt the Equi-Zenith Angle method which is the same as in our previous works [1]. The background counts are estimated from the number of events averaged over 20 off-source bins of the same size as the on-source bin located at the equi-zenith angle. The radius of the on/off-source bin is set to $R_{\rm sw}(\Sigma\rho) = 6.9/\sqrt{\Sigma\rho}$ (deg.). In order to efficiently extract signals in the higher energy region at low background level, the lower limit of $R_{\rm sw}$ is set to 0.5°, which corresponds to $\sim 90\%$ containment of photons above 100 TeV.

To generate air shower events in the atmosphere, Employed are the CORSIKA code v7.4000 with EPOS-LHC for the high-energy hadronic interaction model and FLUKA code v2011.2b for the low-energy hadronic interaction model. The very-high-energy photons at the top of atmosphere are inputted, assuming the power-law spectrum with a differential index -2.9 above 0.3 TeV. The generated secondary particles in an air shower are fed into the detector response simulation for the AS array developed based on the GEANT4 code v4.10.00. The MC simulation for the MD array considering the overburden has been developed based on the GEANT4 code. The electromagnetic and hadronic cascades by the secondary particles in the overburden, as well as the ray tracing of Cherenkov lights emitted in the water cells are simulated by the GEANT4 code. The number of photoelectrons detected in the 20-inch PMT is converted to N_μ referring to the single muon peakin each cell. The muon cut is determined to maximize the figure of merit $N_\gamma^{\rm MC}/\sqrt{N_\gamma^{\rm MC} + N_{\rm CR}^{\rm DATA}}$, where $N_\gamma^{\rm MC}$ and $N_{\rm CR}^{\rm DATA}$ denote the expected number of photons by the MC and the number of background events in the data after the muon cut. The photon-like events are defined as the remaining events after the muon cut.

Figure 5 (b) shows a significance map above 10 TeV in the direction of Cygnus OB1 obtained by the Tibet ASγ experiment. The centroid of gamma-ray emissions is estimated at (R.A., Dec.) $=(304.99° \pm 0.11° 36.84° \pm 0.08°)$ with the pre-trial (post-trial) detection significance of 6.7σ (6.2σ). We name this source TASG J2019+368. The centroid of TASG J2019+368 is consistent with that reported by HAWC [20] within the 1σ level, and by VERITAS [11] within the 2σ level. The pulsar PSR J2021+3651, located 0.23° east of the TASG J2019+368 centroid, has a nebula extending westwards from the pulsar, PWN G75.2+0.1, which is coincident with the location of TASG J2019+368. Figure 6 (b) shows the angular distribution of the events observed above 10 TeV. The experimental data can be fitted with a Gaussian function with a source extension of $\sigma_{\rm EXT} = 0.28° \pm 0.07°$ above 10 TeV, consistent with the extension reported by VERITAS [11] (HAWC [19]) at the 2.1σ (0.3σ) level. The χ^2/ndf of the fitting is 49.1/38. Figure 7 (b) shows the differential gamma-ray energy spectrum of TASG J2019+368, which is in good agreement with the HAWC spectrum and makes a reasonable connection with the VERITAS spectrum in 2014. The measured spectrum is expressed either as $dF/dE = N_0(E/40\,\text{TeV})^{-\Gamma}$ with $N_0 = (10.6 \pm 1.3) \times 10^{-16}$ TeV^{-1}cm^{-2}s^{-1} and $\Gamma = 2.70 \pm 0.13 (\chi^2/\text{ndf} = 10.4/5)$, or assuming an exponential cutoff as $dF/dE = N_0(E/40\text{TeV})^{-\Gamma}\exp(E/E_{cut})$ with $N_0 = (3.6 \pm 2.0) \times 10^{-15}$ TeV^{-1}cm^{-2}s^{-1}, $\Gamma = 1.6 \pm 0.5$ and $E_{cut} = 44 \pm 21$ TeV (χ^2/ndf = 3.0/4).

Figure 5 (a) shows a detection significance map around the gamma-ray source detected by the Tibet ASγ experiment with photon energies above 10 TeV in the direction of Cygnus OB2. The sky is gridded in $0.1° \times 0.1°$ pixels and the significance value of each pixel calculated according to [27] is smoothed by a circular search window of radius, R_w centered at the pixel. Assuming a symmetrical two-dimensional Gaus-

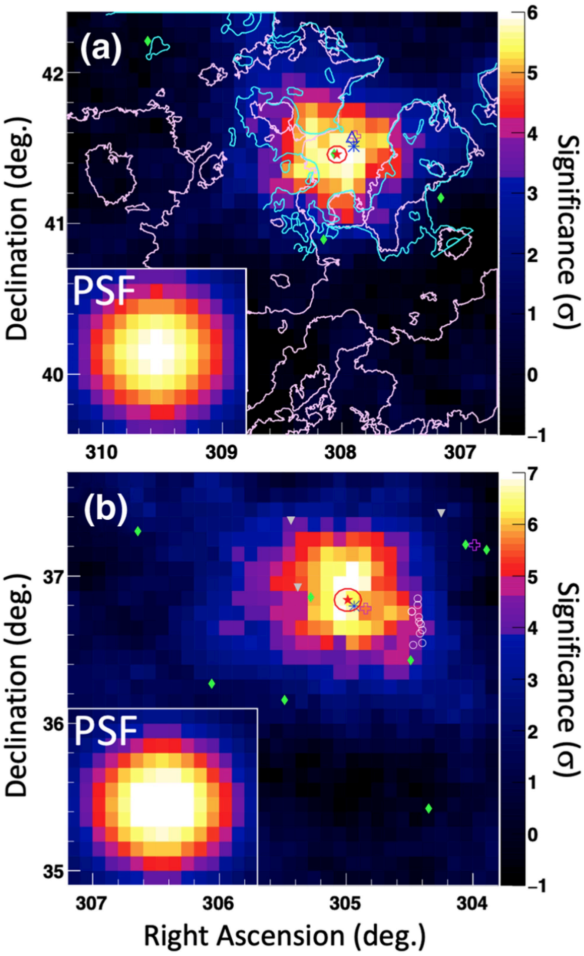

Fig. 5. From Ref.[2], references therein. The gamma-ray emission source detected above 10 TeV in the directions of Cygnus OB2 for (a) and Cygnus OB1 for (b), respectively. The figure (a) is a significance map around the source, smoothed by search windows. The point spread function (PSF) is shown in the inset figure. The red-filled star with a position error circle is the centroid of TASG J2032+414 in the Cygnus OB2 region obtained by the Tibet ASγ experiment, while the magenta open cross is the centroid of VER J2031+415, and the blue asterisk is that of HAWC J2031+415. The green-filled diamonds show Fermi-LAT sources. The blue open triangle indicates the centroid of MAGIC J2031+4134. The green-filled diamond coincident with our gamma-ray emission centroid is the pulsar PSR J2032+4127. The sky-blue contours indicate 1420 MHz radio emissions provided by the Canadian Galactic Plane Survey, and the pink contours indicate 24 μm infrared emissions by the Cygnus-X Spitzer Legacy Survey [30, 31]. The figure (b) is a significance map around the source. The red-filled star with a position error circle is the centroid of TASG J2019+368 in the Cygnus OB1 region obtained by the Tibet ASγ experiment. The white open circles are NuSTAR X-ray sources [32], and the gray-filled inverted triangles are Wolf-Rayet stars [33]. The green–filled diamond located at 0.23° east of our emission centroid is the pulsar PSR J2021+3651. The magenta open cross located at (R.A., Dec.) = (303.99°, 37.21°) is another VERITAS source VER J2016+371 [11]s, which is not detected significantly in this work.

sian distribution for the gamma-ray excess, we fit the events within the $4^\circ \times 4^\circ$ region around the source using the unbinned maximum likelihood method. The centroid of gamma-ray emissions detected at the pre-trial (post-trial) detection significance of 5.3σ (4.7σ) above 10 TeV is estimated at (R.A., Dec.) $= (308.04^\circ \pm 0.08^\circ, 41.46^\circ \pm 0.06^\circ)$. We name this

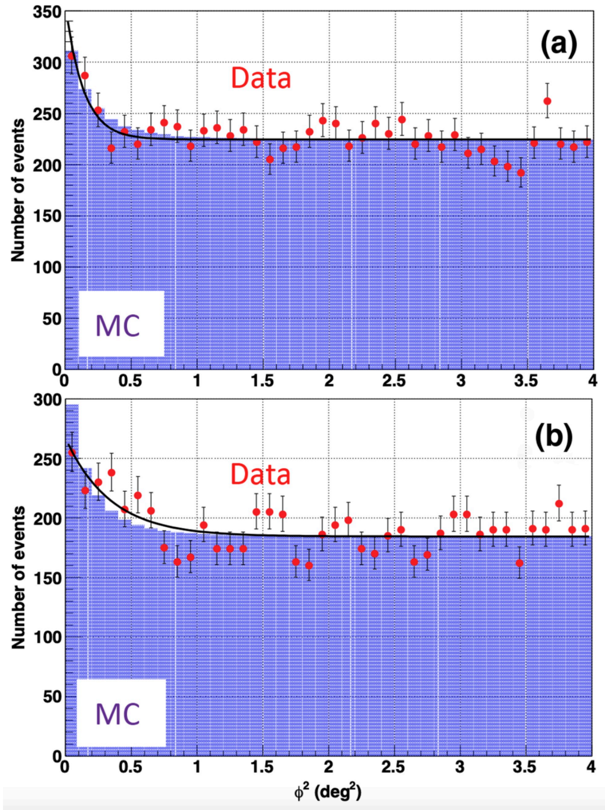

Fig. 6. From Ref.[2], references therein. The figure (a) shows the distribution of the number of events observed with photon energies above 10 TeV as a function of the square of the opening angle between the estimated arrival direction and the centroid of TASG J2032+414 in the Cygnus OB2 region, while the figure (b) shows the distribution of the number of events observed with photon energies above 10 TeV as a function of the square of the opening angle between the estimated arrival direction and the centroid of TASG J2019+368 in the Cygnus OB1 region. The red-filled circles are the experimental data, with the best fit Gaussian function indicated by the solid line. The blue histogram is the distribution of events expected by the MC simulation assuming a point-like gamma-ray source.

source TASG J2032+414. The location of TASG J2032+414 is in good agreement with that of the pulsar PSR J2032+4127 and consistent with that of HAWC J2031+415 [28] at the 1.7σ level, while it appears to deviate from that of TeV J2032+4130 reported in [29] at the 2.8σ level.

Figure 6 (a) shows the distribution of the number of events observed with photon energies above 10 TeV as a function of the square of the opening angle ϕ between the estimated arrival direction and the centroid of TASG J2032+414. To estimate a possible source extension, we perform the χ^2 fitting of the data with the function $A\exp[-\phi^2/2(\sigma_{\rm PSF}^2+\sigma_{\rm EXT}^2)]+N_{\rm B\,G}$ where A and $\sigma_{\rm EXT}$ are two fitting parameters and $\sigma_{\rm PSF} = 0.36^\circ$ and $N_{\rm BG} = 224.5$ are the point spread function (PSF) of our instrument above 10 TeV and the number of background events estimated from the background cosmic-ray data, we get $\sigma_{\rm EXT} = 0.00^\circ \pm 0.14^\circ$, which is consistent with that obtained from the maximum likelihood fitting described above. The χ^2/ndf of the fitting is 33.8/38. With a large error of 0.14°, the $\sigma_{\rm EXT}$ above 10 TeV does not indicate whether TASG J2032+414 is extended or not even

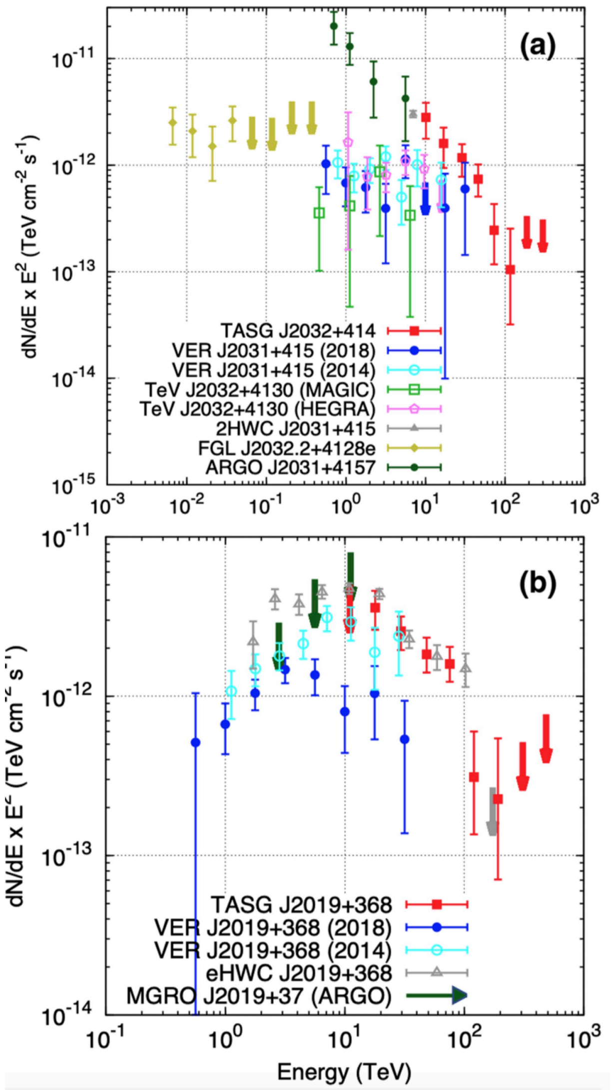

Fig. 7. From Ref.[2], references therein. The figure (a) shows the differential gamma-ray energy spectra of TASG J2032+414 in the Cygnus OB2 region with 95 % C.L. upper limits measured by this work (red filled squares/arrows). The blue-filled circles/arrows (sky-blue open circles) show the gamma-ray spectrum reported by VERITAS in 2018 (2014) [10, 11], the gray filled triangle by HAWC [16], and the dark-green filled circles by ARGO [14]. Additionally, the gold-filled diamonds are reported by Fermi-LAT [11], the green open squares by MAGIC [9], and the pink pentagons/arrow by HEGRA [7]. The figure (b) shows the differential gamma-ray energy spectra of TASG J2019+368 in the Cygnus OB1 region with 95% C.L. upper limits measured by this work (red-filled squares/arrows). The blue-filled circles(sky-blue open circles) show the gamma-ray spectrum reported by VERITAS in 2018 (2014) [11, 21], the gray open triangles/arrow by HAWC [16, 19], and dark-green filled arrow by ARGO [14].

if it is consistent with the previous measurements at multi-TeV energies by IACTs, ARGO and HAWC within the 2σ level [7, 9, 11, 14, 28, 29]. Figure 7 (a) shows the differential energy spectrum of TASG J2032+414. Although there is a discrepancy in flux at multi-TeV energies, our flux data points above 10 TeV are consistent with the previous measurements by IACTs if the spill-over of gamma-ray signals outside their integration radius is taken into account. Our spectrum from 10 TeV to 120 TeV can be expressed by a simple power-law as $dF/dE = N_0(E/40\ \mathrm{TeV})^{-\Gamma}$ where $N_0 = (4.13 \pm 0.83) \times 10^{-16}\ \mathrm{TeV}^{-1}\mathrm{cm}^{-2}\mathrm{s}^{-1}$ is the differential gamma-ray flux at 40 TeV and $\Gamma = 3.12 \pm 0.21$ is the spectral index (χ^2/ndf = 1.6/4).

For more details on the gamma rays in the 100 TeV region from Cygnus OB1 and OB2, see [2].

Figure 8 shows the distribution of sub-PeV gamma-ray-like events in the equatorial coordinates. To single out diffuse gamma-ray signals from an overwhelming amount of cosmic-ray background events, we employ a tighter muon cut than in the point-like source analysis. With the tighter muon cut, we have succeeded in reducing the cosmic-ray background events down to approximately 10^{-6} above 398 TeV. As a result, 38 gamma-ray-like events survive after the cut above 398 TeV, and 23 gamma-ray-like events are observed along the galactic disk within $|b| < 10°$ against low (2.73) cosmic-ray background events [3] estimated by real cosmic-ray data.

The high galactic-latitude events ($|b| > 20°$) are assumed to be the cosmic-ray background events in this analysis. The highest-energy event among the 23 events along the galactic plane has unprecedentedly as high as 957 TeV, nearly 1 PeV. Surprisingly, the observed gamma rays above 398 TeV do not come from any known TeV gamma-ray objects as is shown in Fig 9, but are widely spread over the galactic disk [3]. These spatially spread gamma rays are thought to have been produced by the interaction of cosmic-ray protons with the interstellar gas in our galaxy. High-energy electrons would interact with low-energy photons filled in our galaxy, and also produce ultra-high-energy (UHE) gamma rays (> 100 TeV). However, UHE gamma rays of electron origin should be generated very close to a source and confined nearby it typically within 1 degree, as the electrons lose their energy rapidly and cannot travel far from their origin. From Fig. 9, the electron origin is rejected. Furthermore, the measured fluxes in the UHE region [3] are in reasonable agreement with a recent model [35] based on the hadronic cosmic-ray interactions, where UHE diffuse galactic gamma rays of electron origin is estimated to be negligible compared to those of cosmic-ray origin.

This is the first experimental evidence that cosmic rays were/are accelerated to PeV energies in our galaxy. This also gives conclusive evidence that cosmic-ray PeVatrons existed/exist in the past and/or present galaxy. The existence of PeVatrons in our galaxy has been a matter of discussion for sixty years since the discovery of cosmic-ray Knee. For the first time, the existence is verified by the Tibet ASγ experiment. This work is also the first experimental proof of theoretical models that cosmic rays accelerated up to the "Knee" energy region are trapped by the magnetic field in our galaxy, forming a pool of cosmic rays.

In addition, four events out of the 23 gamma-ray-like events located within $|b| < 10°$ above 398 TeV concentrate in the Cygnus Cocoon region (around $l = 80°$, $b = +1°$ in Fig. 8), which is a very promising candidate for a PeVatron [15, 36, 28]. This work provides further strong evidence that the Cygnus Cocoon is a Pevatron.

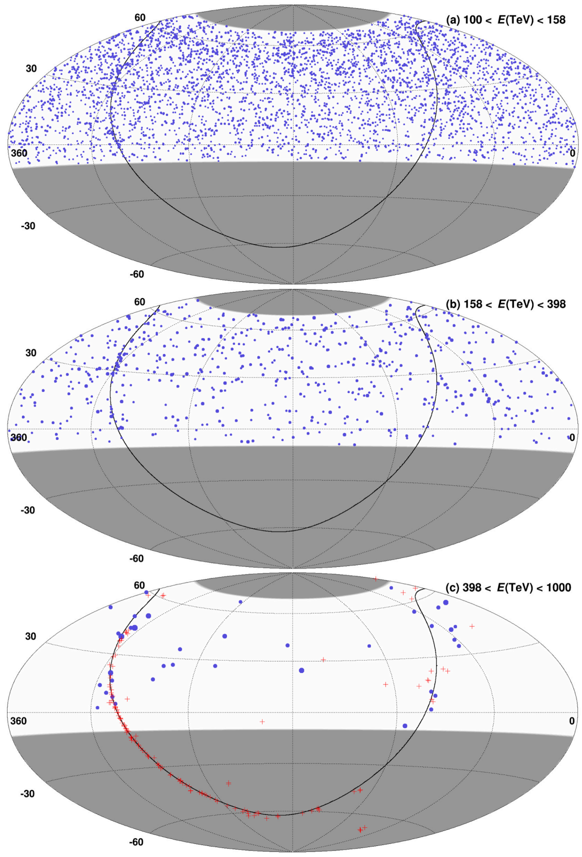

Fig. 8. Figure from [3]. he arrival direction of each gamma-ray like event observed with (a) $100 < E < 158$ TeV, (b) $158 < E < 398$ TeV, and (c) $398 < E < 1000$ TeV, respectively, in the equatorial coordinate. The blue solid circles show arrival directions of gamma-ray like events observed by the Tibet AS+MD array. The area of each circle is proportional to the measured energy of each event. The red plus marks show directions of the known galactic TeV sources (including the unidentified sources) listed in the TeV gamma-ray catalog [34]. The solid curve indicates the galactic plane, while the shaded areas indicate the sky-regions outside the Field of View of the Tibet AS+MD array.

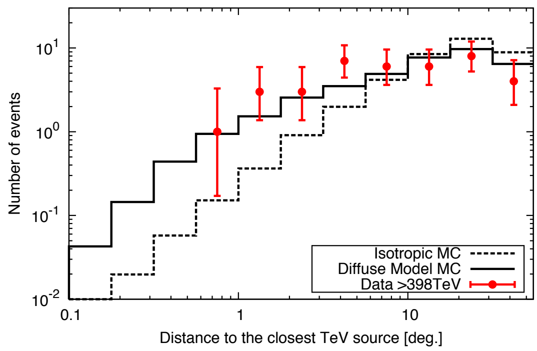

Fig. 9. Figure from [3]. The distribution of the angular distance between the arrival direction of each observed gamma-ray like event with $E > 398$ TeV and the direction of its closest known TeV source listed in the TeV gamma-ray catalog [34]. The red solid circles show the observed data, while the dashed and solid histograms display the MC results expected from the isotropic event distribution and the diffuse gamma-ray model [35], respectively, to be observed with our geometrical exposure.

Fig. 10. YAC2 set up at Yangbajing.

3. Other Activities

The emulsion-pouring facilities can meet the demands for making any kind of nuclear emulsion plates which are used for cosmic ray or accelerator experiments. The thermostatic emulsion-processing facilities are operated in order to develop nuclear emulsion plates or X-ray films. Using these facilities, it is also possible to make and develop emulsion pellicle in 600-micron thickness each. In this way, these facilities have been open to all the qualified scientists who want to carry out joint research programs successfully. Of recent, however, the shrinking demand for the facilities let us decide that we should suspend calls for joint research programs to utilize the emulsion-pouring facilities, starting from 2012.

4. Ongoing Research Plans with MD

(1) Chemical composition of primary cosmic rays making the knee in the all-particle energy spectrum

We have measured the energy spectra of primary cosmic-ray protons, helium, all particles around the knee energy region. The main component responsible for making the knee structure in the all particle energy spectrum is heavier nuclei than helium. The next step is to identify the chemical component making the knee in the all particle energy spectrum. We have a plan to install an Yangbajing Air shower Core detector array (YAC) near the center of Tibet III to distinguish the chemical component making the knee. We completed construction of YAC2 (124 detectors over ~500m^2 in area), as is shown in Fig. 10, and started data-taking in 2014. YAC2 aims at mainly studying the energy spectra of proton and helium components in the knee energy region.

(2) Gamma-ray astronomy in the 100 TeV region

For the purpose of detecting high-energy cosmic gamma rays with an air shower array, a large underground muon detecter[37] is very effective to reduce cosmic-ray background. We added a large (~3,400 m^2) underground water

Cherenkov muon detector (Tibet-MD) array under the present Tibet air shower array (Tibet AS ∼65,700 m^2). By Tibet AS + MD, we aim at background-free detection of celestial point-source gamma rays around 100 TeV with the world-best sensitivity and at locating the origins (PeVatrons) of cosmic rays accelerated up to the knee (PeV) energy region in the northern sky. The measurement of cut off energies in the energy spectra of such gamma rays in the 100 TeV region may contribute significantly to understanding of the cosmic- ray acceleration limit at the acceleration sites. Above 100 TeV, the angular resolution of Tibet AS with 2-steradian wide field of view is 0.2° and the hadron rejection power of Tibet MD is typically 1/1000 for a point-like source.

Development of Monte Carlo simulation is under way for comparison with real data. Various analysis tools are also extensively being developed.

As is described in the text, we succeeded in the first detection of photons with energies above 100 TeV from Crab in the world, opening a new energy (sub-PeV) window in astronomy. We have also succeeded in detection of gamma rays in the 100 TeV region from G106.3+2.7, Cygnus OB1 and OB2 regions as well as sub-PeV diffuse gamma rays from the galactic disk. Analyses are under way in search of other sub-PeV gamma-ray sources.

Bibliography

Papers in refereed journals

[1] "Multi-TeV Gamma-Ray Observation from the Crab Nebula Using the Tibet-III Air Shower Array Finely Tuned by the Cosmic-Ray Moon's Shadow", M. Amenomori *et al.*, Astrophysical Journal, **692** , 61-72 (2009).

[2] "Gamma-Ray Observation of the Cygnus Region in the 100-TeV Energy Region", M. Amenomori et al., Phys. Rev. Lett. **127**, 031102 (2021).

[3] "First Detection of sub-PeV Diffuse Gamma Rays from the Galactic Disk: Evidence for Ubiquitous Galactic Cosmic Rays beyond PeV Energies", M. Amenomori*et al.*, Phys. Rev. Lett., **125** 141101 (2021).

[4] "First Detection of Photons with Energies beyond 100 TeV from an Astrophysical Source", M. Amenomori*et al.*, Physical Review Letters, **123** :051101-1-6 (2019).

[5] "Energy determination of gamma-ray induced air showers observed by an extensive air shower array", K. Kawata*et al.*, Experimental Astronomy, **44** 1-9 (2017).

[6] F. Aharonian et al., Astron. Astrophys. **393**, L37 (2002).

[7] F. Aharonian et al., Astron. Astrophys. **431**, 197 (2005).

[8] A. Konopelko et al., Astrophys. J. **658**, 1062 (2007).

[9] J. Albert et al., Astrophys. J. Lett. **675**, L25 (2008).

[10] E. Aliu et al., Astrophys. J. **783**, 16 (2014).

[11] A. U. Abeysekara et al., Astrophys. J. **861**, 134 (2018).

[12] A. A. Abdo et al., Astrophys. J. Lett. **664**, L91 (2007).

[13] A. A. Abdo et al., Astrophys. J. **753**, 159 (2012).

[14] B. Bartoli et al., Astrophys. J. Lett. **745**, L22 (2012).

[15] B. Bartoli et al., Astrophys. J. **790**, 152 (2014).

[16] A. U. Abeysekara et al., Astrophys. J. **843**, 40 (2017).

[17] M. Ackermann et al., Science **334**, 1103 (2011).

[18] A. A. Abdo et al., Astrophys. J. Lett. **658**, L33 (2007).

[19] A. U. Abeysekara et al., Phys. Rev. Lett. **124**, 021102 (2020).

[20] A. Albert et al., Astrophys. J. **905**, 76 (2020).

[21] E. Aliu et al., Astrophys. J. **788**, 78 (2014).

[22] M. S. E. Roberts, J. W. T. Hessels, S. M. Ransom, V. M. Kaspi, P. C. C. Freire, F. Crawford, and D. R. Lorimer, Astrophys. J. Lett. **577**, L19 (2002).

[23] A. A. Abdo et al., Astrophys. J. **700**, 1059 (2009).

[24] J. W. T. Hessels, M. S. E. Roberts, S. M. Ransom, V. M. Kaspi, R. W. Romani, C.-Y. Ng, P. C. C. Freire, and B. M. Gaensler, Astrophs. J. **612**, 389 (2004).

[25] T. Mizuno, N. Tanaka, H. Takahashi, J. Katsuta, K.Hayashi, and R. Yamazaki, Astrophys. J. **841**, 104 (2017).

[26] M. Amenomori et al., Astrophys. J. **633**, 1005 (2005).

[27] T.-P. Li and Y.-Q. Ma, Astrophys. J. **272**, 317 (1983).

[28] A. U. Abeysekara et al., Nat. Astron. Lett. **5**, 465 (2021).

[29] A. U. Abeysekara et al., Astrophys. J. Lett. **867**, L19 (2018).

[30] I. M. Beerer et al., Astrophys. J. **720**, 679 (2010).

[31] K. E. Kraemer et al., Astron. J. **139**, 2319 (2010).

[32] E. V. Gotthelf et al., Astrophys. J. **826**, 25 (2016).

[33] K. A. van der Hucht, New Astron. Rev. **45**, 135 (2001).

[34] S. Wakely and D. Horan, available at http://tevcat.uchicago.edu .

[35] P. Lipari and S. Vernetto, Phys. Rev. D **98**, 043003 (2018).

[36] F. Aharonian, R. Yang and E. de Oña Wilhelmi, Nature Astronomy **3**, 561 (2019).

[37] "Exploration of a 100 TeV gamma-ray northern sky using the Tibet air-shower array combined with an underground water-Cherenkov muon-detector array", T.K. Sako *et al.*, Astroparticle Physics, **32** , 177-184 (2009).

The Tibet ASγ Collaboration

M. Amenomori[1], S. Asano[2], Y. W. Bao[3], X. J. Bi[4], D. Chen[5], T. L. Chen[6], W. Y. Chen[4], Xu Chen[4], Y. Chen[3], Cirennima[6], S. W. Cui[7], Danzengluobu[6], L. K. Ding[4], J. H. Fang[4,8], K. Fang[4], C. F. Feng[9], Zhaoyang Feng[4], Z. Y. Feng[10], Qi Gao[6], A. Gomi[11], Q. B. Gou[4], Y. Q. Guo[4], Y. Y. Guo[4], H. H. He[4], Z. T. He[7], K. Hibino[12], N. Hotta[13], Haibing Hu[6], H. B. Hu[4], K. Y. Hu[4,8], J. Huang[4], H. Y. Jia[10], L. Jiang[4], P. Jiang[5], H. B. Jin[5], K. Kasahara[14], Y. Katayose[11], C. Kato[2], S. Kato[15], T. Kawashima[15], K. Kawata[15], M. Kozai[16], D. Kurashige[11], Labaciren[6], G. M. Le[17], A. F. Li[18,9,4], H. J. Li[6], W. J. Li[4,10], Y. Li[5], Y. H. Lin[4,8], B. Liu[19], C. Liu[4], J. S. Liu[4], L. Y. Liu[5], M. Y. Liu[6], W. Liu[4], X. L. Liu[5], Y.-Q. Lou[20,21,22], H. Lu[4], X. R. Meng[6], Y. Meng[4,8], K. Munakata[2], K. Nagaya[11], Y. Nakamura[15], Y. Nakazawa[23], H. Nanjo[1], C. C. Ning[6], M. Nishizawa[24], M. Ohnishi[15], S. Okukawa[11], S. Ozawa[25], L. Qian[5], X. Qian[5], X. L. Qian[26], X. B. Qu[27], T. Saito[28], Y. Sakakibara[11], M. Sakata[29], T. Sako[15], T. K. Sako[15], J. Shao[4,9], M. Shibata[11], A. Shiomi[23], H. Sugimoto[30], W. Takano[12], M. Takita[15], Y. H. Tan[4], N. Tateyama[12], S. Torii[31], H. Tsuchiya[32], S. Udo[12], H. Wang[4], Y. P. Wang[6], Wangdui[6], H. R. Wu[4], Q. Wu[6], J. L. Xu[5], L. Xue[9], Z. Yang[4], Y. Q. Yao[5], J. Yin[5], Y. Yokoe[15], N. P. Yu[5], A. F. Yuan[6], L. M. Zhai[5], C. P. Zhang[5], H. M. Zhang[4], J. L. Zhang[4], X. Zhang[3], X. Y. Zhang[9], Y. Zhang[4], Yi Zhang[33], Ying Zhang[4], S. P. Zhao[4], Zhaxisangzhu[6] and X. X. Zhou[10]

[1]Department of Physics, Hirosaki University, Hirosaki 036-8561, Japan.
[2]Department of Physics, Shinshu University, Matsumoto 390-8621, Japan.
[3]School of Astronomy and Space Science, Nanjing University, Nanjing 210093, China.
[4]Key Laboratory of Particle Astrophysics, Institute of High Energy Physics, Chinese Academy of Sciences, Beijing 100049, China.
[5]National Astronomical Observatories, Chinese Academy of Sciences, Beijing 100012, China.
[6]Department of Mathematics and Physics, Tibet University, Lhasa 850000, China.
[7]Department of Physics, Hebei Normal University, Shijiazhuang 050016, China.
[8]University of Chinese Academy of Sciences, Beijing 100049, China.
[9]Institute of Frontier and Interdisciplinary Science and Key Laboratory of Particle Physics and Particle Irradiation (MOE), Shandong University, Qingdao 266237, China.
[10]Institute of Modern Physics, SouthWest Jiaotong University, Chengdu 610031, China.
[11]Faculty of Engineering, Yokohama National University, Yokohama 240-8501, Japan.
[12]Faculty of Engineering, Kanagawa University, Yokohama 221-8686, Japan.
[13]Faculty of Education, Utsunomiya University, Utsunomiya 321-8505, Japan.
[14]Faculty of Systems Engineering, Shibaura Institute of Technology, Omiya 330-8570, Japan.
[15]Institute for Cosmic Ray Research, University of Tokyo, Kashiwa 277-8582, Japan.
[16]Institute of Space and Astronautical Science, Japan Aerospace Exploration Agency (ISAS/JAXA), Sagamihara 252-5210, Japan.
[17]National Center for Space Weather, China Meteorological Administration, Beijing 100081, China.
[18]School of Information Science and Engineering, Shandong Agriculture University, Taian 271018, China.
[19]Department of Astronomy, School of Physical Sciences, University of Science and Technology of China, Hefei 230026, China.
[20]Department of Physics and Tsinghua Centre for Astrophysics (THCA), Tsinghua University, Beijing 100084, China.
[21]Tsinghua University-National Astronomical Observatories of China (NAOC) Joint Research Center for Astrophysics, Tsinghua University, Beijing 100084, China.
[22]Department of Astronomy, Tsinghua University, Beijing 100084, China.
[23]College of Industrial Technology, Nihon University, Narashino 275-8576, Japan.
[24]National Institute of Informatics, Tokyo 101-8430, Japan.
[25]National Institute of Information and Communications Technology, Tokyo 184-8795, Japan.
[26]Department of Mechanical and Electrical Engineering, Shangdong Management University, Jinan 250357, China.
[27]College of Science, China University of Petroleum, Qingdao 266555, China.
[28]Tokyo Metropolitan College of Industrial Technology, Tokyo 116-8523, Japan.
[29]Department of Physics, Konan University, Kobe 658-8501, Japan.
[30]Shonan Institute of Technology, Fujisawa 251-8511, Japan.
[31]Research Institute for Science and Engineering, Waseda University, Tokyo 162-0044, Japan.
[32]Japan Atomic Energy Agency, Tokai-mura 319-1195, Japan.
[33]Key Laboratory of Dark Matter and Space Astronomy, Purple Mountain Observatory, Chinese Academy of Sciences, Nanjing 210034, China.

(The Tibet ASγ Collaboration as of 2021)

ALPACA Project

[Spokesperson: M. Takita]

ICRR, The Univ. of Tokyo, Kashiwa, Chiba 277-8582

Cosmic rays are supposed to be accelerated up to the knee energy (PeV) region at supernova remnants (SNRs), star formation regions and PWNe in our galaxy. Therefore, we naturally expect gamma rays at 100 TeV energies, which originate in π^0 decays produced by the accelerated cosmic rays interacting with matter surrounding the acceleration sites. The gamma-ray emission of electron origin might be highly suppressed above 10 TeV due to rapid decrease of inverse-Compton cross section by the Klein-Nishina effect as well as synchrotron radiation energy loss in the strong magnetic field around the acceleration sites. The detection and spectral measurement of gamma rays in the 100 TeV region from their celestial sources, together with multi-wavelength (radio, X-ray, gamma-ray) observations, will be an important experiment enabling us to discriminate between the two processes (cosmic-ray/electron origins), to locate the acceleration site (PeVatron which accelerate cosmic rays up to PeV energies) of cosmic rays and to verify the standard acceleration model of cosmic rays. Furthermore, diffuse gamma rays from the Fermi bubbles recently reported by the Fermi-LAT group and sub-PeV neutrino events[1] detected by IceCube suggests that the Fermi bubbles be a PeVatron candidate. Similarly, the energy spectrum of diffuse gamma rays from the extended region around the galactic center marginally measured by HESS up to approximately 10 TeV also strongly indicates existence of PeVatron[2], from which we expect to detect gamma rays at 100 TeV energies. In 2021, the Tibet ASγ experiment succeeded in the first detection of sub-PeV diffuse gamma rays from the glactic disk. The natural interpretation is that the sub-PeV gamma rays are of cosmic ray origin. Therefore, this is the first experimental evidence that PeVatrons exist in our galaxy. However, there has been no agreed-upon PeVatron in the northern sky so far. Thus, a wide field-of-view gamma-ray imaging at 100 TeV energies in the southern sky, where the HESS sources[3], the Fermi bubbles and the galactic center are located within field of view, will be a key experiment.

5. Experiment

The ALPACA[4],[5] (Andes Large area PArticle detector for Cosmic ray physics and Astrophysics) is a cosmic-ray experiment with a large surface air shower array with a large underground muon detector array The experimental site (approximately 500 m$\times$500 m $\sim$250,000 m^2 in total area) is located on a flat high land called Chacaltaya Plateau (4,740 m above sea level, 16°23' S, 68°08' W), as shown in Fig. 1, around Mount Chacaltaya, near La Paz, Bolivia. In some part in this area, our detectors will be constructed.

We plan to set up a 3,700 m^2 underground (approximately one to a few meters) muon detector array (MD) and an 83,000 m^2 air shower array (AS). MD of water Cherenkov type is composed of eight pools with each pool (approximately 1 m deep) containing twelve 56 m^2 unit detectors. AS is made up of 401 1 m^2 plastic scintillation counters at 15 m spacing.

The AS field of view is roughly 2 steradian. The expected angular resolution of AS is approximately 1 degree at 5 TeV and 0.2 degrees around 100 TeV for gamma rays. For 100 TeV gamma rays, the AS energy resolution is estimated to be $\sim$20-25 %. The hadron rejection power of MD is more than 99.9 % at 100 TeV, while keeping most of gamma-ray events. Long-term detector stability, angular resolution, pointing accuracy and energy scale can be calibrated by the cosmic-ray shadow in the Moon as well as by some of the bright stable TeV gamma ray sources in the southern sky.

Fig. 1. From Ref.[4]. Experimental site for the ALPACA experiment, Chacaltaya Plateau ia (4,740 m above see level, 16°23' S, 68°08' W), near Mount Chacaltaya, in Bolivia.

6. Covered Physics

Our reserch target is divided into four in ALPACA:

1. Measurement of high-energy (5 TeV – 1 PeV) cosmic gamma rays.

2. Measurement of cosmic ray energy spectra around the Knee energy region (100 TeV – 100 PeV).

3. Measurement of cosmic ray anisotropy $>$ 5 TeV at sidereal time frame.

4. Measurement of the Sun shadow in cosmic rays $>$ 5 TeV.

We aim at low-background detection of celestial gamma rays in the 100 TeV region with the world-best sensitivity (an order of magnitude better than any previous/existing experiments) and at locating the origins of cosmic rays accelerated up to the knee energy region in the southern sky. Presuming a Crab-like gamma-ray source extending up with power-law index -2.6 located in the southern sky, the ALPACA experiment is sensitive to the source with $\sim$15 % Crab intensity during one calendar year, as is demonstrated in Fig. 2.

The AS + MD in the southern hemisphere will be a unique/complementary experiment to on-going experiments (FERMI, CALET, DAMPE, HESS, VERITAS, MAGIC, Tibet ASγ, HAWC, LHAASO) and future projects (CTA, SWGO) in this field, which are either located in the northern hemisphere or aiming at gamma-ray astronomy below 10 TeV region, or having narrow field-of-view, or not expected to start operation in the near future (within 5 to 10 years). Thus, the new energy window in the 100 TeV region observing gamma rays with wide field-of-view will be opened first in the southern sky by the ALPACA experiment. We expect to detect established more than a dozen of sources, i.e., young SNRs (SN1006, RX J1713.7-3946, RX J0852.0-4622), Pulsar Wind Nebulae, the galactic center, etc) in the 100 TeV region, some

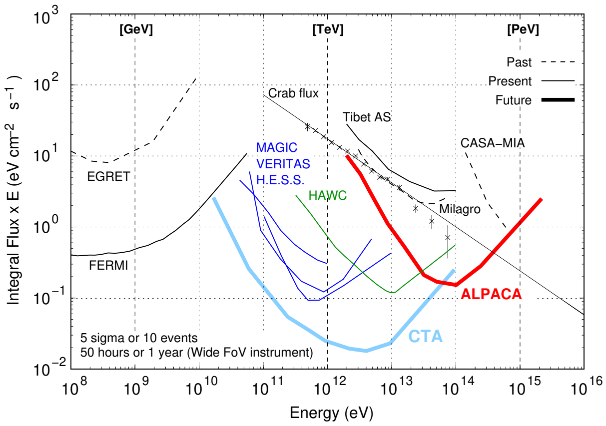

Fig. 2. Sensitivity of ALPACA to high-energy gamma-ray point source. Experimental data points are from HEGRA. The ALPACA sensitivity is evaluated from Ref.[6].

of which may be cosmic-ray PeVatron candidates. Furthermore, our wide field-of-view sensitivity to diffuse gamma rays allows us to study extremely diffuse gamma-ray sources which are difficult to detect by IACTs. The diffuse gamma rays from the Fermi bubbles recently reported by the Fermi-LAT group may be clearly detected, if they extend up to the 100 TeV region. Similarly, detection of diffuse gamma rays above 100 TeV from extended region from the galactic center is promising, where the gamma-ray energy spectrum strongly suggests existence of PeVatron. The sub-PeV diffuse gamma rays along the galactic disk in the southern sky are an interesting target to understand the PeV cosmic-ray propagation in our galaxy. Detection and spectral measurement of gamma rays in the 100 TeV region from these celestial sources, together with multi-wavelength (radio, X-ray, gamma-ray) observations, are key points enabling us to discriminate between the two processes (cosmic-ray/electron origins), to locate the acceleration site of cosmic rays and to examine the standard acceleration and propagation model of cosmic rays. In astronomical point of view, we will open the ultra-high-energy (above 100 TeV) window in gamma-ray astronomy in the southern sky. Besides, gamma-ray emission from near-by extragalactic sources, e.g. M87, Cen A, gamma rays of dark matter origin, those from the Sun disk recently obseved by Fermi[9] may be interesting subjects.

We also aim at measuring energy spectra of proton, helium and iron components separately around the knee energy region with the new AS + MD. The standard cosmic-ray acceleration model at SNR predicts the knee energy of each nucleus component being proportional to Z (atomic number). We can discriminate proton and iron components by MD, as an iron nucleus produces approximately 2 times more muons than a proton with the same energy. Thus, the cosmic-ray acceleration scenario (SNR shock acceleration) will be verified by observing the linearly Z(atomic number)-dependent knee(=bent) positions of proton, helium, iron components around the knee energy region.

Precise cosmic-ray anisotropy measurement at sidereal time frame in the TeV energy region in the southern sky provides unique data for the community to understand the magnetic field structure in the heliosphere. The ALPACA experiment gives complementary data in the TeV region to those from IceCube above a few tens of TeV.

Furthermore, measurement of the Sun shadow in cosmic rays above the TeV energy region in the southern hemisphere also helps understand the modeling of the magnetic fields between the Sun and the Earth, complementary to the observations in the northern hemisphere.

7. ALPAQUITA

As a proto-type experiment, the ALPAQUITA[7] air shower array which is ∼25 % of the ALPACA air shower array in area is being constructed at the experimental site, Chacaltaya Plateau. The containers including materials and equipments necessary to construct the ALPAQUITA air shower array arrived at La Paz, Bolivia in early 2019. The main infrastructures including electricity, experimental hut, fence, cable guide drains are ready in 2021. Due to COVID19 problems, the construction of ALPAQUITA air shower array was delayed. The ALPAQUITA air shower array is under construction now, as is seen in Fig. 3. Due to COVID19 problems, We aim at completing construction of the ALPAQUITA air shower array under which we will add a ∼900-m^2 muon detector array in 2022.

Fig. 3. ALPAQUITA air shower array under construction.

The ALPAQUITA sensitivity to gamma rays from a point source is estimated by a Monte Carlo simulation[7], as is shown in Fig. 4. Even with the ALPAQUI TA air shower array with a 900 m^2 MD, we expect to detect several bright 100 TeV gamma-ray sources.

8. ALPACA(half)

The budget which affords to construct approximately half of ALPACA was funded in 2020. We replanned to set up ALPACA(half), a 3,700 m^2 underground (approximately one to a few meters) muon detector array (MD) and an 83,000 m^2 air shower array (AS), shown in Fig. 5. MD of water Cherenkov type is composed of four pools with each pool (approximately 1 m deep) containing sixteen 56 m^2 unit detectors. AS is made up of 200 1 m^2 plastic scintillation counters at 21 m

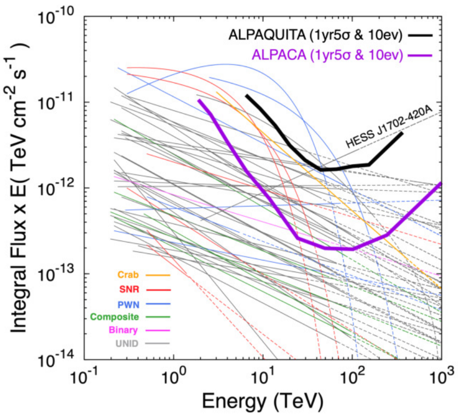

Fig. 4. From [7]. Sensitivity of the ALPAQUITA air shower array with a 900 m^2 MD (black curve) to point-like gamma-ray sources. The measured energy spectra of the H.E.S.S. sources are represented by solid curves, while the dashed curves represent the extrapolations of the measured spectra.

spacing. The performance of ALPACA(half)[8] for cosmic gamma rays above 100 TeV is expected to be similar to that of ALPACA.

We will finish contruction of ALPACA(half) in 2023.

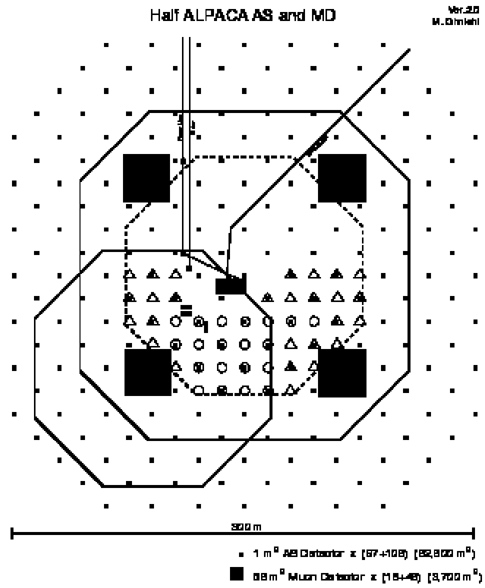

Fig. 5. Schematic view of the ALPACA(half) experiment. The small black squares indicate 200 1 m^2 plastic scintillation detectors at 21m spacing, forming an air shower array with 83,000 m^2 in area.The black large rectangles indicate four underground muon detector pools, each of which contains sixteen 56 m^2 muon detector units. The total area of the underground muon detector array is 3,700 m^2. The area enclosed in the lower-left octagon represents ALPAQUITA.

Bibliography

Papers and references

[1] C. Lunardini et al., PRD, **92**, 021301-1-5 (2015).

[2] A. Abramoswski et al., Nature, **531**, 476 (2016).

[3] H. Abdalla et al., A&A **612**, A1 (2018).

[4] M. Takita for the ALPACA Collaboration, THE EUROPEAN PHYSICAL JOURNAL, **145**, 01002-1-3, (2017).

[5] F. Aceves de la Cruz et al. (The ALPACA Collaboration), Proc. of ICRC2021, POS(ICRC2021)733, Online, July 12-23, (2021).

[6] T. K. Sako et al., Astroparticle Physics, **32**, 177 (2009).

[7] S. Kato et al (The ALPACA Collaboration), Experimental Astronomy, **52**, 85-107 (2021).

[8] F. Aceves de la Cruz et al. (The ALPACA Collaboration), Proc. of ICRC2021, POS(ICRC2021)899, Online, July 12-23, (2021).

[9] C. Y. Kenny et al., arXiv:1508.06276v1.

The ALPACA Collaboration, as of 2021

F. Aceves de la Cruz[1], S. Asano[2], C. A. H. Condori[3], E. de la Fuente[1,4], J. L. Garcia-Luna[1], A. Gomi[5], K. Hibino[6], N. Hotta[7], A. Jimenez-Meza[8], Y. Katayose[9], C. Kato[2], S. Kato[10], T. Kawashima[10], K. Kawata[10], T. Koi[11], H. Kojima[12], D. Kurashige[5], J. Lozoya[13], R. Mayta[14,15], P. Miranda[3], K. Munakata[2], K. Nagaya[5], Y. Nakamura[10], Y. Nakazawa[16], C. Nina[3], M. Nishizawa[17], S. Ogio[14,15], M. Ohnishi[10], S. Okukawa[5], F. Orozco[4], A. Oshima[11], M. Raljevich[3], H. Rivera[3], T. Saito[18], Y. Sakakibara[5], T. Sako[10], T. K. Sako[10], S. Shibata[12], A. Shiomi[16], M. Subieta[3], N. Tajima[19], W. Takano[6], M. Takita[10], Y. Tameda[20], K. Tanaka[21], R. Ticona[3], I. Toledano-Juarez[22,23], H. Tsuchiya[24], Y. Tsunesada[14,15], S. Udo[6], K. Yamazaki[11] and Y. Yokoe[10]

[1]Departamento de Física, CUCEI, Universidad de Guadalajara, Guadalajara, Jalisc o, Mexico.

[2]Department of Physics, Shinshu University, Matsumoto, Nagano 390-8621, Japan.

[3]Instituto de Investigaciones Físicas, Universidad Mayor de San Andrés, La Paz 8635, Bolivia.

[4]Doctorado en Tecnologías de la Información, CUCEA, Universidad de Guadalaj ara, Zapopan, Jalisco, Mexico.

[5]Graduate School of Engineering Science, Yokohama National University, Yokohama, Ka nagawa 240-8501, Japan.

[6]Faculty of Engineering, Kanagawa University, Yokohama, Kanagawa 221-8686, Japan.

[7]Utsunomiya University, Utsunomiya, Tochigi 321-8505, Japan.

[8]Departamento de Tecnologíias de la Información, CUCEA, Universidad de Guad alajara, Zapopan, Jalisco, Mexico.

[9]Faculty of Engineering, Yokohama National University, Yokohama, Kanagawa 240-8501, Japan.
[10]Institute for Cosmic Ray Research, University of Tokyo, Kashiwa, Chiba 277-8582 , Japan.
[11]College of Engineering, Chubu University, Kasugai, Aichi 487-8501, Japan.
[12]Chubu Innovative Astronomical Observatory, Chubu University, Kasugai, Aichi 487 -8501, Japan.
[13]Departamento de Ciencias de la Información y Desarrollo Tecnológico, Cu tonala, Universidad de Guadalajara, Tonalá, Jalisco, Mexico.
[14]Graduate School of Science, Osaka City University, Osaka, Osaka 558-8585, Japan .
[15]Nambu Yoichiro Institute for Theoretical and Experimental Physics, Osaka City U niversity, Osaka, Osaka 558-8585, Japan.
[16]College of Industrial Technology, Nihon University, Narashino, Chiba 275-8576, Japan.
[17]National Institute of Informatics, Chiyoda, Tokyo 101-8430, Japan.
[18]Tokyo Metropolitan College of Industrial Technology, Arakawa, Tokyo 116-8523, J apan.
[19]RIKEN, Wako, Saitama 351-0198, Japan.
[20]Faculty of Engineering, Osaka Electro-Communication University, Neyagawa, Osaka 572-8530, Japan.
[21]Graduate School of Information Sciences, Hiroshima City University, Hiroshima, Hiroshima 731-3194, Japan.
[22]Doctorado en Ciencias Físicas, CUCEI, Universidad de Guadalajara, Guadalaja ra, Jalisco, Mexico.
[23]Maestría en Ciencia de Datos, Departamento de Métodos Cuantitativos, CU CEA, Universidad de Guadalajara, Zapopan, Jalisco, Mexico.
[24]Japan Atomic Energy Agency, Tokai-mura, Ibaraki 319-1195, Japan.

High Energy Astrophysics Group

[Spokesperson: K. Asano]
ICRR, The Univ. of Tokyo, Kashiwa, Chiba 277-8582

Overview

The high energy astrophysics group has been making theoretical studies of violent astrophysical phenomena, in which nonthermal cosmic-ray particles are being accelerated. Targets of the group's study include high energy astrophysical objects such as supernova remnants/explosions, pulsars, pulsar wind nebulae, black hole/neutron star mergers, jets from active galactic nuclei (AGNs), and gamma-ray bursts (GRBs). We especially study the formation of relativistic outflows, particle acceleration in jets, emission mechanisms of electromagnetic waves or neutrinos, and electromagnetic counterparts for compact binary mergers. Our research carries the multi-messenger astronomy forward, which probes astronomical phenomena through collaborating observations of electromagnetic waves, cosmic rays, neutrinos, and gravitational waves. Gravitational-wave astronomy is also our target. We have been probing the formation history of massive stars from the early universe to the present time with the observation results by gravitational-wave detectors.

Research Topic 1: Multi-Messenger Signals from the Coma Cluster

Galaxy clusters are considered to be gigantic reservoirs of cosmic rays (CRs). Some of the clusters are found with extended radio emission, which provides evidence for the existence of magnetic fields and CR electrons in the intra-cluster medium. The mechanism of radio halo (RH) emission is still under debate, and it has been believed that turbulent reacceleration plays an important role. We study the reacceleration of CR protons and electrons in detail by numerically solving the Fokker–Planck equation, and show how radio and gamma-ray observations can be used to constrain CR distributions and resulting high-energy emission for the Coma cluster. We take into account the radial diffusion of CRs and follow the time evolution of their one-dimensional distribution, by which we investigate the radial profile of the CR injection that is consistent with the observed RH surface brightness. We find that the required injection profile is nontrivial, depending on whether CR electrons have a primary or secondary origin. Although the secondary CR electron scenario predicts larger gamma-ray and neutrino fluxes, it is in tension with the observed RH spectrum for hard injection indexes, $\alpha < 2.45$. This tension is relaxed if the turbulent diffusion of CRs is much less efficient than the fiducial model, or the reacceleration is more efficient for lower-energy CRs. In both the secondary and primary scenario, we find that galaxy clusters can make a sizable contribution to the all-sky neutrino intensity if the CR energy spectrum is nearly flat.

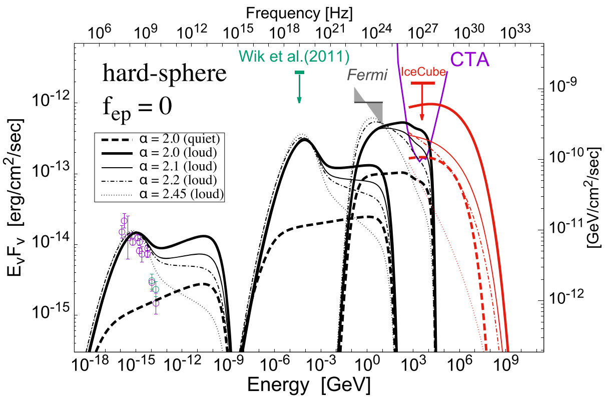

Fig. 1. Nonthermal electromagnetic and all-flavor neutrino spectra for the Coma cluster. From left to right, synchrotron, inverse-Compton, and π^0 gamma emission are shown in black curves. The red curves show neutrino fluxes. The “loud” and “quiet” states are shown in the thick solid and thick dashed curves, respectively. The loud-state spectra for different injection spectral index α are also shown: $\alpha = 2.1$ (thin solid), 2.2 (thin dotted–dashed), and 2.45 (thin dotted).

Research Topic 2: Interpretation for CALET Electron and Positron Spectrum

Focusing on the electron and positron spectrum measured with the Calorimetric Electron Telescope (CALET), which shows characteristic structures, we calculate the flux contributions of cosmic rays that have escaped from randomly appearing supernova remnants. We adopt a Monte Carlo method to take into account the stochastic nature of the appearance of nearby sources. We find that without a complicated energy dependence of the diffusion coefficient, simple power-law diffusion coefficients can produce spectra similar to the CALET spectrum, even with a dispersion in the injection index. The positron component measured with AMS-02 is consistent with a bump-like structure around 300 GeV in the CALET spectrum. One to three nearby supernovae can contribute up to a few tens of percent of the CALET flux at 2–4 TeV, while ten or more unknown and distant (>500 pc) supernovae account for the remaining several tens of percent of the flux. The CALET spectrum, showing a sharp drop at $\sim$ 1 TeV, allows for a contribution of cosmic rays from an extraordinary event that occurred $\sim$ 400 kyr ago. This type of event releases electrons/positrons with a total energy more than 10 times the average energy for usual supernovae, and its occurrence rate is lower than one three-hundredth of the usual supernova rate.

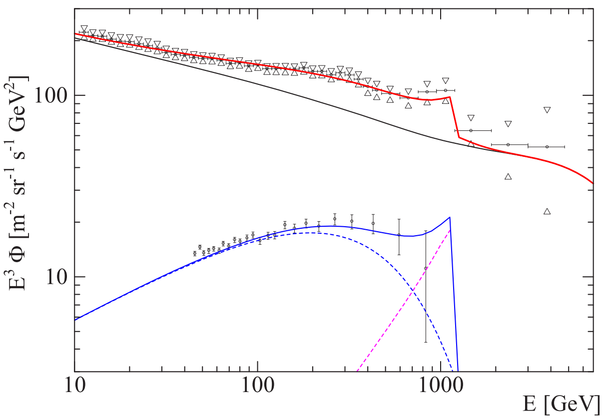

Fig. 2. An example of electron and positron spectra with additional components consistent with the positron spectrum measured by AMS-02. The upper spectral data is the CALET data. The red line is the sum of the electron–positron pair component (double the positron flux denoted by the blue solid line) and the supernova electron component (the black solid line), which is a realization of the same Monte Carlo simulations. The positron component (the blue solid line) is the sum of the two components denoted by dashed lines. The blue dashed line is a positron component and the magenta dashed line is calculated from an electron–positron pair ejection that occurred 420 kyr ago at a distance of 1 kpc.

Research Topic 3: Collisionless Relativistic Jet

After the discovery of relativistic jets in early 20th century, the formation and acceleration mechanism of relativistic jets are not still understood. Recent observation of M87, which is one of the best laboratories to study jets, discovered the triple-ridge structure in its jet. The triple-ridge structure can be interpreted as the observational feature of the spine-sheath structure of the jet, which is composed of the fast-flowing spine and the slow-flowing sheath. The spine structure is, especially, not reproduced by relativistic magnetohydrodynamic simulations in which the macroscopic physics can be solved. This indicates that the kinetic plasma (i.e., microscopic) effects may be important for the spine jet structure formation.

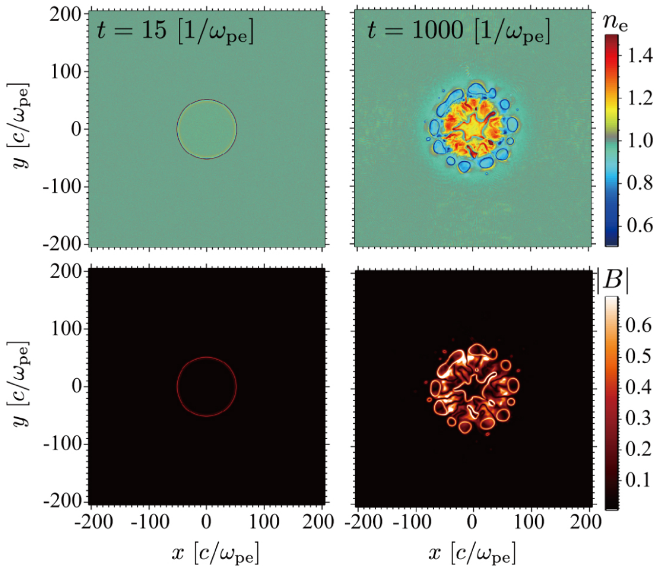

Fig. 3. The electron number density (top) and the magnetic field strength (bottom) in the early (left) and later (rihgt) stages of the particle-in-cell simulation. The simulation domain is on the transverse plane of the jets. The number density of the electrons accelerated by MI-driven-MRs increases with time in the jet center. The physical quantities in the figures are displayed with an arbitrary unit.

We, therefore, studied the kinetic plasma dynamics in collisionless relativistic jets with velocity shear, by carrying out particlein- cell simulations in the transverse plane of a jet. It was discovered that intermittent magnetic reconnections (MRs) are driven by mushroom instability (MI), which is an important kinetic-scale plasma instability in the plasma shear flows with relativistic bulk speed. We referred to this sequence of kinetic plasma phenomena as "MI-driven MR." The MI-driven MRs intermittently occur with moving the location of the reconnection points from the vicinity of the initial velocity-shear surface toward the center of the jet. As a consequence, the number density of high-energy electrons that are accelerated by MI-driven MRs increases with time in the region inside the initial velocity-shear surface with the accompanying generation and subsequent amplification of magnetic fields by MI. The maximum Lorentz factor of electrons increases with initial bulk Lorentz factor of the jet. The MI-driven MR might be related to the formation of the spine structure in relativistic jets.

Research Topic 4: Radio Observation of Sgr A* and Theoretical Interpretation

EAVN (East Asia VLBI Network) has been developed to observe the highly resolved radio images of nearby active galactic nuclei by using VLBI (Very Long Baseline Interferometry) techniques. We firstly observed the relatively nearby region of the central black hole ($\lesssim 10^3 r_{\rm g}$, where $r_{\rm g}$ is the gravitation radius of the black hole) in Sgr A* at the wavelength 1.3cm and 7mm. In lower frequency bands including 1.3cm and 7mm, the effects of the scattering caused by the interstellar plasma can drastically make the images of Sgr A* drastically blurred due to the effects of the diffraction and refraction. By using the state-of-the-art models of the scattering screen of the interstellar plasma, the intrinsic images of Sgr A* is successfully obtained. The morphology of the intrinsic images are almost circular rather than elliptic, whose bright region extends down at least upto several 100 r_g.

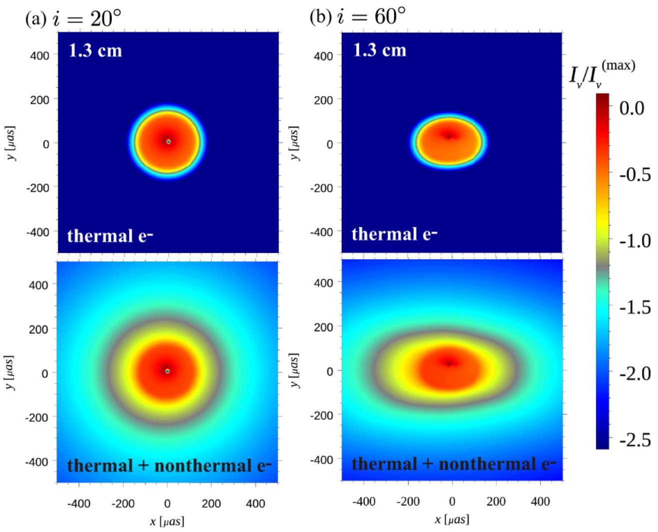

Fig. 4. The theoretical images of Sgr A* at 1.3cm assuming viewing angle $i = 20°$ (left) and 60° (right). The top and bottom panels display the model with thermal electron only and thermal plus nonthermal electrons, respectively. The effects of the synchrotron emission via nonthermal electrons significantly enlarge the size of the bright region and consistent with the observed data.

To interpret the results, we have calculated the images and spectra of the Sgr A* accretion flow by using a general relativistic radiative transfer code `RAIKOU`. A toy model so called Keplerian shell model is assumed for the accreting plasma onto Sgr A*. We have found that the circular mophology of the images can be reproduced when the viewing angle, which is the angle between the rotation axis of the accretion flow and the line of sight, is $\lesssim 30°$–$40°$, i.e., the neary face-on view. The observed large image sizes, importantly, requires the accelerated electrons. This may give us the important informations for the origin of the cosmic rays in the region near the Sgr A*.

Research Topic 5: Radio jets bent by magnetic fields

Galaxy clusters are known to harbor magnetic fields, the nature of which remains an open question. Radio observations of clusters can be used to study the distributed populations of cosmic-ray electrons and the magnetic field of the intracluster medium. However, the measurement of the magnetic fields from radio intensity is inherently uncertain owing to the many assumptions. In this study, we focus on the second-brightest radio galaxy, MRC 0600-399, in the merging galaxy cluster Abell 3376. We first time discovered the evidence of the interaction between a radio jet and an intracluster magnetic field through the unprecedented combination of brightness sensitivity, dynamic range, and angular resolution of a new 1.28 GHz MeerKAT continuum image (left panel of figure 5). The jets from galaxy MRC 0600-399 bend at where the cluster plasma property has changed, and the collimated jet further extends over 100 kpc from the bend point. In addition to this, we identified the diffuse radio emissions elongated not only to the bending direction but also to the opposite direction. These are unusual features in the typical bent jets. To understand the main mechanism of the origin of the unusual bent jet, we have performed magnetohydrodynamic simulations of the interaction between the jet and the intracluster field. We found that the motion of the jet across the ordered magnetic fields surrounding the cluster is suppressed due to the magnetic field tension. Then, the jet changes direction along with the ordered field. The overall morphology of the bent jet bears remarkable similarities with the simulations (right panel of figure 5). Our results provided new physical insight into the dynamics of radio jets, but also a novel tool for the measurement of the intracluster magnetic field from high-quality radio observations.

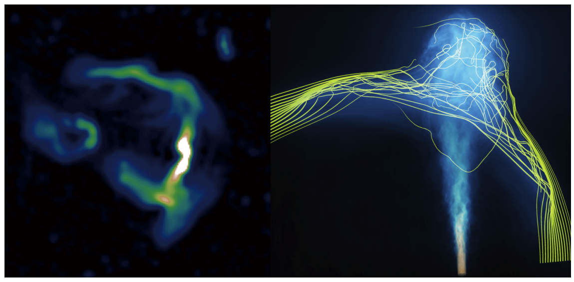

Fig. 5. The observed image of MRC 0600-399 (left) and the simulation of the interaction between galactic jets and magnetic fields calculated by ATERUI II (right).(Credit: [Left] Chibueze, Sakemi, Ohmura et al. (2021) Modification from Nature Fig. 1 (b). [Right] Takumi Ohmura, Mami Machida, Hirotaka Nakayama, 4D2U Project, NAOJ)

Research Topic 6: Neutron star merger ejecta and Kilonova Emission

We predicted the kilonova lightcurve models in various setups based on the latest numerical relativity simulations and radiative transfer simulations, and discussed the property of the progenitor employing our kilonova lightcurve models.

We studied the long-term evolution of ejecta formed in a binary neutron star (BNS) merger that results in a long-lived remnant NS by performing a hydrodynamics simulation with the outflow data of a numerical relativity simulation as the initial condition. At the homologously expanding phase, the total ejecta mass reaches $\approx 0.1\,M_\odot$ with an average velocity of $\approx 0.1\,c$ and lanthanide fraction of ≈ 0.005. We further perform the radiative-transfer simulation employing the obtained ejecta profile. We find that, contrary to a naive expectation from the large ejecta mass and low lanthanide fraction, the optical emission is not as bright as that in GW170817/AT2017gfo, while the infrared emission can be brighter. This light curve property is attributed to preferential diffusion of photons toward the equatorial direction due to the prolate ejecta morphology, large opacity contribution of Zr, Y, and lanthanides, and low specific heating rate of the ejecta. Our results suggest that these light curve features could be used as an indicator for the presence of a long-lived remnant NS. We also found that the bright optical emission broadly consistent with GW170817/AT2017gfo is realized for the case that the high-velocity ejecta components in the polar region are suppressed. These results suggest that the remnant in GW170817/AT2017gfo is unlikely to be a long-lived NS, but might have collapsed to a black hole within $\mathscr{O}(0.1)$ s.

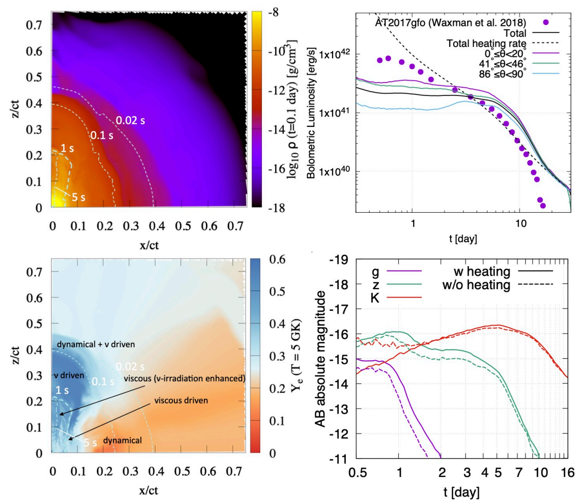

Fig. 6. The left top and bottom panels denote the rest-mass density and electron fraction profile of neutron star merger ejecta, respectively, obtained by the long-term hydrodynamics simulations using the outflow data of a numerical relativity simulation as the initial condition. The right top and bottom panels denote the bolometric and broad-band kilonova light curves calculated by performing radiative-transfer simulations for obtained ejecta profiles.

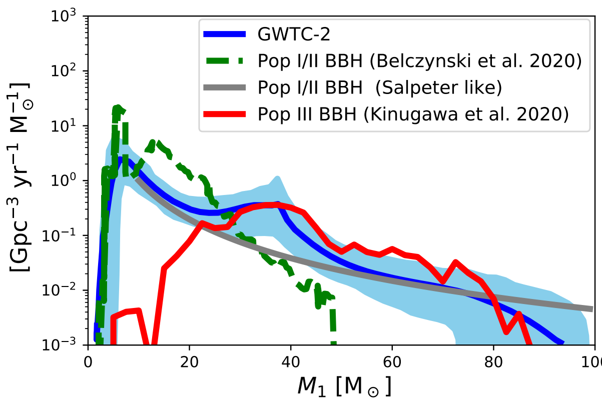

Fig. 7. BBH merger rate density as a function of primary mass (M_1). The blue line and the light blue region are the population distribution and 90% credible interval of the power law + peak model by GWTC-2, respectively. The green dashed line is the Pop I/II BBH merger rate density. The gray line is the Salpeter like power law model ($M_1^{-2.35}$) for Pop I/II BBHs which is normalized by GWTC-2 rate at $M_1 = 10M_\odot$. The red line shows the Pop III BBH merger rate density.

Research Topic 7: Gravitational Wave Astronomy

We perform the binary evolution of zero-metal (population III or Pop III) stars by using population synthesis simulations. We find that Pop III binaries tend to be binary black holes (BBHs) with chirp mass $M_{\rm chirp} \sim 30\ M_\odot$ and they can merge at present day due to long merger time. These Pop III binaries might contribute to some part of the massive BBH gravitational wave (GW) sources detected by aLIGO/aVIRGO (Fig.7). The probability number distribution function of binary black hole mergers observed by LIGO/Virgo O3a has double peaks as a function of chirp mass $M_{\rm chirp}$, total mass $M_{\rm total}$, primary black hole mass M_1, and secondary one M_2, respectively. The larger chirp mass peak is at $M_{\rm chirp} \sim 30M_\odot$. For initial mass functions of Pop III in the form of $f(M) \propto M^{-\alpha}$, population synthesis numerical simulations with $0 \le \alpha \le 1.5$ are consistent with O3a data for $M_{\rm chirp} \gtrsim 20M_\odot$.

We also calculate a binary population synthesis calculation incorporating very massive Pop III stars up to 1500 $M_\odot$ and investigate the nature of BBH mergers. Above the pair-instability mass gap, we find that the typical primary BH mass is 135-340 $M_\odot$. The maximum primary BH mass is as massive as 686 $M_\odot$ (Fig. 8). The BBHs with both of their components above the mass gap have low effective inspiral spin ~ 0. So far, no conclusive BBH merger beyond the mass gap has been detected, and the upper limit on the merger rate density is obtained. If the initial mass function of very massive Pop III stars is simply expressed as $\zeta_m(m) \propto m^{-\alpha}$ (single power law), we find that $\alpha \gtrsim 2.8$ is needed in order for the merger rate density not to exceed the upper limit. In the future, the gravitational wave detectors such as Einstein Telescope and Pre-DECIGO will observe BBH mergers at high redshift. We suggest that we may be able to impose a stringent limit on the Pop III IMF by comparing the merger rate density obtained from future observations with that derived theoretically.

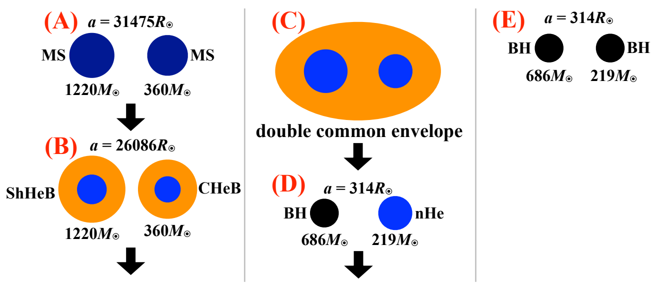

Fig. 8. Evolutionary channel leading to the BBH with the most massive primary BH. 'MS', 'CHeB', 'ShHeB' and 'nHe' stand for the main sequence phase, the core helium burning phase, shell helium burning phase and naked helium star, respectively.

Research Topic 8: Observational Study of Giant Radio Pulses

Giant radio pulses (GRPs) are sporadic bursts emitted by some pulsars that last a few microseconds and are hundreds to thousands of times brighter than regular pulses from these sources. The only GRP-associated emission outside of radio wavelengths is from the Crab Pulsar, where optical emission is enhanced by a few percentage points during GRPs. We observed the Crab Pulsar simultaneously at x-ray and radio wavelengths, finding enhancement of the x-ray emission by $3.8 \pm 0.7\%$ (a 5.4σ detection) coinciding with GRPs. This implies that the total emitted energy from GRPs is tens to hundreds of times higher than previously known.

Research Topic 9: CALET Project

We have joined CALET, CALorimetric Electron Telescope, which is a mission for the Japanese Experiment Module-Exposed Facility (JEM-EF) on the International Space Station. The CALET mission aims at revealing unsolved problems in high energy phenomena of the Universe by carrying out accurate measurements of high energy spectra

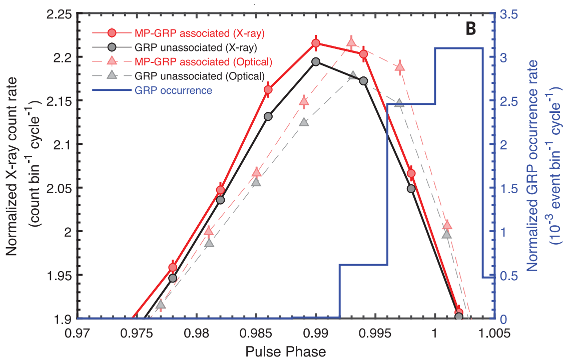

Fig. 9. X-ray and optical pulse profiles of the Crab Pulsar compared with GRPs. Black and red circle symbols connected with solid lines show the x-ray profiles without and with GRP association, respectively, with error bars indicating the 1σ statistical uncertainties (error bars of the black circle and gray triangle points are too small to be visible). The blue histogram shows the GRP occurrence distribution. The faint dashed lines (black and red triangle symbols) show the optical profiles without and with GRP association, respectively, normalized by an arbitrary scaling.

of electrons, gamma-rays and nuclei.

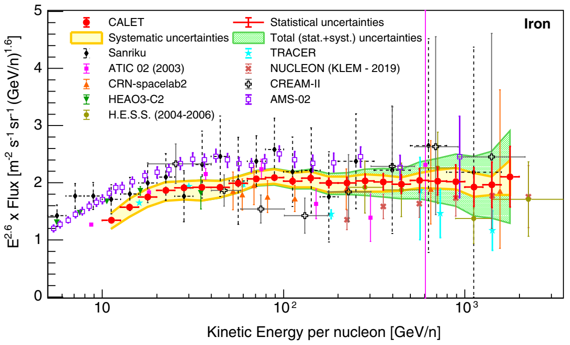

Fig. 10. Iron spectrum measured by CALET (red points).

The energy spectra of iron in cosmic-rays obtained with CALET is shown in Figure 10. The measurement is based on observations carried out from January 2016 to May 2020. The observed differential spectrum is consistent within the errors with previous experiments. In the region from 50 GeV$/n$ to 2 TeV$/n$ our present data are compatible with a single power law with spectral index -2.60 $\pm$ 0.03.

Bibliography

Papers in refereed journals

1. H. Abdalla, R. Adam, F. Aharonian, et al. “H.E.S.S. and MAGIC Observations of a Sudden Cessation of a Very-High-Energy γ-ray Flare in PKS 1510–089 in May 2016”, Astron. Astrophys., 648, A23(22pp) (2021).

2. T. Enoto, T. Terasawa, S. Kisaka, et al. “Enhanced X-Ray Emission Coinciding with Giant Radio Pulses from the Crab Pulsar”, Science, 372, 187-190 (2021)

3. J. C. Algaba, J. Anczarski, K. Asada, et al. “Broadband Multi-Wavelength Properties of M87 during the 2017 Event Horizon Telescope Campaign”, Astrophys. J. Lett., 911, L11(43pp) (2021).

4. Takaaki Kitaki, Shin Mineshige, Ken Ohsuga, Tomohisa Kawashima “The Origins and Impact of Outflow from Super-Eddington Flow”, Pub. Astron. Soc. J., 73, 450-466 (2021).

5. R. Narayan, D. C. M. Palumbo, M. D. Johnson, et al. “The Polarized Image of a Synchrotron-Emitting Ring of Gas Orbiting a Black Hole”, Astrophys. J., 912, 35(26pp) (2021).

6. James O. Chibueze, Haruka Sakemi, Takumi Ohmura, Mami Machida, Hiroki Akamatsu, Takuya Akahori, Hiroyuki Nakanishi, Viral Parekh, Ruby van Rooyen, and Tsutomu T. Takeuchi “Jets from MRC 0600-399 Bent by Magnetic Fields in the Cluster Abell 3376”, Nature, 593, 47-50 (2021).

7. Nanae Domoto, Masaomi Tanaka, Shinya Wanajo, Kyohei Kawaguchi “Signatures of r-Process Elements in Kilonova Spectra”, Astrophys. J., 913, 26(12pp) (2021).

8. Kyohei Kawaguchi, Sho Fujibayashi, Masaru Shibata, Masaomi Tanaka, Shinya Wanajo “A Low-Mass Binary Neutron Star: Long-Term Ejecta Evolution and Kilonovae with Weak Blue Emission”, Astrophys. J., 913, 100(24pp) (2021).

9. Tomoya Kinugawa, Takashi Nakamura, Hiroyuki Nakano “Gravitational Waves from Population III Binary Black Holes are Consistent with LIGO/Virgo O3a Data for the Chirp Mass Larger than $\sim 20M_{\odot}$”, Mon. Not. Roy. Astro. Soc., 504, L28-L33 (2021).

10. V. A. Acciari, S. Ansoldi, L. A. Antonelli, K. Asano, et al. “Multiwavelength Variability and Correlation Studies of Mrk 421 during Historically Low X-Ray and γ-Ray Activity in 2015-2016”, Mon. Not. Roy. Astro. Soc., 504, 1427-1451 (2021).

11. O. Adriani, Y. Akaike, K. Asano, et al. “Measurement of the Iron Spectrum in Cosmic Rays from 10 GeV$/n$ to 2.0 TeV$/n$ with the Calorimetric Electron Telescope on the International Space Station”, Phys. Rev. Lett., 126, 241101(7pp) (2021).

12. Kotaro Hijikawa, Ataru Tanikawa, Tomoya Kinugawa, Takashi Yoshida, Hideyuki Umeda “On the Population III Binary Black Hole Mergers beyond the Pair-Instability Mass Gap”, Mon. Not. Roy. Astro. Soc., 505, L69-L73 (2021).

13. Ataru Tanikawa, Tomoya Kinugawa, Takashi Yoshida, Kotaro Hijikawa, Hideyuki Umeda “Population III Binary Black Holes: Effects of Convective Overshooting on Formation of GW190521”, Mon. Not. Roy. Astro. Soc., 505, 2170-2176 (2021).

14. Yuh Tsunetoe, Shin Mineshige, Ken Ohsuga, Tomohisa Kawashima, Kazunori Akiyama "Polarization Images of Accretion Flow around Supermassive Black Holes: Imprints of Toroidal Field Structure", Pub. Astron. Soc. J., 73, 912-928 (2021).

15. V. A. Acciari, S. Ansoldi, L. A. Antonelli, A. Arbet Engels, M. Artero, K. Asano, et al. "First Detection of VHE Gamma-Ray Emission from TXS 1515–273, Study of its X-ray Variability and Spectral Energy Distribution", Mon. Not. Roy. Astro. Soc., 507, 1528-1545 (2021).

16. M. Janssen, H. Falcke, M. Kadler, et al. "Event Horizon Telescope Observations of the Jet Launching and Collimation in Centaurus A", Nature Astron., 5, 1017-1028 (2021).

17. V. A. Acciari, S. Ansoldi, L. A. Antonelli, A. Arbet Engels, M. Artero, K. Asano, et al. "Investigation of the Correlation Patterns and the Compton Dominance Variability of Mrk 421 in 2017", Astron. Astrophys., 655, A89(36pp) (2021).

18. Kosuke Nishiwaki, Katsuaki Asano, Kohta Murase "Particle Reacceleration by Turbulence and Radio Constraints on Multimessenger High-Energy Emission from the Coma Cluster", Astrophys. J., 922, 190(23pp) (2021).

19. V. A. Acciari, S. Ansoldi, L. A. Antonelli, A. Arbet Engels, M. Artero, K. Asano, et al. "Search for Very High-Energy Emission from the Millisecond Pulsar PSR J0218+4232", Astrophys. J., 922, 251(14pp) (2021).

20. C. B. Adams, W. Benbow, A. Brill, et al. "Observation of the Gamma-Ray Binary HESS J0632+057 with the H.E.S.S., MAGIC, and VERITAS Telescopes", Astrophys. J., 923, 241(30pp) (2021).

21. K. Satapathy, D. Psaltis, F. Ozel, et al. "The Variability of the Black-Hole Image in M87 at the Dynamical Time Scale", Astrophys. J., 925, 13(19pp) (2022).

22. Katsuaki Asano, Yoichi Asaoka, Yosui Akaike, Norita Kawanaka, Kazunori Kohri, Holger M. Motz, Toshio Terasawa "Monte Carlo Study of Electron and Positron Cosmic-Ray Propagation with the CALET Spectrum", Astrophys. J., 926, 5(10pp) (2022).

23. Ataru Tanikawa, Takashi Yoshida, Tomoya Kinugawa, Alessandro A. Trani, Takashi Hosokawa, Hajime Susa, Kazuyuki Omukai "Merger Rate Density of Binary Black Holes through Isolated Population I, Ⅱ , Ⅲ and Extrmely Metal-Poor Binary Star Evolution", Astrophys. J., 926, 83(21pp) (2022).

24. I. Cho, G.-Y. Zhao, T. Kawashima, et al. "The Intrinsic Structure of Sagittarius A* at 1.3 cm and 7 mm", Astrophys. J., 926, 108(17pp) (2022).

25. V. A. Acciari, S. Ansoldi, L. A. Antonelli, A. Arbet Engels, M. Artero, K. Asano, et al. "Multiwavelength Study of the Gravitationally Lensed Blazar QSO B0218+357 between 2016 and 2020", Mon. Not. Roy. Astro. Soc., 510, 2344-2362 (2022).

26. V. A. Acciari, T. Aniello, S. Ansoldi, L. A. Antonelli, A. Arbet Engels, M. Artero, K. Asano, et al. "Investigating the Blazar TXS 0506+056 through Sharp Multiwavelength Eyes during 2017–2019", Astrophys. J., 927, 197(15pp) (2022).

27. Tomohisa Kawashima, Seiji Ishiguro, Toseo Moritaka, Ritoku Horiuchi, Kohji Tomisaka "Mushroom-Instability-Driven Magnetic Reconnections in Collisionless Relativistic Jets", Astrophys. J., 928, 62(10pp) (2022).

28. V. A. Acciari, S. Ansoldi, L. A. Antonelli, A. Arbet Engels, M. Artero, K. Asano, et al. "Combined Searches for Dark Matter in Dwarf Spheroidal Galaxies Observed with the MAGIC Telescopes, Including New Data from Coma Berenices and Draco", Phys. Dark Uni., 35, 100912(10pp) (2022).

Other Activities

Ashra NTA

[Spokesperson : M. Sasaki]

Collaboration list:
ICRR, The University of Tokyo, Chiba, Japan: **M. Sasaki, T. Aoki**; Physics Department, Toho University, Chiba, Japan: **S. Ogawa**; Academia Sinica, Taipei, Taiwan: **S. Haino**; Institute for Interdisciplinary Science, Okayama University, Okayama, Japan: **K. Yoshimura**; IPNS, KEK, Ibaraki, Japan: **M. Tanaka**; et al.

VHE Physics and Astronomy

Very-high energy (VHE) physics is the development of a higher energy frontier that is complementary to HEP using accelerators to investigate interactions in space caused by fundamental particles and to study the structure and fundamental interactions of elementary particles. Probing for VHE elementary particles will also enable the discovery of VHE celestial objects and the elucidation of their phenomena. In VHE objects, 1st- and 2nd-generation neutrinos should be emitted with photons from the process by accelerated protons, but they remain unidentified. Comparison of VHE neutrino and photon flux spectra from the same object will also allow for fundamental particle physics and cosmological investigations. VHE neutrinos and photons can also probe super heavy dark matter and dark energy.

Neutrinos and photons are well-known subatomic particles from the Standard Model and travel straight in magnetic fields, making them powerful probes for ultra-high-energy particle physics astronomy (VHEPA). Neutrino oscillations cause neutrino fluxes to homogenize between generations during propagation. Tau neutrino observations are also tau appearance experiments. VHE tau neutrinos skim the earth, are converted to tau, and after decaying in air become an upward air shower at a shallow elevation angle, emitting Cherenkov light and fluorescence. The NTA unit is a unique wide-angle, high-precision optical system with a light-branching trigger imaging system. This detection scheme is particularly powerful for the simultaneous observation of Cherenkov light and fluorescence from VHE tau and photons.

NTA for VHE Tau and Photon probes

NTA will radially observe air-shower light in a vast amount of night-time air on the mountain within more than π sr field of view covered with 1 minute square pixels [1]. Earth-skimming or mountain-hitting tau neutrino is converted to tau in the rock, and tau decays make upward air shower. The upward tau shower signal is very clear and there are almost no background events. Downward coming photon showers are observed in both Cherenkov and fluorescence light. The Cherenkov light coming from a large zenith angle earns a large effective detection area. The lookout layout allows Cherenkov and fluorescence observations over a wide energy range. Due to the narrow Cherenkov cone of the tau shower, distance is needed to gain effective area. But fluorescence is useful for observing near showers coming from behind. The Xmax is at a distance of roughly 1km from the detector, and even 1-PeV class taus can be detected as shown here. This is a good advantage of look-out layout on the mountain.

The geo-propagation of tau by GEANT and ALLM simulations revealed emergent tau remembers the tau neutrino direction above 1 PeV with much better than 1 minute of accuracy. We also confirmed shower reconstruction with CORSIKA simulation, resulting in the point-back resolution of $0.1^\circ/\sqrt{E_{sh}/PeV}$ where E_{sh} is the shower energy. The emergent tau energy is deformed from the parent tau neutrino energy due to the inelastic nature of the charge current interaction and energy loss in the rock. But it still allows for a relatively good energy reconstruction of ν_τ with the energy around 1 PeV. We confirmed energy resolution of nu-tau with ANIS simulation, resulting in 20 or 40 % around 1 PeV depending on the elevation angle.

Regarding the NTA's view of the southern sky, NTA can always cover the Galactic bulge of the night sky (Figure 11 upper). The NTA detector unit's field of view center should be aligned with this arc, considering a high multi-eye observation ratio.

NTA Galactic bulge monitor with viewing radius of 20 degrees has a good advantage of including 12 % of total mass of the dark matter halo, which corresponds to mass of 3×10^{56} GeV assuming the Einasto profile. The effective detection area of the surface detector has a geometrical problem of the COS-dependent at large zenith angle. These plots are the accumulated sums of annual galactic center observation hours per altitude angle. In the NTA case, galactic center is in the moonless night sky for 980 hours in a year. In the case of a detector at 16.4 degrees south latitude and a 45 degrees zenith angle cut, the observation time must be less than 2300 hours per year even if 100 % duty cycle. The factor is roughly 2.3.

NTA proto-project, Ashra-1, was placed in 2008 at the north side (Figure 11 bottom). It allows for binocular and trinocular observation, resulting in a high multi-eye observation rate. The basic design is a 1.5-fold scaled-up version of the Ashra-1 light collector, and four of these collectors are stacked together to form one NTA detector unit with the same field of view (Figure 12). The effective pupil diameter is 3 m, providing good light gathering power. It can also facilitate

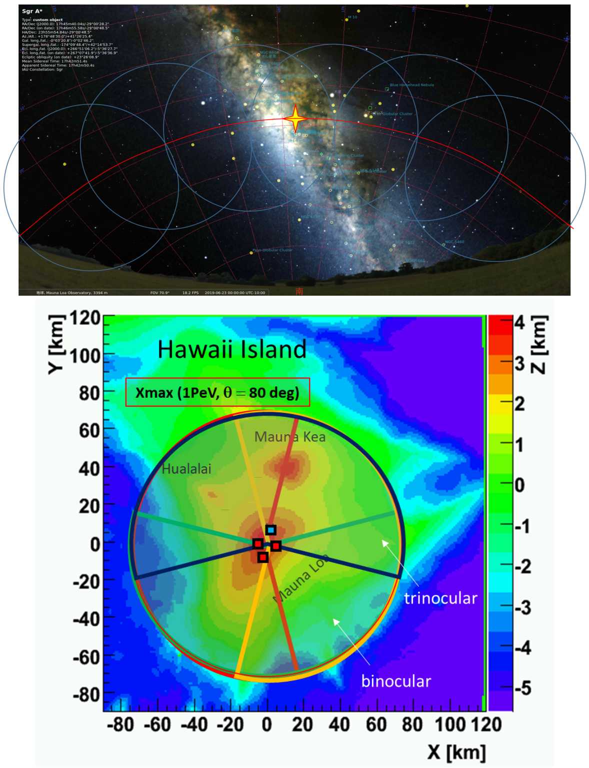

Fig. 11. Superimposed on the image of the Milky Way galaxy, the position and orbit of the galactic center is represented by a yellow cross and red arc (*top*). The contour map of Hawaii Island is input to our MC simulation (*bottom*). The radius of the wheel represents the distance to Xmax of the 1PeV shower coming toward NTA at 80 degrees zenith. Four stations will be placed on the mountainside. One station is responsible for 210 degree azimuth range indicated by four fans.

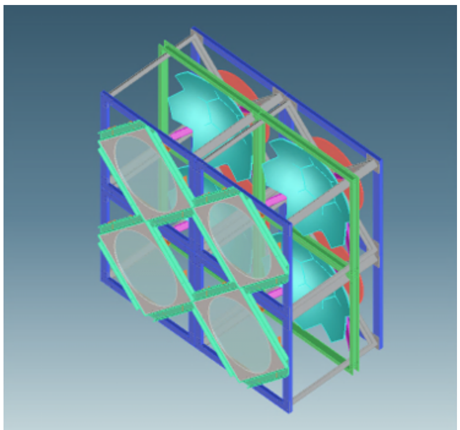

Fig. 12. The basic design is a 1.5-fold scaled-up version of the Ashra-1 light collector, and four of these collectors are stacked together to form one NTA detector unit with the same field of view.

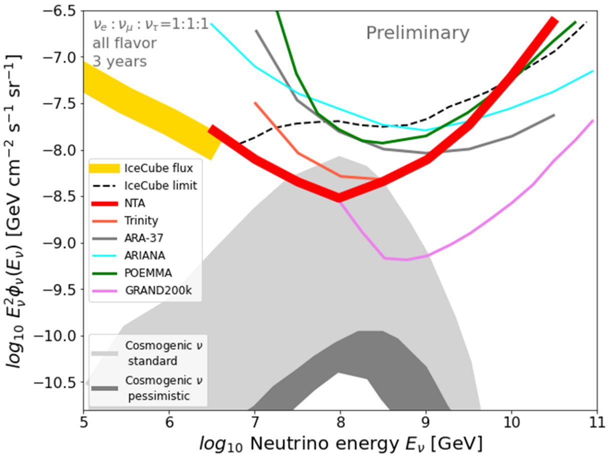

Fig. 13. A comparison of diffuse neutrino sensitivity from various VHE neutrino detectors. NTA has the best sensitivity from a few PeV to 100 PeV [2]-[11].

background muon rejection, transport and construction.

NTA Diffuse Neutrino Sensitivity

Figure 13 shows a comparison of diffuse neutrino sensitivity from various VHE neutrino detectors. NTA has the best sensitivity from a few PeV to 100 PeV. Trinity observes Earth skimming neu-tau as well as NTA but only with Cherenkov light. The sensitivity of its higher energy part is determined by the large zenith angle shower, which is consistent with NTA. The NTA sensitivity at lower energy is superior to that of Trinity due to the tau shower fluorescence observed near the mountain surface as mentioned earlier.

Conclusions

This is the era of synergy between HEP and VHEP. The energy front around the unitarity bound interesting e.g. super heavy dark matter. Combined detection of PeV tau and photons will open up more comprehensive studies of VHEP and VHEA. NTA is most sensitive to PeV tau (ν) and photon, with good coverage and accuracy, which will take over important results from TeV and pass more developed results to EeV.

Bibliography

[1] NTA LOI (look-in layout array), M. Sasaki and G. W.-S. Hou,ArXiv:1408.6244 (2014). NTA look-out layout summit array, M. Sasaki, PoS (ICRC2017) 941. M. Sasaki, ICHEP2022.

[2] J. Álvarez-Muñiz,et al.,Mechanics and Astronomy 63, 219501 (2019).

[3] J. F. Krizmanic,et al.,UHECR2018 (Paris).

[4] C. R. Persichilli,Thesis,Univ. California (2018).

[5] P. Allison,et al.,Phys. Rev. D93, 082003 (2016).

[6] R. A. Batista,et al.,J. Cosmol. Astropart. Phys., 01, 002, (2019).

[7] M. Aartsen,et al.,Phys. Rev. D98,062003 (2018).

[8] A. Aab,et al.,arXiv:1708.06592.

[9] P. Gorham,et al.,arXiv:1902.04005.

[10] A. M. Otte,Phys. Rev. D99, 083012 (2019).

[11] M. Sasaki,PoS (ICRC2019) 1003.

γI Group

γI Project

γI Consortium

[Spokesperson : R.Enomoto]

Collaboration list:

ICRR, The University of Tokyo, Chiba, Japan: **R. Enomoto**; National Institute of Technology, Sendai College, Miyagi, Japan: **M. Kagaya**; College of Science, Ibaraki University, Ibaraki, Japan: **H. Katagiri, R. Kimijima, K. Harada, K. Yoshida**; Faculty of Medical Engineering and Technology, Kitasato University, Kanagawa, Japan: **H. Muraishi, S. Ishikawa**; IPNS, High Energy Accelerator Research Organization, Ibaraki, Japan: **M. M. Tanaka**; National Cancer Center Hospital East, Chiba, Japan: **D. Kano, T. Watanabe**

Overview

We have conducted a feasibility study of a gamma-ray imager specializing in de-excitation lines with energies in the range of 2–10 MeV that is capable of searching for low-energy cosmic rays around 1 GeV. The imager is an electron-tracking Compton camera using scintillation fibers. The principal investigator of this project is H. Katagiri of Ibaraki University. First, we developed a small prototype camera in 2018 and a realistic simulation model based on the Geant4 simulation toolkit. Using the simulation model and environmental cosmic-ray muon data, we developed a method for reconstructing tracks of charged particles and an energy calibration method. We also designed and developed a large prototype camera which allows us to investigate the multiple scattering events of gamma rays, and evaluated the performance of a CMOS camera on the gamma-ray imager. Note that we applied for a patent for reconstructing the energy and direction of gamma rays, which was found when designing the large camera. In this report, we first show the background and purpose of the research. Then, we describe the concept and design of the gamma-ray camera and finally report the current status.

1 Background and purpose

The question of where and how cosmic rays in our galaxy are accelerated is a long-standing important issue in astroparticle physics. The major part of Galactic cosmic rays is thought to be accelerated in blast waves of supernova remnants (SNRs), but until now it has not been completely solved. To study such hypothesis, it is important to observe the gamma rays produced by the interaction of cosmic rays in SNRs with the surrounding material. To date, gamma rays in TeV energies from SNRs have been detected by imaging atmospheric Cherenkov telescopes (e.g., [1], [2], [3], [4], [5]), and GeV gamma rays from several tens of SNRs have been discovered by the Large Area Telescope (LAT) on board the Fermi Gamma-ray Space Telescope (Fermi) (e.g., [6]). Recently, the detection of the gamma-ray emission from the SNR G106.3+2.7 above 100 TeV was reported by Tibet ASγ Collaboration [7]. These observations have indicated particle acceleration in GeV to PeV energies in SNRs in our Galaxy.

However, some of the fundamental problems remain in the research of Galactic cosmic-ray. The followings are some of the key questions. (1) Are high-energy particles in SNRs really cosmic-ray nuclei? Gamma rays have been detected in many SNRs, but for most SNRs, we cannot firmly rule out the possibility that they come from cosmic-ray electrons. Currently, one of the most direct evidences of cosmic-ray nuclei in an SNR is the detection of gamma rays from decays of π^0 particles generated by the interaction between cosmic-ray nuclei and interstellar material by the LAT instrument on board the Fermi observatory (e.g., [8]). A spectrum of π^0-decay gamma rays has a characteristic broad peak around 70 MeV (Figure 14), but since the lower detection threshold of the LAT instrument is around 60 MeV, such peak shapes have not been clearly investigated. In addition, since the effective area of

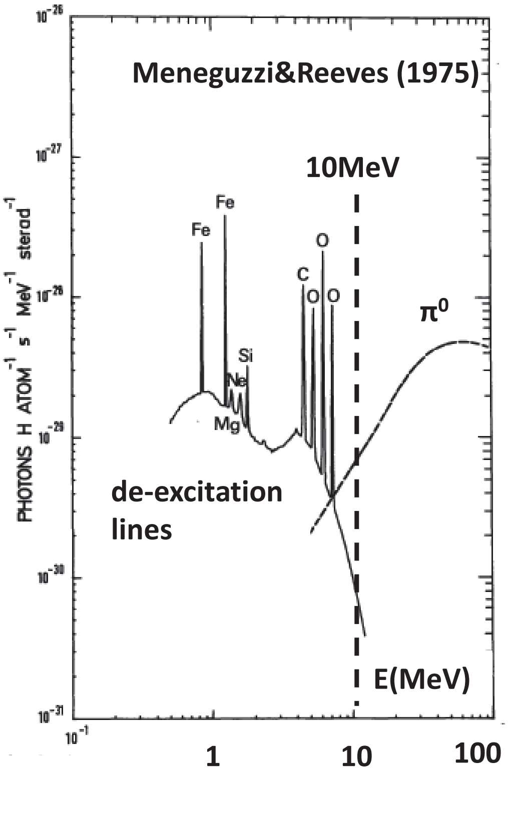

Fig. 14. Predicted gamma-ray emissivity from the interaction of Galactic cosmic rays with the interstellar gas [9].

the LAT decreases sharply below 100 MeV, the search for π^0 decay gamma rays is restricted to only very bright gamma-ray-emitting SNRs. (2) Is the cosmic-ray energy budget of the Milky way mainly explained by SNRs? At present, gamma-ray observations have revealed that particle acceleration operates in many SNRs, thus the cosmic-ray energy budget seems to be satisfied given that the particles accelerated in the SNRs are mainly cosmic-ray nuclei. However, it should be noted that π^0-decay gamma rays are not generated unless protons have a momentum of above $\sim$ 1 GeV/c, and they are not sensitive to low-energy cosmic rays below 1 GeV. They can be responsible for a substantial part of the energy density of cosmic rays based on the measurements beyond the heliopause by Voyager 1 [10], which are thought to be free of solar modulation, but currently, there is no direct probe for low-energy cosmic rays more distant from the Earth.

The observation of de-excitation line gamma rays can be a smoking gun to solve the questions (1) and (2) in the cosmic-ray research. Such lines with the energy of several hundred keV to about 10 MeV seen in Figure 14 are produced when low-energy cosmic rays and the interstellar matter interact. However, it is difficult to identify those below 2 MeV because the spectrum in these energy ranges is contaminated by nuclear gamma-ray lines from radioactive decay of unstable isotopes produced in massive star or supernova nucleosynthesis. Therefore, we will develop a gamma-ray imager specializing in de-excitation lines in 2–10 MeV energies that is capable of searching for low-energy cosmic rays around 1 GeV and verify its performance experimentally. The proposed gamma-ray imager in this report is an electron-tracking Compton camera using scintillation fibers.

2 Concept and design of the electron-tracking Compton camera using scintillation fibers

The purpose of this study is to develop a gamma-ray camera specializing in de-excitation lines in 2–10 MeV energies and to verify its performance experimentally. In this subsection, we describe the concept and design of our electron-tracking Compton camera using scintillation fibers.

A Compton camera utilizes the Compton scattering process, which is the dominant gamma-ray interaction in 2–10 MeV energies. It allows us to measure the distribution of gamma rays in these energies with a wide field of view without using any heavy shielding or collimator. The Imaging Compton Telescope (COMPTEL) on board the Compton Gamma-ray Observatory (CGRO [11]) was the first major application of a Compton camera for MeV gamma-ray astronomical observations in the 1990s. However, no observational evidence for the de-excitation lines from an SNR was found, and the predicted flux is close to the level of the COMPTEL sensitivity [12]. Measuring the track of a recoil electron produced by Compton scattering is one of the powerful methods to reduce a substantial amount of the background and improve the detection sensitivity dramatically. The left figure in Figure 15 illustrates a method used in searching for a radiation source using a conventional Compton camera. The directions of gamma rays are determined by Compton kinematics from the energies deposited in the scatterer and absorber. With this method, the direction of a gamma ray can be limited to a ring shape (the left figure in Figure 16) but cannot be determined uniquely. Thus, the background increases due to the contamination from other radiation sources. If a detector with high positional resolution is adopted as a scatterer, the direction of a gamma ray

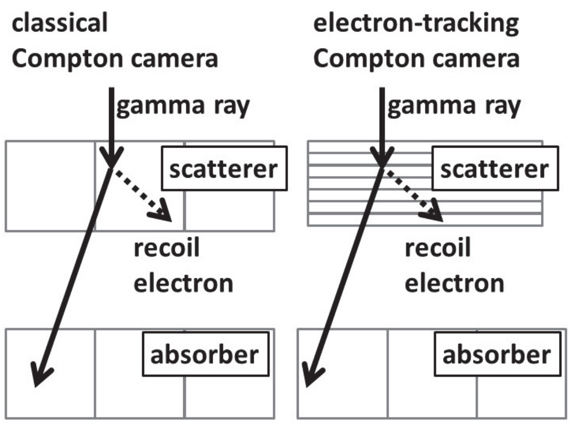

Fig. 15. Schematic diagram of Compton reconstruction: (left) without the electron-track information and (right) with the electron-track information.

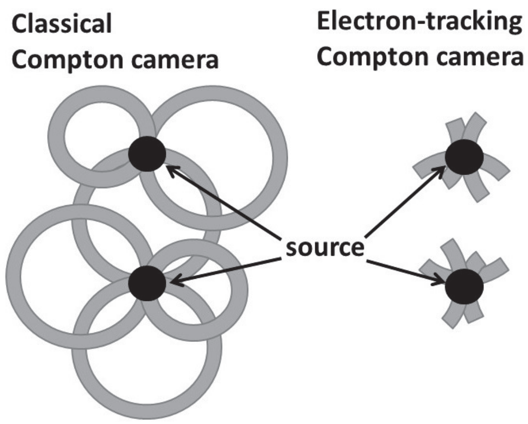

Fig. 16. Schematic explanation of Compton reconstruction: (left) without the electron-track information, (right) with the electron-track information.

can be uniquely determined event by event by capturing the direction of a recoil electron as shown in the right figures in Figure 15 and Figure 16 (electron-tracking Compton camera) respectively. We are conducting the feasibility study of an electron-tracking Compton camera using scintillation fibers. Scintillation fibers can achieve a large fiducial volume inexpensively with positional resolution of a few hundreds of μm although the energy resolution is limited. The schematics of the measurement system is shown in Figure 17. The system of the camera under development is described in detail below.

Multilayer fiber plates

A single fiber plate is composed of many fibers, and each plate is stacked and rotated 90° with respect to the one above or below to obtain a three-dimensional position. The track length of a recoil electron with respect to a 4.4 MeV gamma ray, which is expected to come from astronomical objects with the highest intensity among de-excitation gamma-ray lines, is about 5 mm at a scattering angle of 15°. The smaller diameter of the fiber we adopt, the more accurate tracking is possible, enabling us to reconstruct gamma-ray events with a small recoil energy, which corresponds to a small scattering angle.

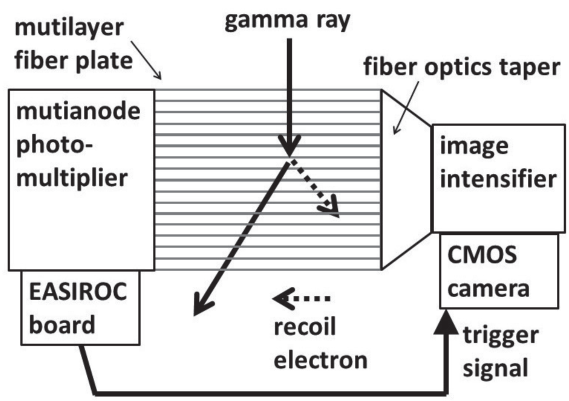

Fig. 17. Schematic view of the measurement system of a prototype camera.

However, both the cost and the difficulty in manufacturing increase with increasing number of readout channels; therefore we adopted 1 mm fiber in this feasibility study. The cross-sectional shape of the available commercial fibers is round or square. We adopted square fibers because they can have high light collection efficiency from their geometry. With a positional accuracy of 1 mm, it is possible to detect the direction of a recoil electron even for low-energy gamma rays (e.g., 1.3 MeV) that can be easily used in a laboratory when a scattering angle is relatively large.

Photodetector and readout system

When the diameter of the fiber is 1 mm, it is necessary to realize the readout of $32 \times 64 = 2048$ fibers equipped with signal amplification to capture faint lights from these fibers. To achieve that, we will build a system that combines an image intensifier and a high-speed readout CMOS camera. Since the diameter of an effective area of the available image intensifier is 17 mm, which is smaller than the fiber plates, fiber optics tapers are used to guide the light from the fiber plates. Photodetectors such as a multianode photomultiplier tube (MAPMT) and a multi-pixel photon counter (MPPC) array are equipped to the other end of the fiber plates to generate a trigger signal for the CMOS camera and to provide a crude spatial distribution of the energy depositions of the fiber plates complementary to the image intensifier.

3 Current status

Development of calibration and analysis methods using the first small prototype camera

To develop the camera mentioned above, first we developed the small prototype camera in 2018 with a limited budget to conduct the pilot studies such as reconstruction of tracks of charged particles and energy calibration. The first camera consists of 8×8 fibers without an optical taper (Figure 18) where the size and shape of the fibers are 1 mm square. Scintillation photons produced in the fibers are directly read out by a 64-channel MPPC array.

Due to its small size, the range of the scattering angle that can be verified is limited, and impossible to verify multiple scattering events. However, since the system is simple and

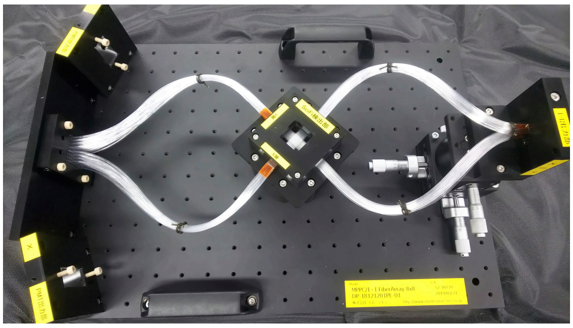

Fig. 18. Photograph of the first prototype camera.

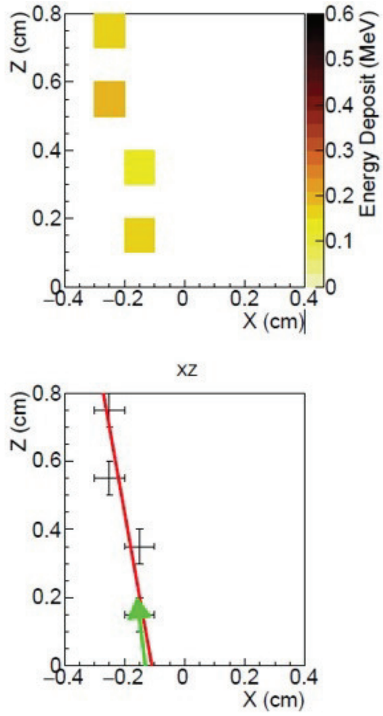

Fig. 19. Images of a simulated cosmic-ray muon event. Top: Distribution of energy deposited by the fibers as seen from the X-layer direction. Note that there are blanks for Y layers because the X and Y layers overlap alternately. Bottom: Reconstruction of a muon track based on the positions of the hit fibers. The solid line represents the reconstructed direction of the track, whereas the green arrow represents the true incident position and direction of the muon.

small, this detector is appropriate for developing calibration and analysis methods. First, we started to build a Compton camera system by combining detectors that serve as absorbers. The absorbers are GAGG(Ce) scintillators with the size of 1 cm cube, which have a short decay time of scintillation light, leading to precise coincidence between the scatterer and absorber. Also, they have high light yield and are expected to have a good energy resolution. We adopted GAGG(Ce) with a shorter decay time of 50 ns than typical ones. We developed an offline analysis program to derive the energy resolution of the GAGG(Ce) scintillators by measuring the energy spectrum of 662 keV gamma rays from ^{137}Cs.

Additionally, to develop an analysis algorithm for actual data, we constructed a realistic simulation model with the Geant4 simulation toolkit [13]. We have developed a simple track reconstruction algorithm based on cosmic-ray muon events (Figure 19). We also developed a method of energy calibration of the fiber plates by simulating cosmic-ray muons and comparing their spectrum of energy deposited in the fiber plates with actual measurements (Figure 20).

Detailed design study and development of the second prototype camera

First, we examined candidate scintillation fibers in detail. The fiber is 1 mm square, and we selected BCF-20 (Saint Gobain) that emits green light that matches the wavelength response of the GaAsP photocathode of an image intensifier used. Furthermore, the reflective surface of the fiber has a two-layer structure known as multi-clad, which has a high light collection efficiency. Using our developed Geant4 particle simulation and the large-scale computer system of the Institute for Cosmic Ray Research (ICRR) at the University of Tokyo, we evaluated the size of the detector within the limited budget where practical measurements are possible with a faint radioactive source in the laboratory. The size is 32 mm $\times$ 32 mm $\times$ 64 mm with the detection efficiency to verify multiple scattering events. Finally, we made the second large prototype camera (Figure 21), where only the lower half of the multilayer fiber plates was manufactured due to the limited budget, and the upper half will be added this year. Also, we applied for a patent for reconstructing the energy and direction of gamma rays, which was found when designing the large camera.

We also developed a signal polarity inversion board for the EASIROC signal readout module used to read out the signals generated by MAPMTs. Since the EASIROC ASIC chip responds only to positive signal inputs, polarity inversion is required to read out negative MAPMT signals. We selected a chip transformer with less signal loss and distortion, and developed a multi-channel signal inversion board. We investigated the distortion of the waveform and frequency response with respect to the input signal, and confirmed that it is acceptable to the use in the camera.

The evaluations of the performance of the CMOS camera such as noise level for each pixel, dynamic range, and delay time due to an external trigger for the image intensifier were conducted and we confirmed that it can be used in the feasibility studies.

Acknowledgments

This study was supported by JSPS KAKENHI Grant Numbers JP19H01919, JP22K03647, a Grant-in-Aid “Research Booster” from Ibaraki University, and a Grant-in-Aid from Takahashi Industrial and Economic Research Foundation. This work was partially carried out by the joint research program of the Institute for Cosmic Ray Research (ICRR), the University of Tokyo. We would like to thank the Open source consortium of instrumentation (Open-It), Japan for its support and Enago (www.enago.jp) for its English language review. We thank T. Yoshida and S. Yanagita at Ibaraki University for useful comments. We also thank M. Kobayashi, Z. Jiang and

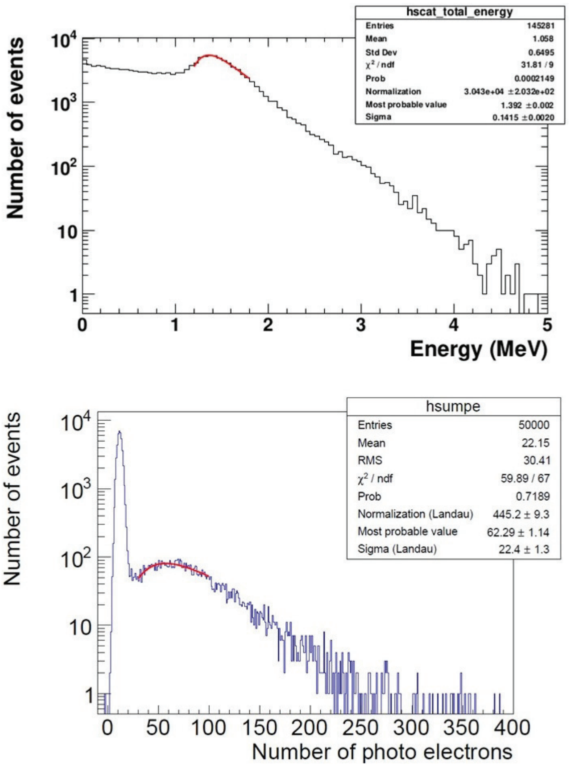

Fig. 20. Energy spectra of cosmic-ray muons: (top) simulation, (bottom) actual measurement. The actual measurement can include signals other than cosmic-ray muons.

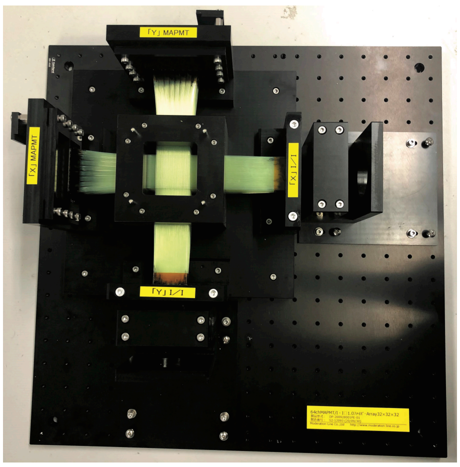

Fig. 21. Photograph of the second prototype camera.

Y. Kawashima at Ibaraki University for their help.

Bibliography

[1] Evidence for TeV gamma-ray emission from the shell type SNR RX J1713.7-3946, Muraishi, H., Tanimori, T., Yanagita, S., et al., Astronomy and Astrophysic, 354, L57 (2000)

[2] The acceleration of cosmic-ray protons in the supernova remnant RX J1713.7-3946, Enomoto, R., Tanimori, T., Naito, T., et al., Nature, 416, 823 (2002)

[3] Detection of Gamma Rays around 1 TeV from RX J0852.0-4622 by CANGAROO-II, Katagiri, H., Enomoto, R., Ksenofontov, L. T., et al. , 619, L163 (2005)

[4] Observation of VHE γ-rays from Cassiopeia A with the MAGIC telescope, Albert, J., Aliu, E., Anderhub, H., et al., Astronomy and Astrophysics, 474, 937 (2007)

[5] Population study of Galactic supernova remnants at very high γ-ray energies with H.E.S.S., H. E. S. S. Collaboration, Abdalla, H., Abramowski, A., et al. 2018, Astronomy & Astrophysics, 612, A3. doi:10.1051/0004-6361/201732125

[6] The First Fermi LAT Supernova Remnant Catalog, Acero, F., Ackermann, M., Ajello, M., et al. 2016, Astrophysical Journal Supplement Series, 224, 8. doi:10.3847/0067-0049/224/1/8

[7] Potential PeVatron supernova remnant G106.3+2.7 seen in the highest-energy gamma rays, Tibet ASγ Collaboration, Amenomori, M., Bao, Y. W., et al. 2021, Nature Astronomy, 5, 460. doi:10.1038/s41550-020-01294-9

[8] Detection of the Characteristic Pion-Decay Signature in Supernova Remnants, Ackermann, M., Ajello, M., Allafort, A., et al. 2013, Science, 339, 807

[9] Nuclear gamma ray production by cosmic rays, Meneguzzi, M. & Reeves, H., 1975, A&A, 40, 91

[10] Galactic Cosmic Rays in the Local Interstellar Medium: Voyager 1 Observations and Model Results, Cummings, A. C., Stone, E. C., Heikkila, B. C., et al. 2016, Astrophysical Journal, 831, 18

[11] Instrument Description and Performance of the Imaging Gamma-Ray Telescope COMPTEL aboard the Compton Gamma-Ray Observatory, Schoenfelder, V., Aarts, H., Bennett, K., et al. 1993, Astrophysical Journal Supplement, 86, 657. doi:10.1086/191794

[12] Nuclear de-excitation line spectrum of Cassiopeia A, Summa, A., Elsässer, D., & Mannheim, K. 2011, Astronomy & Astrophysics, 533, A13. doi:10.1051/0004-6361/201117267

[13] Geant4–a simulation toolkit, Agostinelli, S., Allison, J., Amako, K., et al. 2003, Nuclear Instruments and Methods in Physics Research A, 506, 250. doi:10.1016/S0168-9002(03)01368-8

ASTROPHYSICS AND GRAVITY DIVISION

Overview

Astrophysics and Gravity Division consists of Gravitational Wave Group, The Observational Cosmology Group, Primary Cosmic Ray Group and Theory Group.

The Gravitational Wave Group conducts experimental research of gravitational waves with researchers of gravitational wave experiments and theory in Japan. The main items are the construction of the large-scale cryogenic interferometer (KAGRA) at Kamioka underground and the operation of CLIO. For this purpose, KAGRA observatory was established at the beginning of the fiscal year of 2016 to assist the construction of KAGRA gravitational wave telescope.

The Observational Cosmology Group studies cosmic history based on deep multi-wavelength observations in collaboration with worldwide researchers. This group has started a new optical deep survey project with the wide-field imager of Hyper Suprime-Cam mounted on the Subaru telescope.

Theory Group conducts both theoretical studies of the Universe and astroparticle physics.

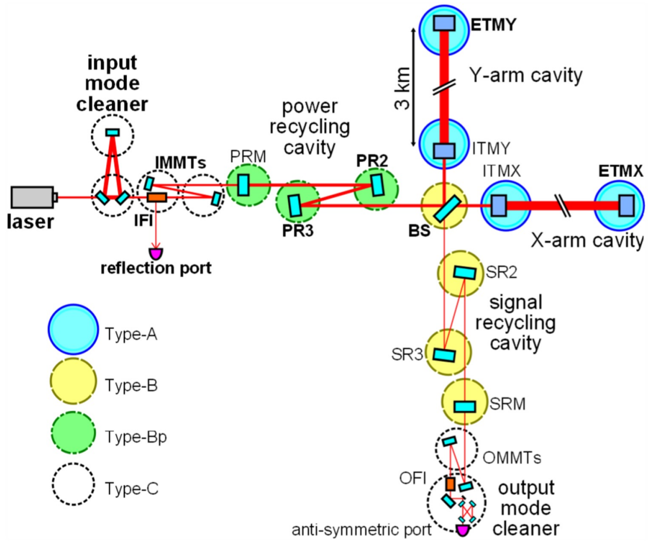

Fig. 1. Schematic view of the bKAGRA interferometer[3]. Type-A, Type-B, Type-Bp, and Type-C are the names of vibration isolation systems for each mirror.

Gravitational Wave Group

KAGRA Project Status

[Spokesperson : Takashi UCHIYAMA]

ICRR, The Univ. of Tokyo, Hida, Gifu 506-1205

Overview

KAGRA, Large-scale Cryogenic Gravitational wave Telescope, aims at detecting gravitational waves and developing gravitational wave astronomy, which was established by the first detection of gravitational waves by LIGO. KAGRA employs a 3 km L-shaped laser interferometer with a cryogenic mirror system placed underground at Kamioka[1]. The KAGRA development is divided into two stages: the initial KAGRA (iKAGRA) and baseline KAGRA (bKAGRA). The iKAGRA interferometer is a simple Michelson interferometer with a 2-Watt laser, room-temperature mirrors, and a simple vibration isolation system. We completed the iKAGRA interferometer with a test run in April 2016[2]. Then we proceeded to bKAGRA.

Figures 1 and 2 show a schematic view of the optical layout of the bKAGRA interferometer and the KAGRA vibration isolation systems. Table 1 shows design parameter of the bKAGRA interferometer[3]. The bKAGRA interferometer will employ a Resonant Sideband Extraction (RSE) interferometer with a 180-Watt laser, cryogenic Sapphire mirrors, and several kinds of vibration isolation systems. The bKAGRA interferometer should attain a sensitivity high enough for the detection of gravitational waves with the help of the high power laser and RSE interferometer to reduce the quantum noise, the cryogenic Sapphire mirrors to reduce the thermal noise, and the vibration isolation systems to reduce the seismic noise. Figure 3 shows designed sensitivities of bKAGRA in the cases of Broadband RSE (BRSE) and of Detuned RSE (DRSE), where the incoherent sum of the fundamental noise sources is assumed. The observation range for an inspiral and merger of neutron-star binary reaches 135 Mpc in BRSE and 153 Mpc in DRSE with the same definition of the observation range as LIGO and Virgo.

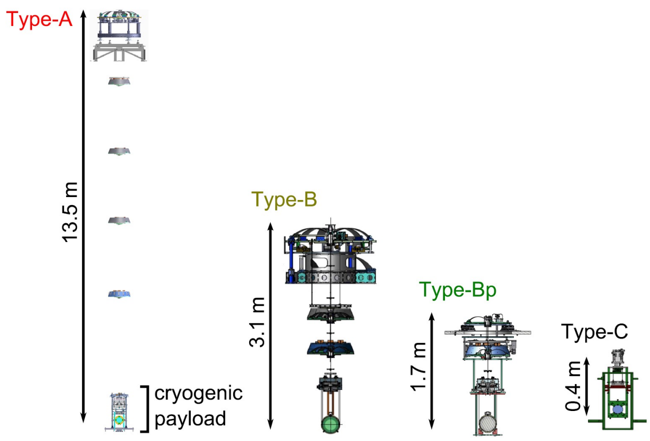

Fig. 2. KAGRA vibration isolation systems[3]. KAGRA equips four kinds of vibration isolation systems as Type-A, Type-B, Type-Bp, and Type-C.

The KAGRA observatory signed the three documents between LIGO and VIRGO in order to realize international joint

Table 1. The design parameters of the bKAGRA interferometer[3].

Arm cavity length	3000 m	Test mass size	ϕ22 cm $\times$ 15 cm
Laser wave length	1064 nm	Mass of test mass	22.8 kg
Input power at PRM	67W	Temperature of test mass	22 K
Arm intra-cavity power	340 kW	Beam radius at test mass	3.5 cm
ITM transmittance	0.4 %	PRC/SRC lengths	66.6 m
PRM transmittance	10 %	Detuning angle	3.5 deg
SRM transmittance	15 %	Homodyne angle	135.1 deg

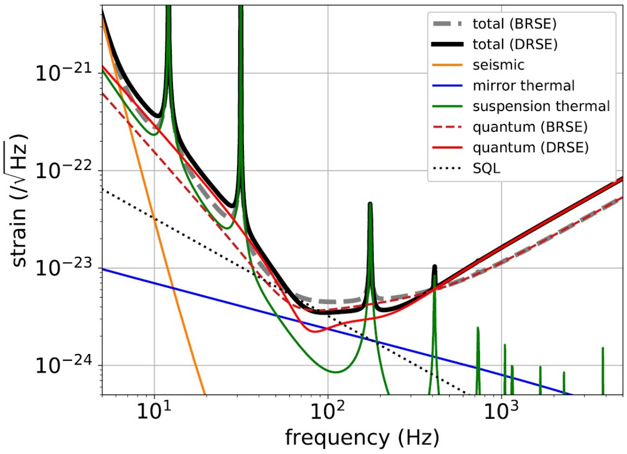

Fig. 3. The designed sensitivity of the bKAGRA interferometer[3]. "total", "seismic", "mirror thermal", "suspension thermal", "quantum", and "SQL" mean total sum of fundamental noise sources shown in this figure, seismic noise including gravity gradient noise, mirror thermal noise, suspension thermal noise, quantum noise, and standard quantum limit, respectively. The figure shows "total" and "quantum noise" in both Broadband RSE (BRSE) and Detuned RSE (DRSE) cases. Observation range for an in-spiral and merger of neutron-star binary reaches 135 Mpc in BRSE and 153 Mpc in DRSE with the same definition of the observation range as LIGO and Virgo.

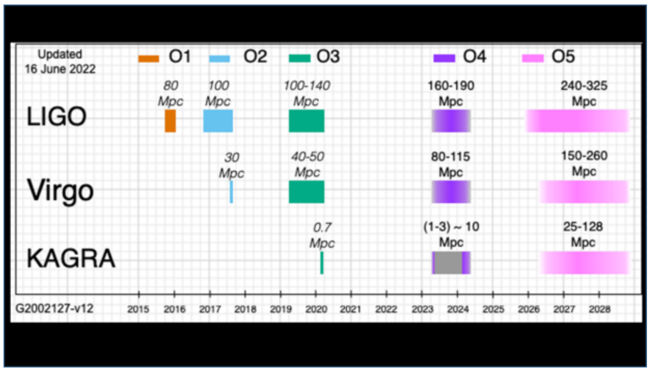

Fig. 4. International observation scenario[7]. The next international collaborative observation called O4 will be started from March 2023 as of June 17, 2022.

observation on October 4, 2019. The documents are the Memorandum of Agreement between VIRGO, KAGRA, and LIGO (main part)[4], Memorandum of Agreement between VIRGO, KAGRA, and LIGO (Attachment A)[5], and Letter of Intent for KAGRA to Join the O3 Run[6]. On the same day, the KAGRA observatory held a completion ceremony.

Figure 4 shows the international collaborative observation scenario[7] as of June 17, 2022. LIGO conducted Observation 1 (O1) from September 12, 2015, to January 19, 2016, and Observation 2 (O2) from November 30, 2016, to August 25, 2017. Virgo joined O2 on August 1, 2017. LIGO and Virgo started Observation 3 (O3) from April 1, 2019. Initially, O3 was planned to continue until the end of April in 2020, but it was suspended on March 27, 2020, due to the influence of the COVID-19[8]. The next international collaborative observation called O4 will be started from March 2023 as of June 17, 2022[7].

In FY2019 we started interferometer commissioning works to reach the sensitivity required to join O3. The required sensitivity of 1 Mpc was defined as an observation range of neutron star binary coalescences[6]. KAGRA reached the required sensitivity almost the end of March 2020. Along with the commissioning works the KAGRA observatory carried out several engineering runs and two Observation runs by the end of April 2020. The first observation run was carried out only by KAGRA with the observation range of 0.5 Mpc from February 25 to March 7, 2020. The second observation run was carried out with GEO600 from April 7 to 21, 2020. This observation called O3GK is regarded as an official joint observation with GEO600 by LIGO, VIRGO, and KAGRA. KAGRA was operated in O3GK with the observation range of almost 0.7 Mpc and duty factor of 53 % has achieved.

Searching for transient gravitational-wave signals in observation data obtained in O3GK has been performed. Dedicated searches for binary coalescence signals and generic transients associated with gamma-ray burst events observed during O3GK have been also performed. No gravitational wave events were identified[9]. Details will be shown in the "Data analysis" section.

After the O3GK observation, we restricted activities by the end of May 2020 to prevent a spread of COVID-19. Activity restrictions have been gradually relaxed from June 2020, and interferometer upgrades and refurbishment works for O4 are underway accordingly. In FY2021 we continued the upgrade and refurbishment works. Details of the works are shown in the following sections.

We also enhanced the international collaborations with the Einstein Telescope (ET) project, LIGO, Virgo, Korean and other Asian groups mainly based on the JSPS core-to-core program.

The rapidly progressing status of KAGRA were presented in many international conferences. Many papers about the progress of KAGRA were also published [10], [11], [12], [13], [14], [15]. We also presented activities on our web-page.[16]

Bibliography

[1] "KAGRA: 2.5 generation interferometric gravitational wave detector", KAGRA collaboration, Nature Astronomy, Vol. 3, January 2019, 35-40

[2] "Construction of KAGRA: an underground gravitational-wave observatory", KAGRA collaboration, Prog. Theor. Exp. Phys. 2018, 013F01 (2018)

[3] "First cryogenic test operation of underground km-scale gravitational-wave observatory KAGRA", KAGRA collaboration, Class. Quantum Grav. 36 165008 (2019)

[4] https://gwdoc.icrr.u-tokyo.ac.jp/cgi-bin/DocDB/ShowDocument?docid=10663

[5] https://gwdoc.icrr.u-tokyo.ac.jp/cgi-bin/DocDB/ShowDocument?docid=10664

[6] https://gwdoc.icrr.u-tokyo.ac.jp/cgi-bin/DocDB/ShowDocument?docid=10813

[7] https://www.ligo.caltech.edu/news/ligo20220617

[8] https://www.ligo.caltech.edu/news/ligo20200326

[9] The LIGO Scientific Collaboration, the Virgo Collaboration, and the KAGRA Collaboration, "First joint observation by the underground gravitational-wave detector KAGRA with GEO 600", Prog. Theor. Exp. Phys. 2022 063F01(37 pages)

[10] "The Current Status and Future Prospects of KAGRA, the Large-Scale Cryogenic Gravitational Wave Telescope Built in the Kamioka Underground", KAGRA collaboration, Galaxies 2022, 10(3), 63

[11] "Application of the Hilbert-Huang transform for analyzing standing-accretion-shock-instability induced gravitational waves in a core-collapse supernova", M. Takeda, Y. Hiranuma, N. Kanda ,K. Kotake, T. Kuroda, R. Negishi, K. Oohara, K. Sakai, Y. Sakai, T. Sawada, H. Takahashi, S. Tsuchida, Y. Watanabe, T. Yokozawa, Physical Review D 104, 084063 (2021)

[12] "Local Hurst exponent computation of data from triaxial seismometers monitoring KAGRA", A. Longo, S. Bianchi, W. Plastinao, K. Miyo, T. Yokozawa, T. Washimi, A. Araya, Pure and Applied Geophysics volume 178, pages3461–3470 (2021)

[13] "The KAGRA underground environment and lessons for the Einstein Telescope", F. Badaracco, C. D. Rossi, I. Fiori, J. Harms, K. Miyo, F. Paoletti, T. Tanaka, T. Washimi, T. Yokozawa, Phys. Rev. D 104, 042006 (2021)

[14] "Effects of lightning strokes on underground gravitational waves observatories", T. Washimi, T. Yokozawa, M. Nakano, T. Tanaka, K. Kaihotsu, Y. Mori, T. Narita, JINST 16 P07033 (2021)

[15] "Method for environmental noise estimation via injection tests for ground-based gravitational wave detectors", Tatsuki Washimi, Takaaki Yokozawa, Taiki Tanaka, Yosuke Itoh, Jun'ya Kume, and Jun'ichi Yokoyama, Class. Quantum Grav. 38 125005 (2021)

[16] http://gwcenter.icrr.u-tokyo.ac.jp/en/

Input and Output Optics

[Spokesperson : Osamu MIYAKAWA]

ICRR, The Univ. of Tokyo, Hida, Gifu 506-1205

The input and output optics (IOO) of KAGRA consists of the pre-stabilization laser (PSL), auxiliary locking system (ALS), input optics chain, output optics chain. PSL includes the intensity stabilization servo (ISS), pre-mode cleaner (PMC), and modulation system for the main interferometer. ALS includes the phase-locking system for the green beam each for X and Y arms, the fiber system, and the locking system for the arm cavities. The input optics chain includes the input mode cleaner (IMC), input Faraday isolator (IFI), and two input mode matching telescopes (MMT). The output optics chain includes the output mode matching telescopes (OMT), output Faraday isolator (OFI), and output mode cleaner (OMC).

In the fiscal year of 2021, KAGRA spent most of the time for upgrading the vibration isolation system, so IOO proceeded some developments of laser outside of KAGRA mine, and stabilized each system of IOO without the main interferometer.

For the high power laser, a 60W high power laser is being developed at the University of Toyama. We found dirty mode shapes around the beam waist. We suspected that mode shapes in master laser were something wrong. We replaced the master laser and the shapes became a little better, however we realized that the shape of beam depends on alignment between the master laser and the power amplifier. Intensity noise, frequency noise are the same with the old master laser, so we have decided we leave it. Another issue was that we saw several moving peaks on the intensity noise. Frequency of peaks changes with time. After some investigations, we concluded that the peaks come from the power supply for LDs. We were afraid to break our current power supply, we decided to leave it without any further investigation until spare power supply and LDs arrive in FY2022. Even we have such peaks, still the intensity noise level of new laser is better than the current KAGRA laser, so we decided to replace the current laser to the new high power laser.

All optical components of ISS will be also replaced to the new design that has two sets of power receiving PDs. This multiple PD setup accepts higher laser power in future. We will develop them in air for O4, and they will be placed into a vacuum chamber for O5.

PMC is basically stably locked almost of time, and we are preparing remote input beam alignment system using pico motors.

As for ALS, it was pointed out that the actuator range for feedback signals was narrow, and we tried to increase the dynamic range to employ two kinds of PZT. One is a short range PZT for high frequency feedback and another is a long range PZT for lower frequency. However we noticed that the long range PZT introduces a huge misalignment to the fiber coupler with a large feedback signal. It must be fixed before O4 starts, or it provides us a narrower feedback range than O3's range.

IMC ASC (Alignment Sensing and Control) is one of the most developed one in FY2021 in IOO. We succeeded in feeding back to 3 MC mirrors and one of the PZT on a steering mirror at the end of PSL table to adjust the angle of input beam for IMC. All the servo works pretty well and keep the alignment even the temperature in the PSL room changed drastically when HEPA filters switched on/off.

We are preparing the whole IOO system working stably for O4 that will start in FY2022.

Cryogenic system

[Spokesperson : Takafumi USHIBA]
ICRR, The Univ. of Tokyo, Hida, Gifu 506-1205

One of the unique features of KAGRA is the use of cryogenic sapphire mirrors in the 3-km arm cavities. The people working in this group are mainly from ICRR, KEK and University of Toyama. Here, we summarize the activity of members of ICRR in FY 2021.

Hardware update of the cryogenic payload A KAGRA sapphire mirror is suspended by a 9-stage suspension and its bottom 4 stages that include sapphire mirror is called cryogenic payload. Figure 5 shows the schematic view of the cryogenic payload.

In the fiscal year 2021, actuators and sensors on the cryogenic payloads were updated to increase the actuation range and improve local control of the payload, respectively. After these update, suspension functions including room temperature parts are checked one by one to confirm that the suspension is acceptable for the observation. ITMX and ETMX passed the check and the vacuum evacuation for their suspensions were started. The check for ITMY and ETMY were started at the end of fiscal year 2021.

Cryogenic system KAGRA uses 6 cryocoolers for cooling one sapphire mirrors. Two is used for cooling the cryogenic payload, two is used for cooling two layers of radiation shields, and the other two is used for cooling duct shields.

In fiscal year 2021, cryocoolers for duct-shield cooling were replaced for achieving maintenance-free long-term operation and improving cooling performance. All 8 duct-shield cryocoolers were replaced and duct-shield cryocoolers for ITMX and ETMX were operated after the vacuum evacuation.

Characterization and local controls of the cryogenic payload To control the angular and logitudinal motion of the suspensions, characterization of the cryogenic payload was performed. Suspension mechanical transfer functions were measured and mechanical resonances below 10 Hz are characterized: Q-values of the resonances are measured.

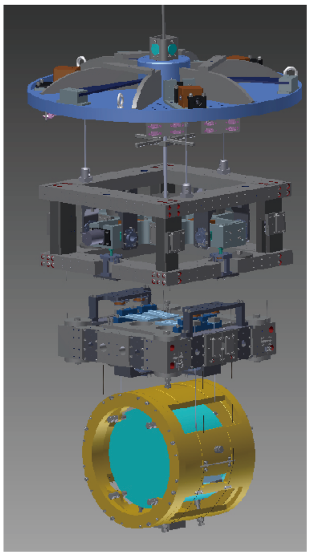

Fig. 5. Schematic view of the cryogenic payload.

After the characterization, local damping control filters were designed and implemented to ITMX and ETMX. Owing to the damping, residual RMS angular motions of ITMX and ETMX could be reduced below 1 urad, which was enough small for initial alignment of the arm cavity. In addition to this, a part of characterization for comparing room temperature performance and cryogenic one was performed.

Acknowledgement Mechanical Engineering Center of KEK makes a large contribution through providing many products for our research.

Integrated DAQ/control system using real time computers

[Spokesperson : Shoichi OSHINO]
ICRR, The Univ. of Tokyo, Hida, Gifu 506-1205

In preparation for the start of international joint observations of gravitational wave, we have expanded our network. We have achieved improved fault tolerance by building a separate network from the previous one. We have also confirmed that this network is capable of 40 Gbps data transfer speed.

We built a separate network from the one we had been using for control, and moved equipment that was not fast enough to communicate to that network. This dramatically reduced the number of times the equipment hung up. In addition, we installed additional optical fiber and network switches in the mine to improve the network environment.

We are creating a new type of I/O chassis. In FY2021 we started mass production of I/O chassis. In total, we created 10 chassis. This new I/O chassis will be able to hold four PCI-e expansion cards and will be connected to the computer via MTP optical fiber cables.

We have created new LVDT drivers, PCal drivers, 20 whitening filters, 10 HP Coil driver boards, and 10 D-sub BNC converter for ADC. We also prepared for building several types of D-sub cables, which were becoming scarce in our inventory.

Detector Charcterization

[Spokesperson : Takahiro Yamamoto]
ICRR, The Univ. of Tokyo, Hida, Gifu 506-1205

Data validation for O3GK The goal of Detector Characterization (DetChar) activities is to improve the reliability of gravitational waves detection by serving the data quality information which is one of criteria for selecting data using gravitational waves searches.

Some data quality indicators were provided in the real-time (o(1s) latency) process as reported in the Annual report 2020-2021.

We conducted to validate all provided indicators as an offline process to publish about the data quality information. There is no major change between online and offline ones. But more detailed information on equipment malfunctions was provided. Calibrated strain signal which passes the data quality check and the data quality information itself are now available on Gravitational Wave Open Science Center [1].

Preparation for O4 The LIGO-Virgo-KAGRA (LVK) Collaboration has now reached an agreement to begin observations in 2023, and preparations for that observation system are underway.

DetChar group lead to unify the data sharing about the detector status and the data quality information in observing runs.

Especially low-latency event validation for the gravitational wave candidates is one of the most important mission for DetChar group. We constructed the framework to share the detector status in various latencis name as Data Quality Report (DQR). DQR activity includes the evaluation of the detector noise status around the time when gravitation wave candidates occurs. In order to unify the contents of information among LVK, we developed the DQR software with LIGO and Virgo's DetChar groups.

Bibliography

[1] R. Abbot *et al.* SoftwareX **13** (2021) 100658.

Environment Monitors

[Spokesperson : Takaaki YOKOZAWA]
ICRR, The Univ. of Tokyo, Hida, Gifu 506-1205

To detect the Gravitational Waves(GWs), the distinguish from the noise is important. Also, because the amplitude of the GW is extremely small, small vibration from essential instruments, small sound from outside of the experimental area and so on can produce noise source contamination that reduces the sensitivity. To evaluate the noise sources, about 100,000 auxiliary channels are recorded by the KAGRA digital system. The main purposes of the physical and environmental monitoring are as followings.

The first is to characterize the underground and cryogenic environment; KAGRA detector has two unique features, underground and cryogenic environment, and those features will be essential in the next-generation detectors. We performed the correlation analysis between GW strain data and monitors. We found several interesting result, one result is that when the strong wind was appeared in the weather station which is placed in the entrance of KAGRA experimental area, the infrasound (~ 0.2 Hz sound) was also appeared inside the mountain. The principle of developing the infrasound would be caused by the vibration of the surface of the mountain. We will continuously monitor the infrasound by increasing the detectable microphone. Next interesting topic was measuring the Schumann resonance inside and outside the mountain. The Schumann resonances are a set of spectrum peaks in the extremely low frequency (ELF) portion of the Earth's electromagnetic field spectrum. Schumann resonances are global electromagnetic resonances, generated and excited by lightning discharges in the cavity formed by the Earth's surface and the ionosphere. The preliminary result showed that the magnetic field of the frequency of the Schumann resonance inside the mountain is larger than that of the outside the mountain, but this reason is under discussing.

The second aim is understanding the interferometer noise by environmental monitors. We installed various PEMs, including accelerometers, microphones, magnetometers, thermometers, weather station and so on. After the O3GK observation, we performed several analysis using observation data. First analysis is the lock loss study. To detect the GW using the interferometer, we must control several degree of freedom, but when some external disturbance occurred, those control became unstable and lock loss happened. To understand the reason of lock loss, we can achieve the longer observation time. The number of identified lock-loss in the O3GK was 75. 10 of lock loss were caused by the saturation of the control and photo detector, 48 of lock loss were related by Abnormal feedback signal, 53 of lock loss were related by the bad interferometer alignment, and 13 of then were the 1 Hz oscillation. Next step is development of the auto analysis tool of lock loss study. Second analysis is the offline noise subtraction using the independent component analysis(ICA). In the O3GK, the acoustic noise limit the sensitivity of KAGRA at middle frequency. By investigating the noise path and by applying the offline noise subtraction, we can perform the improvement of the sensitivity. ICA is the method of blind source separation, this can be used as the non-gaussian noise subtraction method by using auxiliary channels such as PEM channels. The result showed that by using the microphone data inside the PSL room, we succeeded to perform the noise subtraction for the whole term of the O3GK period.

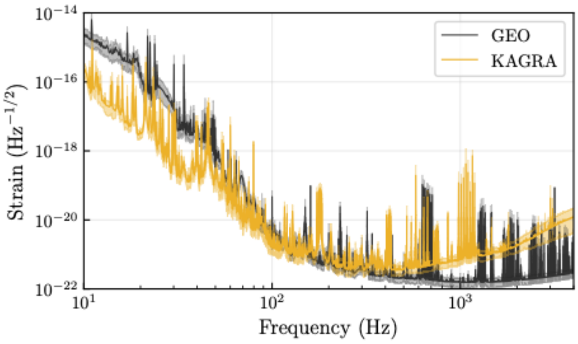

Fig. 6. Noise amplitude spectral density of GEO (black) and KAGRA (yellow) during O3GK run.

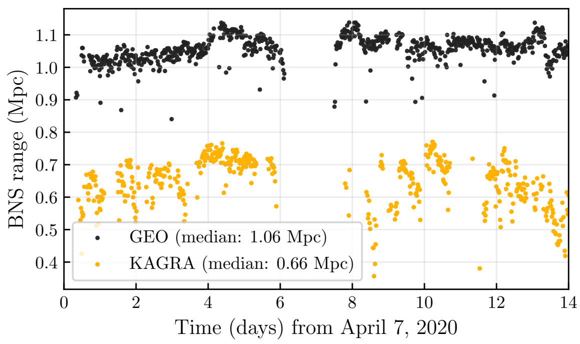

Fig. 7. BNS inspiral ranges for GEO and KAGRA over the joint run.

Data Analysis

[Spokesperson : Hideyuki Tagoshi]

ICRR, The Univ. of Tokyo, Kashiwa, Chiba, 277-8582

KAGRA signed a Memorandum of Agreement (MoA) between LIGO and Virgo. The MoA defines the policy of the joint data analysis and the data sharing. Based on this MoA, all data analysis activities are now done jointly with LIGO and Virgo. In LIGO-Virgo-KAGRA (LVK) collaboration, there is a Data Analysis Council (DAC) which is a committee which manage data analysis activities in LVK. Under DAC, there are four working groups regarding gravitational wave signal search, Compact Binary Coalescence working group (CBC), Burst working group (Burst), Continuous Wave Working group (CW), and Stochastic background working group (Stochastic). In LVK, there is also Operations group which manages various data related activities. Those include calibration, detector characterization, computing and software, low latency, open data, run planning and so on. In KAGRA, Data Analysis Committee manages data analysis and date related activities.

KAGRA performed an observing run from April 7th to 20th, 2020 (UTC) together with GEO 600 in Germany. Originally, this observation was supposed to be done jointly with LIGO and Virgo at the end of the 3rd observing run of LIGO and Virgo. However, while KAGRA was preparing the observing run, the LIGO and Virgo detectors were forced to terminate operations on March 27, 2020 (UTC) due to the COVID-19 pandemic. Fortunately, however, GEO600 in Germany was operating and continuously taking data. Thus, GEO and KAGRA decided to perform an observing run jointly. In LIGO-Virgo-KAGRA (LVK) collaboration, this observation was officially approved as an joint observation under the LVK framework. This observing run was named O3GK.

In this year, we have continued the analysis of O3GK data. Figure 6 represents the Noise amplitude spectral density of GEO (black) and KAGRA (yellow) during O3GK run. Narrow peaks in the spectra are due to such sources as resonances of the suspension system (violin modes) and harmonics of the electrical grid frequency (50 Hz for GEO and 60 Hz for KAGRA). Figure 7 represents the detectable distance of the inspiral of binary neutron stars (BNS).

Several gravitational wave event searches were performed.

GRB Name	Data Source	Type
200412A	*Fermi*-GBM	Long
200415A	*Fermi*-GBM, IPN	Short
200418A	*Fermi*-GBM	Long
200420A	*Fermi*-GBM	Short

Table 2. GRBs observed during O3GK run times when both detectors were taking science-quality data.

Those include all-sky searches for binary neutron star coalescences by using the GstLAL pipeline, all-sky searches for unmodeled short duration burst waves with the coherent WaveBurst pipeline, targeted CBC searches associated with short Gamma Ray Bursts (GRBs) by using pyGRB pipeline, and targeted un-modeled burst searches associated with short and long GRBs by using X-pipeline. No candidate gravitational wave events were identified.

The analyzed GRB events are listed in Table 2. Among them, a short GRB, GRB 200415A, was subsequently associated with a magnetar giant flare in the nearby galaxy NGC253 at 3.5 Mpc based on its sky position, temporal and spectral properties and inferred energy. Since the distance is very short, it is especially interesting to search for gravitational wave signals associated with this GRB. However, the sensitivity of O3GK observing run was not sensitive to observe such a distance, and we could not constrain the progenitor of this GRB.

The lack of detected events in this observing run is expected given the sensitivity of the GEO–KAGRA network at the time. However, the sensitivity of KAGRA is expected to improve by more than two orders of magnitude later in this decade, becoming comparable to that of the LIGO and Virgo detectors. Our analyses have demonstrated the ability to incorporate KAGRA data into standard transient search pipelines that have been used to detect GW in LIGO and Virgo data.

These results were published in PTEP[1]. The O3GK data was publicly released at GWOSC site [2].

As one of the main computing resources in KAGRA, the main data server of KAGRA (System A) is located at ICRR Kashiwa. It has a 2.5PiB data storage. All KAGRA data taken at Kamioka are packed into one file for every 32 seconds, and are transferred continuously to the main data server at Kashiwa. Beside this, low latency data transfer is also done by packing only the gravitational wave channel and a few other channels into one file for every 1 seconds. For low latency data transfer, the latency of about 3 seconds is achieved from Kamioka to Kashiwa (this time include the time necessary for calibration). In order to share the low latency data file among LIGO-Virgo-KAGRA, the low latency data files are also transferred to a server at LIGO Caltech. On the other hand, low latency data files of LIGO and Virgo detectors are transferred from Caltech to the main data server at Kashiwa.

An additional KAGRA main data server (System B) is under construction at ICRR Kashiwa. It has a 4 PiB data storage. System B will be operational in 2022.

Bibliography

[1] The LIGO Scientific Collaboration, the Virgo Collaboration, and the KAGRA Collaboration, PTEP 2022, 063F01 (2022).

[2] The LIGO Scientific Collaboration, the Virgo Collaboration, and the KAGRA Collaboration, The O3GK Data Release, https://doi.org/10.7935/38s2-7g84 (2022).

Observational Cosmology Group

[Spokesperson : Yoshiaki Ono]

ICRR, The Univ. of Tokyo, Kashiwa, Chiba 277-8582

EMPRESS. IV. Extremely Metal-poor Galaxies Including Very Low-mass Primordial Systems with $M_* = 10^4$*–*$10^5 M_\odot$ *and* 2%*–*3% *(O/H): High (Fe/O) Suggestive of Metal Enrichment by Hypernovae/Pair-instability Supernovae* [1]

In collaboration with the members of National Astronomical Observatory of Japan, Kavli Institute for the Physics and Mathematics of the Universe, Carnegie Observatories, University of Copenhagen, Waseda University, Subaru Telescope, SOKENDAI (The Graduate University for Advanced Studies), University of Geneva, NSF's National Optical-Infrared Astronomy Research Laboratory, Leiden University, ETH Zurich, University of Lyon, Ehime University, Swinburne University of Technology, and The University of Tokyo.

We present Keck/LRIS follow-up spectroscopy for 13 photometric candidates of extremely metal-poor galaxies (EMPGs) selected by a machine-learning technique applied to the deep ($\sim$ 26 AB mag) optical and wide-area ($\sim$ 500 deg^2) Subaru imaging data in the EMPRESS survey. Nine out of the 13 candidates are EMPGs with an oxygen abundance (O/H) less than $\sim$ 10% solar value (O/H)$_\odot$, and four sources are contaminants of moderately metal-rich galaxies or no emission-line objects. Notably, two out of the nine EMPGs have extremely low stellar masses and oxygen abundances of 5×10^4–$7\times10^5 M_\odot$ and 2%–3% (O/H)$_\odot$, respectively. With a sample of five EMPGs with (Fe/O) measurements, two (three) of which are taken from this study (the literature), we confirm that two EMPGs with the lowest (O/H) ratios of $\sim 2\%$ (O/H)$_\odot$ show high (Fe/O) ratios of ~ 0.1, close to the solar abundance ratio. Comparing galaxy chemical enrichment models, we find that the two EMPGs cannot be explained by a scenario of metal-poor gas accretion/episodic star formation history due to their low (N/O) ratios (Figure 8). We conclude that the two EMPGs can be reproduced by the inclusion of bright hypernovae and/or hypothetical pair-instability supernovae (SNe) preferentially produced in a metal-poor environment. This conclusion implies that primordial galaxies at $z \sim 10$ could have a high abundance of Fe that did not originate from Type Ia SNe with delays and that Fe may not serve as a cosmic clock for primordial galaxies.

Bibliography

[1] Isobe, Y., Ouchi, M., Suzuki, A., Moriya, T., Nakajima, K., Nomoto, K., Rauch, M., Harikane, Y., Kojima, T., Ono, Y., Fujimoto, S., Inoue, A. K. , Kim, J. H., Komiyama, Y., Kusakabe, H., Lee, C.-H., Maseda, M., Matthee, J., Michel-Dansac, L., Nagao, T., Nanayakkara, T., Nishigaki, M., Onodera, M., Sugahara, Y., Xu, Y., 2022, The Astrophysical Journal, 925, 111

GOLDRUSH. IV. Luminosity Functions and Clustering Revealed with 4,000,000 Galaxies at $z \sim 2$*–*7*: Galaxy-AGN Transition, Star Formation Efficiency, and Implication for Evolution at* $z > 10$ [2]

In collaboration with the members of Shanghai Jiao Tong University, Saint Mary's University Kitami Institute of Technology, University of Arizona, The University of Tokyo, Laboratoire d'Astrophysique de Marseille, University of Geneva, University of Copenhagen, NRC Herzberg Astronomy and Astrophysics, National Astronomical Observatories of China, Waseda University, and Ehime University.

We present new measurements of rest-UV luminosity functions and angular correlation functions from 4,100,221 galaxies at $z \sim 2$–7 identified in the Subaru/Hyper Suprime-Cam survey and CFHT Large Area U-band Survey. The obtained luminosity functions at $z \sim 4$–7 cover a very wide UV luminosity range of ~ 0.002–$2000 L^*_{\rm UV}$ combined with previous studies, confirming that the dropout luminosity function is a superposition of the active galactic nucleus (AGN) luminosity function dominant at $M_{\rm UV} \lesssim -24$ mag and the galaxy

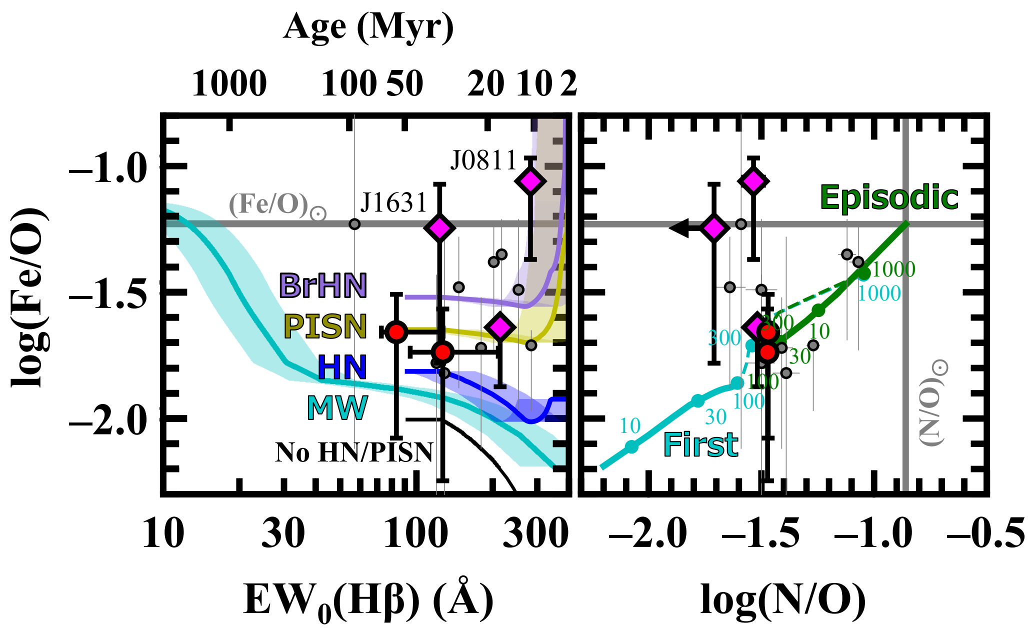

Fig. 8. Fe/O ratio as a function of $EW_0(H\beta)$ and N/O described in the left and right panels, respectively. The red circles and magenta diamonds are our EMPGs and those found in the literature. The gray circles indicate local metal-poor galaxies reported in the literature, for which we only show errors of Fe/O. In the left panel, the cyan, blue, purple, and yellow curves with the shaded regions show the MW, the HN 100%, the BrHN 20%, and the PISN models, respectively. The black curve indicates the No HN/PISN model. In the right panel, the cyan and green curves represent evolution tracks of Fe/O and N/O when first and episodic starbursts occur in a galaxy, respectively. The numbers accompanied by the curves indicate the ages in the unit of Myr. We draw the evolution tracks with solid and dashed lines before and after 100 Myr, respectively, because all the EMPGs shown in the left panel have ages $\lesssim 100$ Myr. To predict Fe/O and N/O ratios, we use previous theoretical models. The gray lines show the solar abundances.

luminosity function dominant at $M_{\rm UV} \gtrsim -22$ mag, consistent with galaxy fractions based on 1037 spectroscopically identified sources. Galaxy luminosity functions estimated from the spectroscopic galaxy fractions show the bright-end excess beyond the Schechter function at $\gtrsim 2\sigma$ levels, possibly made by inefficient mass quenching, low dust obscuration, and/or hidden AGN activity. By analyzing the correlation functions at $z \sim 2$–6 with HOD models, we find a weak redshift evolution (within 0.3 dex) of the ratio of the star formation rate (SFR) to the dark matter accretion rate, SFR/$\dot{M}_{\rm h}$, indicating the almost constant star formation efficiency at $z \sim 2$–6, as suggested by our earlier work at $z \sim 4$–7. Meanwhile, the ratio gradually increases with decreasing redshift at $z < 5$ within 0.3 dex, which quantitatively reproduces the cosmic SFR density evolution, suggesting that the redshift evolution is primarily driven by the increase of the halo number density due to the structure formation, and the decrease of the accretion rate due to the cosmic expansion. Extrapolating this calculation to higher redshifts assuming the constant efficiency suggests a rapid decrease of the SFR density at $z > 10$ with $\propto 10^{-0.5(1+z)}$, which will be directly tested with the James Webb Space Telescope (Figure 9).

Bibliography

[2] Harikane, Y., Ono, Y., Ouchi, M., Liu, C., Sawicki, M., Shibuya, T., Behroozi, P. S., He, W., Shimasaku, K., Arnouts, S., Coupon, J., Fujimoto, S., Gwyn, S., Huang, J., Inoue, A. K. , Kashikawa, N., Komiyama, Y., Matsuoka, Y., Willott, C. J., 2022, The Astrophysical Journal Supplement Series, 259, 20

SILVERRUSH. IX. Lyα Intensity Mapping with Star-forming Galaxies at $z = 5.7$ and 6.6: A Possible Detection of Extended Lyα Emission at $\gtrsim 100$ Comoving Kiloparsecs around and beyond the Virial-radius Scale of Galaxy Dark Matter Halos [3]

In collaboration with the members of Waseda University, Graduate University for Advanced Studies (SOKENDAI), University of Geneva, NSF's National Optical-Infrared Astronomy Research Laboratory, Ehime University, The University of Tokyo, Kitami Institute of Technology, and The Open University of Japan.

We present results of the cross-correlation Lyα intensity mapping with Subaru/Hyper Suprime-Cam (HSC) ultra-deep narrowband images and Lyα emitters (LAEs) at $z = 5.7$ and 6.6 in a total area of 4 deg^2. Although an overwhelming amount of data quality controls have been performed for the narrowband images, we further conduct extensive analyses evaluating systematics of large-scale point-spread function wings, sky subtractions, and unknown errors based on physically uncorrelated signals and sources found in real HSC images and object catalogs, respectively. Removing the systematics, we carefully calculate cross-correlations between Lyα intensity of the narrowband images and the LAEs. We tentatively identify very diffuse Lyα emission with the $\simeq 3\sigma$

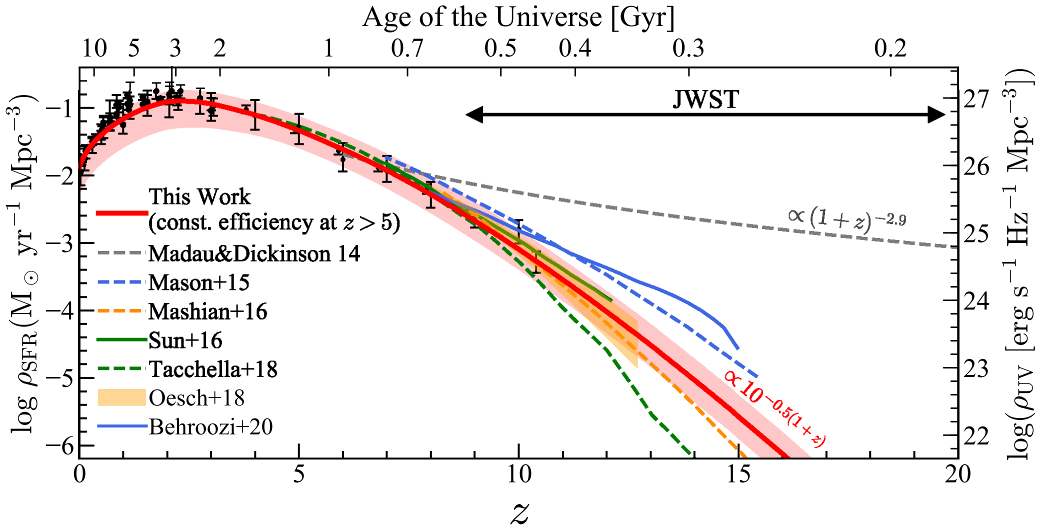

Fig. 9. Comparison of the cosmic SFR density at $z > 7$. The red curve with the shade represents the cosmic SFR density calculated in this work based on the constant star formation efficiency at $z > 5$, integrated down to the SFR of $0.3M_\odot$ yr^{-1} ($M_{\rm UV} = -17$ mag), as previous studies. The gray dashed curve shows the extrapolation of the relation of previous work at $z > 6$. The other curves show predictions from models in the literature. All results are converted to use the Salpeter IMF.

($\simeq 2\sigma$) significance at $\gtrsim 100$ comoving kiloparsecs (ckpc) far from the LAEs at $z = 5.7$ (6.6), around and probably even beyond a virial radius of star-forming galaxies with $M_{\rm h} \sim 10^{11} M_\odot$ (Figure 10). The diffuse Lyα emission possibly extends up to 1000 ckpc with the surface brightness of 10^{-20}–10^{-19} erg s^{-1} cm^{-2} arcsec^{-2}. We confirm that the small-scale (< 150 ckpc) Lyα radial profiles of LAEs are consistent with those obtained by recent Multi-Unit Spectroscopic Explorer observations. Comparisons with numerical simulations suggest that the large-scale ($\sim$ 150–1000 ckpc) Lyα emission are not explained by unresolved faint neighboring galaxies including satellites, but by a combination of Lyα photons emitted from the central LAE and other unknown sources, such as cold-gas streams and galactic outflow. We find no evolution in the Lyα radial profiles of our LAEs from $z = 5.7$ to 6.6, where theoretical models predict a flattening of the profile slope made by cosmic reionization, albeit with our moderately large observational errors.

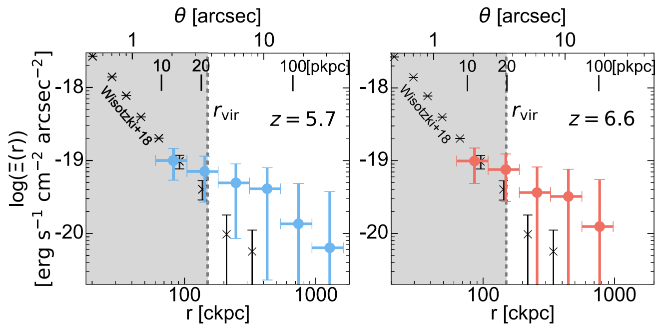

Fig. 10. Cross-correlation function between the LAEs and the Lyα emission intensity after subtracting the systematics. The filled circles in the left (right) panel represent the weighted mean of the results in UD-COSMOS and UD-SXDS fields of $z = 5.7$ (6.6). The S/Ns of the outer three data points are lower than 1. The black crosses correspond to the stacked Lyα radial profile at $z = 5$–6 that is taken from the observational results of MUSE in the literature. The gray dashed lines show the DMH virial radius ($r_{\rm vir}$) of the LAEs in our samples whose DMH masses are estimated to be $M_{\rm h} \sim 10^{11} M_\odot$.

Bibliography

[3] Kakuma, R., Ouchi, M., Harikane, Y., Ono, Y., Inoue, A. K., Komiyama, Y., Kusakabe, H., Liu, C.-H., Matsuda, Y., Matsuoka, Y., Mawatari, K., Momose, R., Shibuya, T., Taniguchi, Y., 2021, The Astrophysical Journal, 916, 22

SILVERRUSH X: Machine Learning-aided Selection of 9318 LAEs at $z = 2.2, 3.3$***,*** 4.9***,*** 5.7***,*** 6.6***, and*** 7.0 ***from the HSC SSP and CHORUS Survey Data*** [4]

In collaboration with the members of Kitami Institute of Technology, Waseda University, Ehime University, University of Tsukuba, The University of Tokyo, National Astronomical Observatory of Japan, The Open University of Japan, University of Copenhagen, Institut Teknologi Bandung, Kindai University, Kure College, University of Geneva, and NSF's National Optical-Infrared Astronomy Research Laboratory.

We present a new catalog of 9318 Lyα emitter (LAE) candidates at $z = 2.2$, 3.3, 4.9, 5.7, 6.6, and 7.0 that are photometrically selected by the SILVERRUSH program with a machine learning technique from large area (up to 25.0 deg^2) imaging data with six narrowband filters taken by the Subaru Strategic Program with Hyper Suprime-Cam and a Subaru intensive program, Cosmic HydrOgen Reionization Unveiled with Subaru. We construct a convolutional neural network that distinguishes between real LAEs and contaminants with a completeness of 94% and a contamination rate of 1%, enabling us to efficiently remove contaminants from the photometrically selected LAE candidates (Figure 11). We confirm that our LAE catalogs include 177 LAEs that have been spectroscopically identified in our SILVERRUSH programs and previous studies, ensuring the validity of our machine learning selection. In addition, we find that the object-matching

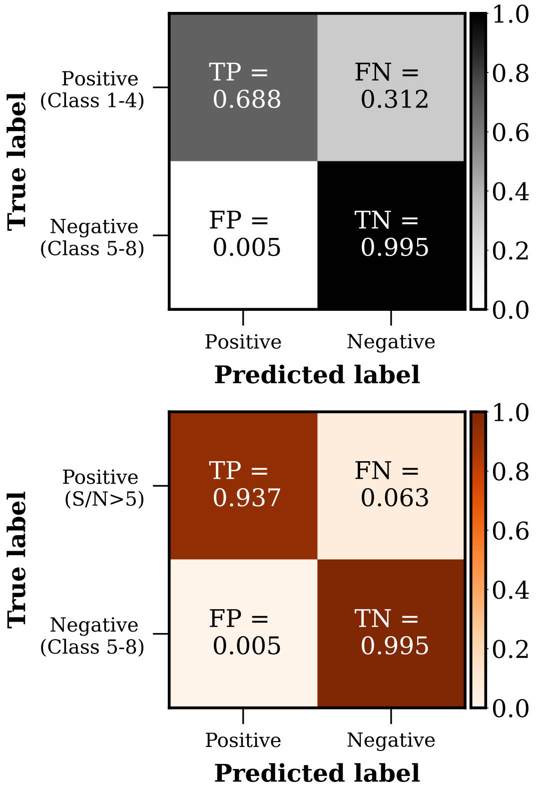

Fig. 11. Confusion matrix. In the top panel, Classes 1–4 (5–8) of the true labels are classified as positive (negative). For the predicted labels, we classify sources as positive if they show a high score of being an LAE. The numbers in the cells denote true positives (TP), false negatives (FN), false positives (FP), and true negatives (TN). In the best case scenario, the confusion matrix has non-zero elements only in its diagonal cells and zero elements in the others. The bottom panel is the same as the top panel, except that positive for the true labels corresponds to simulated LAEs with S/N > 5.

rates between our LAE catalogs and our previous results are $\simeq 80\%$–100% at bright NB magnitudes of $\lesssim 24$ mag. We also confirm that the surface number densities of our LAE candidates are consistent with previous results. Our LAE catalogs will be made public on our project webpage.

Bibliography

[4] Ono, Y., Itoh, R., Shibuya, T., Ouchi, M., Harikane, Y., Yamanaka, S., Inoue, A. K., Amagasa, T., Miura, D., Okura, M., Shimasaku, K., Iwata, I., Taniguchi, Y., Fujimoto, S., Iye, M., Jaelani, A. T., Kashikawa, N., Kikuchihara, S., Kikuta, S., Kobayashi, M. A. R. , Kusakabe, H., Lee, C.-H., Liang, Y., Matsuoka, Y., Momose, R., Nagao, T., Nakajima, K., Tadaki, K., 2021, The Astrophysical Journal, 911, 78

First HETDEX Spectroscopic Determinations of Lyα and UV Luminosity Functions at $z = 2$–3: Bridging a Gap between Faint AGNs and Bright Galaxies [5]

In collaboration with the members of The University of Texas at Austin, The Pennsylvania State University, Max Planck Institute for Extraterrestrial Physics, Ludwig-Maximilians University Munich, The State University of New Jersey, NYC College of Technology, Flatiron Institute, University of Oxford, University of the Western Cape, and Lawrence Berkeley National Laboratory.

We present Lyα and ultraviolet (UV)-continuum luminosity functions (LFs) of galaxies and active galactic nuclei (AGNs) at $z = 2.0$–3.5 determined by the untargeted optical spectroscopic survey of the Hobby-Eberly Telescope Dark Energy Experiment (HETDEX). We combine deep Subaru imaging with HETDEX spectra resulting in 11.4 deg^2 of fiber spectra sky coverage, obtaining 18,320 galaxies spectroscopically identified with Lyα emission, 2126 of which host type 1 AGNs showing broad (FWHM > 1000 km s^{-1}) Lyα emission lines. We derive the Lyα (UV) LF over 2 orders of magnitude covering bright galaxies and AGNs in $\log L_{\mathrm{Ly}\alpha}/[\mathrm{erg\,s^{-1}}] = 43.3$–$45.5$ ($-27 < M_{\mathrm{UV}} < -20$) by the $1/V_{\mathrm{max}}$ estimator (Figure 12). Our results reveal that the bright-end hump of the Lyα LF is composed of type 1 AGNs. In conjunction with previous spectroscopic results at the faint end, we measure a slope of the best-fit Schechter function to be $\alpha_{\mathrm{Sch}} = -1.70^{+0.13}_{-0.14}$, which indicates that α_{Sch} steepens from $z = 2$–3 toward high redshift. Our UV LF agrees well with previous AGN UV LFs and extends to faint-AGN and bright-galaxy regimes. The number fraction of Lyα-emitting objects (X_{LAE}) increases from $M^*_{\mathrm{UV}} \sim -21$ to bright magnitude due to the contribution of type 1 AGNs, while previous studies claim that $X_{\mathrm{Ly}\alpha}$ decreases from faint magnitudes to M^*_{UV} , suggesting a valley in the XLyα–magnitude relation at M^*_{UV}. Comparing our UV LF of type 1 AGNs at $z = 2$–3 with those at $z = 0$, we find that the number density of faint ($M_{\mathrm{UV}} > -21$) type 1 AGNs increases from $z \sim 2$ to 0, as opposed to the evolution of bright ($M_{\mathrm{UV}} < -21$) type 1 AGNs, suggesting AGN downsizing in the rest-frame UV luminosity.

Bibliography

[5] Zhang, Y., Ouchi, M., Gebhardt, K., Mentuch C. E., Liu, C., Davis, D., Jeong, D., Farrow, D. J., Finkelstein, S. L., Gawiser, E., Hill, G. J., Kakuma, R., Acquaviva, V., Casey, C. M., Fabricius, M., Hopp, U., Jarvis, M. J., Landriau, M., Mawatari, K., Mukae, S., Ono, Y., Sakai, N., Schneider, D. P., 2021, The Astrophysical Journal, 922, 167

Theory Group

Overview

The theory group is active in elementary particle physics focusing on particle phenomenology, and in astroparticle physics focusing on particle cosmology. In particle physics, the main topics are theoretical studies of dark matter, inflation and extensions of the standard model. In astroparticle physics, the main topics are theoretical studies of inflation, thermal history of the early universe, dark matter, baryogenesis and big-bang nucleosynthesis.

After the discovery of the Higgs boson, the LHC has shown no strong hints on new physics. In this situation, we need to reconsider many ideas of new physics models as well

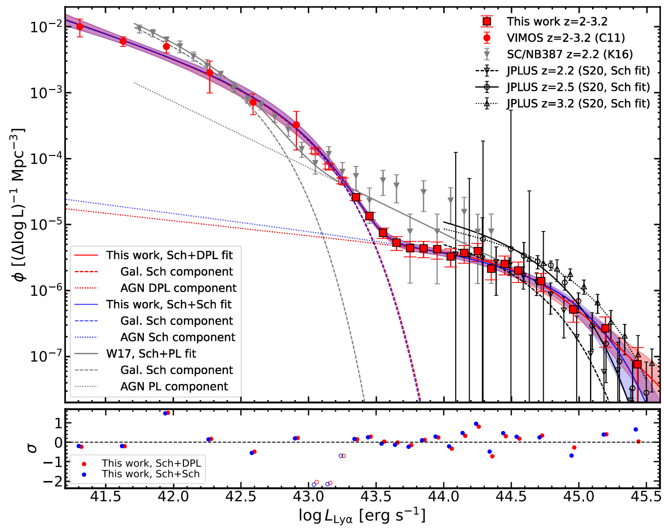

Fig. 12. Top: best-fit Lyα LF of our LAE sample with $2 < z < 3.2$ (red squares) and previous results at $2.0 < z < 3.2$ (red circles). The red (blue) line shows our best-fit result of model 1 (2) with the measurements of our study and previous work, with the shaded region corresponding to the 1σ uncertainty (68.27% equal-tailed credible interval). The black open downward triangles (dashed line), circles (solid line), and upward triangles (dotted line) represent the binned Lyα LFs (best Schechter fit) from previous work at $z \sim 2.25$, 2.54, and 3.24, respectively. The gray triangles indicate the previous results. We also show with gray lines the fitting results in the literature. The dashed, dotted, and solid gray lines indicate their best-fit Schechter component, power-law component, and overall LF, respectively. Bottom: residuals of models 1 (red) and 2 (blue) fit in units of the uncertainty in each luminosity bin.

as conventional strategies to search for them. Accordingly, our studies on beyond the Standard Model physics becomes more and more diverse.

Since the LIGO detectors detected the first confirmed gravitational waves (GWs) from colliding black holes on September 14, 2015, new era of GW astronomy began. So far, six GW events were detected by LIGO. Among them is the first detection of GW from binary neutron star. The discovery suggested strongly the existence of kilonova which can produce r-process elements. If they continue to find GW events from black holes and neutron stars, their origin becomes one of the most interesting topics.

The supersymmetric (SUSY) extension of the standard model (SM) in the particle physics is considered to be one of the most promising models beyond the standard model. It solves the naturalness problem for the Higgs boson mass term in the standard model, and it is also compatible with the grand unified theories (GUTs). Although no hints of the superparticles have been indicated from the LHC yet, the SUSY models are the most attractive candidates beyond the Standard Model. Our group has been studying phenomenological and cosmological aspects of the SUSY models.

Recent cosmological observations including the Planck data determine precisely the mean densities of matter and baryon in the Universe, and existence of non-baryonic dark matter is established. Weakly interacting massive particles (WIMPs) are considered to be good candidates of the dark matter. They act as the cold dark matter in the structure formation of the universe. Our group has been studying model building for dark matter and detectability in direct and indirect search experiments.

For understanding of the early universe, a role of the elementary particle physics is crucial. Recent progress in the particle physics such as grand unification theories and supersymmetry leads us to a more deeper insight into the fundamental aspects of the early universe. In the inflationary universe, the quantum fluctuations of the scalar field which drives the inflation become the density fluctuations and lead to formation of the structure observed in the present universe. On the other hand cosmology and astrophysics are used to test new theories in particle physics. Such particle cosmology is one of main subjects of our group.

Big Bang Nucleosynthesis (BBN) is one of the most important subjects in modern cosmology. Predicted abundances of the light elements are very sensitive to the cosmological scenario. On the other hand, physics beyond the standard model predicts the new particles which would have existed at the BBN epoch. Such particles may spoil the success of BBN, which leads to constraints on the new particles and the particle physics models.

The grand unified theories predict that our universe undergoes several vacuum phase transitions. In the course of phase transitions topological defects (monopoles, cosmic strings and domain walls) are generally produced depending on symmetries of the vacua. Our group has studied evolution of various topological defects.

Particle Phenomenology

[Spokesperson : M. Ibe]
ICRR, The Univ. of Tokyo, Kashiwa, Chiba 277-8582

Beyond Standard Model

• Muon g - 2 in gauge mediation without SUSY CP problem [1]

In collaboration with the members of ICRR, Kavli IPMU

We discuss gauge mediated supersymmetry breaking models which explain the observed muon anomalous magnetic moment and the Higgs boson mass simultaneously. The successful explanation requires the messenger sector which violates the relation motivated by the grand unification theory (GUT). The naive violation of the GUT relation, however, ends up with the CP problem. We propose a model in which the phases of the gaugino masses are aligned despite the violation of the GUT relation. We also consider a model which generates the μ-term and the additional Higgs soft masses squared without causing CP violation. As a result, we find a successful model which explains the muon anomalous magnetic moment and the Higgs boson mass. The model is also free from the CP, flavor-changing neutral current and the lepton flavor violation problems caused by the subdominant gravity mediation effects.

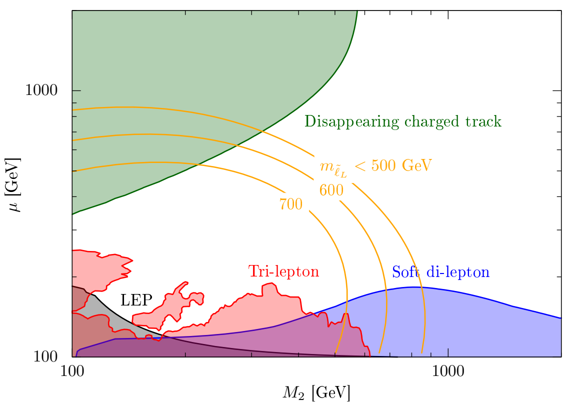

Fig. 13. The current collider constraints on the Higgsino-Wino system. The orange lines show the rough upper limits on the left-handed slepton mass to explain the observed a_μ.

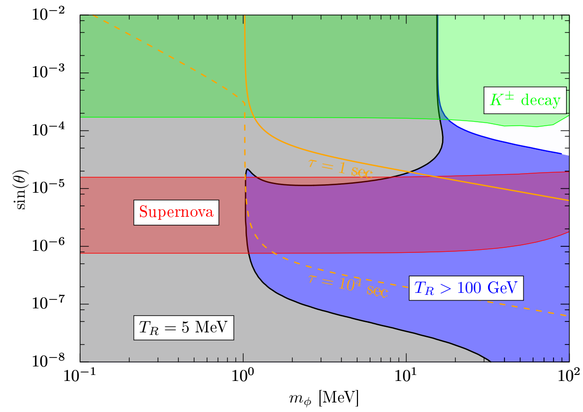

Fig. 14. The cosmological constraints on the dark scalar model. The gray region shows the most conservative constraint, which is excluded even for an extremely low reheating temperature. The blue region shows the excluded region for the reheating temperature greater than 100 GeV. The white region is cosmologically consistent region.

• Gauge kinetic mixing and dark topological defects [2]

In collaboration with the members of Rikkyo Univ., ICRR, Kavli IPMU, TD-Lee Inst., Morpho, Inc.

We discuss how the topological defects in the dark sector affect the Standard Model sector when the dark photon has a kinetic mixing with the QED photon. In particular, we consider the dark photon appearing in the successive gauge symmetry breaking, $\mathrm{SU}(2) \to \mathrm{U}(1) \to \mathbb{Z}_2$, where the remaining $\mathbb{Z}_2$ is the center of $\mathrm{SU}(2)$. In this model, the monopole is trapped into the cosmic strings and forms the so-called bead solution. As we will discuss, the dark cosmic string induces the QED magnetic flux inside the dark string through the kinetic mixing. The dark monopole, on the other hand, does not induce the QED magnetic flux in the $\mathrm{U}(1)$ symmetric phase, even in the presence of the kinetic mixing. Finally, we show that the dark bead solution induces a spherically symmetric QED magnetic flux through the kinetic mixing. The induced flux looks like the QED magnetic monopole viewed from a distance, although QED satisfies the Bianchi identity everywhere, which we call a pseudo magnetic monopole.

• Cosmological constraints on dark scalar [3]

In collaboration with the members of ICRR, Kavli IPMU

We discuss cosmological constraints on a dark scalar particle mixing with the Standard Model Higgs boson. We pay particular attention to the dark scalar production process when the reheating temperature of the Universe is very low, which allows us to give a conservative limit on the low-mass scalar particle. We also study the effect of the self-interaction of the dark scalars and find this has a significant impact on the cosmological constraints. We obtain the most conservative cosmological constraint on the dark scalar, which is complementary to accelerator experiments and astrophysical observations.

Bibliography

[1] M. Ibe, S. Kobayashi, Y. Nakayama and S. Shirai, JHEP **07** (2021), 098 doi:10.1007/JHEP07(2021)098 [arXiv:2104.03289 [hep-ph]].

[2] T. Hiramatsu, M. Ibe, M. Suzuki and S. Yamaguchi, JHEP **12** (2021), 122 doi:10.1007/JHEP12(2021)122 [arXiv:2109.12771 [hep-ph]].

[3] M. Ibe, S. Kobayashi, Y. Nakayama and S. Shirai, JHEP **03** (2022), 198 doi:10.1007/JHEP03(2022)198 [arXiv:2112.11096 [hep-ph]].

Dark Matter

• Chiral composite asymmetric dark matter [1]

In collaboration with the members of Kavli IPMU, ICRR

The asymmetric dark matter (ADM) scenario solves the baryon-dark matter coincidence problem when the dark matter (DM) mass is of $\mathscr{O}(1)$GeV. Composite ADM models based on QCD-like strong dynamics are particularly motivated since the strong dynamics naturally provides the DM mass of $\mathscr{O}(1)$GeV and the large annihilation cross-section simultaneously. In those models, the sub-GeV dark photon often plays an essential role in transferring the excessive entropy in the dark sector into the visible sector, i.e., the Standard Model sector. This paper constructs a chiral composite ADM model where the $U(1)_D$ gauge symmetry is embedded into the chiral flavor symmetry. Due to the dynamical breaking of the chiral flavor symmetry, the model naturally provides the masses of the dark photon and the dark pions in the sub-GeV range, both of which play crucial roles for a successful ADM model.

Bibliography

[1] M. Ibe, S. Kobayashi and K. Watanabe, JHEP **07** (2021), 220 doi:10.1007/JHEP07(2021)220 [arXiv:2105.07642

[hep-ph]].

Particle Cosmology

[Spokesperson : M. Kawasaki]
ICRR, The Univ. of Tokyo, Kashiwa, Chiba 277-8582

Beyond Standard Model

• Lepton Asymmetric Universe [1]

In collaboration with the members of ICRR, Kavli IPMU

The recent observation of ^{4}He implies that our universe has a large lepton asymmetry. We consider the Affleck-Dine (AD) mechanism for lepton number generation. In the AD mechanism, non-topological solitons called L-balls are produced, and the generated lepton number is confined in them. The L-balls protect the generated lepton number from being converted to baryon number through the sphaleron processes. We study the formation and evolution of the L-balls and find that the universe with large lepton asymmetry suggested by the recent ^{4}He measurement can be realized.

Bibliography

[1] M. Kawasaki and K. Murai, [arXiv:2203.09713 [hep-ph]].

Inflation

• Gravitational wave trispectrum in the axion-SU(2) model [1]

In collaboration with the members of Waseda Univ, RESCEU, ICRR, Kavli IPMU, Max Planck Institute, NIT Kagawa

We study the trispectrum of the gravitational waves (GWs) generated through the dynamics of an axionic spectator field and SU(2) gauge fields during inflation. In non-Abelian gauge theory, the gauge fields have four-point self-interactions, which induce the tree-level GW trispectrum. We formulate this type of the GW trispectrum including the non-dynamical contributions and evaluate it in the equilateral limit as a unique signal of this model. We find that the ratio of the GW trispectrum to the cube of the scalar power spectrum can be as large as $\mathcal{O}(10^6)$ in the viable parameter space, which could be captured in the CMB observations.

• SU(N) natural inflation [2]

In collaboration with the members of Waseda Univ, RESCEU, KEK, SOKENDAI, ICRR, Kavli IPMU

We study SU(N) gauge fields that couple to the inflaton through the Chern-Simons term. We provide a general procedure to construct homogeneous, isotropic, and attractor solutions of the gauge fields during inflation. The gauge fields develop various VEVs corresponding to different spontaneous symmetry breaking patterns of SU(N) where embedded SU(2) subgroups are broken with the spatial rotation SO(3) symmetry. As specific examples, we construct the stable solutions for $N = 3$ and 4. We also numerically solve the gauge field dynamics and confirm that our analytic solutions are complete and attractor. It is straightforward to apply our procedure to the other simple Lie groups.

• Gauge field production and Schwinger reheating in runaway axion inflation [3]

In collaboration with the members of Univ. of Tokyo, RESCEU, ICRR

In a class of (pseudoscalar) inflation, inflationary phase is followed by a kination phase, where the Universe is dominated by the kinetic energy of the inflaton that runs away in a vanishing scalar potential. In this class of postinflationary evolution of the Universe, reheating of the Universe cannot be achieved by the inflaton particle decay, which requires its coherent oscillation in a quadratic potential. In this study, we explore the U(1) gauge field production through the Chern-Simons coupling between the pseudoscalar inflaton and the gauge field during the kination era and examine the subsequent pair-particle production induced by the amplified gauge field known as the Schwinger effect, which can lead to reheating of the Universe. We find that with a rough estimate of the Schwinger effect for the Standard Model hyper U(1) gauge field and subsequent thermalization of the pair-produced particles, a successful reheating of the Universe can be achieved by their eventual domination over the kinetic energy of the inflaton, with some reasonable parameter sets. This can be understood as a concrete realization of the "Schwinger reheating". Constraints from the later-time cosmology are also discussed.

• Inflation with two-form field: the production of primordial black holes and gravitational waves [4]

In collaboration with the members of Waseda Univ., RESCEU, ICRR, Max Planck Institute, Leiden Univ.

Antisymmetric tensor field (two-form field) is a ubiquitous component in string theory and generally couples to the scalar sector through its kinetic term. In this paper, we propose a cosmological scenario that the particle production of two-form field, which is triggered by the background motion of the coupled inflaton field, occurs at the intermediate stage of inflation and generates the sizable amount of primordial black holes as dark matter after inflation. We also compute the secondary gravitational waves sourced by the curvature perturbation and show that the resultant power spectra are testable with the future space-based laser interferometers.

• Universality of linear perturbations in SU(N) natural inflation [5]

In collaboration with the members of Waseda U., RESCEU, ICRR, Kavli IPMU, RIKEN

We prove the universality of predictions for linear perturbations from the entire class of models of inflation driven by a pseudo-scalar field coupled to an SU(N) gauge boson, where SU(2) subgroups in the SU(N) crossed with the background spatial SO(3) spontaneously break into a single SO(3). The effect of which SU(2) subgroup in SU(N) acquires a VEV through spontaneous symmetry breaking can be quantified by a single parameter λ, which always appears in combination with the gauge coupling constant g. In the linear perturbations, as well as the background system, the same dynamics and predictions as in the chromo-natural inflation hold for its SU(N) extension by replacing $g \to g\lambda$. The latter models thereby draw the same prediction curve on the n_s-r plane as the former at the tree level as long as $g\lambda$ stays constant during inflation. We briefly discuss possible transitions from one value of λ to another during inflation and the observational prospects.

• Gravitational waves detectable in laser interferometers from axion-SU(2) inflation [6]

In collaboration with the members of Waseda U., RESCEU, ICRR

Chromo-natural inflation (CNI) is an inflationary model where an axion coupled with SU(2) gauge fields acts as the inflaton. In CNI, the gauge fields have nonzero vacuum expectation values (VEVs), which results in the enhancement of gravitational waves (GWs). The original CNI is ruled out by the Planck observations due to the overproduction of GWs. In this work, we consider an inflationary model where the gauge fields acquire nonzero VEVs after the CMB modes exit the horizon. Moreover, we add to the model another field that dominates the universe and drives inflation after the axion starts to oscillate and the gauge field VEVs vanish. By performing numerical simulations, we find a parameter space where the enhanced GWs do not violate the CMB constraints and can be detected by the future GWs observations such as LISA, BBO, and ET.

Bibliography

[1] T. Fujita, K. Murai, I. Obata and M. Shiraishi, JCAP **01** (2022) no.01, 007 doi:10.1088/1475-7516/2022/01/007 [arXiv:2109.06457 [astro-ph.CO]].

[2] T. Fujita, K. Mukaida, K. Murai and H. Nakatsuka, Phys. Rev. D **105** (2022) no.10, 103519 doi:10.1103/PhysRevD.105.103519 [arXiv:2110.03228 [hep-ph]].

[3] S. Hashiba, K. Kamada and H. Nakatsuka, JCAP **04** (2022) no.04, 058 doi:10.1088/1475-7516/2022/04/058 [arXiv:2110.10822 [hep-ph]].

[4] T. Fujita, H. Nakatsuka, I. Obata and S. Young, [arXiv:2202.02401 [astro-ph.CO]].

[5] T. Fujita, K. Murai and R. Namba, Phys. Rev. D **105** (2022) no.10, 103518 doi:10.1103/PhysRevD.105.103518 [arXiv:2203.03977 [hep-ph]].

[6] T. Fujita, K. Imagawa and K. Murai, [arXiv:2203.15273 [astro-ph.CO]].

Axions

• Axion dark matter search using arm cavity transmitted beams of gravitational wave detectors [1]

In collaboration with the members of JAXA, ICRR, Univ. of Wisconsin-Milwaukee, Waseda Univ., Univ. of Tokyo, PRESTO, Max Planck Institute

Axion is a promising candidate for ultralight dark matter which may cause a polarization rotation of laser light. Recently, a new idea of probing the axion dark matter by optical linear cavities used in the arms of gravitational wave detectors has been proposed [Phys. Rev. Lett. 123, 111301 (2019)]. In this article, a realistic scheme of the axion dark matter search with the arm cavity transmission ports is revisited. Since photons detected by the transmission ports travel in the cavity for odd-number of times, the effect of axion dark matter on their phases is not cancelled out and the sensitivity at low-mass range is significantly improved compared to the search using reflection ports. We also take into account the stochastic nature of the axion field and the availability of the two detection ports in the gravitational wave detectors. The sensitivity to the axion-photon coupling, $g_{a\gamma}$, of the ground-based gravitational wave detector, such as Advanced LIGO, with 1-year observation is estimated to be $g_{a\gamma} \sim 3 \times 10^{-12}$ GeV^{-1} below the axion mass of 10^{-15} eV, which improves upon the limit achieved by the CERN Axion Solar Telescope.

• Free Streaming Length of Axion-Like Particle After Oscillon/ I-ball Decays [2]

In collaboration with the members of ICRR, Kavli IPMU

Axion-like particles (ALPs) are pseudoscalar bosons predicted by string theory. The ALPs have a shallower potential than a quadratic one, which induces the instability and can form the solitonic object called oscillon/I-ball. Although the lifetime of oscillons can be very long for some type of potentials, they finally decay until the present. We perform the numerical lattice simulations to investigate the decay process of oscillons and evaluate the averaged momentum of ALPs emitted from the oscillon decay. It is found that, if oscillons decay in the early universe, the free-streaming length of ALPs becomes too long to explain the small-scale observations of the matter power spectrum. We show that oscillons with long lifetimes can change the density fluctuations on small scales, which leads to stringent constraints on the ALP mass and the oscillon lifetime.

• Anisotropies in Cosmological 21 cm Background by Oscillons/I-balls of Ultra-light Axion-like Particle [3]

In collaboration with the members of ICRR, Kavli IPMU

Ultra-light axion-like particle (ULAP) with mass $m \sim 10^{-22}$ eV has recently been attracting attention as a possi-

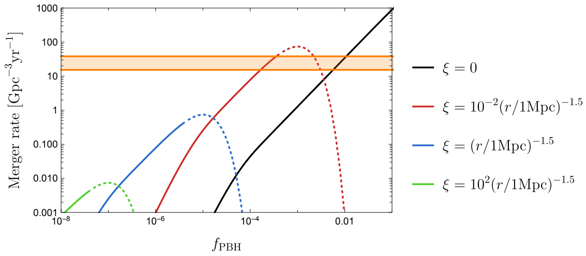

Fig. 15. The merger rate distribution of PBHs with the mass 30 $M_\odot$ and the abundance f_{PBH}. The orange line is the observed merger rate of LIGO-VIRGO experiment, $\mathscr{R} = 23.9^{+14.3}_{-8.6}\ \mathrm{Gpc}^{-3}\mathrm{yr}^{-1}$. The different lines represent the significance of the clustering with $\xi = \xi_*(r/1\mathrm{Mpc})^{-2}$. The dotted lines represent the condition $r_{\mathrm{mean}} < y_t(x_t)$, where PBHs are produced too close to avoid three–body problem.

ble solution to the small-scale crisis. ULAP forms quasi-stable objects called oscillons/I-balls, which can survive up to a redshift $z \sim 10$ and affect the structure formation on a scale $\sim \mathscr{O}(0.1)$ Mpc by amplifying the density fluctuations. We study the effect of oscillons on 21 cm anisotropies caused by neutral hydrogen in minihalos. It is found that this effect can be observed in a wide mass range by future observations such as Square Kilometer Array (SKA) if the fraction of ULAP to the total dark matter density is $\mathscr{O}(0.01–0.1)$.

Bibliography

[1] K. Nagano, H. Nakatsuka, S. Morisaki, T. Fujita, Y. Michimura and I. Obata, Phys. Rev. D **104** (2021) no.6, 062008 doi:10.1103/PhysRevD.104.062008 [arXiv:2106.06800 [hep-ph]].

[2] K. Imagawa, M. Kawasaki, K. Murai, H. Nakatsuka and E. Sonomoto, [arXiv:2110.05790 [hep-ph]].

[3] M. Kawasaki, K. Miyazaki, K. Murai, H. Nakatsuka and E. Sonomoto, [arXiv:2112.10464 [astro-ph.CO]].

Primordial Black Holes

• Strong clustering of primordial black holes from Affleck-Dine mechanism [1]

In collaboration with the members of ICRR, Kavli IPMU

Primordial black hole (PBH) is a fascinating candidate for the origin of binary merger events observed by LIGO-Virgo collaboration. The spatial distribution of PBHs at formation is an important feature to estimate the merger rate. We investigate the clustering of PBHs formed by Affleck-Dine (AD) baryogenesis, where dense baryon bubbles collapse to form PBHs. We found that formed PBHs show a strong clustering due to the stochastic dynamics of the AD field. Including the clustering, we evaluate the merger rate and isocurvature perturbations of PBHs, which show significant deviations from those without clustering.

Bibliography

[1] M. Kawasaki, K. Murai and H. Nakatsuka, JCAP **10** (2021), 025 doi:10.1088/1475-7516/2021/10/025 [arXiv:2107.03580 [astro-ph.CO]].

Big Bang Nucleosynthesis

• EMPRESS. VIII. A New Determination of Primordial He Abundance with Extremely Metal-Poor Galaxies: A Suggestion of the Lepton Asymmetry and Implications for the Hubble Tension [1]

In collaboration with the members of ICRR, Univ. of Tokyo, NAOJ, Kavli IPMU, Univ. College London, Waseda Univ., SOKENDAI, Osaka Univ., Univ. of Nevada, Univ. of Geneva, Univ. of Notre Dame, Tohoku Univ., Monash Univ., Kitami Institute of Technology, Cosmic DAWN Center, Niels Bohr Institute, Ichinoseki College, Osaka Sangyo Univ., RESCEU, Carnegie Observatories, Univ. of Hyogo, Nagoya Univ., Univ. of Tsukuba, Univ. of Arizona

The primordial He abundance Y_P is a powerful probe of cosmology. Currently, Y_P is best determined by observations of metal-poor galaxies, while there are only a few known local extremely metal-poor ($< 0.1 Z_\odot$) galaxies (EMPGs) having reliable He/H measurements with HeIλ10830 near-infrared (NIR) emission. Here we present deep Subaru NIR spectroscopy and He/H determinations for 10 EMPGs, combining the existing optical data and the Markov chain Monte Carlo algorithm. Adding the existing 3 EMPGs and 51 moderately metal-poor ($0.1 - 0.4 Z_\odot$) galaxies with reliable He/H estimates, we obtain $Y_P = 0.2379^{+0.0031}_{-0.0030}$ by linear regression in the (He/H)-(O/H) plane, where our observations increase the number of EMPGs from 3 to 13 anchoring He/H of the most metal-poor gas in galaxies. Although our Y_P measurement and previous measurements are consistent, our result is slightly (1σ) smaller due to our EMPGs. Including the existing primordial deuterium D_P constraints, we estimate the effective number of neutrino species to be $N_{eff} = 2.41^{+0.19}_{-0.21}$ showing a ¿ 2 σ tension with the Standard Model value ($N_{eff} = 3.046$), which may be a hint of an asymmetry in electron-neutrino ν_e and anti-electron neutrino $\bar{\nu}_e$. Allowing the degeneracy parameter of electron-neutrino ξ_e to vary as well as N_{eff} and the baryon-to-photon ratio η, we obtain $\xi_e = 0.05^{+0.03}_{-0.03}$, $N_{eff} = 3.22^{+0.33}_{-0.30}$, and $\eta \times 10^{10} = 6.13^{+0.04}_{-0.04}$ from the Y_P and D_P measurements with a prior of η taken from Planck Collaboration et al. (2020). Our constraints suggest a $\nu_e - \bar{\nu}_e$ asymmetry and allow for a high value of N_{eff} within the 1σ level, which could mitigate the Hubble tension.

Bibliography

[1] A. Matsumoto, M. Ouchi, K. Nakajima, M. Kawasaki, K. Murai, K. Motohara, Y. Harikane, Y. Ono, K. Kushibiki and S. Koyama, *et al.* [arXiv:2203.09617 [astro-ph.CO]].

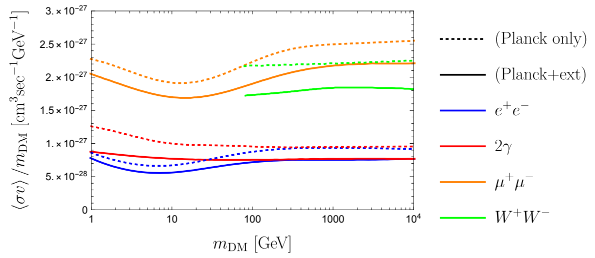

Fig. 16. CMB constraints on the annihilation cross section for four decay channels of dark matter. We plot the 95% exclusion contours of $\langle\sigma v\rangle/m_{\rm DM}$ (vertical axes) for mass of dark matter (horizontal axes). We calculate the posterior distribution using two sets of data: "Planck only" uses the Planck CMB data for TT-, TE- and EE-modes and "Planck+ext" uses BAO, DES, and the CMB lensing power spectrum data in addition to the Planck CMB data.

CMB

• Revisiting CMB constraints on dark matter annihilation [1]

In collaboration with the members of ICRR, Kavli IPMU, Univ. of Tokyo, KEK

The precision measurements of the cosmic microwave background power spectrum put a strong constraint on the dark matter annihilation cross section since the electromagnetic energy injection by the dark matter annihilation affects the ionization history of the universe. In this paper, we update our previous simulation code for calculating the ionization history with the effect of dark matter annihilation by including Helium interactions and improving the precision of calculations. We give an updated constraint on the annihilation cross section and mass of dark matter using the modified RECFAST code with the Planck 2018 datasets.

• Constraints on small-scale primordial density fluctuation from cosmic microwave background through dark matter annihilation [2]

In collaboration with the members of ICRR, Kavli IPMU, Tohoku Univ, Univ. of Tokyo

The cosmic microwave background (CMB) observation by the Planck satellite precisely determines primordial curvature fluctuations on larger scales than $\mathscr{O}(1)$ Mpc, while the small-scale curvature fluctuation is still less constrained. The constraint on small-scale fluctuations is highly improved if we assume the standard thermal relic dark matter scenario. When small-scale fluctuations are large enough, dense regions collapse to form small halos even in a redshift $z \gtrsim 10^3$, which is called ultracompact minihalos. These minihalos enhance the annihilation of the dark matter and it is constrained by observations such as extragalactic gamma rays and the CMB. We revisit the effect of minihalos formed by the small-scale density fluctuations and calculate the ionization history modified by the dark matter annihilation. We perform the Markov Chain Monte Carlo method to constrain the size of small-scale curvature fluctuations by the CMB power spectrum. It is found that the constraint from the CMB power spectrum is comparable to that from the extragalactic gamma rays. We confirm that our constraint mainly comes from the energy injection in early time ($z \gtrsim 100$) and hence it is independent of the uncertainty of minihalo properties in the late time.

• Is cosmic birefringence due to dark energy or dark matter? A tomographic approach [3]

In collaboration with the members of ICRR, Kavli IPMU, Max Planck Institute

A pseudoscalar "axionlike" field, ϕ, may explain the 3σ hint of cosmic birefringence observed in the EB power spectrum of the cosmic microwave background (CMB) polarization data. Is ϕ dark energy or dark matter? A tomographic approach can answer this question. The effective mass of dark energy field responsible for the accelerated expansion of the Universe today must be smaller than $m_\phi \simeq 10^{-33}$ eV. If $m_\phi \gtrsim 10^{-32}$ eV, ϕ starts evolving before the epoch of reionization and we should observe different amounts of birefringence from the EB power spectrum at low ($l \lesssim 10$) and high multipoles. Such an observation, which requires a full-sky satellite mission, would rule out ϕ being dark energy. If $m_\phi \gtrsim 10^{-28}$ eV, ϕ starts oscillating during the epoch of recombination, leaving a distinct signature in the EB power spectrum at high multipoles, which can be measured precisely by ground-based CMB observations. Our tomographic approach relies on the shape of the EB power spectrum and is less sensitive to miscalibration of polarization angles.

Bibliography

[1] M. Kawasaki, H. Nakatsuka, K. Nakayama and T. Sekiguchi, JCAP **12** (2021) no.12, 015 doi:10.1088/1475-7516/2021/12/015 [arXiv:2105.08334 [astro-ph.CO]].

[2] M. Kawasaki, H. Nakatsuka and K. Nakayama, JCAP **03** (2022) no.03, 061 doi:10.1088/1475-7516/2022/03/061 [arXiv:2110.12620 [astro-ph.CO]].

[3] H. Nakatsuka, T. Namikawa and E. Komatsu, Phys. Rev. D **105** (2022) no.12, 123509 doi:10.1103/PhysRevD.105.123509 [arXiv:2203.08560 [astro-ph.CO]].

Observational Cosmology

• Physics of star-formation history and the luminosity function of galaxies therefrom [1]

In collaboration with the members of ICRR, Kavli IPMU

We show that the star formation history, the reionization history and the present luminosity function of galaxies are reproduced in a simple gravitational collapse model within the ΛCDM regime to almost a quantitative accuracy, when the physical conditions, the Jeans criterion and the cooling process, are taken into account. Taking a reasonable set of the model parameters, the reionisation takes place sharply at around redshift $1+z \simeq 7.5$, and the resulting luminosity function turns off at $L \simeq 10^{10.7} L_\odot$, showing the consistency between the star formation history and the reionisation of the Universe. The model gives the total amount of stars $\Omega_{\rm star} = 0.004$ in units of the critical density compared to the observation 0.0044 with the recycling factor 1.6 included. In order to account for the observed star formation rate and the present luminosity function, the star formation efficiency is not halo mass independent but becomes maximum at the halo mass $\simeq 10^{12} M_\odot$ and is suppressed for both smaller and larger mass haloes.

Bibliography

[1] M. Fukugita and M. Kawasaki, Mon. Not. Roy. Astron. Soc. **513** (2022) no.1, 8-14 doi:10.1093/mnras/stac774 [arXiv:2111.01389 [astro-ph.GA]].

OBSERVATORIES and A RESEARCH CENTER

Location of the Institute and the Observatories

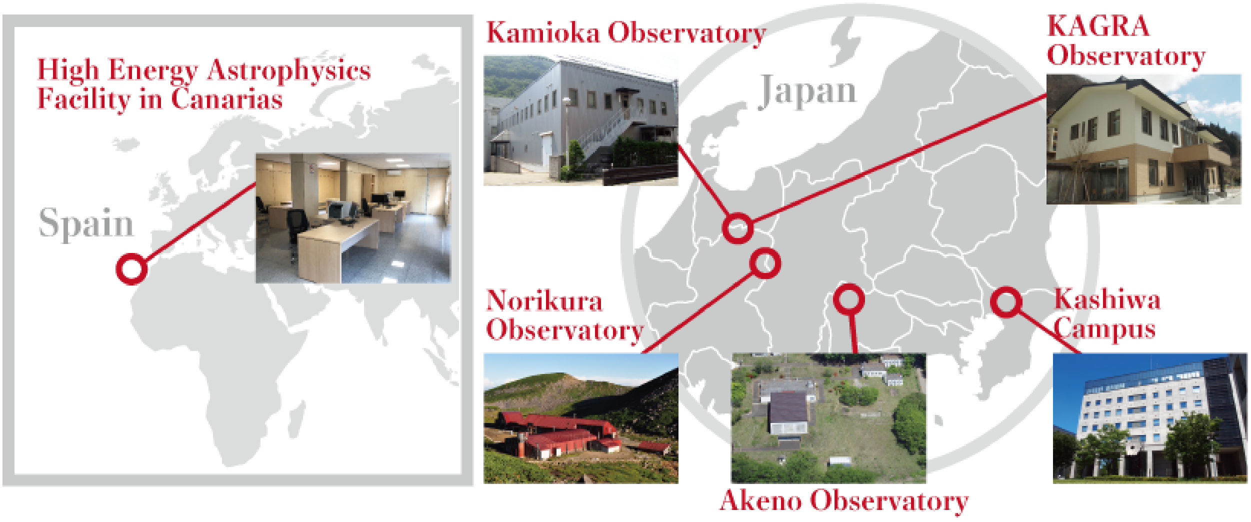

Norikura Observatory

Location:	Norikuradake, Nyukawa-cho, Takayama-shi, Gifu Prefecture 506-2100
Telephone (Fax):	+81-50-3730-3809
Telephone (satellite):	+81-90-7721-5674
Telephone (car):	+81-90-7408-6224

Akeno Observatory

Location:	5259 Asao, Akeno-machi, Hokuto-shi, Yamanashi Prefecture 408-0201
Telephone / Fax:	+81-551-25-2301 / +81-551-25-2303

Kamioka Observatory

Location:	456 Higashi-mozumi, Kamioka-cho, Hida-shi, Gifu Prefecture 506-1205
Telephone / Fax:	+81-578-85-2116 / +81-578-85-2121

KAGRA Observatory

Location:	238 Higashi-mozumi, Kamioka-cho, Hida-shi, Gifu Prefecture 506-1205
Telephone / Fax:	+81-578-85-2343 / +81-578-85-2346

Research Center for Cosmic Neutrinos

Location:	5-1-5 Kashiwanoha, Kashiwa, Chiba Prefecture 277-8582
Telephone / Fax:	+81-4-7136-3138 / +81-4-7136-3115

High Energy Astrophysics Facility in Canarias

Location:	C/Via Lactea, s/n E-38205 La Lagua - Tenerife Espana

NORIKURA OBSERVATORY

Introduction

Norikura Observatory (36.10°N and 137.55°E) was founded in 1953 and attached to ICRR in 1976. It is located at 2770 m above sea level, and is the highest altitude manned laboratory in Japan (Fig. 1). Experimental facilities of the laboratory are made available to all the qualified scientists in the field of cosmic ray research and associated subjects. The AC electric power is generated by the dynamo and supplied throughout the observatory. The observatory can be accessed easily by car and public bus in summer (July-September). The 60th anniversary of Norikura Observatory was celebrated in 2013.

Fig. 1. Norikura Observatory

Norikura Observatory gave manned operation to the observations by the qualified scientists all the year until the year 2003. However, the feasibility of the automatic operation of Norikura Observatory during winter period has been tested since winter 2004 in order to study the possibilities to reduce maintenance and labor costs without causing serious inconveniences for the researches. A long-distance (∼40km) wireless LAN system (11M bps) was set up in 2003. Two new easy-to-handle and easy-to-maintain dynamos of 115 KVA each, as shown in Fig. 2 were installed in 2004 as well. The unmanned operation of Norikura Observatory has been mostly successful in winter, during which the battery backed-up solar panels and/or wind power generators kept supplying the electricity to the wireless LAN and on-going cosmic-ray experiments.

Present major scientific interests of the laboratory is focused on the modulation of high energy cosmic rays in the interplanetary space associated with the solar activity, the generation of energetic particles by the solar flares, and the particle acceleration mechanism in thunderclouds, all of which require long-term observation. These researches have been carried out by the group of user universities, where ICRR provides them with laboratory facility. A part of the facility has been open for the environmental study at high altitude such as aerosol-related mechanism in the atmosphere, observation of total ozone and UV solar radiation, for botanical study in the high-altitude environment, etc..

Fig. 2. A dynamo of 115KV.

Cosmic Ray Physics

Space weather observation

Space weather observation is actively made by a 25 m^2 muon hodoscope at Norikura Observatory[1],[2],[3],[4],[5],[6],[7],[8],[9],[10]. Mt. Norikura muon hodoscope has started operation in May, 1998 and successfully observed a clear precursory signature of the interplanetary shock arrival at Earth. With its improved angular resolution of muon incident direction, the detector succeeded for the first time to observe a loss-cone signature which is an intensity deficit within a narrow cone around the interplanetary magnetic field (IMF). The observation of the loss-cone precursor gives us unique information for the space weather forecast and for understanding the interplanetary disturbances in near Earth space.

Following this successful observation, we installed a small muon hodoscope in Kuwait City, Kuwait as the fourth detector in our Global Muon Detector Network (GMDN) with other three multidirectional muon detectors in Nagoya (Japan), Hobart (Australia), and São Martinho (Brazil). The GMDN has started operation in March, 2006 monitoring the intensity of ~ 50 GeV cosmic rays over an entire sky around Earth. The cosmic ray observations using muon detector are complementary to observations with neutron monitors monitoring a lower energy range below ~ 10 GeV and the observations with GMDN have a great advantage particularly in precise measurement of the cosmic ray anisotropy, i.e. the dependence of intensity on incident direction in space, which gives us valuable information of the spatial distribution of the cosmic ray density in three dimensions. The Mt. Norikura muon hodoscope and GMDN have revealed the dynamic variations of the anisotropy which give us important information of the space weather. It has been already confirmed that the GMDN can measure the rapid variation of the anisotropy in the "cosmic ray burst" observed in June 2015 in 10 minute time resolution. The Kuwait muon hodoscope was enlarged three times in March 2016 and one minute data are now available from all of four detectors in the GMDN enabling us to analyze the anisotropy in 1 minute time resolution.

Recently, we also developed the method of the correction of the atmospheric temperature effect on muon count rate by using the GMDN data. This is a significant step, because it makes possible for the first time the analysis of the long-term variation of $\sim$ 50 GeV cosmic ray density (i.e. isotropic intensity) which was possible so far only for cosmic ray below $\sim$ 10 GeV using the neutron monitor data nearly free from the temperature effect. We have already published the long-term variation of the anisotropy observed by Nagoya muon detector.

Solar neutron observation

Observation of solar neutrons in solar cycle 24 has continued at Norikura Observatory of ICRR since fiscal 2007 to understand the acceleration mechanism of high energy (>100 MeV) ions associated with solar flares[11]. These neutrons are produced by the interaction between accelerated ions and the solar atmosphere. Neutrons are not reflected by the interplanetary magnetic field, and thought to be more informative than accelerated ions themselves to study the acceleration mechanism at the solar surface. Solar neutron events detected on the ground are rare, and about 10 events were reported before solar cycle 24. The group led by Institute for Space-Earth Environmental Research, Nagoya University has operated a worldwide network of 7 solar neutron telescopes in the world. The solar neutron telescope operated at Norikura Observatory has an area of 64 m^2, which is largest among the 7 stations. The solar neutron telescope at Norikura consists of plastic scintillation detector and proportional counters. The neutron is detected when a recoil proton is produced in the scintillator, and the energy of the recoil proton is measures. Proportional counters are used both to veto charged particles and measure the direction of recoil protons. The telescope is operated by solar power during the winter period when the Norikura observatory is closed.

Solar cycle 24 was its maximum in February 2014 and has decreased its activity since then. We searched for solar neutron signals from the world-wide network of the solar neutron telescopes between January 2010 and December 2014 when the large ($\geq$X1.0 class) solar flare occurred. No solar neutron event was detected by this search. We statistically studied the relation between upper limits of the neutron flux and the energy of soft X-rays during the solar flare. This comparison was also made for the successful detections of solar neutrons before solar cycle 24. The conclusion from this study is that the total energy obtained by neutrons during solar flare does not exceed 0.1 % of the total energy of soft X-rays.

Relativistic electron acceleration in thunderstorm electric field and high-energy atmospheric phenomena at lightning

The Gamma-Ray Observation of Winter THundercloud (GROWTH) collaboration is aiming at revealing high-energy atmospheric phenomena occurring at lightning and in thunderstorms[12],[13],[14],[15],[16]. The project started in 2006 and has detected bremsstrahlung gamma rays from relativistic electrons accelerated by strong electric fields in winter thunderstorms. This gamma-ray radiation events were named "long burst" by our group (as known as gamma-ray glow), which lasts for a minute time-scale corresponding with passage of a thundercloud above our detectors. Winter thunderstorms observed along the Japan sea are ideal targets for our observation campaigns thanks to its low altitude of the cloud base and frequent energetic lightning, while observations of summer thunderclouds at mountain tops are also important to measure the phenomena very close to or even inside thunderstorms. Our collaboration has used the Mount Norikura cosmic ray observatory to study the long bursts, and successfully recorded events.

The GROWTH collaboration newly launched multi-point mapping observation campaigns in 2015. The primary purpose is to study life cycle of the electron acceleration sites in thunderstorms comparing with weather-monitoring data. Another purpose of the project is to reveal mysterious "short burst" events, which have been sometimes detected in our past observations, associated with lightning discharges with its duration shorter than a second. Financially supported by the ICRR joint research programme, academic crowdfunding "academist", and JSPS/MEXT KAKENHI grant, we have developed portable and high-performance radiation detectors. In FY2016 and FY2017, the collaboration deployed radiation detectors at the Mt. Norikura cosmic ray observatory. So far, there is no detection of "long burst" nor "short burst" events from summer thunderclouds during the two years. However, we successfully used these summer campaigns as pilot observations toward the winter campaigns to check our operation and capability of the detectors. The Norikura observations are also educationally important as a training yard for Ph.D students in the team. In 2017 winter, our new mapping system at Kashiwazaki, Niigata, provided us a chance to solve the mystery of the short burst. This phenomena is revealed to be photonuclear reaction triggered by gamma rays from a lightning discharge. This discovery was selected, by the Physics World, as one of the top 10 breakthrough in the physics field in 2017. We are now trying to develop the "high-energy atmospheric physics" of lightning and thunderstorms, a new interdisciplinary field combining the gamma-ray and radio observations.

Study of Secondary Cosmic Rays from Thundercloud at Mt. Norikura

In order to study the relativistic electron acceleration mechanism by thundercloud-derived electric field and the relation between thunder and cosmic-ray air shower, we started an experiment in 2015, mainly using gamma-ray detectors at Norikura Observatory of Institute for Cosnic Ray Research, the University of Tokyo. This experiment consists of gamma-ray detectors, a lightning sensor, an electric field meter, a weather monitor, and an air shower array. Gamma-ray detectors using three crystals, NaI, CsI, and BGO respectively, cover the energy range over 3 orders of magnitude from 70 keV to 120 MeV as a whole.

Observation period: 22 days from August 24 to September 14, 2015
During this time, the thundercloud did not pass, and no gamma-ray burst derived from thundercloud was detected. However, the gamma ray detector was able to observe gamma rays derived from radon of less than 3 MeV as expected during rainfall. Also, gamma ray detectors using CsI and BGO for detecting gamma rays of 3 MeV or more did not observe an increase in gamma rays of 3 MeV or more. This means that gamma rays from radon can be distinguished from contributions from other gamma rays not derived from radon, and it can be expected that these detectors can operate normally even when they are installed at an altitude about 4000 m for a certain future project.

Observation period: 30 days from July 19 to September 16, 2016 (excluding the summer season)
No direct lightning strike event occurred during the observation period, but 6 atmospheric electric field fluctuations exceeding 30 kV/m, which seemed to be an influence of thunder cloud passage, were observed. In one of the events, it seems there was a lightning strike in the vicinity.

Observation period: 41 days from July 31 to September 9, 2017
Unfortunately, during this observation period there was no lightning strike nearby, but it was observed that the thundercloud passed several times. Currently, the data at the time of the thundercloud passing is being analyzed in detail (Fig. 3).

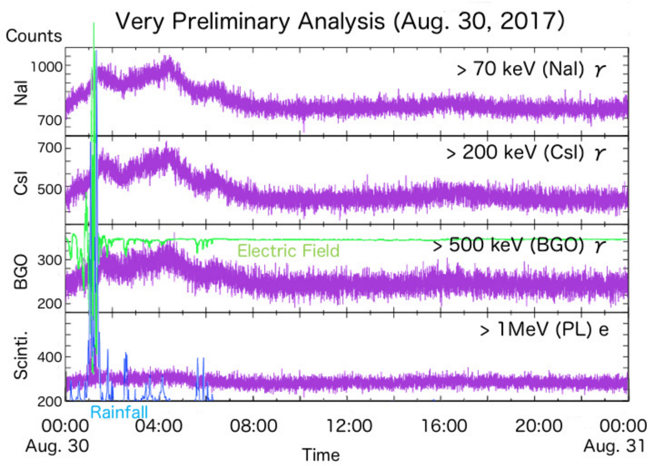

Fig. 3. Electric field (green), rainfall (blue), count value (purple) of each detector at the time of thundercloud passing.

Study of gamma ray bursts from mountain-top thunderclouds

We observed gamma ray bursts that arise in relation to thunderclouds at the Norikura Observatory of ICRR(2,770 m above sea level)[17],[18],[19],[20]. Measurement was carried out by placing PANDA64 detector outdoors of the observatory. The detector is made of 64-module plastic scintillators(total mass about 640 kg) developed for reactor operation monitoring. Our measurement has unprecedented features including high statistics, good energy response, direction sensitivity and neutron identification.

Long-duration persistent bursts were observed 12 times in 54 days from July to September 2014 and their energy spectrum extended up to 25 MeV in the largest burst. The duration of the bursts ranged from a few to ten minutes. Since these bursts were found in the energy range higher than 3 MeV, they were not attributed to the rain fallout of radon and its daughter nuclei.

According to the thundercloud information provided by the Japan Meteorological Agency, the bursts were observed when there was thunder activity near the observatory. The observation is qualitatively in good agreement with thundercloud radiation bursts previously observed in mountain areas or coastal areas of the Sea of Japan.

Monte Carlo simulation showed that the bremsstrahlung γ-rays by source electrons with monochromatic energy of 40–80 MeV falling downwards from altitude of 400–1000 m produced the observed total energy spectra of the bursts well. It is supposed that secondary cosmic ray electrons, which act as seed, were accelerated in electric field of thunderclouds and multiplied by relativistic runaway electron avalanche.

The estimated energy of the source electrons was higher than that of the bursts we previously observed at Ohi Power Station at sea level. Additionally, estimated electron flux at the estimated source height was remarkably lower than that of the Ohi site. These results give new restrictions to the model of electron acceleration and multiplication process in electric field of thunderclouds.

Development of high energy proton irradiation technique for devices used in spaceship

Space exploration is presently interesting in business field. Ion beam irradiation verification for devices to be mounted on spaceships is required to simulate cosmic rays expected in the universe to estimate lifetime of these devices[21],[22],[23],[24].

Flux estimation technique of primary ion beam in wide range from an accelerator is needed In this kind of cosmic ray simulation field. The desired flux of the ion beam for this kind of field is between 10^2 and 10^6 protons$\cdot$cm^{-2} $\cdot$s^{-1} in typical proton cases. Plastic scintillators can be used in lower intense region to count direct primary ions, while ionization chambers can be used in higher intense region to count ionization caused by primary ions. But there have been no definite modalities available to measure throughout this whole intensity region.

One of the candidate techniques is to measure secondary γ-ray intensity emitted through a beam transport, which has nearly a maximum energy of the primary ion beam around 100 MeV for this kind of simulation field. This technique has a feature that detector components do not occupy the beam path and the presence of the detector do not influence the main simulation field at all.

NaI(Tl) scintillator system for high energetic γ-ray measurement which had been used in previous thunder lightning γ-ray measurement was used. This system has a 5-inch NaI(Tl) scintillator with NT100GPS pulse hight analysis system of Laboratory Equipment. Ion beam accelerator experiments using 100 MeV proton beam were carried out at the Wakasa Wan Energy Research Center (WERC). Background measurements were carried out at Norikura Observatory of ICRR in summer, where one can expect high energetic γ-ray, which has the similar energy region compared to the accelerator field of this study. EFM100 atmospheric electric field monitor system of Boltek was added at Norikura to measure accidental high energetic γ-rays caused by thunder lightning.

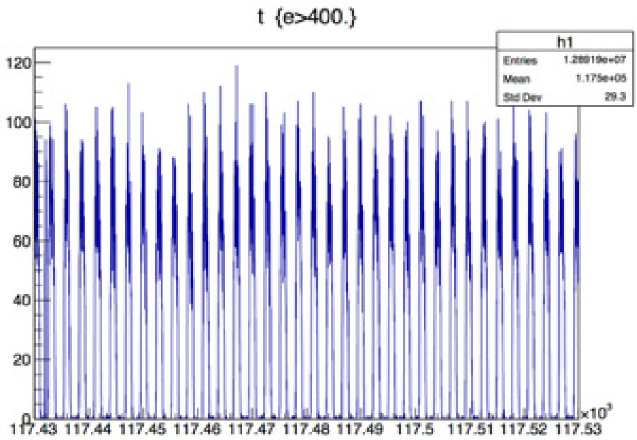

Fig. 4. Time structure of γ-ray above 3 MeV at WERC 100 MeV proton beam delivery. Vertical axis shows γ intensity (events/ms) while horizontal shows time after beginning of the operation (s).

As shown in Fig.4 of a time structure of γ-ray during 100 MeV proton beam delivery duration obtained at WERC, the result clearly shows that this measurement system can distinguish the beam ON/Off, while this system is still in verification for a quantitative discussion. The dead time of the system should be defined.

In the meantime, thunder lightning events were searched using data obtained at Norikura. No events have been distinguished. The whole data at Norikura show a stable condition of the whole system for a couple of months.

With the help of this study, the trial to carry out cosmic ray simulation at the ion beam accelerator facility (WERC) has been successfully carried out. One will keep trying to estimate the quantitative property of the system in ion beam environment.

Development of high energy proton irradiation technique for devices used in spaceship

Aircraft crew are exposed to elevated levels of cosmic rays at aviation since the dose rate of cosmic rays increases with altitude. The occupational doses of aircraft crew have generally been evaluated by model calculation. It is necessary to verify the calculation with measurements to maintain accuracy and credibility of dose assessment. The purposes of this study were to construct a compact and inexpensive cosmic-ray neutron monitoring system which was based on a rem-counter at Norikura Observatory (2770 m above sea level), and to examine the feasibility of it. The monitoring system was installed in the Norikura Observatory in 2014. It consisted of an extended-energy neutron rem counter with wide energy range from 25 meV to 5 GeV, a custom-made data logger connected to LAN, and a battery power unit. The measured data was received in National Institute of Radiological Science in Chiba-city via the ICRR network. This monitoring system succeeded in continuous monitoring more than ten months twice during 2014 to 2016. The averaged counting rate was about 1 count per minute, which was equivalent to neutron ambient dose equivalent rate of about 15 nSv/h by the preliminary evaluation. It is a future problem to reveal the cause of the reduction in counting rate seen over from November to April.

Evaluation of Response to the Gamma-ray of the Emulsion Telescope (2007, 2013)

GRAINE project (Gamma-Ray Astro-Imager with Nuclear Emulsion) has been developing the observation of cosmic γ-ray in the energy range 10 MeV–100 GeV with precise (0.08° at 1–2 GeV), polarization-sensitive, large-aperture-area ($\sim$10 m^2) balloon-borne telescope using nuclear emulsion film[25],[26],[27],[28],[29],[30],[31]. Under the development of the telescope, we performed test observation at Norikura Observatory (2770 m a.s.l.) in 2007 and 2013 using prototype emulsion telescope in order to confirm detection performance using atmospheric γ-ray.

2007 test was the first trial of the detection to the γ-ray spread wide incoming angle. We established configuration of the telescope and its analysis scheme. Based on this experience, we finalized the design of the first balloon-borne emulsion telescope and performed 1st balloon experiment (GRAINE 2011) at the Taiki Aerospace Research Field of JAXA in June 2011.

In 2013 test, we introduced self-produced nuclear emulsion gel film with higher volume occupancy of silver bromide crystals with respect to conventional ordinary gel in order to improve track finding efficiency as well as signal-to-noise ratio. We obtained high ($>$ 97%) track finding efficiency in a single film and confirmed γ-ray detection capability at 100 MeV energy region (Figure 5).
Based on this experience, we performed 2nd balloon experiment (obs/Norikura/GRAINE 2015) in Japan-Australia JAXA collaborative balloon experiment at the Alice Springs balloon-launching station in May 2015.

Environmental Study

Aerosol sampling at Mt. Norikura

Aerosol in the atmosphere has been sampled since 2013 at the Norikura observing site using air-samplers to investigate the production of cosmogenic nuclide ^{7}Be in a free troposphere above 2 km in the altitude. The aerosol size distribution of ^{7}Be was measured for the aerosols sampled by an Andersen sampler enable to separate aerosols to nine classes from 0.43 μm to 11 μm. The 81.7% of ^{7}Be was covered with the aerosol sizes less than 1.1 μm and the ^{7}Be with the aerosol sizes above 1.1 μm decrease with an exponential function. The ^{7}Be concentration at Mt. Norikura was approximately 9.4 times greater than that at the ground level in Yamagata-city (Fig.6.). Its ratio is almost consistent to a simulated ratio 8.8 of ^{7}Be productions due to secondary cosmic rays in the atmosphere by EXPACS. This experimental result is useful for an estimation of altitude distribution of cosmogenic nuclide.

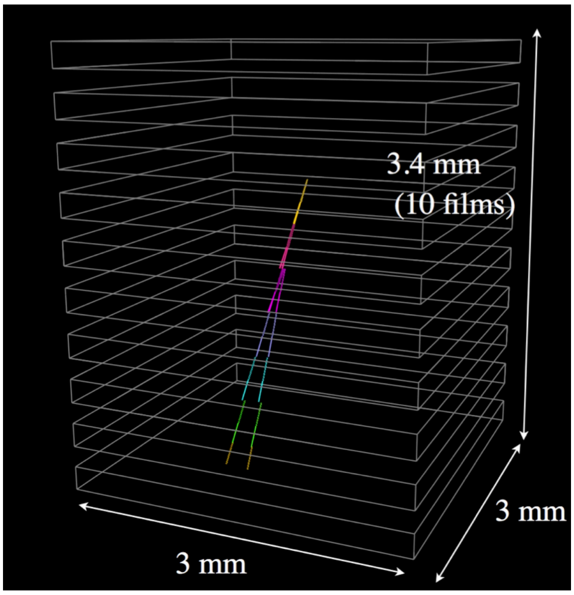

Fig. 5. 3-D view of $\gamma \to e^+ + e^-$ detected in the chamber employed in the observation test at Norikura Observatory. The reconstructed energy of this event was 160 MeV.

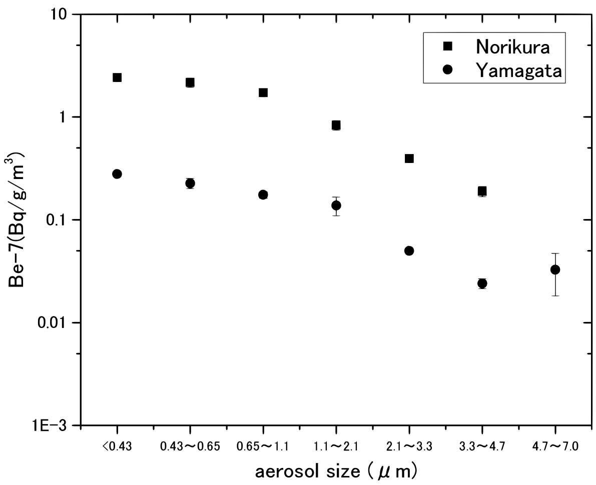

Fig. 6. ^{7}Be concentration as a function of aerosol size

Adaptation of alpine plants to severe environmental conditions

Trees in the alpine regions experience harsh conditions including strong winds, low temperatures, desiccation, and heavy snow. Thus, plants growing in such regions are predicted to have adaptations to these environmental stressors. Through the inter-university research of ICRR, we obtained an opportunity to intensively study plant responses to environmental factors. We identified several characteristics unique to alpine plants, some of which contradict conventional knowledges[32],[33],[34].

1. Adaptation of leaf cuticles in sub-alpine fir (Abies mariessii) at the alpine tree-line

Leaf browning and death are frequently observed in evergreen conifers at the alpine tree-line. These are thought to due to increased transpiration caused by a thinner cuticle and/or mechanical damage to the cuticle by wind-blown snow and ice particles. However, in the sub-alpine fir (Abies mariessii) at Mt. Norikura, mechanical damage was not observed, and the cuticle was rather thick, which may be an adaptation against overwintering at the alpine regions.

2. Embolism of sub-alpine fir (Abies mariessii) at the alpine tree-line

Trees at high altitudes experience severe embolism (loss of xylem conductivity for water) during winters, which is attributed to the entrapment of air in xylem conduits during frost-drought. However, in the sub-alpine fir (Abies mariessii) at Mt. Norikura, air-filled conduits were not observed even in severely-embolized (complete loss of conductivity) shoots. Rather, the pits (valves of partitions inter-conduits) closed before the severe frost-drought in mid-winter, thereby resulting in severe-embolism (complete loss of conductivity). Thus, by pit (valve) cloure, shoots could maintain water in the xylem throughout the winter, which is thought to be an adaptation against lethal filling of air in the conduits during severe frost-drought.

3. Photosynthesis of Haimatsu (Pinus pumila)

At wind-exposed sites on Mt. Norikura, photosynthesis in Haimatsu was suppressed by lower mesophyll CO_2 conductance, and not by stomatal closure.

Investigation of alpine plants on Mt. Norikura

We studied mainly the following three researches on Mt. Norikura after 2012[35],[36],[37],[38],[39],[40],[41],[42],[43],[44],[45],[46],[47],[48],[49].

1) Long-term monitoring and community assembly of alpine plants

We made 40 plots for long-term monitoring of alpine vegetation because climate change possibly affects distributions of alpine plants. We also examined the community assembly process of alpine plants at the 40 plots from the view points of habitat filtering and limiting similarity. Habitat filtering and limiting similarity relate environmental conditions and interspecific competition, respectively. It is suggested that habitat filtering is more important than limiting similarity for the community assembly of alpine plants.

2) Soil respiration rates along an altitudinal gradient

This study investigated seasonal changes of soil respiration rates from forest soil along an altitudinal gradient (1600 m to 2800 m above sea level). The soil respiration rate positively correlated with soil temperatures and forest biomass. It is suggested that forest productivity is an important factor for soil respiration rates.

3) Genetic differentiation of Solidago virgaurea complex

Plant species distributed along wide altitudinal or latitudinal gradients show phenotypic variation due to their heterogeneous habitats. This study investigated whether phenotypic variation in populations of the Solidago virgaurea complex along an altitudinal gradient is caused by genetic differentiation. Population genetic analyses with microsatellite markers were used to infer the genetic structure and levels of gene flow between populations. However, the population genetic analysis suggested an extremely low level of genetic differentiation of neutral genes among the nine populations. This study suggests that genome regions responsible for adaptive traits may differ among the populations despite the existence of gene flow and that phenotypic variation of the S. virgaurea complex along the altitudinal gradient is maintained by strong selection pressure.

Bibliography

[1] " Solar neutron events in association with large solar flares in November 2003", Watanabe, K. *et al.*, Adv. Space Res., **38**, 425–430, 2006.

[2] K. Munakata, M. Kozai, P. Evenson, T. Kuwabara, C. Kato, M. Tokumaru, M. Rockenbach, A. Dal Lago, R. R. S. Mendonca, C. R. Braga, N. J. Schuch, H. K. Al Jassar, M. M. Sharma, M. L. Duldig, J. E. Humble, I. Sabbah, and J. Kota, "Cosmic Ray Short Burst Observed with the Global Muon Detector Network (GMDN) on June 22, 2015", Astrophys. J., 862:170 (9pp), 2018 (August 1).

[3] R. R. S. Mendonca, C. R. Braga, E. Echer, A. Dal Lago, M. Rockenbach, N. J. Schuch,, K. Munakata, "Deriving the solar activity cycle modulation on cosmic ray intensity observed by Nagoya muon detector from October 1970 until December 2012", Proc. IAU Sympo., 328, 1-4 (IAU-16-IAUS328-0453), 2016 (October 20).

[4] R. R. S. Mendonca, C. R. Braga, E. Echer, A. Dal Lago, K. Munakata, T. Kuwabara, M. Kozai, C. Kato, M. Rockenbach, N. J. Schuch, H. K. Al Jassar, M. M. Sharma, M. Tokumaru, M. L. Duldig, J. E. Humble, P. Evenson, I. Sabbah, "Temperature effect in secondary cosmic rays (muons) observed at ground: analysis of the global muon detector network data", Astrophys. J., 830:88 (25pp), 2016 (October 20). Cited by 2.

[5] M. Kozai, K. Munakata, C. Kato, T. Kuwabara, M. Rockenbach, A. Dal Lago, N. J. Schuch, C. R. Braga, R. R. S. Mendon, H. K. Al Jassar, M. M. Sharma, M. L. Duldig, J. E. Humble, P. Evenson, I. Sabbah, and M. Tokumaru, "Average spatial distribution of cosmic rays behind the interplanetary shock– Global Muon Detector Network observations", Astrophys. J., 825:100 (19pp), 2016 (July 10). Cited by 7.

[6] D. Ruffolo1, A. Saiz, P.-S. Mangeard, N. Kamyan, P. Muangha, T. Nutaro, S. Sumran, C. Chaiwattana, N. Gasiprong, C. Channok, C. Wuttiya, M. Rujiwarodom, P. Tooprakai, B. Asavapibhop, J. W. Bieber, J. Clem, P. Evenson, and K. Munakata, "Monitoring short-term cosmic-ray spectral variations using neutron monitor time-delay measurements", Astrophys. J., 817:38 (12pp), 2016 (January 20). Cited by 8.

[7] M. Kozai, K. Munakata, C. Kato, T. Kuwabara, J. W. Bieber, P. Evenson, M. Rockenbach, A. Dal Lago, N. J. Schuch, M. Tokumaru, M. L. Duldig, J. E. Humble, I. Sabbah, H. K. Al Jassar, M. M. Sharma, J. Kota, "The spatial density gradient of galactic cosmic rays and its solar cycle variation observed with the Global Muon Detector Network", Earth, Planets and Space, 66, 151-158, 2014 (November 14). Cited by 12.

[8] K. Munakata, M. Kozai, C. Kato, J. Kota, "Long term variation of the solar diurnal anisotropy of galactic cosmic rays observed with the Nagoya multi-directional muon detector", Astrophys. J., 791:22, 1-16, 2014 (August 10). Cited by 19.

[9] M. Rockenbach, A. Dal Lago, N. J. Schuch, K. Munakata, T. Kuwabara, A. G. Oliveira, E. Echer, C. R. Braga, R. R. S. Mendonca, C. Kato, M. Kozai, M. Tokumaru, J. W. Bieber, P. Evenson, M. L. Duldig, J. E. Humble, H. K. Al Jassar, M. M. Sharma, I. Sabbah, "Global muon detector network use d for space weather applications", Space Sci. Rev., 182, 1-18, 2014 (May 9). Cited by 18.

[10] K. Munakata, "For space weather applications", Space Sci. Rev., 182, 1-18, 2014 (May 9).

[11] D. Lopez et al., Estimates of the neutron emission during solar flares in the rising and maximum period of solar cycle 24, Astroparticle Physics, 76 (2016) 19-28.

[12] Enoto, T. and Wada, Y. and Furuta, Y. and Nakazawa, K. and Yuasa, T. and Okuda, K. and Makishima, K. and Sato, M. and Sato, Y. and Nakano, T. and Umemoto, D. and Tsuchiya, H, "Photonuclear reactions triggered by lightning discharge", Nature 551, (2017) 481-484.

[13] Dwyer, J. R. and Smith, D. M. and Cummer, S. A., "High-Energy Atmospheric Physics: Terrestrial Gamma-Ray Flashes and Related Phenomena", 173 (2012) 133-196.

[14] Tsuchiya, H. and Enoto, T. and Torii, T. and Nakazawa, K. and Yuasa, T. and Torii, S. and Fukuyama, T. and Yamaguchi, T. and Kato, H. and Okano, M. and Takita, M. and Makishima, K., "Observation of an Energetic Radiation Burst from Mountain-Top Thunderclouds", Physical Review Letters, 102, (2009) 255003.

[15] Wada, Y. and Bowers, G. S. and Enoto, T. and Kamogawa, M. and Nakamura, Y. and Morimoto, T. and Smith, D. M. and Furuta, Y. and Nakazawa, K. and Yuasa, T. and Matsuki, A. and Kubo, M. and Tamagawa, T. and Makishima, K. and Tsuchiya, H., "Termination of Electron Acceleration in Thundercloud by Intracloud/Intercloud Discharge", Geophysical Research Journal 45, (2018) 5700-5707.

[16] Tsuchiya, H. and Enoto, T. and Yamada, S. and Yuasa, T. and Kawaharada, M. and Kitaguchi, T. and Kokubun, M. and Kato, H. and Okano, M. and Nakamura, S. and Makishima, K., "Detection of High-Energy Gamma Rays from Winter Thunderclouds", Physical Review Letters, 99, (2007) 165002.

[17] Yo Kato, “Observational study of thundercloud radiation bursts using a segmented organic scintillator installed at a mounaintop”, Ph.D. thesis, The University of Tokyo, September, 2015.

[18] Y. Kato, “Thundercloud-related radiation bursts observed at a coastal area and a mountaintop using segmented organic scintillators”, Thunderstorms and Elementary Particle Acceleration (TEPA-2015), 5-9 October 2015, Yerevan, Armenia.

[19] Y. Kato, “Development of Plastic Anti-neutrino Detector Array (PANDA)”, Applied Antineutrino Physics(AAP) 2015, 7-8 December 2015, Virginia Tech Research Center, United States.

[20] Y. Kato “Observation of thundercloud radiation bursts using segmented plastic scintillators”, European Geosciences Union General Assembly (EGU), 8-13 April 2018, Austria Center Vienna, Austria.

[21] T. Torii *et al*., ”Gradual increase of energetic radiation associated with thunderstorm activity at the top of Mt. Fuji”, Geophys. Res. Lett 36(13) , 2009.

[22] T. Kuritai *et al*., ”The Status of the synchrotron of the Wakasa Wan Energy Research Center”, Proc. 12th Annual Meeting of the Particle Accelerator Societ of Japan, 288, 2015.

[23] K. Kume, T. Torii, M. Takita and T. Hasegawa, ”Development of a beam fluence measurement technique at atmosphere”, Igaku Butsuri, Vol.36 Suppl.3 178, 2016 (in Japanese).

[24] K. Kume, T. Hasegawa, S. Hatori, M. Takita and H. Tsuji, ”Space engineering application of therapeutic broad beam for cosmic rai simulation”, Igaku Butsuri, Vol.37 Suppl. 112, 2017 (in Japanese).

[25] Satoru Takahashi,Ph.D Thesis (2011) Nagoya University, http://hdl.handle.net/2237/14900.

[26] Hiroaki Kawahara, Master Thesis (2015), Nagoya University.

[27] “GRAINE project: gamma-ray observation with a balloon-borne emulsion telescope”, Hiroki Rokujo on behalf of GRAINE Collaboration, Proceeding of Science KMI2013 (2014) 042.

[28] “GRAINE project: The first balloon-borne, emulsion gamma-ray telescope experiment”, S. Takahashi, S. Aoki, K. Kamada, S. Mizutani, R. Nakagawa, K. Ozaki and H. Rokujo, PTEP 2015 (2015) no.4, 043H01.

[29] “Gamma-Ray Astro-Imager with Nuclear Emulsion, GRAINE (in Japanese)”, Satoru Takahashi, Shigeki Aoki for GRAINE collaboration, Journal of the SPSTJ, Vol,78(2015) No.4, pp.228-234.

[30] “GRAINE 2015, a balloon-borne emulsion γ-ray telescope experiment in Australia”, Satoru Takahashi et al. (GRAINE collaboration), PTEP 2016 (2016) no.7, 073F01.

[31] “GRAINE project, prospects for scientific balloon-borne experiments”, Satoru Takahashi, Shigeki Aoki for GRAINE collaboration, Advances in Space Research, Articles in press.

[32] Nakamoto A., Ikeda T., Maruta E. (2013) Needle browning and death in the flagged crown of Abies mariesii in the timberline ecotone of the alpine region in central Japan. Trees 27:815-825.

[33] Maruta E., Yazaki K.(submitted) Mechanism of embolism as induced by pit closure during winter in subalpine fir (Abies mariesii)on Mt. Norikura.

[34] Nagano S., Nakano T., Hikosaka K., Maruta E. (2013) Pinus pumila photosynthesis is suppressed by water stress in a wind-exposed mountain site. Arctic, Antarctic, and Alpine Research 45:229-237.

[35] Takahashi, K., Hirosawa, T. and Morishima, R. (2012) How the timberline formed: altitudinal changes in stand structure and dynamics around the timberline in central Japan. Annals of Botany 109: 1165-1174.

[36] Takahashi, K. and Okuhara, I. (2013) Forecasting the effects of global warming on radial growth of subalpine trees at the upper and lower distribution limits 3n central Japan. Climatic Change 117: 278-287.

[37] Takahashi, K. and Obata, Y. (2014) Growth, allometry and shade tolerance of understory saplings of four subalpine conifers in central Japan. Journal of Plant Research127: 329-338.

[38] Takahashi, K. (2014) Effects of wind and thermal conditions on timberline formation in central Japan: a lattice model. Ecological Research 29:121-131.

[39] Takahashi, K. and Koike, S. (2014) Altitudinal differences in bud burst and onset and cessation of cambial activity of four subalpine tree species. Landscape and Ecological Engineering 10:349-354.

[40] Takahashi, K. and Murayama, Y. (2014) Effects of topographic and edaphic conditions on alpine plant species distribution along a slope gradient on Mount Norikura, central Japan. Ecological Research 29: 823-833.

[41] Singh, D., Takahashi, K., Park, J. and Adams, J. M. (2016) Similarities and contrasts in the archaeal community of two Japanese mountains: Mt Norikura compared to Mt Fuji. Microbial Ecology 71: 428-441.

[42] Takahashi, K. and Furuhata, K. (2016) Shoot growth and seasonal changes of non-structural carbohydrate concentrations at the upper and lower distribution limits of three conifers. Landscape and Ecological Engineering 12: 239-245.

[43] Takahashi, K. and Tanaka, S. (2016) Relative importance of habitat filtering and limiting similarity on species assemblages of alpine and subalpine plant communities. Journal of Plant Research 129: 1041-1049.

[44] Takahashi, K. and Matsuki, S. (2017) Morphological variations of the Solidago virgaurea L. complex along an elevational gradient on Mt. Norikura, central Japan. Plant Species Biology 32: 238-246.

[45] Kerfahi, D., Tateno, R., Takahashi, K., Cho, H., Kim, H. and Adams, J. M. (2017) Development of soil bacterial communities on volcanic ash microcosms in a range of climates. Microbial Ecology 73: 775-790.

[46] Sakurai, A. and Takahashi, K. (2017) Flowering phenology and reproduction of the Solidago virgaurea L. complex along an elevational gradient on Mt. Norikura, central Japan. Plant Species Biology 32: 270-278.

[47] Dong, K., Moroenyane, I., Tripathi, B., Kerfahi, D., Takahashi, K., Yamamoto, N., An, C., Cho, H., and Adams, J. (2017) Soil nematodes show a mid-elevation diversity maximum and elevational zonation on Mt. Norikura, Japan. Scientific Reports 7: 3028.

[48] Hirano, M., Sakaguchi, S. and Takahashi, K. (2017) Phenotypic differentiation of the Solidago virgaurea complex along an elevational gradient: Insights from a common garden experiment and population genetics. Ecology and Evolution 7: 6949-6962.

[49] Takahashi, K., Otsubo, S. and Kobayashi, H. (2017) Comparison of photosynthetic traits of codominating subalpine conifers Abies veitchii and A. mariesii in central Japan. Landscape and Ecological Engineering 14: 91-97.

AKENO OBSERVATORY

Introduction

The Akeno Observatory is situated in Akeno of Hokuto-city, 20 km northwest of Kofu and 130 km west of metropolitan Tokyo. The location is at the longitude of 138.5°E and the latitude of 35.8°N. The altitude is ∼900 m above sea level. It was established in 1977 as a research center for air shower studies in the very high energy region, and it has been administered by the ICRR as a facility of joint-university-use.

The 40th anniversary of the Akeno Observatory was held in 2017.

Akeno Air Shower Experiments

The Akeno Air Shower Experiment started in 1979 with an array covering 1 km^2 area (the 1 km^2 array, see Fig.1). The array was enlarged to 20 km^2 in 1984 and was gradually expanded to the Akeno Giant Air Shower Array (AGASA) of approximately 100 km^2 area by 1990. The AGASA was built to detect Ultra-High Energy Cosmic Rays (UHECRs) in the energy range of 10^{20} eV.

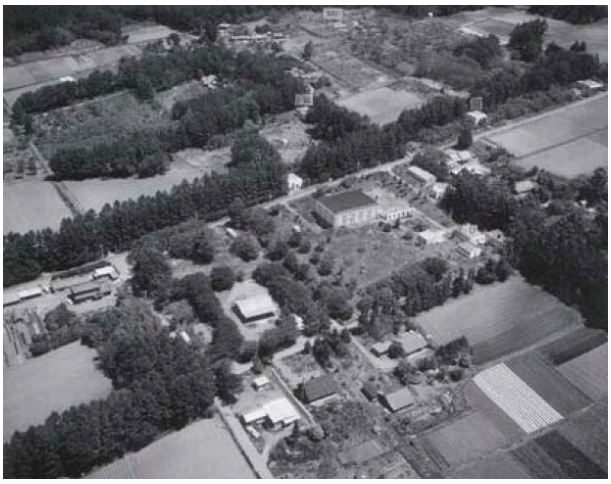

Fig. 1. Aerial View of Akeno Observatory and 1 km^2 Array Area

One of the distinctive features of Akeno experiments is that the measurements were made over five decades of energies well covering 10^{15} eV - 10^{20} eV by using both the surface detector for electromagnetic component, and the shielded detector for muon component (Fig.2). The wide energy coverage was accomplished by the arrays of scintillation detectors of various inter-detector spacings from 3 m to 1 km and with different triggering conditions. This feature of Akeno air shower measurement is well demonstrated in Fig.3, in which the spectra from Akeno 1 km^2 array for $10^{14.5}$ eV - $10^{18.8}$ eV [2] and AGASA for $10^{18.5}$ eV - $10^{20.3}$ eV [3] are plotted.

*2 M. Nagano et al., J. Phys. **G10**, 1295 (1984); M. Nagano et al., J. Phys. **G18**, 423 (1992).

*3 M. Takeda et al., Astropart. Phys. **19**, 447 (2003).

Fig. 2. One of the muon detector housings with concrete shielding.

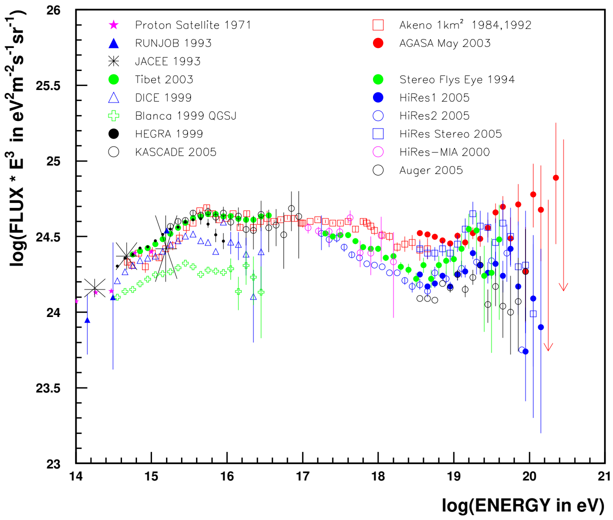

Fig. 3. Akeno energy spectrum measurements for 10^{15} eV - 10^{20} eV.

AGASA

The AGASA was composed of 111 surface detectors, each with plastic scintillator of 2.2 m^2 area and 5 cm thickness. The counters were deployed with ∼1 km spacing covering the ground area of approximately 100 km^2 in the suburban area of Akeno, outside of the observatory campus. The AGASA served as the largest air shower array in the world since its commissioning in 1990 until it stopped data taking in January 2004, when the construction of the succeeding experiment, Telescope Array (TA), started in Utah. The AGASA was dismantled in 2007 together with other Akeno air shower arrays.

An exposure of 5.8 × 10^{16} m^2 s sr above 10^{19} eV was accumulated by AGASA in 13 years of operation. Extensive air showers with zenith angles smaller than 45° and with core locations inside the array area were used for the analysis. The AGASA reported an extension of the energy spectrum beyond the predicted Greisen-Zatsepin-Kuzmin (GZK) cutoff in 1998 [4] and a total of eleven UHECR events were observed above 10^{20} eV by 2003.

Measurement of UHECRs

Since the AGASA measurement in 1998, the High Resolution Fly's Eye (HiRes) [5], the Pierre Auger Observatory (PAO) [6], and the Telescope Array (TA) [7] measured the energy spectra of UHECRs with higher statistics.

The HiRes observed the UHECR using the fluorescence telescope. The PAO and the TA measure the energy spectra using the surface array consisting of either water tanks (PAO) or plastic scintillators (TA), but the energy scale of the array is determined by the fluorescence telescope using a subset of events observed by the fluorescence telescope and surface array at the same time. The adoption of the energy scale by the fluorescence telescopes is based on its small dependence on the air shower simulation.

The energy spectra above 10^{18} eV by AGASA and other experiments are compiled and compared by the working group represented by UHECR experiments in the UHECR2012 symposium held in 2012 [8]. The result is plotted in Fig.4 with the energy scale of each experiment adjusted to a reference energy, which is set halfway between PAO and TA/HiRes.

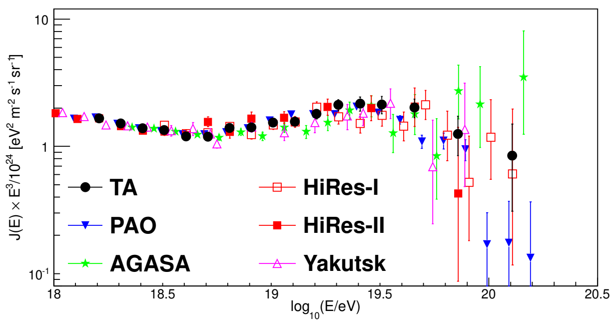

Fig. 4. Compilation of UHECR energy spectra (UHECR2012). The energy scales were adjusted as ×1.10 for PAO, ×0.91 for TA and HiRes, ×0.65 for AGASA and ×0.56 for Yakutsk.

The HiRes, PAO and TA confirmed a flux suppression above approximately $10^{19.7}$ eV. Although the AGASA spectrum does not demonstrate the cutoff structure, the number of events above 10^{20} eV became only two after the energy rescaling, making the claim of the extended spectrum statistically insignificant. The estimate of systematic uncertainty of the energy measurement is approximately 20% for all the experiments, and rescalings for the TA/HiRes and PAO are within this limit. Rescaling of the surface array energy for AGASA and Yaktsuk indicates that there exist larger systematic uncertainties than originally estimated by running the air shower simulation. This difference of energy scale obtained by the surface array and by the fluorescence telescope remains as a basic question in the understanding of the air shower phenomena.

Recent Research Activities

The study of UHECRs by AGASA in Akeno was succeeded by the TA experiment in Utah, USA since 2008. After the cessation of AGASA, the Akeno Observatory has been used for small scale cosmic ray experiments, astrophysical observations and as a test and maintenance facility by the ICRR and university researchers. Fig.5 shows a recent photograph of the main site of the Akeno Observatory.

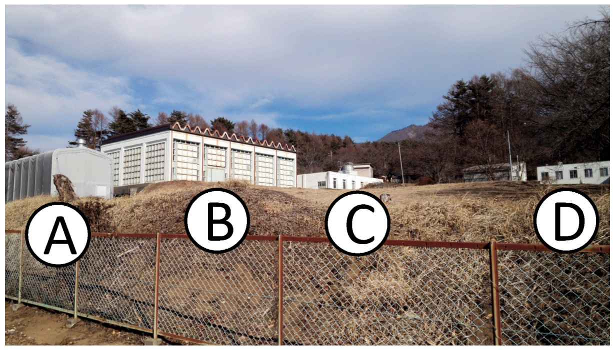

Fig. 5. The main site of the Akeno Observatory. There are the movable tent for a small atmospheric Cherenkov telescope (A), the large experimental hall (B), the research building (C) and the lodging facility (D) from the left.

In 2020, as countermeasures against COVID-19 infection, an air conditioner and a heat-exchange ventilator were installed in the large room of the research building, and a heat-exchange ventilator was installed in the dining room of the lodging facility along with some other measures.

Observation by the multi-color imager for transients, survey and monstrous explosions (MITSuME) by N. Kawai (Tokyo Institute of Technology) et al.

One of the three MITSuME robotic telescopes was installed in the Akeno Observatory in 2003 (Fig. 6). The telescope has an aperture of 50 cm, an FOV of 28' × 28' and is equipped with a tricolor CCD camera capable of $g'R_CI_C$-bands photometry (g':400∼550 nm, Rc:570∼730 nm, Ic:730∼ 850 nm). It is operated remotely from the Tokyo Tech at the Ookayama Campus via a dedicated line. The operation of the telescope has continued in FY2021 as described below [9].

Upon receiving a GRB alert, it directs the telescope toward the GRB direction within two minutes, and makes a prompt observation of the GRB and its afterglow. The follow-up observation of GRBs was continued by the MITSuME telescope. Information about GRB events was reported to Gamma-Ray Burst (GRB) Coordinates Network Circular (GCNC).

In order to perform follow-up visible-light observations of gravitational wave objects, the MITSuME participated in

*4 M. Takeda et al., Phys. Rev. Lett. **81**, 1163 (1998).
*5 R.U. Abbasi et al., Phys. Rev. Lett. **100**, 101101 (2008).
*6 J. Abraham et al., Phys. Lett. **B685**, 239 (2010).
*7 T. Abu-Zayyad et al., Astrophys. J. **768**, L1 (2013).
*8 http://indico.cern.ch/conferenceDisplay.py?confId=152124

*9 N. Kawai et al., Research Result Presentations Meeting of the ICRR Inter-University Research Program 2021.

J-GEM (Japanese collaboration for Gravitational-wave ElectroMagnetic follow-up) and GROWTH(Global Relay of Observatories Watching Transients Happen) to establish worldwide observation network focusing on the electromagnetic identification of gravitational wave sources as one of scientific themes. In FY2021, the observation of gravitational wave by LIGO/Virgo was stopped. Therefore, the MITSuME participated in the follow-up observation of IceCube neutrino events that was derived from J-GEM.

The MITSuME team also conducted long-term monitoring observations of X-ray binary starts and blazars. The MITSuMe has also participated OISTER (Optical and Infrared Synergetic Telescopes for Education and Research).

Fig. 6. The dome in which the MITSuME telescope was installed in Akeno.

Observation of galactic cosmic rays by large area muon telescope by A. Oshima (Chubu University) et al.

Four layers of proportional counter telescopes, each with 25 m^2 area, were installed in three muon houses in Akeno and have been continuously measuring the cosmic ray muons since 2003. Fig. 2 shows one of the three muon houses (M1, M5, M8). The mode energy of the primary cosmic rays is approximately 2.5 GeV corresponding to 2m thick concrete ceiling of the muon house at the latitude of the Akeno Observatory. The measurement in Akeno is combined with a simultaneous measurement by the GRAPES-3 experiment at Ooty in India, and this telescope aims at measuring the modulation effects and anisotropy of galactic cosmic rays in the region of about 100 GeV and detecting trasient phenomena of cosmic rays. It is expected to understand cosmic-ray flow in the universe magnetic field and to obtain a clue to the solution of cosmic-ray propagation. And it is challenging to establish the method of a new space weather observation by simultaneous multi-directional observations with high statistical precision.

In FY2021, the data acquisition at M5 was restored in November and tuned in December. However, almost continuous observations have been made at M5 over the past 3.5 years except during power outages, etc [10].

*[10] A. Oshima et al., Research Result Presentation Meeting of the ICRR Inter-University Research Program 2021.

Research and development for a small atmospheric Cherenkov telescope at the Akeno Observatory by T. Yoshikoshi (ICRR) et al.

An alt-azimuth telescope with an aperture of three meters (Fig. 7) was setup in the Akeno Observatory for various prototype tests with atmospheric Cherenkov observations of gamma rays on the ground [11]. This telescope is the only telescope to observe atmospherice Cherenkov light emitted from air showers induced by TeV gamma rays in Japan.

In January 2021, the telescope was used to observe the Crab Pulsar in the visible light region for about ten hours. The collected data were analyzed in FY2021. The result was used to improve the signal-to-noise ratio of the Crab Pulsar observation and to study the removal of external noise.

Fig. 7. The Cherenkov telescope at the tour of the 40th anniversary of the Akeno Observatory in 2017.

Dark matter and Interstellar Meteoroid Study (DIMS) at the Akeno Observatory by F. Kajino (Konan University) et al.

The Dark Matter and Interstellar Meteoroid Study (DIMS) is a new experiment that aims at searching for macroscopic dark matter and interstellar meteoroids [12][13][14]. Nuclearites are nuggets of stable Strange Quark Matter (SQM), which are neutral in charge and hypothetical super-heavy macroscopic particles (macros), and may be important components of the dark matter in our universe. Nuclearites of galactic origins is expected to have a typical velocity of about 250 km/s in galactic frame. The DIMS team studies the possibility of searching for such fast moving particles using very high-sensitivity CMOS camera with a wide field of view. In the first stage, the DIMS system consists of 4 high-sensitivity CMOS camera stations. and is going to be constructed at the Telescope Array cosmic-ray experimental site in Utah, USA. Due to COVID-19 pandemic, the DIMS team did not transport the DIMS systems to Utah, and one of the systems was installed on the roof of the research building at the Akeno Observatory as shown in Fig. 8. The observed Geminids Meteor Shower taken by

*[11] M. Ohishi et al., 33rd ICRC, (Rio deJaneiro), 587 (2013).
*[12] D. Barghini et al., PoS(ICRC2021)500.
*[13] D. Shinto et al., PoS(ICRC2021)502.
*[14] F. Kajino et al., PoS(ICRC2021)554

the DIMS camera at the Akeno Observatory was shown in Fig. 9. The preliminary results on limiting magnitudes of stars and the number of meteors as a function of magnitude were reported [15]. Three camera systems are installed at the Kiso Observatory, Shinshu University and Akeno Observatory for stereoscopic observations.

Fig. 8. The DIMS camera installed on the roof of the research building at the Akeno Observatory in August 2021.

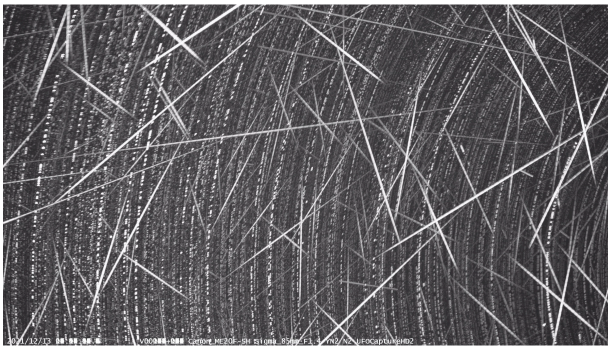

Fig. 9. Geminids Meteor Shower that was taken by DIMS camera at the Akeno Observatory on December 13th, 2021. Approximately 500 meteoroids are superimposed on the photograph.

Research and development for the Telescope Array observation in Utah by the TA collaboration and others

All the TA fluorescence imaging cameras and a part of the TA surface detectors were assembled in the Akeno Observatory by the TA collaboration team. All the unit mirrors of the TA fluorescence telescope were tested and the atmospheric monitoring lidar of TA using YAG laser was developed. In JFY 2015, the R&D of the surface detectors were performed for the TAx4 project that aims at quadrupling the TA surface detector array in Utah. In August in 2016, 2017 and 2018 the TAx4 and TALE (TA Low Energy extension) scintillator counters were assembled.

The assembly of the surface detectors for the TALE-infill array [16] that is described in the TA section was scheduled at the Akeno Observatory in 2020, but due to the COVID-19 epidemic, the assembly had to be postponed. The 50 surface detectors for the TALE-infill array were assembled at the Akeno Observatory from the middle of October to early November in 2021. Figure 10 shows one of the surface detectors that was being assembled.

Fig. 10. A surface detector for the TALE-infill array that was being assembled at the Akeno Observatory. The student was aligning the ends of bundled fibers.

*15 F. Kajino et al., Research Result Presentation Meeting of the ICRR Inter-University Research Program 2021.

*16 S. Ogio et al., "The status of the TALE surface detector array and a TALE infill project", PoS(ICRC2021)255.

KAMIOKA OBSERVATORY

Kamioka observatory is located at 1000 m underground (2700 m water equivalent) in the Kamioka Mine, Gifu prefecture, about 200 km west of Tokyo. The observatory was established in 1995 in order to operate Super-Kamiokande experiment (SK). The underground laboratories are located under Mt.Ikeno-yama and accessible to the experimental site through a 1.7 km horizontal tunnel. The observatory also has surface research buildings and a dormitory located at the distance of 15 minutes drive from the entrance of the underground laboratories.

The Super-Kamiokande experiment had discovered neutrino oscillations through the observations of atmospheric and solar neutrinos (see the section for Neutrino and Astroparticle Division). The atmospheric neutrino oscillation was confirmed by the long baseline neutrino oscillation experiment, K2K, using accelerator neutrino beam, which was conducted between 1999 and 2004. A new long baseline neutrino oscillation experiment (the T2K experiment) using a high intensity beam, 50 times of the K2K neutrino beam, by the J-PARC proton accelerator has started in 2009. In 2011, the experiment has observed 6 ν_e appearance events indicating non-zero θ_{13} which was as yet determined the last neutrino oscillation parameter. From 2014, T2K started taking data using an anti- neutrino beam, and confirmed the disappearance of muon antineutrinos through oscillations. Candidate events for the appearance of electron anti-neutrinos were also found. Additionally, T2K published in 2020 an indication that CP symmetry is not conserved in neutrino oscillations, with the probability of the observations being the results of a random fluctuation if CP symmetry was conserved being less than 5%.

The low cosmic ray flux and low seismic noise environment in the underground site enables us to conduct various researches. There is a 100 m long laser interferometer, which is a prototype of the 3 km gravitational wave antenna (KAGRA). Using the low radioactive background environment in the Kamioka Mine, a dark matter experiment, called XMASS was conducted in Lab-C. The XMASS group constructed a 800kg liquid xenon detector and data were taken from 2010 to 2019. Searches for dark matter interactions and rare phenomena in liquid xenon have been conducted using the obtained data. The R&D study of a tracking type detector for dark matter detection led by the Kobe University group (the NEWAGE experiment) has also been performed in Lab-B. A double beta decay experiment using ^{48}Ca (the CANDLES experiment) led by the Osaka University group has been running in Lab-D. The study to improve the neutrino detection sensitivity by adding gadolinium to Super-Kamiokande (called SK-Gd project) has been performed at Lab-E. A Low background Germanium detector and ICP-MS system are equipped in Lab-1 and Lab-A to measure extremely low radioactive backgrounds. Lab-G area was excavated in 2015 and the SK-Gd equipments which include a Gd dissolving system, a pretreatment system and a Gd-water circulation system were installed in 2016. Other preparations for Gd-loading have been performed including a tank open work to repair the water leak from the SK tank in 2018 and the test of the SK-Gd equipments in 2019. In 2020, SK added soluble Gd salt into the water. The next-generation neutrino experiment project, Hyper-Kamiokande, was started in 2020. The construction has been running underground the Kamioka mine, aiming to begin observations in 2027.

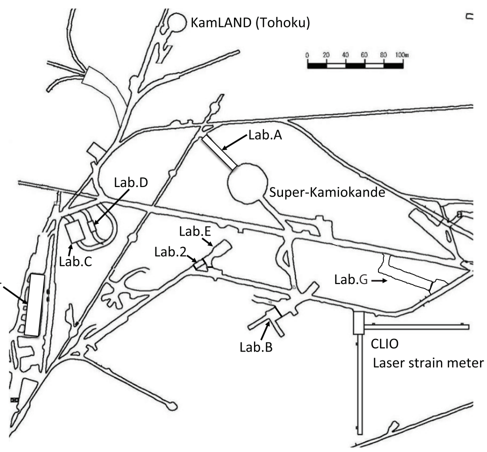

Fig. 1. Kamioka Underground Observatory.

Fig. 2. The surface buildings in Mozumi.

KAGRA OBSERVATORY

KAGRA observatory is located in the Ikenoyama-mountain on the border between Gifu and Toyama prefecture, about 35 km south of Toyama city in Japan. The observatory was established in 2016 in order to operate Large-scale Cryogenic Gravitational Wave Telescope ”KAGRA”. KAGRA itself has a L-shape tunnel facility, and it is located more than 200m under Mt.Ikeno-yama. The corner station of the L-shape tunnel is accessible through a 500-m horizontal access tunnel from Atotsu area. The observatory has its own surface research buildings and rental space in the community center of Hida city located about 5km away from the Atotsu entrance of KAGRA.

KAGRA aims to observe gravitational waves (GWs) as one of observatories of the world GW detection network including Advanced-LIGO, Advanced-Virgo and planned LIGO-India. KAGRA project (formerly named LCGT) was partially approved in 2010 as one of Leading-edge Research Infrastructure Program, and also supported by Program for Promoting Large-scale Science Projects, Subsidy for Facilities Expense and Grants-in-Aid for Scientific Research from Ministry of Education, Culture, Sports, Science and Technology (MEXT).

In the KAGRA project, Institute for Cosmic Ray Research plays a role of a host promoting institute, and National Astronomical Observatory of Japan (NAOJ) and High Energy Accelerator Research Organization (KEK) are the co-host institutions, then more than 417 researchers in 85 institutes and universities in the world are collaborating for construction and data analysis of KAGRA.

The tunnel excavation started in May 2012, and finished in March 2014. After that, the basic laboratory environment was prepared until September 2015. A Michelson interferometer with 3km arm (iKAGRA) was demonstrated in March 2016, and the first engineering run was performed until May 2016. In 2019, all the interferometer components had been installed to complete the KAGRA Observatory that adopts a power recycled Fabry-Perot Michelson type interferometer with the resonant sideband extraction. On February 25th, 2020, KAGRA started its first observation run. After performing the two week observation run ”O3GK” with GEO600 on April 2020, KAGRA will be upgraded and prepared for the joint observation with LIGO and Virgo ”O4” which is expected to start in March 2023.

Fig. 1. Surface Research Building.

Fig. 2. Atotsu Entrance of KAGRA.

RESEARCH CENTER FOR COSMIC NEUTRINOS

The Research Center for Cosmic Neutrinos (RCCN) was established in April 1999 to conduct research on neutrinos and related topics. The members of the Center participate in the Super-Kamiokande experiment, which is the neutrino research facility representing ICRR, maximize our knowledge of neutrinos by analyzing the observed neutrino data in Super-Kamiokande and the long-baseline neutrino oscillation experiment T2K, and explore new avenues for neutrino research by promoting the exchange of the research ideas between theoretical and experimental physicists. We are also participating in the Hyper-Kamiokande project, a next-generation large-scale experiment, and developing the detector elements and preparing the construction.

RCCN, together with the computer committee, oversees the operation of the central computer system in ICRR (Fig 1). The computer facility has high performance to analyze huge amount of data, and has been operated without any serious trouble since it was upgraded in 2020. Since 2004, RCCN has been accepted inter-university programs related to activities in the low-background underground facility also (Fig 2). In FY2021, we accepted 12 programs, including both domestic and international applications.

Since 2009, ICRR and Kavli Institute for the Physics and Mathematics of the Universe (Kavli IPMU) have held two public lectures a year, one in the spring and one in the summer. The lecture was broadcast in real time and archived on YouTube, and was viewed approximately 3,800 times in total. The lecture was titled ”The Mysteries of a Universe Full of Matter,” and invited Associate Professor Asaoka and Professor Murayama of Kavli IPMU to give lectures on the Hyper-Kamiokande project and neutrinos, respectively. The two lecturers also cross-talked with the participants to answer their questions.

Fig. 1. Photo of the central computer facility in ICRR upgraded in 2014.

Fig. 2. Photo of the low-background underground facility in ICRR.

HIGH ENERGY ASTROPHYSICS FACILITY IN CANARIAS

High Energy Astrophysics Facility in Canarias, established on April 1, 2019 in La Palma, Canary Islands, Spain is the actual base of international collaborations on CTA (Cherenkov Telescope Array) project co-hosted by CTA group of ICRR.

The Cherenkov Telescope Array (CTA) is the next generation ground-based observatory for gamma-ray astronomy at very-high energies, participated by more than 1400 researchers from 31 countries. With more than 100 telescopes located in the northern and southern hemispheres, CTA will be the world's largest and most sensitive high-energy gamma-ray observatory. The CTA-Japan consortium is making a significant contribution to the construction of Large-sized Telescopes (LSTs), four proto types of which are planned to construct at northern hemisphere site in La Palma. The first LST was completed and made the first light at the end of December of 2018.

Establishment of the local corporation assets were needed for daily activities such as local procurement and employment to manage and operate the site. High Energy Astrophysics Facility in Canarias was established as a room inside the building of CALP (The Centro de Astrofísica en La Palma), a branch of IAC (Instituto de Astrofisca de Canarias).

Fig. 1. High Energy Astrophysics Facility in Canarias.

APPENDICES

A. ICRR Workshops and Ceremonies

Kashiwa Dark Matter Symposium 2021

Date: Nov.29-Dec.2, 2021
Place: Online

Outline: For the third time, ICRR organized the yearly Kashiwa Dark Matter symposium taking place online from November 29 to December 2, 2021. The symposium covered recent updates from the Dark Matter searches in the different fields of collider, direct, and indirect searches and developments in Dark Matter theory and astrophysics. Special focus was drawn to search for Primordial Black Holes. The symposium lasted four days, over five hours each day.

The talks and oral discussions were held on Zoom. The coffee breaks and poster session were held using the Gather.Town tool, with more than 40 participants discussing the posters at the poster session. Additionally, a Slack workspace was available for offline discussions and the talks were additionally live streamed worldwide on YouTube.

The theory session opened the symposium with a focus on electroweak dark matter. The following Astrophysics Session focused the implications of observations of dwarf spheroidal and ultrafaint galaxies for Indirect Dark Matter searches. In the Indirect Detection session, besides high-energy gamma-ray searches, attention was drawn on new search strategies at lower photon energies from MeV to radio emission. In the Direct Detection session, both latest noble gas and cryogenic detection efforts were discussed. In the collider session, measurements with the LHC and Belle experiments at KEK were presented.

As in the last years, all talks and posters are publicly available on the webpage (https://kashiwa-darkmatter-symposia.org/), and also many of the talks are archived on YouTube. Also, a prize was awarded to the best presentation and poster summary video, which can be watched on YouTube.

Participants: 317 participants from 28 countries worldwide.

Fig. 1. Kashiwa Dark Matter Symposium 2021

SAZERAC SIPS Early Galaxy Formation Near and Far — Preparing for a Long Journey with JWST —

Date: Nov.29-Dec.3, 2021
Place: Online

Outline: The international online conference, SAZERAC SIPS Early Galaxy Formation Near and Far — Preparing for a Long Journey with JWST —, was held in November 29 - December 3 on zoom.

In this international conference, 240 researchers, 170 out of whom joined outside Japan, particpated, and discussed local dwarf galaxies with both observational and theoretical perspectives to reveal how the local dwarf galaxies help us understand the early formation of high-redshift galaxies in the JWST era. The discussions included HST/COS surveys targeting the rest-frame UV emission of local-dwarf galaxies whose high-redshift counterparts would be studied with JWST with good sensitivity. Ground-based large-area data, such as those taken by SDSS and Subaru programs, pinpointed premature dwarf galaxies, and the evolution of such population over cosmic time was also discussed, which builded a bridge between local galaxies and high-redshift galaxies at the epoch of reionization.

We had a total of 60 Presentations, 44 Talks and 16 Poster/Recorded talks (+lightning talks). There are interaction and poster sessions twice in a day and Q&A sessions that were held via zoom and the conference slack channel, where we encouraged questions from students and young astronomers. The conference is recorded and published in the YouTube channel, https://www.youtube.com/channel/UCvrk105bi1U7sMgkEUEneSw

Participants: 240 participants from 23 countries worldwide

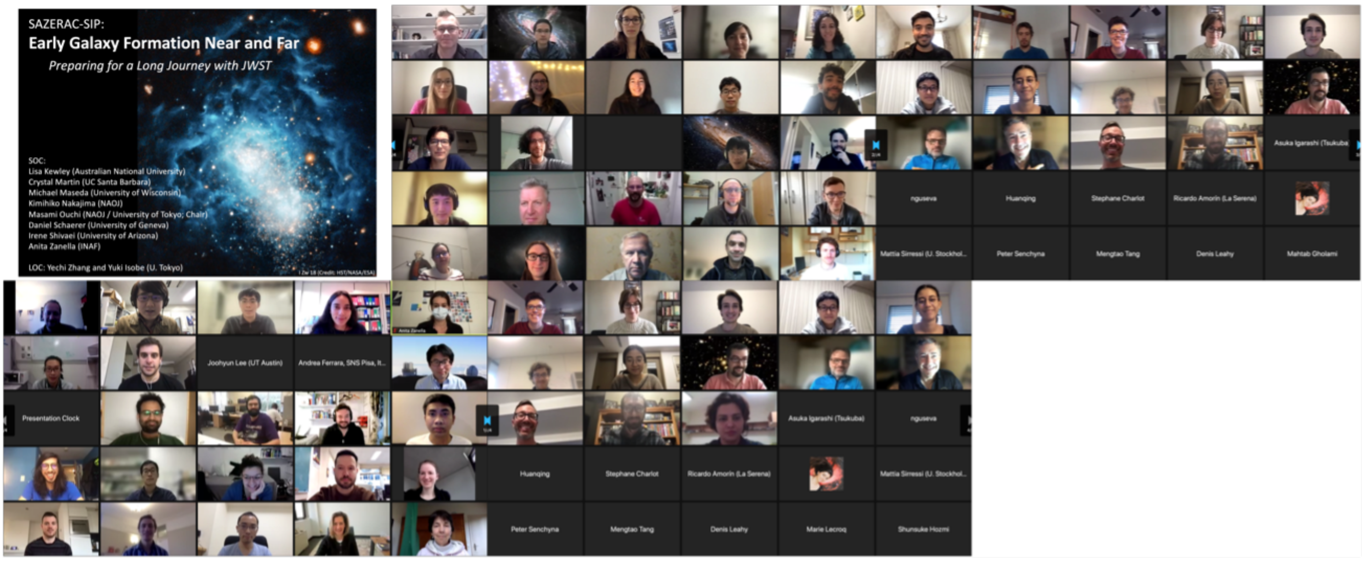

Fig. 2. Conference group photo

Black Hole Astrophysics with VLBI 2022

Date: Feb. 7-9, 2022
Place: ICRR, The University of Tokyo and Online

Outline: The workshop "Black Hole Astrophysics with VLBI 2022" was held from the 7th to the 9th of February 2022 at ICRR. The workshop focused on the various aspects of the black hole astrophysics from horizon scale to the global scale, motivated by the recent progress of the VLBI observation including the Event Horizon Telescope (EHT).

A Total of 92 people joined this workshop. Attendees are mainly from the institutes in east Asia, while some of the participants are from those in US and Europe. Due to the situation of covid-19, the number of persons attending on site was limited to 13 people and the most of attendees remotely joined the workshop via zoom and slack. The 11 invited talks, 17 contributed talks, and 7 poster talks are given during the workshop.

The workshop brought researchers working on observation and theory/simulations to discuss our present understanding of the spacetime of black holes, the physics of accretion flow, jets, winds, and the related high energy phenomena around compact objects. In particular, from the observational side, the EHT observation of the polarization features of M87* and a recent update of the long-term East Asia VLBI Network (EAVN) observation of the precession feature of M87 jet were sensationally demonstrated. From the theoretical side, the recent theoretical studies of black hole magnetosphere in the context of the jet formation mechanism are deeply discussed.

Participants: 92 participants.

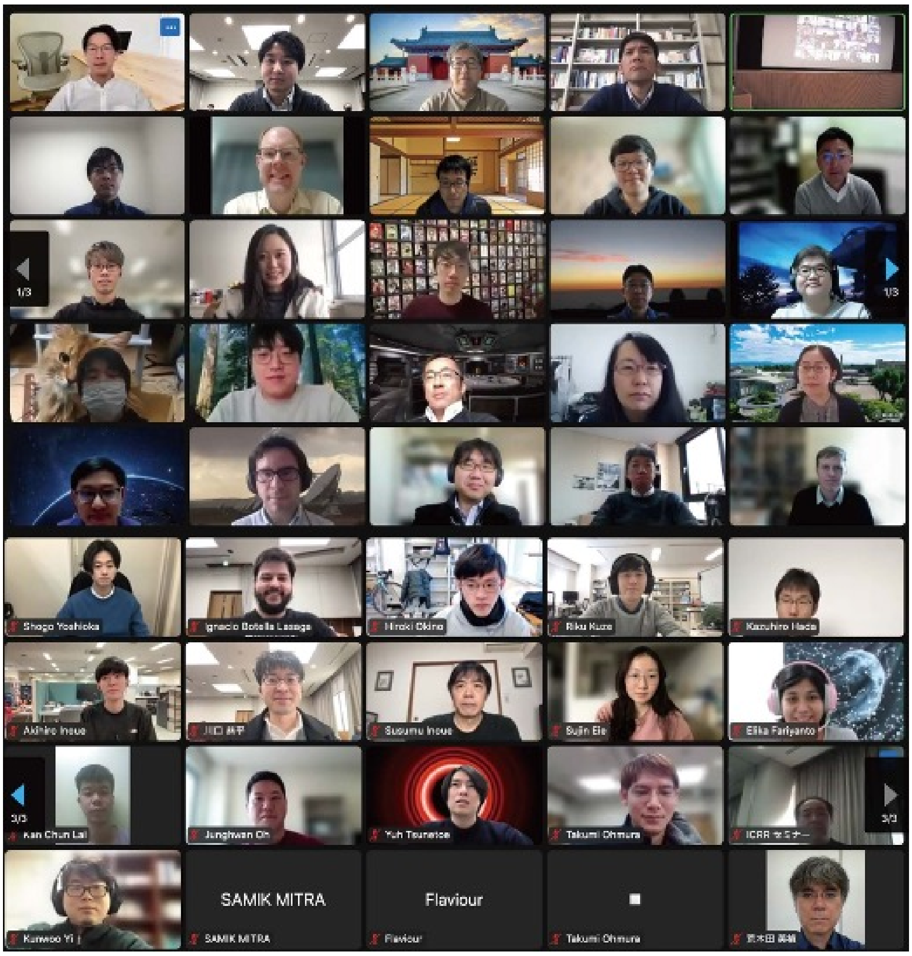

Fig. 3. Zoom window showing participants in the symposium, onsite in the large Seminar Room, ICRR and from other places

UTokyo NY Event by ICRR
"Exploring the Universe with Multi-Messengers"

Date: Feb. 12, 2022
Place: Online

Outline: UTokyo NY Event "Exploring the Universe with Multi-Messengers" was held by Institute for Cosmic Ray Research, The University of Tokyo on February 12, 2022 (EDT).

This event was the first symposium organized by ICRR to connect people living in Japan, the USA and the other areas in the world, commemorating the University of Tokyo New York Office (UTokyoNY) after its full renovation. As one of the UTokyoNY events, ICRR was very happy to be supported by the External Relations Promotion Group, UTokyo and UTokyoNY. Initially, the event had planned to be held at a real venue in New York with online mode but decided to be operated completely online from midnight-Japan due to the COVID-19 situation.

At the symposium, Prof. Masato Takita acts as a moderator and researchers from ICRR and other research institutes and universities in the USA made presentations on their cutting-edge research topics to the general-public. During the symposium, four research fields: Cherenkov Telescope Array (CTA), Telescope Array (TA), Tibet/ALPACA Experiment, gravitational wave observation at LIGO and KAGRA were featured. Researchers from ICRR and the USA in turns made presentations on their latest topics and answered questions from the audience (Zoom chat and Sli.do).

Participants: More than 300 people on Zoom and YouTube

Fig. 4. Speakers in the symposium. From upper left: Prof. Takita, Prof. Sagawa, President Masuyama (top), President Spergel, Director Kajita, Prof. Teshima (upper middle), Prof. Mukherjee, Prof.Farrar, PI Fritschel (lower middle), Prof. Shawhan, Prof. Tagoshi (bottom)

Workshop ”Synergies at New Frontiers at Gamma-rays, Neutrinos and Gravitational Waves”

Date: March. 24-25, 2022

Place: ICRR, The University of Tokyo and Online

Outline: The goal of this workshop was to connect scientific communities in Japan working at different wavelengths and messengers. The participants explored potential synergies between several multi-messenger windows of the highly-energetic Universe using the following large experiments: the gamma-ray observatory CTA, with its first Large Size Telescope (LST1) in operation, the cosmic ray detector CALET, the gamma-ray imaging Cherenkov telescopes MAGIC, the gravitational wave project KAGRA and the neutrino observatories Super-Kamiokande and Hyper-Kamiokande.

The idea for this workshop came from recent discoveries of high-energy cosmic neutrinos and gravitational waves from astrophysical objects that have led to the new era of multimessenger astrophysics. Observatories and experiments are now more than ever able to observe the sky in different energy ranges and with different messengers. Each class of messengers – photons, neutrinos, cosmic-rays and gravitational waves – provides distinct and valuable information of the most violent phenomena in the Universe. Only with multi-messenger astronomy will we be able to fully unveil the mechanisms at operation in different galactic and extragalactic sources.

The workshop was originally intended to take place in 2020, however it was delayed to 2022 due to COVID pandemic. It was finally held in hybrid style: speakers gathered in person at ICRR and the audience connected online via ZOOM. Furthermore, we created a Slack channel for easier communication and discussion. A total of 70 researchers participated in this event, 25 onsite and 45 online.

Participants: 70 participants (25 onsite, 45 online)

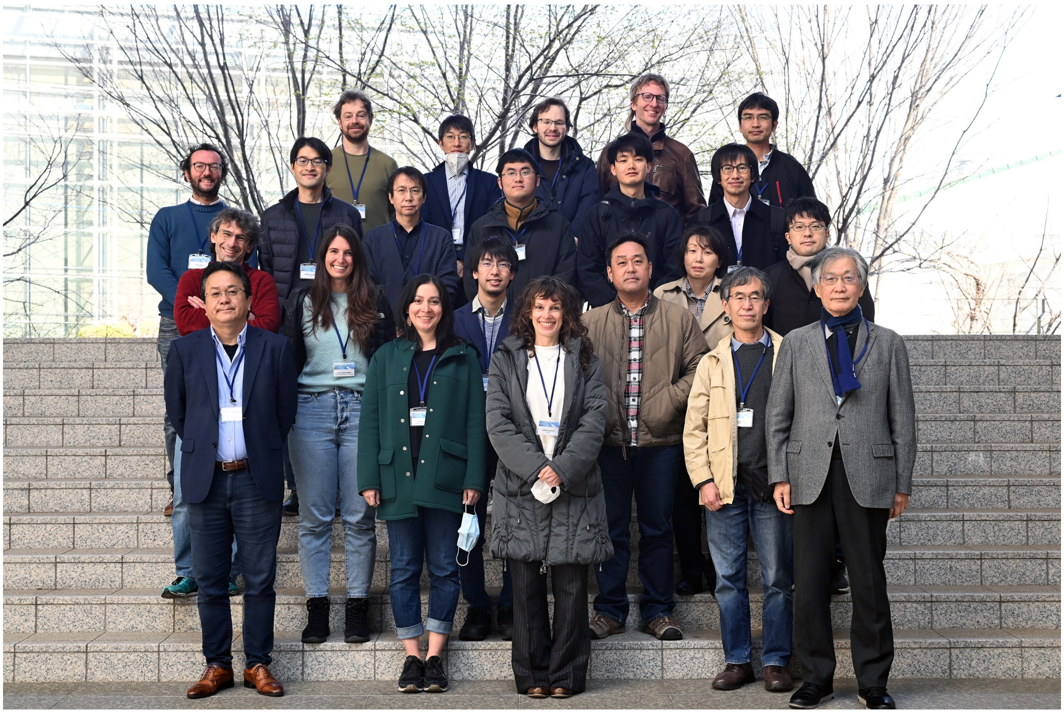

Fig. 5. Memorial photo of participants taken at piloti of ICRR during the Symposium

B. ICRR Seminars

1. May, 27, 2021: Dr. Masato Takita (ICRR), “First observation of sub-PeV galactic diffuse gamma rays by the Tibet ASgamma experiment”
2. August, 2, 2021: Dr. Eduardo de la Fuente Acosta (Departamento de Fisica, CUCEI, Universidad de Guadalajara, and ICRR), “PeVatrons and Star Formation Regions”
3. October, 13, 2021: Dr. Yasuo Fukui (Department of Physics, Nagoya University), “Quantification of the hadronic and leptonic gamma-ray components in the TeV gamma ray supernova remnant RX J1713.7-3946”
4. December, 8, 2021: Dr. Moritz Huetten (ICRR), “Searches for Dark Matter with the MAGIC and CTA gamma-ray telescopes: Latest results and a glimpse into the future”

C. List of Publications

(a) Papers Published in Journals

1. ”Search for solar electron anti-neutrinos due to spin-flavor precession in the Sun with Super-Kamiokande-IV”, Super-Kamiokande Collaboration, Astroparticle Physics Volume **139**, June 2022, 102702, Mar. 2022.
2. ”First Gadolinium Loading to Super-Kamiokande”, The Super-Kamiokande Collaboration, Nuclear Inst. and Methods in Physics Research, A **1027** (2022) 166248, Dec. 2021.
3. ”Diffuse supernova neutrino background search at Super-Kamiokande”, Super-Kamiokande Collaboration, PHYSICAL REVIEW D **104**, 122002 (2021), Dec. 2021.
4. ”Precise measurement of the scintillation decay constant of $ZnWO_4$ crystal”, M Shibata, H Sekiya, K Ichimura, Prog. Theor. Exp. Phys. **2022** 013C01, Oct. 2021.
5. ”Search for neutrinos in coincidence with gravitational wave events from the LIGO-Virgo O3a Observing Run with the Super-Kamiokande detector”, The Super-Kamiokande Collaboration, 2021 ApJ **918** 78, Sep. 2021.
6. ”Search for tens of MeV neutrinos associated with gamma-ray bursts in Super-Kamiokande”, Super-Kamiokande Collaboration, Prog. Theor. Exp. Phys. **2021**, 103F01, Jul. 2021.
7. ”The NEUT neutrino interaction simulation program library”, Yoshinari Hayato, Luke Pickering, Eur.Phys.J.ST **230**(2021)24, 4469-4481, Jun. 2021.
8. ”Measurements of $\bar{\nu}_\mu$ and $\bar{\nu}_\mu + \nu_\mu$ charged-current cross-sections without detected pions or protons on water and hydrocarbon at a mean anti-neutrino energy of 0.86 GeV”, T2K Collaboration, PTEP **2021** (2021) 4, 043C01, Dec. 2021.
9. ”Improved constraints on neutrino mixing from the T2K experiment with 3.13×10^{21} protons on target”, T2K Collaboration, Phys.Rev.D **103** (2021) 11, 112008, Dec. 2021.
10. ”First T2K measurement of transverse kinematic imbalance in the muon-neutrino charged-current single-π^+ production channel containing at least one proton”, T2K Collaboration, Phys.Rev.D **103** (2021) 11, 112009, May. 2021.
11. ”Simultaneous measurement of the muon neutrino charged-current cross section on oxygen and carbon without pions in the final state at T2K”, T2K Collaboration, PhysRevD.**101**.112004, May, 2021.
12. ”T2K measurements of muon neutrino and antineutrino disappearance using 3.13×10^{21} protons on target”, T2K Collaboration, PhysRevD.**103**.L011101, May, 2021.
13. ”First Measurement of the Charged Current antinumu Double Differential Cross Section on a Water Target without Pions in the final state”, T2K Collaboration, Phys.Rev.D **102** (2020) 1, 012007, Apr. 2021.
14. ”Supernova Model Discrimination with Hyper-Kamiokande”, Hyper-Kamiokande Collaboratioonn, Astrophys.J. **916** (2021) 1, 15, Jul. 2021.

15. ”Comparison of validation methods of simulations for final state interactions in hadron production experiments”, S. Dytman, Y. Hayato, R. Raboanary, J. T. Sobczyk, J. Tena-Vidal and N. Vololoniaina, Phys.Rev.D **104** (2021) 5, 053006, Sep. 2021.

16. ”Scintillation light increase of carbontetrafluoride gas at low temperature”, K. Mizukoshi, T. Maeda, Y. Nakano, S. Higashino and K. Miuchi, JINST **16** P12033, Dec. 2021.

17. ”Evaluation of the radon adsorption efficiency of activated carbon fiber using tetrafluoromethane”, Y Kotsar, Y Nakano, Y Takeuchi, K Miuchi, Progress of Theoretical and Experimental Physics, Volume **2022**, Issue 2, 023H01, Feb. 2022.

18. ”History of Solar Neutrino Observations”, Masayuki Nakahata, Progress of Theoretical and Experimental Physics, ptac039, Mar. 2022.

19. ”Search for event bursts in XMASS-I associated with gravitational-wave events”, K. Abe et al., Astroparticle Physics Volume **139**, June 2022, 102702, May. 2021.

20. ”^{222}Rn emanation measurements for the XENON1T experiment”, E. Aprile et al., The European Physical Journal C volume **81**, Article number: 337 (2021), Apr. 2021.

21. ”Search for inelastic scattering of WIMP dark matter in XENON1T”, E. Aprile et al., Phys. Rev. D **103**, 063028, Mar. 2021.

22. ”Search for Coherent Elastic Scattering of Solar ^{8}B Neutrinos in the XENON1T Dark Matter Experiment (2021), arXiv:2012.02846”, E. Aprile et al., Phys. Rev. Lett. **126**, 091301, Mar. 2021.

23. ”Improved quality tests of R11410-21 photomultiplier tubes for the XENONnT experiment ”, V.C. Antochi et al., 2021 JINST **16** P08033, Aug. 2021.

24. ”Characterization of new silicon photomultipliers with low dark noise at low temperature”, K. Ozaki, S. Kazama, M. Yamashita, Y. Itow and S. Moriyama, 2021 JINST **16** P03014, Mar. 2021.

25. ”Broadband Multi-wavelength Properties of M87 during the 2017 Event Horizon Telescope Campaign”, J.C. Albaga et al. (EH Telescope, MAGIC collaboration), Astrophys.J.Lett. **911** (2021) 1, L11, April.2021.

26. ”Gamma-Ray Bursts at TeV Energies: Observational Status”, Koji Noda and Robert Daniel Parsons, Galaxies **2022**, 10(1), 7, Jan. 2022.

27. ”Combined searches for dark matter in dwarf spheroidal galaxies observed with the MAGIC telescopes, including new data from Coma Berenices and Draco”, MAGIC collaboration, Physics of the Dark Universe, Volume **35**, article id. 100912., Mar. 2022.

28. ”Investigating the Blazar TXS 0506+056 through Sharp Multiwavelength Eyes During 2017-2019”, MAGIC collaboration, The Astrophysical Journal, Volume **927**, Issue 2, id.197, 15 pp., Mar. 2022.

29. ”Multiwavelength study of the gravitationally lensed blazar QSO B0218+357 between 2016 and 2020”, MAGIC collaboration, Monthly Notices of the Royal Astronomical Society, Volume **510**, Issue 2, pp.2344-2362, Feb. 2022.

30. ”Observation of the Gamma-Ray Binary HESS J0632+057 with the H.E.S.S., MAGIC, and VERITAS Telescopes”, VERITAS collaboration, MAGIC collaboration, H.E.S.S. collaboration, The Astrophysical Journal, Volume **923**, Issue 2, id.241, 30 pp., Dec. 2021.

31. ”Search for Very High-energy Emission from the Millisecond Pulsar PSR J0218+4232”, MAGIC collaboration, The Astrophysical Journal, Volume **922**, Issue 2, id.251, 14 pp., Dec. 2021.

32. ”Investigation of the correlation patterns and the Compton dominance variability of Mrk 421 in 2017”, MAGIC collaboration, FACT collaboration, Astronomy & Astrophysics, Volume **655**, id.A89, 36 pp., Nov.2021.

33. ”First detection of VHE gamma-ray emission from TXS 1515-273, study of its X-ray variability and spectral energy distribution”, MAGIC collaboration, Monthly Notices of the Royal Astronomical Society, Volume **507**, Issue 1, pp.1528-1545, Oct. 2021.

34. ”Multiwavelength variability and correlation studies of Mrk 421 during historically low X-ray and γ-ray activity in 2015-2016”, MAGIC collaboration, Monthly Notices of the Royal Astronomical Society, Volume **504**, Issue 1, pp.1427-1451, Jun. 2021.

35. ”H.E.S.S. and MAGIC observations of a sudden cessation of a very-high-energy γ-ray flare in PKS 1510-089 in May 2016”, H.E.S.S. collaboration, MAGIC collaboration, Astronomy & Astrophysics, Volume **648**, id.A23, 22 pp., Apr. 2021.

36. ”Particle identification and analysis in the SciCRT using machine learning tools”, R. Garcia, M. Anzorena, T. Sako et al., Nucl. Inst. Meth A **1003**(2021), 165326, Jul. 2021.

37. ”Observation of variations in cosmic ray single count rates during thunderstorms and implications for large-scale electric field changes”, R.U. Abbasi et al. (The Telescope Array Collaboration), Phys. Rev. D **105**, 062002, Mar. 2022.

38. ”Proper motions of water masers in the star-forming region IRAS 23139+5939”, Eduardo DE LA FUENTE, Publ. Astron. Soc. Japan (2021) **73** (6), 1669–1680, Nov. 2021.

39. ”Performance of RHICf detector during operation in 2017”, O. Adriani, E. Berti, L. Bonechi, R. D’Alessandro, Y. Goto, B. Hong, Y. Itow, K. Kasahara, M.H. Kim, H. Menjo, I. Nakagawa, K. Ohashi, T. Sako, N. Sakurai, K. Sato, R. Seidl, K. Tanida, S. Torii and A. Tricomi, 2021 JINST **16** P10027, Oct. 2021.

40. ”Surface detectors of the TAx4 experiment”, R.U. Abbasi et al. (The Telescope Array Collaboration), Nuclear Inst. and Methods in Physics Research, A **1019** (2021) 165726, Dec. 2021.

41. ”Population III Binary Black Holes: Effects of Convective Overshooting on Formation of GW190521”, Ataru Tanikawa, Tomoya Kinugawa, Takashi Yoshida, Kotaro Hijikawa, and Hideyuki Umeda, MNRAS **505**, 2170–2176 (2021) , May. 2021.

42. ”Polarization Images of Accretion Flow around Supermassive Black Holes: Imprints of Toroidal Field Structure”, Yuh Tsunetoe, Shin Mineshige, Ken Ohsuga, Tomohisa Kawashima, and Kazunori Akiyama, Publ. Astron. Soc. Japan (2021) **73** (4), 912–928, Aug. 2021.

43. ”A Low-Mass Binary Neutron Star: Long-Term Ejecta Evolution and Kilonovae with Weak Blue Emission”, Kyohei Kawaguchi, Sho Fujibayashi, Masaru Shibata, Masaomi Tanaka, and Shinya Wanajo, 2021 ApJ **913** 100, May. 2021.

44. ”The origins and impact of outflow from super-Eddington flow”, Takaaki Kitaki, Shin Mineshige, Ken Ohsuga, and Tomohisa Kawashima, Publ. Astron. Soc. Japan (2021) **73** (2), 450–466, Mar. 2021.

45. ”Gravitational Waves from Population III Binary Black Holes are Consistent with LIGO/Virgo O3a Data for the Chirp Mass Larger than $\sim$20$M_\odot$”, Tomoya Kinugawa, Takashi Nakamura, and Hiroyuki Nakano, MNRASL **504**, Issue 1, L28–L33, Apr. 2021.

46. ”Signatures of r-Process Elements in Kilonova Spectra”, Nanae Domoto, Masaomi Tanaka, Shinya Wanajo, and Kyohei Kawaguchi, 2021 ApJ **913** 26, May. 2021.

47. ”X-ray hot spots in the eastern ear of the supernova remnant W 50 and the microquasar SS 433 system”, Ryota Hayakawa, Shinya Yamada, Hirotaka Suda, Yuto Ichinohe, Ryota Higurashi, Haruka Sakemi, Mami Machida, Takumi Ohmura, Satoru Katsuda, Hideki Uchiyama, Toshiki Sato, Hiroki Akamatsu, and Magnus Axelsson, Publ. Astron. Soc. Japan (2022) , Mar. 2022.

48. ”MeerKAT’s view of double radio relic galaxy cluster Abell 3376”, James O. Chibueze, Hiroki Akamatsu, Viral Parekh, Haruka Sakemi, Takumi Ohmura, Ruby van Rooyen, Takuya Akahori, Hiroyuki Nakanishi, Mami Machida, Tsutomu T Takeuchi, Oleg Smirnov, Dane Kleiner, and Filippo M. Maccagni,, Publ. Astron. Soc. Japan (2022) , Mar. 2022.

49. ”Mushroom-Instability-Driven Magnetic Reconnections in Collisionless Relativistic Jets”, Tomohisa Kawashima, Seiji Ishiguro, Toseo Moritaka, Ritoku Horiuchi, and Kohji Tomisaka, 2022 ApJ **928** 62, Mar. 2022.

50. ”Can Population III Stars be Major Origins of both Merging Binary Black Holes and Extremely Metal Poor Stars?”, Ataru Tanikawa, Gen Chiaki, Tomoya Kinugawa, Yudai Suwa, and Nozomu Tominaga, Publ. Astron. Soc. Japan (2022) , Mar. 2022.

51. ”The Intrinsic Structure of Sagittarius A* at 1.3 cm and 7 mm”, I. Cho, G.-Y. Zhao, T. Kawashima, et al., 2022 ApJ **926** 108, Feb. 2022.

52. ”Monte Carlo Study of Electron and Positron Cosmic-Ray Propagation with the CALET Spectrum”, Katsuaki Asano, Yoichi Asaoka, Yosui Akaike, Norita Kawanaka, Kazunori Kohri, Holger M. Motz, and Toshio Terasawa,, 2022 ApJ **926** 5, Feb. 2022.

53. ”The Variability of the Black-Hole Image in M87 at the Dynamical Time Scale”, K. Satapathy, D. Psaltis, F. Ozel, et al., 2022 ApJ **925** 13, Jan. 2022.

54. ”Merger rate density of binary black holes through isolated Population I, II, and III binary star evolution”, Ataru Tanikawa, Takashi Yoshida, Tomoya Kinugawa, Alessandro A. Trani, Takashi Hosokawa, Hajime Susa, and Kazuyuki Omukai, 2022 ApJ **926** 83, Feb. 2022.

55. ”Event Horizon Telescope observations of the jet launching and collimation in Centaurus A”, M. Janssen, et al., Nat Astron **5**, 1017–1028 (2021), Jul. 2021.

56. ”Measurement of the Iron Spectrum in Cosmic Rays from 10 GeV/n to 2.0 TeV/n with the Calorimetric Electron Telescope on the International Space Station”, O. Adriani, Y. Akaike, K. Asano, et al.,, Phys. Rev. Lett. **126**, 241101 , Jun. 2021.

57. ”Particle Reacceleration by Turbulence and Radio Constraints on Multi-Messenger High-Energy Emission from the Coma Cluster”, Kosuke Nishiwaki, Katsuaki Asano, and Kohta Murase, Astrophys.J. **922** (2021) 2, 190, Nov. 2021.

58. ”Jets from MRC 0600-399 Bent by Magnetic Fields in the Cluster Abell 3376”, James O. Chibueze, Haruka Sakemi, Takumi Ohmura, Mami Machida, Hiroki Akamatsu, Takuya Akahori, Hiroyuki Nakanishi, Viral Parekh, Ruby van Rooyen, and Tsutomu T. Takeuchi,, Nature **593**, 47–50 (2021), May. 2021.

59. ”The Polarized Image of a Synchrotron-Emitting Ring of Gas Orbiting a Black Hole”, Ramesh Narayan, et al.,, ApJ **912**, 35(26pp) (2021), May. 2021.

60. ”On the Population III Binary Black Hole Mergers beyond the Pair-Instability Mass Gap”, Kotaro Hijikawa, Ataru Tanikawa, Tomoya Kinugawa, Takashi Yoshida, and Hideyuki Umeda, MNRAS **505**, L69–L73 (2021) , May. 2021.

61. ”Enhanced X-Ray Emission Coinciding with Giant Radio Pulses from the Crab Pulsar”, T. Enoto, T. Terasawa, S. Kisaka, et al. , Science **372**, 187-190, Apr. 2021.

62. ”First Detection of sub-PeV Diffuse Gamma Rays from the Galactic Disk: Evidence for Ubiquitous Galactic Cosmic Rays beyond PeV Energies”, M. Amenomori et al. (Tibet ASgamma Collaboration), Phys. Rev. Lett. **126**, 141101, Apr. 2021.

63. ”Trigger time acquisition system for ground based air shower experiments”, T. Ohura, M. Ohnishi, Y. Katayose, NIM A **1028** (2022) 166363, Jan. 2022.

64. ”Detectability of southern gamma-ray sources beyond 100 TeV with ALPAQUITA, the prototype experiment of ALPACA”, S. Kato et al., (The ALPACA Collaboration), Experimental Astronomy volume **52**, pages 85–107 (2021), Oct. 2021.

65. ”Gamma-Ray Observation of the Cygnus Region in the 100-TeV Energy Region”, M. Amenomori et al. (Tibet AS γ Collaboration), PHYSICAL REVIEW LETTERS/**127**, 031102 (2021), Jul. 2021.

66. ”Development of an omnidirectional Compton camera using CaF2(Eu) scintillators to visualize gamma rays with energy below 250 keV for radioactive environmental monitoring in nuclear medicine facilities”, H. Katagiri , N. Narita , R. Enomoto , H. Muraishi , D. Kano , T. Watanabe, R. Wakamatsu , M. Kagaya , M.M. Tanaka, Nucl. Inst. Meth A **996** (2021) 165133, Apr. 2021.

67. ”High Performance Heat Conductor with Small Spring Constant for Cryogenic Applications”, Tomohiro Yamada, Takayuki Tomaru, Toshikazu Suzuki, Takafumi Ushiba, Nobuhiro Kimura, Suguru Takada, Yuki Inoue, Takaaki Kajita, Cryogenics, **116**, 103280(2021), Jun. 2021.

68. ”Unified mapmaking for an anisotropic stochastic gravitational wave background”, Jishnu Suresh, Anirban Ain, and Sanjit Mitra, Phys. Rev. D **103**, 083024, Apr. 2021.

69. ”Method for environmental noise estimation via injection tests for ground-based gravitational wave detectors”, T. Washimi, T. Yokozawa, T. Tanaka, Y. Itoh, J. Kume, J. Yokoyama, Class. Quantum Grav. **38** 125005, May. 2021.

70. ”Prospects for estimating parameters from gravitational waves of superspinar binaries”, Nami Uchikata, Tatsuya Narikawa, Phys. Rev. D **104**, 024059 (2021), Jul. 2021.

71. ”Gravitational-wave constraints on the GWTC-2 events by measuring the tidal deformability and the spin-induced quadrupole moment”, Tatsuya Narikawa, Nami Uchikata, Takahiro Tanaka, Phys. Rev. D **104**, 084056 (2021), Oct. 2021.

72. ”Gravitational wave physics and astronomy in the nascent era”, Arimoto et al., Prog. Theor. Exp. Phys. 2021, 0000 (83 pages), Apr. 2021.

73. ”Investigation of crackling noise in the vibration isolation systems of the KAGRA gravitational wave detector”, Y Zhao, S Kirii, Y Liu, T Uchiyama, R Takahashi, S Kawamura, Physics Letters A, Volume **416**, 127664, Nov. 2021.

74. ”Effects of lightning strokes on underground gravitational waves observatories”, T. Washimi, T. Yokozawa, M. Nakano, T. Tanaka, K. Kaihotsu, Y. Mori, T. Narita, IOP, JINST **16** P07033, Jul. 2021.

75. ”The KAGRA underground environment and lessons for the Einstein Telescope”, Francesca Badaracco, Jan Harms, Camilla De Rossi, Irene Fiori, Kouseki Miyo, Taiki Tanaka, Takaaki Yokozawa, Federico Paoletti, and Tatsuki Washimi, Phys. Rev. D **104**, 042006 (2021), Aug. 2021.

76. ”Local Hurst exponent computation of data from triaxial seismometers monitoring KAGRA”, A. Longo, S. Bianchi, W. Plastinao, K. Miyo, T. Yokozawa, T. Washimi, A. Araya, Pure and Applied Geophysics volume **178**, pages3461–3470 (2021), Jul. 2021.

77. ”Application of the Hilbert-Huang transform for analyzing standing-accretion-shock-instability induced gravitational waves in a core-collapse supernova”, M. Takeda, Y. Hiranuma, N. Kanda ,K. Kotake, T. Kuroda, R. Negishi, K. Oohara, K. Sakai, Y. Sakai, T. Sawada, H. Takahashi, S. Tsuchida, Y. Watanabe, T. Yokozawa, Physical Review D **104**, 084063 (2021), Oct. 2021.

78. ”A nonparametric method to assess the significance of events in the search for gravitational waves with false discovery rate”, Hirotaka Yuzurihara, Shuhei Mano, Hideyuki Tagoshi, PTEP 2021 **(2021)** 12, 123F01, Dec. 2021.

79. ”Diving below the spin-down limit: Constraints on gravitational waves from the energetic young pulsar PSR J0537-6910”, R. Abbott et al,(LIGO Scientific Collaboration, Virgo Collaboration, and KAGRA Collaboration, NICER), ApJL **913** L27, May. 2021.

80. ”Constraints on cosmic strings using data from the third Advanced LIGO-Virgo observing run”, R. Abbott et al. (LIGO Scientific Collaboration, Virgo Collaboration, and KAGRA Collaboration), Phys. Rev. Lett. **126**, 241102, Jun. 2021.

81. ”Observation of Gravitational Waves from Two Neutron Star–Black Hole Coalescences”, R. Abbott et al. (LIGO Scientific Collaboration, Virgo Collaboration, and KAGRA Collaboration), ApJL **915** L5, Jun. 2021.

82. ”Upper Limits on the Isotropic Gravitational-Wave Background from Advanced LIGO’s and Advanced Virgo’s Third Observing Run”, R. Abbott et al. (LIGO Scientific Collaboration, Virgo Collaboration, and KAGRA Collaboration), Phys. Rev. D **104** (2021) 022004, Jul. 2021.

83. ”Search for anisotropic gravitational-wave backgrounds using data from Advanced LIGO’s and Advanced Virgo’s first three observing runs ”, R. Abbott et al. (LIGO Scientific Collaboration, Virgo Collaboration, and KAGRA Collaboration), Phys. Rev. D **104**, 022005, Jul. 2021.

84. ”Constraints from LIGO O3 data on gravitational-wave emission due to r-modes in the glitching pulsar PSR J0537-6910”, R. Abbott et al. (LIGO Scientific Collaboration, Virgo Collaboration, and KAGRA Collaboration), 2021 ApJ **922** 71, Nov. 2021.

85. ”Searches for Continuous Gravitational Waves from Young Supernova Remnants in the Early Third Observing Run of Advanced LIGO and Virgo”, R. Abbott et al. (LIGO Scientific Collaboration, Virgo Collaboration, and KAGRA Collaboration), 2021 ApJ **921** 80, Nov. 2021.

86. ”All-sky search for short gravitational-wave bursts in the third Advanced LIGO and Advanced Virgo run”, R. Abbott et al. (The LIGO Scientific Collaboration, the Virgo Collaboration, and the KAGRA Collaboration), Phys. Rev. D **104**, 122004 , Dec. 2021.

87. ”All-sky search for continuous gravitational waves from isolated neutron stars in the early O3 LIGO data”, R. Abbott et al. (LIGO Scientific Collaboration, Virgo Collaboration, and KAGRA Collaboration), Phys. Rev. D **104**, 082004 , Oct. 2021.

88. ”All-sky search for long-duration gravitational-wave bursts in the third Advanced LIGO and Advanced Virgo run”, R. Abbott et al. (LIGO Scientific Collaboration, Virgo Collaboration, and KAGRA Collaboration), Phys. Rev. D **104**, 102001 , Nov. 2021.

89. ”Constraints on dark photon dark matter using data from LIGO’s and Virgo’s third observing run”, R. Abbott et al. (LIGO Scientific Collaboration, Virgo Collaboration, and KAGRA Collaboration), Phys. Rev. D **105**, 063030, Mar. 2022.

90. ”Search for intermediate-mass black hole binaries in the third observing run of Advanced LIGO and Advanced Virgo”, R. Abbott et al. (LIGO Scientific Collaboration, Virgo Collaboration, and KAGRA Collaboration), A&A **659**, A84 (2022), Mar. 2022.

91. ”Search for continuous gravitational waves from 20 accreting millisecond x-ray pulsars in O3 LIGO data”, R. Abbott et al. (LIGO Scientific Collaboration, Virgo Collaboration, and KAGRA Collaboration), Phys. Rev. D **105**, 022002, Jan. 2022.

92. ”SILVERRUSH. IX. Lyα Intensity Mapping with Star-forming Galaxies at z = 5.7 and 6.6: A Possible Detection of Extended Lyα Emission at $\gtrsim$100 Comoving Kiloparsecs around and beyond the Virial-radius Scale of Galaxy Dark Matter Halos”, R. Kakuma, et al.,, 2021 ApJ **916** 22, Jul. 2021.

93. ”EMPRESS. III. Morphology, Stellar Population, and Dynamics of Extremely Metal Poor Galaxies (EMPGs): Are EMPGs Local Analogs of High- z Young Galaxies?”, Y. Isobe, et al., 2021 ApJ **918** 54, Sep. 2021.

94. ”Probing Feedback via IGM tomography and Lyα forest with Subaru PFS, TMT/ELT, & JWST”, K. Nagamine, et al., 2021 ApJ **914** 66, Jun. 2021.

95. ”RELICS: A Candidate z$\sim$6.8 Strong [OIII] emitter and Other Properties of z$\geq$5.5 Galaxies Inferred from Spitzer and Hubble Imaging”, V. Strait, et al., 2021 ApJ **910** 135, Apr. 2021.

96. ”ALMA Lensing Cluster Survey: Bright [CII] 158 μm Lines from a Multiply Imaged Sub-L* Galaxy at z=6.0719”, S. Fujimoto et al., 2021 ApJ **911** 99, Apr. 2021.

97. ”Accelerated galaxy growth and environmental quenching in a protocluster at z=3.24”, K. Shi, et al., 2021 ApJ **911** 46, Apr. 2021.

98. ”Subaru High-z Exploration of Low-luminosity Quasars (SHELLQs). XVI. 69 New Quasars at 5.8 $<$ z $<$ 7.0”, Matsuoka, Yoshiki; et al., 2022 ApJS **259** 18, Feb. 2022.

99. ”GOLDRUSH. IV. Luminosity Functions and Clustering Revealed with $\sim$4,000,000 Galaxies at z$\sim$2-7: Galaxy-AGN Transition, Star Formation Efficiency, and Implication for Evolution at z $>$ 10”, Harikane, Yuichi; Ono, Yoshiaki; Ouchi, Masami; Liu, Chengze; Sawicki, Marcin; Shibuya, Takatoshi ; Behroozi, Peter S. ; He, Wanqiu ; Shimasaku, Kazuhiro; Arnouts, Stephane ; Coupon, Jean ; Fujimoto, Seiji; Gwyn, Stephen; Huang, Jiasheng ; Inoue, Akio K.; Kashikawa, Nobunari; Komiyama, Yutaka; Matsuoka, Yoshiki; Willott, Chris J, 2022 ApJS **259** 20, Mar. 2022.

100. ”CHORUS. IV. Mapping the Spatially Inhomogeneous Cosmic Reionization with Subaru HSC”, Yoshioka, Takehiro ; Kashikawa, Nobunari ; Inoue, Akio K. ; Yamanaka, Satoshi ; Shimasaku, Kazuhiro ; Harikane, Yuichi ; Shibuya, Takatoshi ; Momose, Rieko ; Ito, Kei ; Liang, Yongming ; Ishimoto, Rikako ; Takeda, Yoshihiro ; Ouchi, Masami ; Lee, Chien-Hsiu, 2022 ApJ **927** 32, Mar. 2022.

101. ”Third data release of the Hyper Suprime-Cam Subaru Strategic Program”, Hiroaki Aihara, et al., Publ. Astron. Soc. Japan (2022) **74** (2), 247–272, Feb. 2022.

102. ”Galaxy morphologies revealed with Subaru HSC and super-resolution techniques. I. Major merger fractions of $L_{UV} \sim$ 3-15 $L^{\star}_{UV}$ dropout galaxies at z $\sim$ 4-7”, Shibuya, Takatoshi ; Miura, Noriaki ; Iwadate, Kenji ; Fujimoto, Seiji; Harikane, Yuichi; Toba, Yoshiki; Umayahara, Takuyaa; Ito, Yohito,, Publ. Astron. Soc. Japan (2022) **74** (1), 73–91, Jan. 2022.

103. ”FOREVER22: galaxy formation in protocluster regions”, Hidenobu Yajima, Makito Abe, Sadegh Khochfar, Kentaro Nagamine, Akio K Inoue, Tadayuki Kodama, Shohei Arata, Claudio Dalla Vecchia, Hajime Fukushima, Takuya Hashimoto, Nobunari Kashikawa, Mariko Kubo, Yuexing Li, Yuichi Matsuda, Ken Mawatari, Masami Ouchi, Hideki Umehata, , MNRAS **509**, 4037–4057 (2022) , Oct. 2021.

104. ”The Hobby-Eberly Telescope Dark Energy Experiment (HETDEX) Survey Design, Reductions, and Detections”, Karl Gebhardt et al., 2021 ApJ **923** 217, Dec. 2021.

105. ”First HETDEX Spectroscopic Determinations of Lyα and UV Luminosity Functions at z = 2-3: Bridging a Gap between Faint AGNs and Bright Galaxies”, Yechi Zhang, Masami Ouchi, Karl Gebhardt, Erin Mentuch Cooper, Chenxu Liu, Dustin Davis, Donghui Jeong, Daniel J. Farrow, Steven L. Finkelstein, Eric Gawiser,, 2021 ApJ **922** 167, Nov. 2021.

106. ”Subaru/FOCAS IFU revealed the metallicity gradient of a local extremely metal-poor galaxy”, Kashiwagi, Yuri ; Inoue, Akio K. ; Isobe, Yuki ; Nakajima, Kimihiko ; Ouchi, Masami ; Ozaki, Shinobu ; Fujimoto, Seiji ; Ono, Yoshiaki ; Kojima, Takashi,, Publ. Astron. Soc. Japan (2021) **73** (6), 1631–1637, Nov. 2021.

107. "ALMA Observations of Lyα Blob 1: Multiple Major Mergers and Widely Distributed Interstellar Media", Umehata, Hideki ; Smail, Ian ; Steidel, Charles C. ; Hayes, Matthew ; Scott, Douglas ; Swinbank, A. M. ; Ivison, R. J. ; Nagao, Toru ; Kubo, Mariko ; Nakanishi, Kouichiro ; Matsuda, Yuichi ; Ikarashi, Soh ; Tamura, Yoichi ; Geach, J. E, 2021 ApJ **918** 69, Sep. 2021.

108. "A Massive Quiescent Galaxy Confirmed in a Protocluster at z = 3.09", Kubo, Mariko ; Umehata, Hideki ; Matsuda, Yuichi ; Kajisawa, Masaru ; Steidel, Charles C. ; Yamada, Toru ; Tanaka, Ichi ; Hatsukade, Bunyo ; Tamura, Yoichi ; Nakanishi, Kouichiro ; Kohno, Kotaro ; Lee, Kianhong ; Matsuda, Keiichi, 2021 ApJ **919** 6, Sep. 2021.

109. "On the Nature of AGN and Star Formation Enhancement in the z = 3.1 SSA22 Protocluster: The HST WFC3 IR View", Monson, Erik B. ; Lehmer, Bret D. ; Doore, Keith ; Eufrasio, Rafael T. ; Bonine, Brett ; Alexander, David M. ; Harrison, Chris M. ; Kubo, Mariko ; Mantha, Kameswara B. ; Saez, Cristian ; Straughn, Amber ; Umehata, Hideki , 2021 ApJ **919** 51, Sep. 2021.

110. "Subaru High-z Exploration of Low-luminosity Quasars (SHELLQs). XIV. A Candidate Type II Quasar at z = 6.1292", Onoue, Masafusa et al., 2021 ApJ **919** 61, Sep. 2021.

111. "EMPRESS. II. Highly Fe-enriched Metal-poor Galaxies with $\sim$1.0 $(Fe/O)_\odot$ and 0.02 $(O/H)_\odot$: Possible Traces of Supermassive (>300 $M_\odot$) Stars in Early Galaxies", Kojima, Takashi et al., 2021 ApJ **913** 22, May. 2021.

112. "SILVERRUSH X: Machine Learning-Aided Selection of 9318 LAEs at z=2.2, 3.3, 4.9, 5.7, 6.6, and 7.0 from the HSC SSP and CHORUS Survey Data", Ono, Yoshiaki; et al., 2021 ApJ **911** 78, Apr. 2021.

113. "Optical Spectroscopy of Dual Quasar Candidates from the Subaru HSC-SSP program", Tang, Shenli et al., 2021 ApJ **922** 83, Nov. 2021.

114. "EMPRESS. IV. Extremely Metal-poor Galaxies Including Very Low-mass Primordial Systems with $M_* = 10^4$-10^5 $M_\odot$ and 2%-3% (O/H): High (Fe/O) Suggestive of Metal Enrichment by Hypernovae/Pair-instability Supernovae", Isobe, Yuki et al., 2022 ApJ **925** 111, Feb. 2022.

115. "A Wide and Deep Exploration of Radio Galaxies with Subaru HSC (WERGS). VI. Distant Filamentary Structures Pointed Out by High-z Radio Galaxies at z$\sim$4", Uchiyama, Hisakazu et al., 2022 ApJ **926** 76, Feb. 2022.

116. "SILVERRUSH. XI. Constraints on the Lyα Luminosity Function and Cosmic Reionization at z = 7.3 with Subaru/Hyper Suprime-Cam ", Goto, Hinako et al., 2021 ApJ **923** 229, Dec. 2021.

117. "Probing Oscillons of Ultra-Light Axion-like Particle by 21cm Forest", Masahiro Kawasaki, Wakutaka Nakano, Hiromasa Nakatsuka, Eisuke Sonomoto,, JCAP04(**2021**)019, Apr. 2021.

118. "Affleck-Dine inflation in supergravity", Masahiro Kawasaki, Shusuke Ueda, JCAP04(**2021**)049, Apr. 2021.

119. "Power spectrum in stochastic inflation", Kenta Ando, Vincent Vennin, JCAP04(**2021**)057, Apr. 2021.

120. "Gravitational waves from type II axion-like curvaton model and its implication for NANOGrav result", Masahiro Kawasaki, Hiromasa Nakatsuka, JCAP05(**2021**)023, May. 2021.

121. "On Stability of Superconducting Current in Cosmic String", Masahiro Ibe, Shin Kobayashi, Yuhei Nakayama, Satoshi Shirai, J. High Energ. Phys. **2021**, 217 (2021)., May. 2021.

122. "Cosmological Constraints on Dark Scalar", Masahiro Ibe, Shin Kobayashi, Yuhei Nakayama, Satoshi Shirai,, J. High Energ. Phys. **2022**, 198 (2022)., Mar. 2022.

123. "Constraints on small-scale primordial density fluctuation from cosmic microwave background through dark matter annihilation", Masahiro Kawasaki, Hiromasa Nakatsuka, Kazunori Nakayama,, JCAP03(**2022**)061, Mar. 2022.

124. "Gauge Kinetic Mixing and Dark Topological Defects", Takashi Hiramatsu, Masahiro Ibe, Motoo Suzuki, Soma Yamaguchi,, J. High Energ. Phys. **2021**, 122 (2021), Dec. 2021.

125. "Gravitational wave trispectrum in the axion-SU(2) model", Tomohiro Fujita, Kai Murai, Ippei Obata, Maresuke Shiraishi,, JCAP01(**2022**)007, Jan. 2022.

126. "Strong clustering of primordial black holes from Affleck-Dine mechanism", Masahiro Kawasaki, Kai Murai, Hiromasa Nakatsuka, JCAP10(**2021**)025, Oct. 2021.

127. "Revisiting CMB constraints on dark matter annihilation", Masahiro Kawasaki, Hiromasa Nakatsuka, Kazunori Nakayama, Toyokazu Sekiguchi,, JCAP12(**2021**)015, Dec. 2021.

128. "Chiral Composite Asymmetric Dark Matter", Masahiro Ibe, Shin Kobayashi, Keiichi Watanabe,, J. High Energ. Phys. **2021**, 220 (2021), Jul. 2021.

129. "Muon g-2 in Gauge Mediation without SUSY CP Problem", Masahiro Ibe, Shin Kobayashi, Yuhei Nakayama, Satoshi Shirai,, J. High Energ. Phys. 2021, 98 **(2021)**, Jul. 2021.

(b) Conference Papers (Proceedings)

1. "Latest Results from the XMASS Experiment", Ichimura, K, 14th Asia-Pacific Physics Conference (APPC), NOV 17-22, 2019

2. "COSMOS X as a general purpose air shower simulation tool", T. Sako, T. Fujii, K. Kasahara, H. Menjo, N. Sakaki, N. Sakurai, A. Taketa, Y. Tameda and the COSMOS X development team, 37th Intrenational Cosmic Ray Conference, JUL 12-23 2021

3. "Telescope Array anisotropy summar", T. Fujii, D. Ivanov, C.C.H. Jui, K. Kawata, J.H. Kim, M.Yu. Kuznetsov, T. Nonaka, S. Ogio, G.I. Rubtsov, H. Sagawa, G.B. Thomson, P.G. Tinyakov, I. Tkachev and S. Troitsky on behalf of the Telescope Array Collaboration, 37th Intrenational Cosmic Ray Conference, JUL 12-23 2021

4. "Mass composition of Telescope Array's surface detectors events using deep learning", I. Kharuk, and O. Kalashev on behalf of the Telescope Array Collaboration, 37th Intrenational Cosmic Ray Conference, JUL 12-23 2021

5. "The UHECR dipole and quadrupole in the latest data from the original Auger and TA surface detectors", P. Tinyakov, L. Anchordoqui, T. Bister, J. Biteau, L. Caccianiga, R. de Almeida, O. Deligny, A. di Matteo, U. Giaccari, D. Harari, J. Kim, M. Kuznetsov, I. Maris, G. Rubtsov, S. Troitsky and F. Urban on behalf of the Pierre Auger and the Telescope Array Collaboration, 37th Intrenational Cosmic Ray Conference, JUL 12-23 2021

6. "Cosmic ray energy spectrum in the 2nd knee region measured by the TALE-SD array", K. Sato on behalf of the Telescope Array Collaboration, 37th Intrenational Cosmic Ray Conference, JUL 12-23 2021

7. "Effects of Galactic magnetic field on the UHECR anisotropy studies", R. Higuchi, T. Sako, K. Kawata, T. Fujii and E. Kido on behalf of the the Telescope Array Collaboration, 37th Intrenational Cosmic Ray Conference, JUL 12-23 2021

8. "Performance and simulation of the surface detector array of the TAx4 experiment", K. Fujisue on behalf of the Telescope Array Collaboration, 37th Intrenational Cosmic Ray Conference, JUL 12-23 2021

9. "Cosmic Ray Composition in the Second Knee Region as Measured by the TALE Hybrid Detector", K. Fujita on behalf of the Telescope Array Collaboration, 37th Intrenational Cosmic Ray Conference, JUL 12-23 2021

10. "Cosmic Ray Energy Spectrum measured by the TALE Fluorescence Detector", T. AbuZayyad on behalf of the Telescope Array Collaboration, 37th Intrenational Cosmic Ray Conference, JUL 12-23 2021

11. "Cosmic Ray Composition between 2 PeV and 2 EeV measured by the TALE Fluorescence Detector", T. AbuZayyad on behalf of the Telescope Array Collaboration, 37th Intrenational Cosmic Ray Conference, JUL 12-23 2021

12. "Insight Into Lightning Initiation via Downward Terrestrial Gamma-ray Flash Observations at Telescope Array", J. Remington on behalf of the Telescope Array Collaboration, 37th Intrenational Cosmic Ray Conference, JUL 12-23 2021

13. "Anisotropy search in the Ultra High Energy Cosmic Ray Spectrum in the Northern Hemisphere using latest data obtained with Telescope Array surface detector", T. Nonaka on behalf of the Telescope Array Collaboration, 37th Intrenational Cosmic Ray Conference, JUL 12-23 2021

14. "Monocular Energy Spectrum using the TAx4 Fluorescence Detector", M. Potts and C. Jui on behalf of the Telescope Array Collaboration, 37th Intrenational Cosmic Ray Conference, JUL 12-23 2021

15. "Recent measurement of the Telescope Array energy spectrum and observation of the shoulder feature in the Northern Hemisphere", D. Ivanov, D. Bergman, G. Furlich, R. Gonzalez, G. B. Thomson and Y. Tsunesada on behalf of the Telescope Array Collaboration, 37th Intrenational Cosmic Ray Conference, JUL 12-23 2021

16. "Telescope Array 10-Year Monocular Spectrum Measurement", D. R. Bergman and G. Furlich on behalf of the Telescope Array Collaboration, 37th Intrenational Cosmic Ray Conference, JUL 12-23 2021

17. "Telescope Array Combined Fit to Cosmic Ray Spectrum and Composition", D. R. Bergman on behalf of the Telescope Array Collaboration, 37th Intrenational Cosmic Ray Conference, JUL 12-23 2021

18. ”Joint analysis of the energy spectrum of ultra-high-energy cosmic rays measured at the Pierre Auger Observatory and the Telescope Array”, Y. Tsunesada on behalf of the Pierre Auger and the Telescope Array Collaboration, 37th Intrenational Cosmic Ray Conference, JUL 12-23 2021

19. ”Analysis of TAx4 hybrid trigger and events”, S. W. Kim on behalf of the Telescope Array Collaboration, 37th Intrenational Cosmic Ray Conference, JUL 12-23 2021

20. ”Reconstruction of Air Shower Events Measured by the Surface Detectors of the TAx4 Experiment”, H. Jeong on behalf of the Telescope Array Collaboration, 37th Intrenational Cosmic Ray Conference, JUL 12-23 2021

21. ”Energy spectrum and the shower maxima of cosmic rays above the knee region measured with the NICHE detectors at the TA site”, Y. Omura, R. Tsuda, Y. Tsunesada, D. R Bergman and J. F. Krizmanicc on behalf of the Telescope Array Collaboration, 37th Intrenational Cosmic Ray Conference, JUL 12-23 2021

22. ”Hotspot Update, and a new Excess of Events on the Sky Seen by the Telescope Array Experiment”, J. Kim, D. Ivanov, K. Kawata, H. Sagawa and G. Thomson on behalf of the Telescope Array Collaboration, 37th Intrenational Cosmic Ray Conference, JUL 12-23 2021

23. ”UHECR arrival directions in the latest data from the original Auger and TA surface detectors and nearby galaxies”, A. di Matteo, L. Anchordoqui, T. Bister, J. Biteau, L. Caccianiga, R. de Almeida, O. Deligny, U. Giaccari, D. Harari, J. Kim, M. Kuznetsov, I. Maris, , G. Rubtsov, P. Tinyakov, S. Troitsky and F. Urban on behalf of the Pierre Auger and the Telescope Array Collaboration, 37th Intrenational Cosmic Ray Conference, JUL 12-23 2021

24. ”The measurements of the cosmic ray energy spectrum and the depth of maximum shower development of Telescope Array Hybrid trigger events”, H. Shin on behalf of the Telescope Array Collaboration, 37th Intrenational Cosmic Ray Conference, JUL 12-23 2021

25. ”Cosmic-ray mass composition with the TA SD 12-year data”, Y. Zhezher on behalf of the Telescope Array Collaboration, 37th Intrenational Cosmic Ray Conference, JUL 12-23 2021

26. ”Mass composition anisotropy with the Telescope Array Surface Detector data”, Y. Zhezher on behalf of the Telescope Array Collaboration, 37th Intrenational Cosmic Ray Conference, JUL 12-23 2021

27. ”Measurement of the Proton-Air Cross Section with Telescope Arrays Black Rock, Long Ridge, and Surface Array in Hybrid Mode ”, R. Abbasi and W. Hanlon on behalf of the Telescope Array Collaboration, 37th Intrenational Cosmic Ray Conference, JUL 12-23 2021

28. ”UHECR mass composition from anisotropy of their arrival directions with the Telescope Array SD”, M. Kuznetsov and P. Tinyakov on behalf of the Telescope Array Collaboration, 37th Intrenational Cosmic Ray Conference, JUL 12-23 2021

29. ”Update on the large-scale cosmic-ray anisotropy search at the highest energies by the Telescope Array Experiment”, T. Fujii on behalf of the Telescope Array Collaboration, 37th Intrenational Cosmic Ray Conference, JUL 12-23 2021

30. ”The status of the TALE surface detector array and a TALE infill project”, A. Iwasaki and S. Ogio on behalf of the Telescope Array Collaboration, 37th Intrenational Cosmic Ray Conference, JUL 12-23 2021

31. ”Telescope Array Surface Detector Energy and Arrival Direction Estimation Using Deep Learning”, O.E. Kalashev, D. Ivanov, M.Yu. Kuznetsov, G.I. Rubtsov, T. Sako, Y. Tsunesada and Y. V. Zhezher on behalf of the Telescope Array Collaboration, 37th Intrenational Cosmic Ray Conference, JUL 12-23 2021

32. ”The atmospheric transparency of Telescope Array observation site by the CLF”, T. Tomida, T. Nakamura, K. Yamazaki, J. Matthews on behalf of the Telescope Array Collaboration, 37th Intrenational Cosmic Ray Conference, JUL 12-23 2021

33. ”Current status and prospects of surface detector of the TAx4 experiment”, E. Kido on behalf of the Telescope Array Collaboration, 37th Intrenational Cosmic Ray Conference, JUL 12-23 2021

34. ”Telescope Array Cloud Ranging Test”, T. Okuda on behalf of the Telescope Array Collaboration, 37th Intrenational Cosmic Ray Conference, JUL 12-23 2021

35. ”Highlights from the Telescope Array experiment”, G. I. Rubtsov on behalf of the Telescope Array Collaboration, 37th Intrenational Cosmic Ray Conference, JUL 12-23 2021

36. ”A simulation study for one-pion exchange contribution on very forward neutron productions in ATLAS-LHCf common events”, K. Ohashi, H. Menjo, Y. Itow and T. Sako, 37th Intrenational Cosmic Ray Conference, JUL 12-23 2021

37. ”Status and Prospects of the LHCf and RHICf experiments”, H. Menjo on behalf of the LHCf and RHICf Collaboration, 37th Intrenational Cosmic Ray Conference, JUL 12-23 2021

38. ”LHCf plan for proton-oxygen collisions at LHC”, E. Berti and L. Bonechib on behalf of the LHCf Collaboration, 37th Intrenational Cosmic Ray Conference, JUL 12-23 2021

39. ”Very-forward π^0 production cross section in $\sqrt{s}$ = 13 TeV measured with the proton-proton collisions at LHCf experiment”, A. Tiberio on behalf of the LHCf Collaboration, 37th Intrenational Cosmic Ray Conference, JUL 12-23 2021

40. ”High-redshift gamma-ray burst for unraveling the Dark Ages Mission - HiZ-GUNDAM -”, Yonetoku, D; Mihara, T; Doi, A; Sakamoto, T; Tsumura, K; Ioka, K; Amaya, Y; Arimoto, M; Enoto, T; Fujii, T; Goto, H; Gunji, S; Hiraga, J; Ikeda, H; Kawai, N; Kurosawa, S; Li, J; Maeda, Y; Mitsuishi, I; Murakami, T; Nakagawa, Y; Ogino, N; Ohno, M; Sawano, T; Sei, K; Serino, M; Sugita, S; Tamagawa, T; Tamura, K; Tanaka, T; Tanimori, T; Tashiro, MS; Tomida, H; Wang, H; Yamaguchi, T; Yamamoto, A; Yamaoka, K; Yamauchi, M; Yatsu, Y; Yoshida, A; Yuhi, D; Akitaya, H; Fukui, A; Ita, Y; Kaneda, H; Kawabata, K; Kawata, Y; Kurimata, M; Matsumoto, T; Matsuura, S; Miyasaka, A; Motohara, K; Narita, N; Noda, H; Ohashi, A; Okita, H; Sano, K; Tanaka, M; Urata, Y; Wada, T; Yamaguchi, H; Yanagisawa, K; Yoshida, M; Asano, K; Inayoshi, K; Inoue, S; Ito, H; Izumiura, H; Kawanaka, N; Kinugawa, T; Kisaka, S; Kiuchi, K; Kyutoku, K; Matsumoto, J; Mizuta, A; Murase, K; Nagakura, H; Nagataki, S; Nakada, Y; Nakamura, T; Niino, Y; Suwa, Y; Takahashi, K; Tanaka, T; Toma, K; Totani, T; Yamazaki, R; Yokoyama, J, Conference on Space Telescopes and Instrumentation - Ultraviolet to Gamma Ray / SPIE Astronomical Telescopes + Instrumentation Conference, DEC 14-18, 2020

41. ”Highlights from Gamma-ray Observation by the Tibet ASγ Experiment”, M. Takita on behalf of the Tibet ASγ Collaboration, 37th Intrenational Cosmic Ray Conference, JUL 12-23 2021

42. ”Sensitivity of the Tibet hybrid experiment (Tibet-III + MD) for primary proton spectrum between 30 TeV and a few hundreds of TeV’s”, D. Kurashige, D. Chen, N. Hotta, J. Huang, Y. Katayose, K. Kawata, M. Ohnishi, T. Saito, T. K. Sako, M. Shibata and M. Takita, 37th Intrenational Cosmic Ray Conference, JUL 12-23 2021

43. ”Observation of Ultra-High-Energy Diffuse Gamma Rays from the Galactic Plane with the Tibet Air Shower Array”, K. Kawata on behalf of the Tibet ASγ Collaboration, 37th Intrenational Cosmic Ray Conference, JUL 12-23 2021

44. ”Gamma-ray Observation of the Cygnus Region with the Tibet Air Shower Array”, Y. Katayose and T. K. Sako on behalf of the Tibet ASγ Collaboration, 37th Intrenational Cosmic Ray Conference, JUL 12-23 2021

45. ”A northern sky survey for ultra-high-energy gamma-ray source using the Tibet air-shower array and muon-detector array”, X. Chen on behalf of the Tibet ASγ Collaboration, 37th Intrenational Cosmic Ray Conference, JUL 12-23 2021

46. ”Gamma-ray Observation of SNR G106.3+2.7 with the Tibet Air Shower Array”, M. Ohnishi on behalf of the Tibet ASγ Collaboration, 37th Intrenational Cosmic Ray Conference, JUL 12-23 2021

47. ”Modeling of the TeV cosmic-ray anisotropy based on intensity mapping in an MHD-simulated heliosphere”, T. K. Sako on behalf of the Tibet ASγ Collaboration, and N. V. Pogorelov, 37th Intrenational Cosmic Ray Conference, JUL 12-23 2021

48. ”Current status of ALPACA for exploring sub-PeV gamma-ray sky in Bolivia”, T. Sako on behalf of the ALPACA Collaboration, 37th Intrenational Cosmic Ray Conference, JUL 12-23 2021

49. ”Half ALPACA and its sensitivity to sub-PeV gamma rays from the Galactic Center”, Y. Yokoe on behalf of the ALPACA Collaboration, 37th Intrenational Cosmic Ray Conference, JUL 12-23 2021

50. ”A simulation study on the performance of the ALPAQUITA experiment”, S. Kato on behalf of the ALPACA Collaboration, 37th Intrenational Cosmic Ray Conference, JUL 12-23 2021

51. ”Ultralight dark matter searches with KAGRA gravitational wave telescope”, Tomohiro Fujita, Jun’ya Kume, Yuta Michimura, Soichiro Morisaki, Koji Nagano, Hiromasa Nakatsuka, Atsushi Nishizawa, Ippei Obata,, TAUP 2021, AUG 26-SEP 23, 2021

52. ”A nonparametric method to assess the significance of events in the search for gravitational waves with false discovery rate”, Yuzurihara, H; Mano, S; Tagoshi, H, Conference on Space-Time Topology Behind Formation of Micro-Macro Magneto-Vortical Structure Manifested by Nambu Mechanics, SEP 28-OCT 01, 2020

D. Doctoral Theses

1. Search for Neutrinos associated with Solar Flares in Super-Kamiokande,
   OKAMOTO, Kouhei,
   Ph.D Thesis, Mar. 2022

2. Novel technique to purify liquid xenon for the XENONnT dark matter search experiment,
   KATO, Nobuyuki,
   Ph.D Thesis, Mar. 2022

3. Exploring the Frontiers of Low-mass Galaxy Formation over the Cosmic History,
   KIKUCHIHARA, Shotaro,
   Ph.D Thesis, Mar. 2022

4. Search for UHECR sources considering the deflection by the galactic magnetic field,
   HIGUCHI, Ryo,
   Ph.D Thesis, Mar. 2022

5. Imprints on Cosmic Microwave Background by WIMP and Axion,
   NAKATSUKA, Hiromasa,
   Ph.D Thesis, Mar. 2022

6. Concrete Models and Phenomenologies of Composite Asymmetric Dark Matter,
   KOBAYASHI, Shin,
   Ph.D Thesis, Mar. 2022

E. Public Relations

(a) ICRR News

ICRR News is a quarterly publication written in Japanese about scientific and educational activities at ICRR.

Below lists the main topics in the issues published in FY 2021:

No.111 (2021 Summer)

- Features : Professor Masato Takita Wins 67th Nishina Memorial Prize for ”Establishment of the sub-PeV gamma ray astronomy and elucidation of the origin of galactic cosmic rays”
- Features : Special Contribution by Jiro Aarafune, Former ICRR Director, ”From Kamiokande To Super-Kamiokande ∼ Remembering Prof. Masatoshi Koshiba ∼”
- Features : Gathering to remember Prof. Masatoshi Koshiba Held at Koshiba Hall in Hongo Campus
- Reports : About 2,300 People Enjoy Online Kashiwa Campus Open Days
- Reports : Super-Kamiokande and KAGRA Open Days Held Online
- Reports : ICRR’s Alumnae, Ms. Momoko Kashino Talks at Event for Female Students, ” Yappari Buturiga Suki”
- Topics : Dr. Oishi’s Recommended Book and Her Comment Displayed at Tamarokuto Scicence Center
- Topics : ICRR Calls for Participation in Spring School 2022
- Topics : Dr. Fedynitch (Telescope Array Group) Wins Best Poster Award at ICRC2021
- Topics : ICRR Calendar 2021 On Sale
- Topics : Annual Report 2020 Published
- Information : Staff Reassignment
- Information : ICRR Seminar

No.112 (2021-22 Winter)

- Features : ”Elucidating Origin of Matter and Evolution of Universe” Hyper-Kamiokande Co-Spokesperson, Prof. Masato Shiozawa
- Features : Associate Professor, Koji Noda Wins JSPS Prize for ”Study of Very High Energy Gamma Ray Emission from Gamma Ray Bursts”
- Reports : ICRR Holds UTokyoNY Event ”Exploring the Universe with Multi-Messengers”
- Reports : Project Assistant Prof. Takashi Sako Talks at Science Café held with Tamarokuto Science Center
- Reports : Assistance Professor Kyohei Kawaguchi Talks at 25th ICRR x IPMU Public Lecture
- Topics : FY2021 ICRR Master and Doctor Thesis Workshop Held Online
- Topics : ICRR and KEK Sign MOU with NCBJ in Poland to Promote Hyper-Kamiokande Project
- Topics : Professor Masami Ouchi Selected as a Highly Cited Researcher 2021
- Topics : ICRR Holds Online Lecture Meeting Commemorating Prof. Takita’s winning of Nishina Memorial Prize
- Topics : Dr. Seiji Fujimoto (formerly affiliated Observational Cosmology Group) Wins Inoue Research Award for Young Scientists
- Topics : CTA LST-1 Awarded European Technology Awards 2021
- Information : Staff Reassignment
- Information : ICRR Seminar

(b) Public Lectures

- ”Central Asia Nobel Fest,” Apr. 14, 2021, Online, Takaaki Kajita (ICRR, The University of Tokyo).
- ”5th Workshop on Korean Neutrino Observatory,” May. 10, 2021, Online, Takaaki Kajita (ICRR, The University of Tokyo).
- ”Public Lecture commemorating the 20th Anniversary of Museum Opening,” Jul. 3, 2021, Children’s Science Musium, Itano-Gun, Tokushima, Takaaki Kajita (ICRR, The University of Tokyo).
- ”Summer Festival for the 30th Anniversary of JSPS Washington Office,” Sep. 3, 2021, Online, Takaaki Kajita (ICRR, The University of Tokyo).
- ”Public Lecture for Junior High School Students in Higashimatsuyama City,” Sep. 28, 2021, Higashimatsuyama Citizen’s Culture Center, Higashimatsuyama-City, Saitama, Takaaki Kajita (ICRR, The University of Tokyo).
- ”Tsukuba Conference 2021,” Sep. 29, 2021, Online, Takaaki Kajita (ICRR, The University of Tokyo).
- ”All Russican Science Festival,” Oct. 9, 2021, Online, Takaaki Kajita (ICRR, The University of Tokyo).
- ”IEEE Nuclear Science Symposium plenary talk,” Oct. 18, 2021, Online, Takaaki Kajita (ICRR, The University of Tokyo).
- ”World Alliance Forum in San Francisco,” Nov. 16, 2021, Online, Takaaki Kajita (ICRR, The University of Tokyo).
- ”Public Lecture commemorating the 25th Anniversary of SK’s Observation,” Nov. 28, 2021, Spirit Garden Hall, Hida-City, Gifu, Takaaki Kajita (ICRR, The University of Tokyo).
- ”Nishina Memorial Public Lecture,” Dec. 5, 2021, Online, Takaaki Kajita (ICRR, The University of Tokyo).
- ”Forum for Graduate School Educational Reform 2021,” Jan. 8, 2022, Osaka University, Suita-City, Osaka, Takaaki Kajita (ICRR, The University of Tokyo).
- ”ISS/KIBO Utilization Symposium 2022,” Feb. 9, 2022, Online, Takaki Kajita (ICRR, The University of Tokyo).
- ”100th Anniversary of the municipal system of Kawagoe City,” Feb. 19, 2022, Westa Kawagoe, Kawagoe-City, Saitama, Takaaki Kajita (ICRR, The University of Tokyo).

- ”Summer Science Workshop for Tokatsu Techno Plaza,” Aug. 6, 2021, Online, Makio Nakamura (ICRR, The University of Tokyo).
- ””Let’s Talk with Researchers” for Kashiwa Campus Open Day,” Oct. 22, 2022, Online, ICRR, The University of Tokyo.
- ”Kashiwa Campus Open Day,” Oct. 23, 2021, Online, Takaaki Kajita, Yuhang ZHAO, Marcel STRZYS (ICRR, The University of Tokyo).
- ”Kashiwa Campus Open Day,” Oct. 24, 2022, Online, Kazumasa Kawata, Moritz Huetten, Masataka Miwa, Takuya Tashiro, Teruyoshi Kawashima (ICRR, The University of Tokyo).
- ”Tokyo Municipal Musashi High School,” Nov. 17, 2021, Musashi High School, Musashino-City, Tokyo, Yoshiaki Ono (ICRR, The University of Tokyo).
- ”The 25th ICRR X IPMU Public Lecture,” Nov. 28, 2021, Online, Kyohei Kawaguchi (ICRR, The University of Tokyo).
- ”Science Café for Tamarokuto Science Center,” Jan. 30, 2022, Online, Takashi Sako (ICRR, The University of Tokyo).
- ”UTokyoNY Event,” Feb. 12, 2022, Online, Hiroyuki Sagawa, Masato Takita, Masahiro Teshima, Hideyuki Tagoshi (ICRR, The University of Tokyo).
- ”The 24th ICRR X IPMU Public Lecture,” Apr. 10, 2021, Online, Yoichi Asaoka (Kamioka Observatory, ICRR, The University of Tokyo).
- ”Kyoto Prefectural Rakuhoku High School,” Jun. 3, 2021, Online, Yosuke Kataoka (Kamioka Observatory, ICRR, The University of Tokyo).
- ”Toyama High School,” Jul. 5, 2021, Toyama High School, Toyama-City, Toyama, Jun Kameda (Kamioka Observatory, ICRR, The University of Tokyo).
- ”Gifu Prefectural Yoshiki High School,” Jul. 9, 2021, Skydome Kamioka, Hida-City, Gifu, Ko Abe (Kamioka Observatory, ICRR, The University of Tokyo).
- ”Nanao High School & NUS High School,” Jul. 14, 2021, Online, Christophe Bronner (Kamioka Observatory, ICRR, The University of Tokyo).
- ”Fuzoku Shimada Junior High School,” Jul. 17, 2021, Online, Masato Shiozawa (Kamioka Observatory, ICRR, The University of Tokyo).
- ”Osaka Seiko Gakuin,” Jul. 19, 2021, Online, Hidekazu Tanaka (Kamioka Observatory, ICRR, The University of Tokyo).
- ”Kofu Minami High Shool / Senior High School Attached to Kyoto University of Education,” Jul. 27, 2021, Online, Makoto Miura (Kamioka Observatory, ICRR, The University of Tokyo).
- ”Yamanashi Prefectural Nirasaki High School,” Sep. 22, 2021, Online, Yosuke Kataoka (Kamioka Observatory, ICRR, The University of Tokyo).
- ””Let’s Talk with Researchers” for Kashiwa Campus Open Day,” Oct. 22, 2021, Online, Kamioka Observatory, ICRR, The University of Tokyo.
- ”Gifu Prefectural Museum’s Public Lecture,” Oct. 24, 2021, Gifu Prefectural Museum, Seki-City, Gifu, Masayuki Nakahata (Kamioka Observatory, ICRR, The University of Tokyo).
- ”Gathering in Memory of Professor Koshiba,” Nov. 7, 2021, Online, Masayuki Nakahata (Kamioka Observatory, ICRR, The University of Tokyo).
- ”Kyoto Prefectural Rakuhoku High School,” Nov. 11, 2021, Online, Motoyasu Ikeda (Kamioka Observatory, ICRR, The University of Tokyo).
- ”Public Lecture,” Nov. 13, 2021, Fuchu Fureai Kan, Toyama-City, Toyama, Masayuki Nakahata (Kamioka Observatory, ICRR, The University of Tokyo).
- ”Super-Kamiokande Open House,” Nov. 20, 2021, Online, Motoyasu Ikeda (Kamioka Observatory, ICRR, The University of Tokyo).
- ”Super-Kamiokande Open House,” Nov. 20, 2021, Online, Yuki Nakano, Shintaro Miki, Yuri Kashiwagi (Kamioka Observatory, ICRR, The University of Tokyo).

- ”Super-Kamiokande Open House,” Nov. 20, 2021, Online, Masayuki Nakahata (Kamioka Observatory, ICRR, The University of Tokyo).
- ”Super-Kamiokande Open House,” Nov. 20, 2021, Online, Kei Ieki (Kamioka Observatory, ICRR, The University of Tokyo).
- ”Super-Kamiokande Open House,” Nov. 20, 2021, Online, Hidekazu Tanaka (Kamioka Observatory, ICRR, The University of Tokyo).
- ”Super-Kamiokande Open House,” Nov. 20, 2021, Online, Masayuki Nakahata (Kamioka Observatory, ICRR, The University of Tokyo).
- ”Public Lecture commemorating the 25th Anniversary of SK’s Observation,” Nov. 28, 2021, Spirit Garden Hall, Hida-City, Gifu, Masayuki Nakahata (Kamioka Observatory, ICRR, The University of Tokyo).
- ”Gunma Prefectural Ota High School & Ota Girl’s High School,” Dec. 9, 2021, Online, Kei Ieki (Kamioka Observatory, ICRR, The University of Tokyo).
- ”Aichi Prefectural Okazakikita High School & Kariya Senior High School,” Dec. 28, 2021, Online, Hiroyuki Sekiya (Kamioka Observatory, ICRR, The University of Tokyo).
- ”Hyper-Kamiokande Online Lecture,” Jan. 15, 2022, Online, Masato Shiozawa (Kamioka Observatory, ICRR, The University of Tokyo).
- ”Public Lecture,” Jul. 21, 2021, Online, Yoshinari Hayato (Kamioka Observatory, ICRR, The University of Tokyo).
- ”Gifu Prefectural Association of Chairpersons of City Council,” Jul. 9, 2021, Furukawa Community Center, Hida-City, Gifu, Masayuki Nakahata (Kamioka Observatory, ICRR, The University of Tokyo).
- ”Public Lecture,” Feb. 25, 2022, Online, Masayuki Nakahata (Kamioka Observatory, ICRR, The University of Tokyo).
- ” 51st Astrophysics / Astrophysics Young Summer School,” Aug. 25, 2021, Online, Hiroyuki Sekiya (Kamioka Observatory, ICRR, The University of Tokyo).
- ”Public Lecture,” Oct. 8, 2021, Online, Hiroyuki Sekiya (Kamioka Observatory, ICRR, The University of Tokyo).
- ”UTokyo’s Lab Tour for High School Students,” Mar. 23, 2022, Online, Yoshinari Hayato (Kamioka Observatory, ICRR, The University of Tokyo).
- ”Open College in Hida,” Oct. 24, 2021, Hida Earth Wisdom Center, Masatake Ohashi (KAGRA Observatory, ICRR, The University of Tokyo).
- ”Open College in Hida,” Oct. 24, 2021, Hida Earth Wisdom Center, Shoichi Oshino (KAGRA Observatory, ICRR, The University of Tokyo).
- ”KAGRA Open House,” Nov. 20, 2021, Online, Masatake Ohashi (KAGRA Observatory, ICRR, The University of Tokyo).
- ”KAGRA Open House,” Nov. 20, 2021, Online, Hirotaka Yuzurihara (KAGRA Observatory, ICRR, The University of Tokyo).
- ”KAGRA Open House,” Nov. 20, 2021, Online, Kenta Tanaka and Chiaki Hirose (KAGRA Observatory, ICRR, The University of Tokyo)(KAGRA Collaborator)(Niigata University).
- ”Osaka Seiko Gakuin Junior/Senior Higsh School,” Jul. 20, 2021, Online, Takafumi Ushiba (KAGRA Observatory, ICRR, The University of Tokyo).
- ”Yamanashi Prefectural Nirasaki High School,” Sep. 29, 2021, Online, Takashi Uchiyama (KAGRA Observatory, ICRR, The University of Tokyo).
- ”Hida Kamioka High School,” Oct. 12, 2021, Online, Tatsuki Washimi (KAGRA Collaborator)(National Astronomical Observatory of Japan).
- ”Fukuoka Prefectural Tochiku Senior High School,” Mar. 28, 2022, Online, Masatake Ohashi (KAGRA Observatory, ICRR, The University of Tokyo).

- ”Toyama High School,” Jul. 5, 2021, Toyama High School, Shoichi Oshino (KAGRA Observatory, ICRR, The University of Tokyo).
- ”Gifu Prefecutral Yoshiki Senior High School,” Jul. 9, 2021, Skydome Kamioka, Hida-City, Gifu, Takaaki Yokozawa (KAGRA Observatory, ICRR, The University of Tokyo).
- ”Hida Kamioka High School,” Jun. 29, 2021, Hida Kamioka High School, Osamu Miyakawa (KAGRA Observatory, ICRR, The University of Tokyo).

(c) Visitors

Kashiwa Campus (Total: 4 groups, 43 people)

- Junior High and High schools: 0 group
- Universities and Graduate schools: 0 group
- Researchers: 2 group
- Inspections: 1 groups
- Press: 1 groups
- Others: 0 group

KAMIOKA Observatory (Total: 32 groups, 155 people)

- Junior High and High schools: 0 group
- Universities and Graduate schools: 3 groups
- Researchers: 8 groups
- Inspections: 14 groups
- Press: 3 groups
- Others: 4 groups

KAGRA Observatory (Total: 31 groups, 143 people)

- Junior High and High schools: 0 group
- Universities and Graduate schools: 7 groups
- Researchers: 2 groups
- Inspections: 13 groups
- Press: 3 group
- Others: 6 groups

F. Inter-University Research Activities

Numbers of Researchers

		Number of Applications	Number of Adoptions	Number of Researchers
Facility Usage				
Kamioka Observatory	Domestic	45	45	1,755
	International	9	9	48
Akeno Observatory	Domestic	6	6	181
	International	2	2	27
Norikura Observatory		11	11	82
Primary Cosmic rays, Kashiwa underground facility		3	3	14
KAGRA Observatory	Domestic	22	22	612
	International	6	6	27
High Energy Astrophysics Facility in Canarias	Domestic	11	11	416
	International	1	1	2
Laboratorial Facilities in Kashiwa		1	1	7
Large-Scale Comping System in Kashiwa	Domestic	14	14	269
	International	1	1	10
Conference Facilities in Kashiwa	Domestic	6	6	267
	International	1	1	5
Overseas Facilities (Utah, Tibet and Bolivia)	Domestic	17	17	207
	International	5	5	40
Annual Sums	Domestic	136	136	3,810
	International	25	25	159

Joint Research				
Neutrino and Astroparticle Research	Domestic	45	45	1,755
	International	10	10	58
High Energy Cosmic Ray Research	Domestic	60	60	1,306
	International	9	9	74
Astrophysics and Gravity Research	Domestic	25	25	687
	International	6	6	27
Research Center for Cosmic neutrinos		6	6	62
Annual Sums	Domestic	136	136	3,810
	International	25	25	159

Research Project Titles

1. Astroparticle physics using the Super-Kamiokande detector
2. Study of atmospheric neutrino flux and neutrino oscillations
3. Study of simulation for atmospheric neutrino
4. Studying the Neutrino Mass Hierarchy With Atmospheric Neutrinos
5. Study of flavor identification of atmospheric and beam neutrinos
6. Study of solar neutrino energy spectrum
7. Precise measurement of Day/Night effect for ^8B solar neutrinos
8. Study for Supernova monitor
9. Study of Supernova Relic Neutrinos

10. Search for proton decay via $e^+\pi^0$ mode
11. Study of proton decay p $\rightarrow \nu K^+$
12. Study in upward-going muons and high energy neutrinos
13. Sidereal daily variation of $\sim$10TeV galactic cosmic ray intensity observed by the Super-Kamiokande
14. Neutrino search associated with astronominal transient events
15. Measurement of charge ratio and polarization of cosmic ray muon using undergraund particle physics experiments
16. Tokai to Kamioka Long Baseline Experiment T2K
17. Neutrino interaction study using accelerator data
18. Study for improvement of neutrino oscillation measurement in T2K expriment
19. Joint Oscillation Analysis With the T2K and Super-Kamiokande Experiments
20. Energy calibration for Super-Kamiokande
21. Development of a new LINAC for Super-Kamiokande energy calibration
22. Research and development of computer simulation of Super-Kamiokande detector
23. Development of low concentration radon detection system
24. Hyper-Kamiokande project
25. Development of the Large Aperture Photodetector for a next-generation neutrino detector
26. Development of software for the next generation neutrino detector
27. Measurement of radon in underground laboratories and evaluate of effects from radon to experiments
28. Study for lowering backgrounds of radioisotopes in large volume detectors
29. Development of a radioactivity assay system for underground experiments
30. Measurement of neutron flux at the Kamioka underground laboratory
31. Trace level radio-activity measurements for SK and underground experiments with an ICP-mass spectrometer
32. RI measurement for SK-Gd project with HPGe detector
33. Generation three direct dark matter search experiment
34. A Search for Dark Matter using Liquid Xenon Detector
35. Detector structure study for future direct dark matter search experiment
36. Development of low radioactivity molecular sieves for dark matter search experiment
37. Research and Development for XENONnT and future Dark Matter searches
38. Direction-sensitive dark matter search
39. A study on the near-infrared emission of liquid xenon
40. Study of double beta decay of ^{48}Ca
41. Studies on the background evaluation using laser spectroscopy analysis
42. Integration of crustal activity observation around the Atotsugawa fault
43. Strain, tilt, seismic measurement in Kamioka-mine
44. Searches for neutrinoless double beta decay with high-pressure Xenon gas detector
45. Soft-error-rate estimation for semiconductor device at underground laboratory

46. R&D for a Small Atmospheric Cherenkov Telescope in Akeno Observatory
47. Development of new surface detector for observation
48. Multi-Color Imager for Transients, Survey and Monstrous Explosions
49. Observation of Galactic Cosmic Ray Intensities using Large Area Muon Telescopes
50. Observation of solar neutrons in solar cycle 25
51. Space weather observation using muon hodoscope at Mt. Norikura
52. Observation of cosmogenic nuclides concentrations at Mt. Norikura
53. Study of secondary cosmic rays from Thundercloud at Mt. Norikura
54. Development of high energy proton irradiation technique for devices used in spaceship
55. Investigation of alpine plants on Mt. Norikura
56. Symbiosis betweem Pinus pumila and Nucifraga caryocatactes on Mt.Norikura
57. Atmospheric mercury speciation dynamics and mercury wet deopsition monitoring at the high-altitude
58. Patch dynamics of Pinus pumila and Vaccinium vitis-idaea at the ridge site of Mt. Norikura
59. Evaluation of atmospheric SO2 to cloud acidification at free troposhere through atmospheric observation at Mt. Norikura
60. Test exepriment of the Fuel cell in Norikura
61. CTA Project
62. Development of Focal Plane Instruments for the CTA Large Sized
63. Development of the readout system for the CTA large sized telescopes
64. Engineering runs of the first Large Size Telescope of CTA and construction of LST2-4 in La Palma Canary Islands, Spain
65. Set-up and Commissioning of the onsite data center for CTA North in La Palma, Spain
66. Localization of very high energy gamma-ray emission region in an active galactic nuclei
67. Development of SiPM modules for CTA-LST
68. Development of the CTA/LST telescope control system
69. Integration and operation of the optical and power systems in CTA LST
70. CTA-Japan Physics Research
71. Development of analysis method and initial observation with CTA Large-Sized Telescope
72. The extreme Universe viewed in very-high-energy gamma rays 2021
73. Development of camera for CTA small-sized telescopes
74. CTA Monte Carlo Simulation
75. Study of High Energy Gamma-ray Objects with the MAGIC telescope
76. Study of Extremely-high Energy Cosmic Rays by Telescope Array
77. R&D of the measurement of atmospheric transparency at the Telescope Array site
78. Research and development of surface detectors for the stable run of the TAx4 experiment
79. Study of very high energy cosmic rays around 10^{17}eV with the TALE hybrid experiment
80. Evaluation of optical system calibration for fluorescence detector optical system with standard light source mounted on UAV

81. Development and analysis of night cloud observation by CCD camera for automatic observation of air fluorescence detector
82. Development of the local center for the fully remote operation of TA-FD
83. Observation of airshower fluorescence light at the TA FD site by using an Imaging UV telescope
84. Observing ultrahigh-energy cosmic rays with new fluorescence detectors at Telescope Array site
85. Research and development of a Fresnel lens air fluorescence telescope for the next generation UHECR observation
86. The position measurement of radiation by one-side readout scintillation detector
87. Experimental Study of High-energy Cosmic Rays in the Tibet ASγ experiment
88. Sidereal daily variation of $\sim$10TeV galactic cosmic ray intensity observed by the Tibet air shower array
89. Study of the composition of cosmic-rays at the Knee
90. A study on variation of interplanetary magnetic field with the cosmic-ray shadow by the sun
91. Air shower observation for high-energy gamma ray and cosmic ray detections at the Chacaltaya Cosmic Ray Observatory
92. Study of High Energetic Radiation from Thundercloud in the Altiplano
93. Study of solar magnetic fields using the cosmic-ray Sun's shadow observed at the southern hemishpere
94. Study of high-energy cosmic-ray anisotropy at the Chacaltaya Cosmic Ray Observatory
95. Development of an advanced Compton camera using SOI pixel semiconductor
96. Design study of a Compton camera for study of cosmic rays
97. Study on High Energy Cosmic-ray Sources by Observations in Space with CALET
98. comprehensive study of high-energy astrophysical phenomena
99. Development of a new code for cosmic-ray air shower simulation
100. Cosmic ray interactions in the knee and the highest energy regions
101. Study of Fast Moving Dark Matters and Meteoroids using High Sensitivity CMOS Camera System
102. Preparatory Activities by the Local Organizing Committee for the 38th International Cosmic Ray Conference
103. YMAP symposium 2021 (Basic Part)
104. Observation with Ahsra
105. Integration of the optical fiber trigger system for Ashra
106. Research of Large-scale Gravitational wave Telescope (XI)
107. Study of Gravitational-wave by cryogenic laser interferometer CLIO in KAMIOKA Mine(V)
108. Development of High Performance Cryogenic Mirror Control System
109. Research on cryogenic payload for KAGRA
110. Deveropment of conduction cooling schemes for KAGRA
111. R&D for the intensity stabilization of the laser system in KAGRA
112. Development of scattered light measurement technique and noise reduction for improving sensitivity in KAGRA II
113. Development of optical cavity for ultranarrow stable lasers
114. Study of Environmental Noise Reduction in KAGRA
115. Study of the investigation methed for the envieronmental noises by injection in KAGRA detector

116. Noise characteristics analysis using machine learning and deep learning and its application to interferometer diagnosis
117. Improving the reliability of KAGRA gravitational wave data by using machine learning technique for glitch detection
118. Calorimetric measurement of absorption coefficient of sapphire at cryogenic temperatures
119. Numerical Simulation of Electro-Magnetic Wave Propagation in Gravitational wave Detector IX
120. Development of a high performance sapphire mirror suspension
121. Control and automatic operation for KAGRA
122. Construction of KAGRA data transfer and storage system (7)
123. Promotion of collaborative research to incorporate KAGRA data into the low latency international gravitational wave search network
124. Construction of the interferometer diagnostic system for gravitational waves searches
125. Promotion of KAGRA scientific collaboration, and development of new methods in gravitational data analysis
126. Search for poorly modeled gravitational wave signal using KAGRA II
127. Environmental investigation for underground gravity measurement at micro-meter scale
128. Precise geophysical observation at the Kamioka underground site and modeling of crustal activities
129. Cosmic Reionization and Galaxy Formation Probed with Large Optical Near-Infrared Telescopes
130. Evolution of the universe and particle physics
131. Detection of time variations for cosmogenic nucleid Be-7
132. Time profile of radioactive Cs concentration and its aerosol size distribution in local area
133. Development of the observation templates of supernova neutrinos considering nuclear equations of state
134. Behavior of radionuclides in the marine environment
135. Frontier of the planetary material science
136. Precise calculation of the atmospheric neutrino flux
137. Light scattering measurement in the water using the Super-Kamiokande detector
138. Search for the nucleon decay including multi pions in Super-Kamiokande
139. New Photogrammetry Calibration and Machine Learning Event Reconstruction for Super-Kamiokande and Hyper-Kamiokande
140. Study of supernova neutrinos in Super-Kamiokande
141. Data Taking, Calibrations, Measurements and Analysis with Super-Kamiokande I - VI
142. Constraining systematics at T2K and SuperKamiokande oscillation analyses using neutrino-nucleus interaction models
143. Development and testing of cost-effective, high-performance PhotoDetector anti-implosion covers for Hyper-Kamiokande
144. Outer Detector for the Hyper-Kamiokande experiment
145. Seal, mechanical and functional tests on the mPMT prototype for external vessel optimizzations
146. Towards a multiphysics liquid Xe TPC with scintillation and charge multiplication readouts
147. A joint observation of near earth space through $\sim$100 GeV cosmic rays using the Akeno and the GRAPES-3 muon telescope
148. Neutrino Telescope Array Light Collector Prototype Test
149. Ultra-high-energy cosmic-ray origin studies with the Telescope Array and TAx4 surface detector

150. Study of the Origin and Nature of Ultra High Energy Cosmic Rays with the Telescope Array
151. Study of Anisotropy of Ultra High Energy Cosmic Rays with Telescope Array and TAx4
152. Understanding the signatures of cosmic ray feedback in the diffuse extra-galactic gamma-ray background with CTA
153. Kashiwa Dark Matter symposium 2021
154. Study of high-energy cosmic rays at a high altitude in Tibet, China
155. Study for Galactic CR origin using the ALPACA air shower array in Bolivia
156. Noise Evaluation and Reduction of Cryogenic Mirror Suspension System in KAGRA
157. Intermediate stage for future cryogenic payload development
158. Filter cavity experiments for the frequency dependent squeezed light source for KAGRA
159. Implementing Sophisticated Data Analysis Methods on KAGRA Data
160. Collaboration for gravitation wave observatory in study dark matter with compact binary coalescence
161. Experimental research on gravitational-wave astrophysics with TOBA

G. List of Committee Members

(a) Board of Councillors

KAJITA, Takaaki	ICRR, The University of Tokyo
SHIOZAWA, Masato	ICRR, The University of Tokyo
TAKITA, Masato	ICRR, The University of Tokyo
KAWASAKI, Masahiro	ICRR, The University of Tokyo
HOSHINO, Masahiro	Graduate School of Science, The University of Tokyo
SAITO, Nobuhito	The University of Tokyo
TOKUSHUKU, Katsuo	Institute of Particle and Nuclear Studies, KEK
AOKI, Shinya	Yukawa Institute for Theoretical Physics, Kyoto University
TSUNETA, Saku	National Astronomical Observatory of Japan
TORII, Shoji	Faculty of Science and Engineering, Waseda University
MORI, Masaki	Ritsumeikan University
YOKOYAMA, Junichi	Research Center for the Early Universe, The University of Tokyo
YAMADA, Toru	Institute of Space and Astronautical Science
ASAI, Shoji	International Center for Elementary Particle Physics, The University of Tokyo
KUSANO, Kanya	Institute for Space-Earth Environmental Research, Nagoya University

(b) Advisory Committee

KAJITA, Takaaki	ICRR, The University of Tokyo
KITANO, Ryuichiro	KEK Theory Center
IOKA, Kunihito	Yukawa Institute for Theoretical Physics, Kyoto University
ISHITSUKA, Masaki	Tokyo University of Science
OZAWA, Kyoichiro	Institute of Particle and Nuclear Studies, KEK
YOKOYAMA, Masashi	Graduate School of Science, The University of Tokyo
TASHIRO, Makoto	Graduate School of Science and Engineering, Saitama University
OGIO, Shoichi	Graduate School of Science, Osaka City University
NISHIJIMA, Kyoshi	Tokai University
ITOW, Yoshitaka	Institute for Space-Earth Environmental Research, Nagoya University
KANDA, Nobuyuki	Graduate School of Science, Osaka City University
NAKAHATA, Masayuki	ICRR, The University of Tokyo
SAGAWA, Hiroyuki	ICRR, The University of Tokyo
KAWASAKI, Masahiro	ICRR, The University of Tokyo
SHIOZAWA, Masato	ICRR, The University of Tokyo
TAKITA, Masato	ICRR, The University of Tokyo
OHASHI, Masatake	ICRR, The University of Tokyo
TESHIMA, Masahiro	ICRR, The University of Tokyo

(c) Inter-University Research Advisory Committee

ITOW, Yoshitaka	Institute for Space-Earth Environmental Research, Nagoya University
ASO, Yoichi	National Astronomical Observatory of Japan
MORI, Masaki	Ritsumeikan University
TAJIMA, Hiroyasu	Institute for Space-Earth Environmental Research, Nagoya University
KUBO, Hidetoshi	Kyoto University
HIBINO, Kinya	Kanagawa University
MIUCHI, Kentaro	Graduate School of Science, Kobe University
TSUNESADA, Yoshiki	Graduate School of Science, Osaka City University
NAKAHATA, Masayuki	ICRR, The University of Tokyo
TAKITA, Masato	ICRR, The University of Tokyo
TAGOSHI, Hideyuki	ICRR, The University of Tokyo
NODA, Koji	ICRR, The University of Tokyo
UCHIYAMA, Takashi (Organizer)	ICRR, The University of Tokyo
KAJITA, Takaaki (Observer)	ICRR, The University of Tokyo

H. List of Personnel

Director
KAJITA, Takaaki,

Vice-Director
NAKAHATA, Masayuki, SAGAWA, Hiroyuki,

ICRR HQ in Kashiwa Campus

- High Energy Cosmic Ray Division

Scientific Staff	ASANO, Katsuaki,	DE LA FUENTE, Eduardo,	ENOMOTO, Ryoji,
	FIASSON, Armand,	HADASCH, Daniela,	KAWATA, Kazumasa,
	KINUGAWA, Tomoya,	KUBO, Hidetoshi,	MAZIN, Daniel,
	NODA, Koji,	NONAKA, Toshiyuki,	OGIO, Shoichi,
	OHISHI, Michiko,	OHNISHI, Munehiro,	SAITO, Takayuki,
	SAKO, Takashi,	SAKO, Takashi,	SASAKI, Makoto,
	SITAREK, Julian,	TAKEDA, Masahiro,	TAKITA, Masato,
	TESHIMA, Masahiro,	VOVK, Ievgen,	YAMAMOTO, Tokonatsu,
	YOSHIDA, Tatsuo,	YOSHIKOSHI, Takanori,	
Technical Staff	AOKI, Toshifumi,	MARUYAMA, Tatsuya,	OHOKA, Hideyuki,
	SEKINO, Koichi,		
Research Fellow	ANZORENA, Marcos,	CERIBELLA, Giovanni,	CHIKAWA, Michiyuki,
	COLOMBO, Eduardo,	FEDYNITCH, Anatoli,	FUKAMI, Satoshi,
	HUETTEN, Moritz,	INADA, Tomohiro,	KAWASHIMA, Tomohisa,
	MARQUEZ, Paniagua Patricia,	NAKAMURA, Yoshiaki,	OHMURA, Takumi,
	STRZYS, Marcel,	TAKAHASHI, Mitsunari,	TAKEISHI, Ryuji,
	ZHEZHER, Yana Valeryevna,		
Secretary	IDOMURA, Takako,	SHIRAGA, Ryoko,	SUGAHARA, Midori,

- Astrophysics and Gravity Division

Scientific Staff	HARIKANE, Yuichi,	IBE, Masahiro,	KAWASAKI, Masahiro,
	ONO, Yoshiaki,	OUCHI, Masami,	
Research Fellow	AOYAMA, Shohei,	EIJIMA, Shintaro,	UMEHATA, Hideki,

Kamioka Observatory

Director	NAKAHATA, Masayuki,		
Scientific Staff	ABE, Ko,	ASAOKA, Yoichi,	BRONNER, Christophe,
	GONIN, Michel,	HAYATO, Yoshinari,	HIRAIDE, Katsuki,
	HOSOKAWA, Keishi,	IEKI, Kei,	IKEDA, Motoyasu,
	ITOW, Yoshitaka,	KAMEDA, Jun,	KATAOKA, Yosuke,
	MIURA, Makoto,	MORIYAMA, Shigetaka,	NAKANO, Yuki,
	NAKAYA, Tsuyoshi,	NAKAYAMA, Shoei,	NISHIMURA, Yasuhiro,
	PRONOST, Guillaume,	SATO, Kazufumi,	SEKIYA, Hiroyuki,
	SHIOZAWA, Masato,	TAKEDA, Atsushi,	TAKEMOTO, Yasuhiro,
	TANAKA, Hidekazu,	YANO, Takatomi,	
Administrative Staff	YOSHIDA, Takuto,		
Public Relations Staff	TAKENAGA, Yumiko,		
Technical Staff	HAMA, Satoshi,	HIGASHI, Tetsuji,	ISHITA, Katsumi,
	NOZAWA, Noriyuki,	ONOUE, Tatsuya,	
Research Administrator	KURACHI, Masafumi,		
Research Fellow	TAKENAKA, Akira,		
Secretary	DOI, Kyoko,	KAMIKAWATO, Rie,	MAEDA, Yukari,
	NISHIDA, Hiromi,		

KAGRA Observatory

Director	OHASHI, Masatake,		
Scientific Staff	KAWAGUCHI, Kyohei,	KIMURA, Nobuhiro,	MIO, Norikatsu,
	MIYAKAWA, Osamu,	MIYOKI, Shinji,	OSHINO, Shoichi,
	TAGOSHI, Hideyuki,	TAKAHASHI, Hirotaka,	TOMARU, Takayuki,
	UCHIYAMA, Takashi,	USHIBA, Takafumi,	YAMAMOTO, Kazuhiro,
	YAMAMOTO, Takahiro,	YOKOZAWA, Takaaki,	YOSHII, Yuzuru,
Administrative Staff	FUNADA, Shinya,	OKINAKA, Mihoko,	
Technical Staff	AOUMI, Masakazu,	KAMIIZUMI, Masahiro,	NAKAGAKI, Koji,
	NODE, Ayako,	OMAE, Akio,	PENA ARELLANO, Fabian,
	SAKAI, Akiko,	SAKAMOTO, Eri,	SHIMODE, Katsuhiko,
	TAKAHASHI, Masahiro,	TAKASE, Takashi,	YASUI, Hiromi,
	YOSHIMURA, Mitsuharu,		
Research Fellow	MIYO, Koseki,	NARIKAWA, Tatsuya,	OHHARA, Kenichi,
	SAITO, Yoshio,	SURESH, Jishnu,	SUZUKI, Toshikazu,
	TANIOKA,Satoshi	TUYENBAHEV, Darkhan,	UCHIKATA, Nami,
	YUZURIHARA, Hirotaka,	ZHAO, Yuhang,	
Secretary	KIKUCHI, Rie,	KUDO, Naomi,	NOJIRI, Midori,

High Energy Astrophysics Facility in Canarias

Director	TESHIMA, Masahiro,

Research Center for Cosmic Neutrinos

Director	OKUMURA, Kimihiro,		
Scientific Staff	KAJITA, Takaaki,	TASHIRO, Takuya,	TOKANAI, Fuyuki,
Technical Staff	SHINOHARA, Masanobu,		
Secretary	KITSUGI, Atsuko,	MASHIMA, Chieko,	

Norikura Observatory

Director	TAKITA, Masato,		
Technical Staff	AWAI, Kyosuke,	HAYAKAWA, Hideaki,	IMANISHI, Hidenori,
	INOME, Yusuke,	OKAZAKI, Nao,	SHIMODAIRA, Hideaki,
	TOMURA, Tomonobu,	USHIMARU, Tsukasa,	

Akeno Observatory

Director	SAGAWA, Hiroyuki,
Technical Staff	KOBAYASHI, Ryoichi,

Graduate Students

Doctor	ABE, Hyuga,	FUJISUE, Kozo,	HAN, Seungho,
	HIGUCHI, Ryo,	HSIEH, Bin-Hua,	ISOBE, Yuki,
	KATO, Nobuyuki,	KATO, Sei,	KATO, Takashi,
	KIKUCHIHARA, Shotaro,	KOBAYASHI, Shin,	KOBAYASHI, Yukiho,
	LEE, Eunsub,	MURAI, Kai,	NAKATSUKA, Hiromasa,
	NAKAYAMA, Yuhei,	NISHIWAKI, Kosuke,	OHTANI, Yoshiki,
	OKAMOTO, Kohei,	OTANI, Francis,	SAKURAI, Shunsuke,
	SHIN, Heungsu,	SONODA, Yutaro,	TANAKA, Kenta,
	TANG, Shenli,	XIA, Junjie,	YOKOE, Yoshichika,
	ZHANG, Yechi,		

Master	ABE, Shotaro,	ABOUNNASR-MARTINS, Théo,	BAXTER, Joshua Ryo,
	CHIBA, Renichi,	GARG, Suyog,	GOTO, Ryota,
	HASHIYAMA, Kazuaki,	IMAGAWA, Kaname,	IWAYA, Masaki,
	KANAMORI, Shotaro,	KANEMURA, Yuki,	KANESHIMA, Ryota,
	KASAI, Kentaro,	KASHIWAGI, Yuri,	KAWASHIMA, Teruyoshi,
	KIBUKAWA, Hirofumi,	KUSAFUKA, Yo,	MATSUMOTO, Akinori,
	MIKI, Shintaro,	MISHIMA, Masataka,	MIWA, Masataka,
	MIYAZAKI, Kazuyoshi	OKIMOTO, Naoya,	SATO, Yuta,
	SHIBA, Hayato,	SHIMIZU, Kotaro,	SHIMODATE, Karin,
	SUGIYAMA, Takumu,	SUN, Dongsheng,	SUZUKI, Ryota,
	TAKAHASHI, Kaoru,	TAMAKI, Masahide,	TOMIYA, Takuya,
	UMEDA, Hiroya,	WANG, Xubin,	WATANABE, Shuhei,
	WATANABE, Keiichi,	XU, Yi,	YAN, Haochen,
	YOSHIDA, Shunsuke,		

Administrative Division

Administrative Staff	AKAIDA, Yohei,	AKASHI, Yoko,	AKIYAMA, Makiko,
	FUKUHARA, Nana,	HIRAGA, Takuya,	ISHIZUKA,Yasushi,
	MARUMORI, Yasuko,	NAKAYA, Yukiko,	OKANO, Yuka,
	ONO, Kazumi,	SAEKI, Yuya,	SAITO, Akiko,
	SATO, Hiroki,	TAKAMICHI, Ryo,	WATANABE, Shinji,
	YAMADA, Takaharu,	YAMAGISHI, Yukinao,	YAMAGUCHI, Akiko,
	YAMASUE, Akiko,		
Research Administrator	ITO, Michiru,	SATO, Ritsuko,	SUGIMOTO, Kumiko,
Public Relations Staff	ITO, Yoriko,	NAKAMURA, Makio,	
Archive Room	NAKAMURA, Kenzo,		

INSTITUTE FOR COSMIC RAY RESEARCH
THE UNIVERSITY OF TOKYO

Address 5-1-5, Kashiwanoha, Kashiwa-shi, Chiba, 277-8582 Japan
TEL +81-4-7136-3102
FAX +81-4-7136-3115
URL www.icrr.u-tokyo.ac.jp